Structure and growth of germanene and silicene on Ag and Al surfaces

Kai Zhang

▶ To cite this version:

Kai Zhang. Structure and growth of germanene and silicene on Ag and Al surfaces. Materials Science [cond-mat.mtrl-sci]. Sorbonne Université, 2021. English. NNT : 2021SORUS438 . tel-03589900v2

HAL Id: tel-03589900

https://theses.hal.science/tel-03589900v2

Submitted on 13 Jul 2022

Sorbonne Université

Ecole doctorale

Physique et chimie des matériaux

ED397

Institut des NanoSciences de Paris

Physico-chimie et dynamique des surfaces

Structure and growth of germanene and silicene on Ag and Al surfaces

Par M. Kai Zhang

Thèse de doctorat de PHYSIQUE

présentée et soutenue publiquement le 18/10/2021

Devant un jury composé de :

M. Yann Girard	Maître de conférences	Rapporteur
M. Gilles Renaud	Ingénieur	Rapporteur
Mme. Marie Dangelo	Maître de conférences	Examinatrice
Mme. Laurence Masson	Professeure	Examinatrice
M. Andrew Mayne	Directeur de recherche	Examinateur
M. Geoffroy Prévot	Directeur de recherche	Directeur de Thèse
M. Romain Bernard	Maître de conférences	Invité

Lorsque j'ai vu votre lettre d'admission, je vous ai demandé quelle était l'histoire de cette lettre. Et vous ne m'en avez pas parlé. Heureusement, je continue votre histoire aujourd'hui… 如你所愿笨鸟要飞起来了 …

À mes très chers maman et papa

Acknowledgements

Foremost, I would like to express my sincere gratitude my supervisor Geoffroy Prévot, for the continuous support of my PhD research, but also for his patience, motivation and enthusiasm. He provides me an excellent experiment platform supported my PhD study. His strictness has deeply influenced me. As a foreigner, it's not easy for me to study in France. Once again, I am deeply grateful to my supervisor.

I would like to acknowledge to the other people who helps me in my research project, Yves Borensztein and Romain Bernard. Likewise, I would like to thank Sébastien Royer for his help and his guidance in setting up the apparatus. I would like thank to all the people in the research unit "PHYSUF". I would like to personally acknowledge Pedro Lourenco for encouraging me.

I would like to acknowledge all my collaborators, Pr. Carmelo Pirri (Université de Haute Alsace), Mickaël Derivaz (IS2M, Mulhouse), Philippe Sonnet (IS2M, Mulhouse), Pr. Laurence Masson (Aix Marseille Université), Davide Sciacca (IEMN, Lille) and the team of SIXS beamline (Synchrotron SOLEIL) for their excellent experimental work.

I would like to thank Dr. Yann Girard and Dr. Gilles Renaud for accepting to report my thesis work and Dr. Laurence Masson, Dr. Andrew Mayne, Dr. Marie Dangelo to join the jury of my thesis defense. A great thanks to China Scholarship Council for awarding the scholarship, which supported my study in France as a PhD student.

Finally, I would like to say a special thank you to my parents, Zhangqing Zhang and Chunjiao Zhou for supporting me all the time. Special thanks to *ma chérie,* Chaojun Tang for her support and her love.

Abstract

The thesis begins with the general introduction of the context of this subject. In this part, the advent of graphene and its properties and the studies of other 2D materials are presented. This is followed by a detailed state of art of silicene and germanene researches. Regarding the growth of Ge on Al(111) or Ag(111), some studies have reported the formation of germanene on the substrate, whereas some studies have suggested the formation of a surface alloy. This thesis provides evidence of the formation of a surface alloy. Chapter 3 give a detailed description of experimental techniques that were used to obtain data, namely scanning tunneling microscopy (STM), Low energy electron diffraction (LEED), and grazing incidence X-ray diffraction (GIXD).

Chapter 4 presents the growth of Ge on the Al(111) surface kept at a fixed temperature in a range of 300K to 360K. Ge evaporation on Al(111) leads to the formation of two reconstructions with one protrusion in the hexagonal unit cell, namely the (3×3) and (√7×√7) structure. From a precise analysis of the in-situ STM image, the relationship between the coverage of the reconstruction and the outgrowth suggests the formation of a surface alloy. The results of combined GIXD measurements and DFT simulations shows that the (3×3) reconstruction corresponds to a two-layer Ge-Al surface alloy.

Chapter 5 reports the growth of submonolayer Ge on Ag(111). Depending upon Ge coverage, Ge deposition on Ag(111) results in the formation of the different surface phases. By the in-situ STM images, the relationship between Ag concentration and Ge coverage give evidence of the formation of a Ge-Ag surface alloy. A combined GIXD measurements and DFT calculations reveals that the structure of striped phase corresponds to the Ag_2Ge surface alloy.

Finally, Chapter 6 concerns the growth of additional Si on the (5×2)/c(10×2) superstructure grown on Ag(110) at a growth temperature of 483K. I demonstrate the existence of a dumbbell silicene honeycomb structure, by means of GIXD measurements and DFT calculations.

Keywords: silicene, silicon, germanene, germanium, surface alloy, scanning tunneling microscopy (STM), grazing incidence X-ray diffraction (GIXD), growth, reconstruction

Résumé substantiel

Dans cette thèse, je présente les études portant sur la structure et la croissance du germanène et du silicène sur des surfaces d'argent et d'aluminium que j'ai menées au cours de mon doctorat. Cette thèse se compose de six chapitres. Dans les deux premiers chapitres, j'introduis la recherche et je présente les résultats antérieurs à mes travaux. Dans le chapitre 3, je décris en détail les techniques expérimentales utilisées et les méthodes d'analyse des données. Dans les chapitres suivants (chapitre 4-6), je présente les résultats de ma recherche sur la croissance de germanène sur la surface Al(111), sur la croissance de germanène sur la surface Ag(111), et sur la croissance de silicene sur la surface Ag(110) respectivement. Le dernier chapitre résume mes conclusions et présente quelques perspectives.

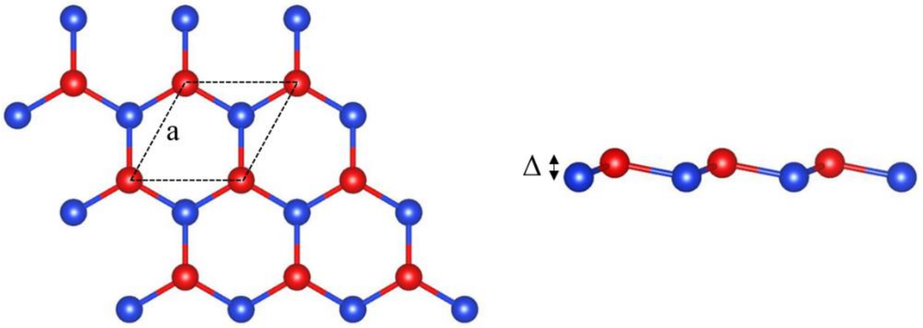

Figure 1 Vue de dessus (à gauche) et latérale (à droite) de la structure du silicène autoportant. La structure est constituée de deux sous-réseaux non équivalents (rouge et bleu) avec une corrugation Δ et la constante de réseau a pour la cellule unitaire (losange en pointillé)

J'aimerais évoquer dans la suite plusieurs points essentiels de ma thèse. Les études théoriques que je mentionne dans le deuxième chapitre de ma thèse prévoient l'existence du silicène et du germanène autoportants (comme le graphène), qui sont respectivement constitué des réseaux hexagonaux 2D de Si et de Ge (v. Fig. 1). Différents du graphène, le silicène ou le germanène en couche n'existent pas dans la nature. La synthèse de ces matériaux peut être réalisée par dépôt sur un substrat.

Plusieurs études ont été menées précédemment sur la croissance du Si sur différents substrats, tels que Ag(111). En particulier, la croissance de Si sur Ag(111) conduit à la formation de silicène avec différentes reconstructions selon la température du substrat. La structure de bande du silicène sur Ag(111) diffère toutefois de celle du silicène autoportant prédite par les calculs basés sur la théorie de la fonctionnelle de la densité (DFT), du fait de l'interaction entre le silicène et le substrat Ag(111). Dans le cas de Si/Ag(110), le dépôt de Si conduit à la formation de nanorubans 1D qui ont une structure de chaine de pentamères de Si imbriqué.

En ce qui concerne la synthèse du germanène sur des substrats, les études antérieures ont été majoritairement faites sur les substrats Al(111) et Ag(111). Dans le cas de Ge/Al(111), certaines études ont démontré la formation du germanène, alors que d'autres études ont proposé la possible formation d'alliages de surface Ge-Al. Dans le cas de Ge/Ag(111), il y a une controverse similaire en ce qui concerne la formation du germanène ou d'un alliage de surface Ge-Ag après le dépôt du Ge.

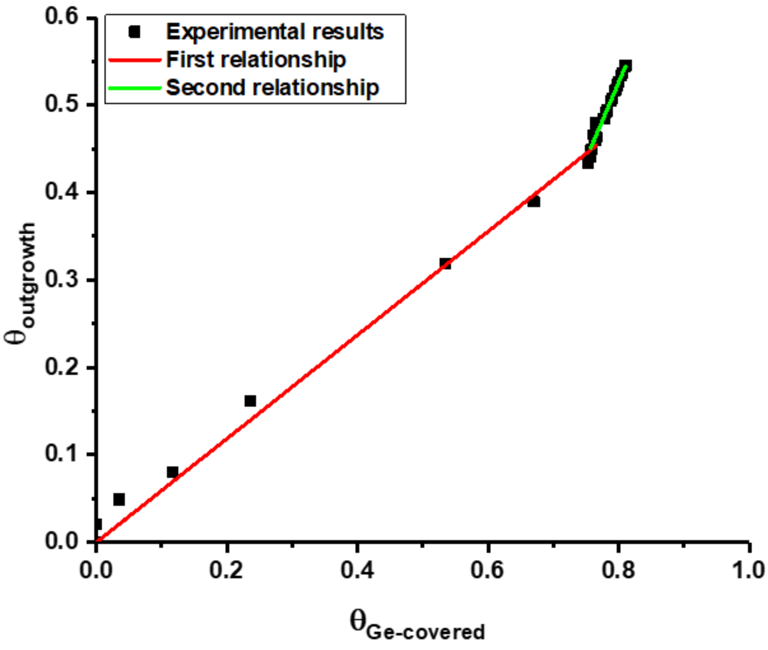

Figure 2 Fraction de l'excroissance en fonction du taux de couverture des zones de reconstruction pendant la croissance à 300K. Le résultat expérimental indiqué par les carrés noirs montre deux relations linéaires indiquées par les lignes solides rouges et vertes, respectivement.

Pour déterminer la structure et la croissance de couches de Ge sur Al(111) et Ag(111) et de couches de Si sur Ag(110), j'ai utilisé la microscopie à effet tunnel (STM), la diffraction des rayons X sous incidence rasante (GIXD), et j'ai analysé les résultats en les comparant à de calculs obtenus (en collaboration) par la théorie de la fonctionnelle de la densité (DFT).

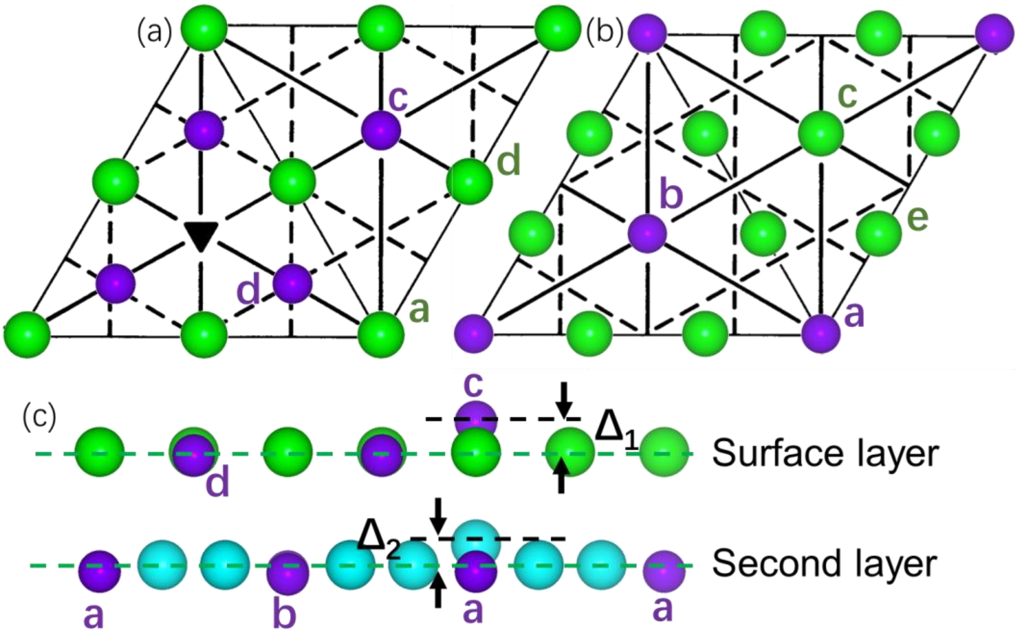

Figure 3 Vue de dessus de (a) la configuration de la première couche et (b) de la deuxième couche. (c) Vue latérale du modèle atomique de la configuration Ge_4Al_4/Ge_2Al_7. Les boules violettes représentent les atomes de Ge. Les boules vertes et bleues indiquent les atomes d'Al dans la première et la deuxième couche, respectivement.

Le chapitre 4 de ma thèse présente les résultats obtenus pour Ge/Al(111). J'ai étudié la croissance de Ge sur la surface Al(111) maintenue à une température fixe dans une plage de 300K à 360K et la structure atomique de la reconstruction $(3\times3)_{Al}$. D'après les mesures STM, l'évaporation du Ge conduit à la formation de deux reconstructions : (3×3)R0° et (√7×√7)R±19.1°. Pendant l'évaporation du Ge à une température de la croissance de ~360 K, j'ai observé une transformation de la structure (√7×√7) vers la structure (3×3). Afin de vérifier la formation d'un alliage de surface Ge-Al, j'ai suivi des mesures de STM en temps réel pour le dépôt de Ge sur la surface Al(111) maintenue à 300K. J'ai observé la formation d'excroissances et de nouvelles terrasses lors du dépôt, ce qui indique que des atomes d'Al du substrat sont remplacés par des atomes de Ge. J'ai mesuré le taux de couverture de la reconstruction et de ces excroissance dans les images STM obtenues in-situ. Comme le montre la Fig. 2, la relation entre ces deux taux de couverture suggère fortement que la croissance de Ge sur la surface de Al(111) donne lieu à la formation de l'alliage de surface Ge-Al, au lieu de la formation du germanène en couche sur Al(111).

J'ai également fait des mesures de GIXD en temps réel sur le dépôt de Ge sur Al(111) à une température de croissance comprise entre 300K et 413K. L'évolution de l'intensité de diffraction montre qu'une basse température de croissance est favorable à la croissance de la structure (√7×√7) et qu'une température de croissance plus élevée favorise la formation de la structure (3×3). J'ai mesuré précisément par GIXD les facteurs de structure associés à la reconstruction (3×3). À partir de l'ajustement brut des données obtenues à travers de GIXD, j'ai testé un grand nombre de modèles. J'ai obtenu deux modèles donnant un meilleur accord avec les expériences, une configuration Ge_4Al_4/Ge_2Al_7 (v. Fig. 3) et une configuration Ge_8/Ge_2Al_7 (v. Fig. 4).

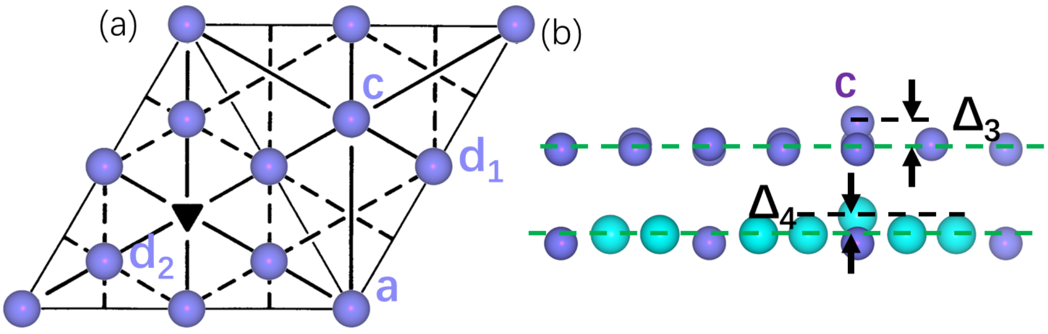

Figure 4 (a) Vue de dessus de la configuration du plan de surface et (b) vue latérale du modèle atomique de la configuration $Ge_8+Ge_2Al_7$. Les boules violettes représentent les atomes de Ge. Les boules bleues représentent les atomes d'Al.

Afin de déterminer la structure, j'ai calculé les facteurs de structure associés à ces deux configurations après relaxation par DFT (calculs effectués par l'IS2M à Mulhouse) et je les ai comparés aux facteurs expérimentaux. Les résultats montre que la configuration optimal Ge_4Al_4/Ge_2Al_7 est stable par DFT, alors que la configuration Ge_8/Ge_2Al_7 relaxée par DFT diffère de la configuration optimale précédemment déterminée. La phase (3×3) correspond donc à l'alliage de surface bicouche Ge4Al4/Ge2Al7 et la formation du germanène sur Al(111) peut être complètement exclue.

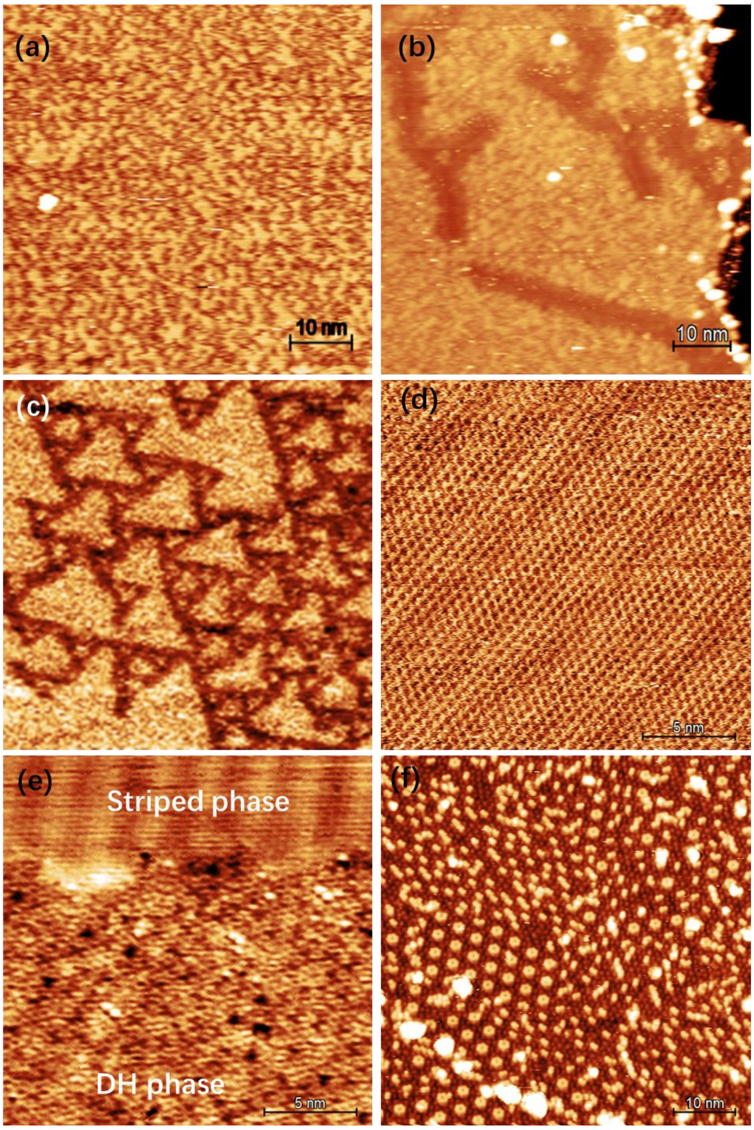

Figure 5 Images STM pendant dépôt de Ge sur Ag(111) à 357K, illustrant (a) la phase Ge diluée, (b) la phase rameaux sombre, (c) la phase triangle (Taille d'image : 100 × 100 nm^2), (d) la striped phase, (d) la phase hexagonale désordonnée, (f) la phase de protrusion en paires et en hexagones. Conditions tunnel : (a-b) V = 1.4 V, I = 30 pA ; (c) V = 1.7V, I = 30pA ; (d) V =0.3 V, I= 0.2 nA ; (e) V =0.1 V, I= 2 nA ; (f) V =1.7 V, I= 20 pA.

Dans le chapitre 5, j'ai étudié la croissance de Ge sur la surface d'Ag(111). En utilisant des mesures de STM en temps réel, j'ai décrit l'évolution des structures successives formées sur Ag(111) lors du dépôt de Ge dans la plage de température [380 K - 430 K]. En fonction du taux de couverture de Ge, le dépôt de Ge sur Ag(111) conduit à la formation des différentes phases de surface (v. Fig. 5) : la phase Ge diluée, la phase rameaux sombre, la phase triangle, la phase bande(SP), la phase hexagonale désordonnée (DH), la phase de protrusions en paires et la phase de protrusions en hexagones.

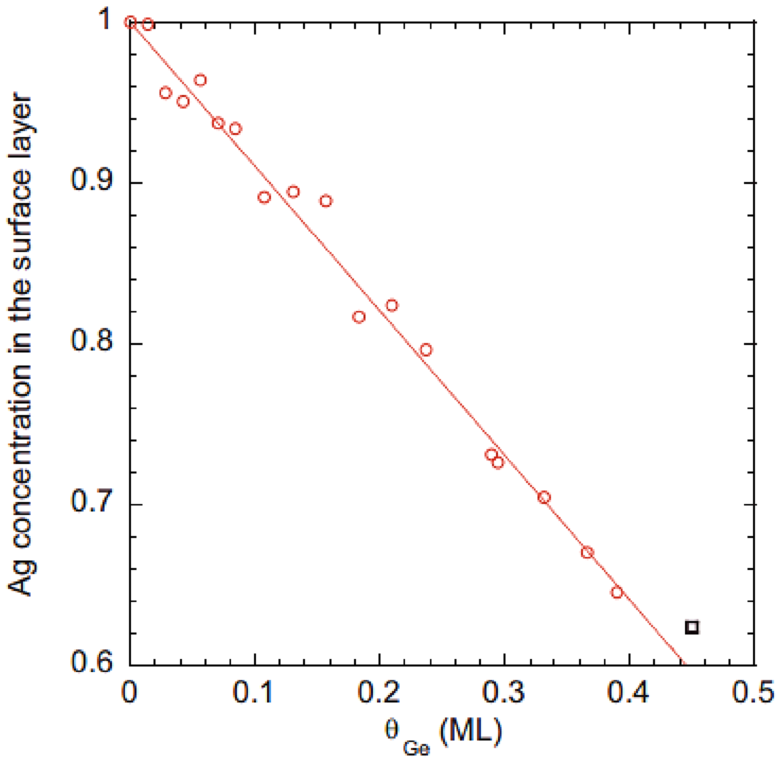

Figure 6 Evolution de la concentration en Ag dans les structures de surface, en fonction du taux de couverture de Ge, pendant le dépôt à 380 K. Les cercles rouges correspondent aux valeurs mesurées dans l'expérience. La ligne est un ajustement linéaire avec une pente de -0,9. Le carré noir correspond à un autre dépôt à la même température sur une zone non affectée par l'effet d'ombrage

Là aussi, le suivi par STM montre la formation d'excroissances et de nouvelles terrasses lors du dépôt, associés au remplacement d'atomes d'Ag par des atomes de Ge. La relation entre le taux de couverture des excroissances et le taux de couverture du Ge (v. Fig. 6), indique que la phase SP correspond à un alliage Ag_2Ge de surface (pour un taux de couverture θ_{Ge} = 1/3MC (ici 1 MC correspond à la densité d'Ag(111)). D'après, cette relation, j'ai estimé que l'achèvement de la phase DH correspond à θ_{Ge} = 0,6MC. Tout cela montre que la structure hexagonale désordonnée peut également être interprétée comme un alliage avec une plus grande proportion d'atomes de Ge. Après l'achèvement de la formation de la phase DH, un dépôt supplémentaire de Ge résulte en la formation des phases de protrusions en paires et en hexagones. En ce qui concerne la phase de protrusions en paires, celles-ci ont la même orientation dans un domaine donné, mais elles ne présentent pas de symétrie hexagonale. Pour la phase de protrusion en hexagones, les motifs présentent une périodicité (√109×√109)R5.5° par rapport à Ag(111)-(1×1).

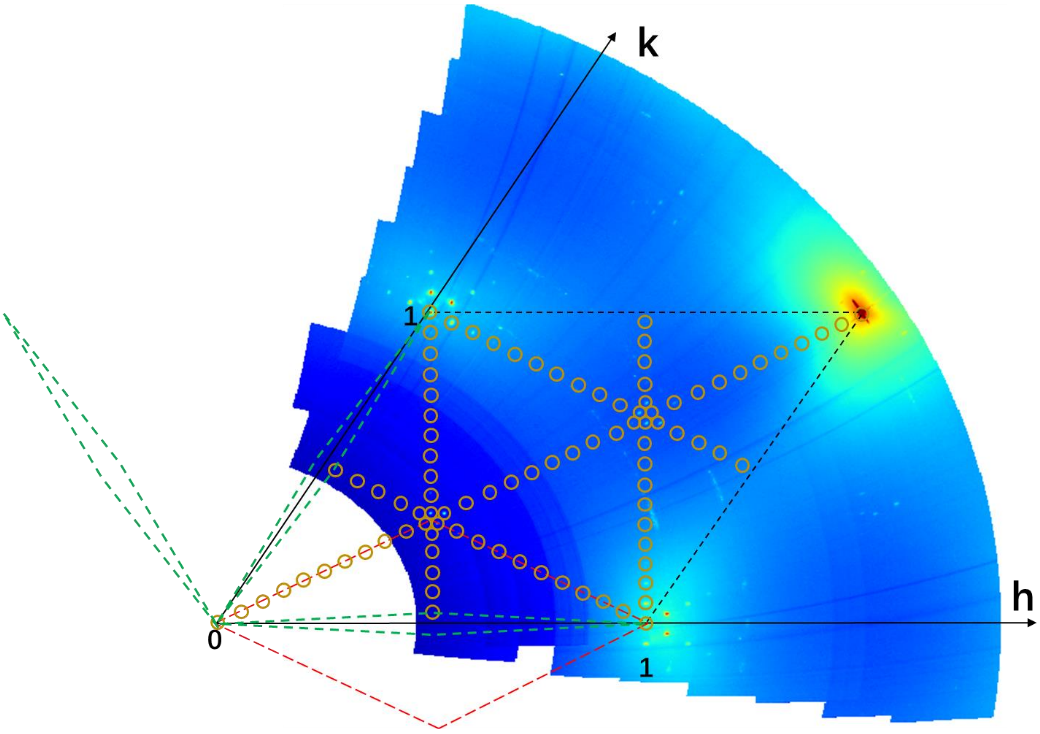

Figure 7 Intensité diffractée pour des conditions dans le plan (l=0,12) après évaporation de θGe ≈1/3 ML et représentation schématique des taches et des tiges de diffraction pour la reconstruction c(31×√3). Le parallélogramme pointillé noir correspond à la cellule unitaire de la surface Ag(111). Le parallélogramme en pointillés rouges correspondent à une supercellule (√3×√3)R30°. Les parallélogrammes pointillé vert correspondent à une supercellule c(31×√3) avec trois orientations possible. Les cercles bruns indiquent les positions (h, k, 0,12) associées à la reconstruction c(31×√3) dans l'espace réciproque.

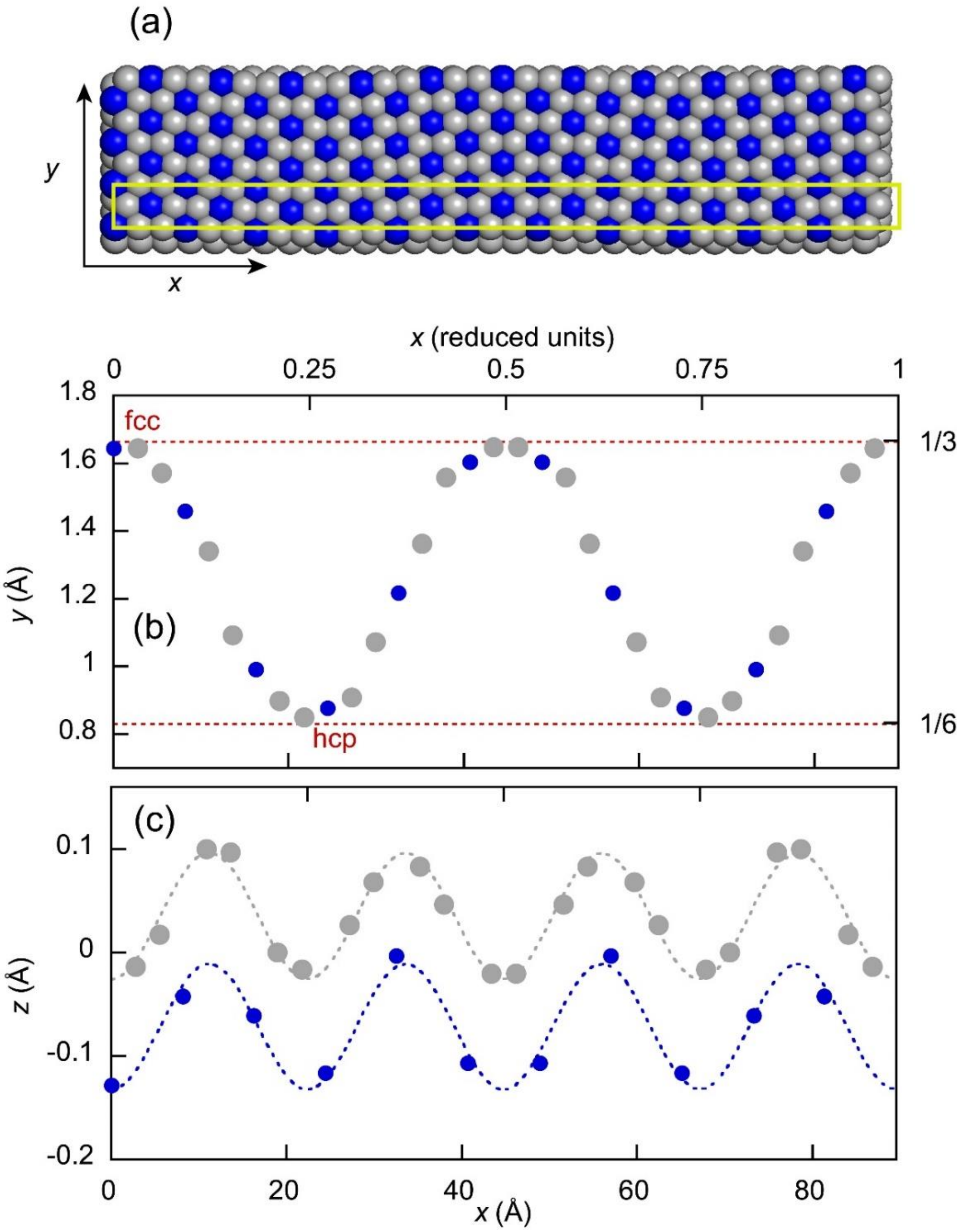

Figure 8 Vue de dessus (a) et profils (b, c) selon x pour les atomes de surface (bleu : Ge, gris : Ag) de la structure atomique de la phase SP. Les échelles latérales x et y sont données à la fois en unités réduites et en Å. La cellule unitaire c(31×√3) est dessinée en jaune.

Concernant les expériences de GIXD, j'ai fait des mesures en temps réel sur la croissance de Ge sur Ag(111) à 420 K. J'ai pu mesurer des signaux diffractés et les associer aux différentes structures observées par STM, plus précisément, les phases triangulaires, SP, DH, et les phases associées aux protrusions. Pour la phase triangulaire, deux types d'organisation quasi-hexagonales sont observées, tournées d'un angle de

30°. J'ai déterminé que la phase SP correspond à une reconstruction c(31×√3). En ce qui concerne la structure de la phase DH, il existe deux possibilités d'indexation : (7×7) ou c(7×√3). Cependant, il est impossible de déterminer la structure de la phase DH. D'après les mesures GIXD, la phase de protrusions en paires pourrait correspondre à une structure incommensurable observée tandis que la phase de protrusions en hexagones correspond bien à une reconstruction (√109×√109).

Concernant la phase SP, correspondant à une reconstruction c(31×√3), j'ai étudié la carte de l'intensité diffractée pour des conditions de diffraction dans le plan (l=0,12) (v. Fig. 7). En utilisant la carte de Patterson calculée à partir des facteurs de structure mesurés pour ces conditions, j'ai suggéré que cette phase SP a une densité atomique 33/31 fois supérieure à celle de la surface Ag(111) et que les positions atomiques ondulent entre les sites fcc et hcp (v. Fig. 8). Ce modèle a été par la suite relaxé par DFT à l'IEMN (Lille). J'ai pu calculer les facteurs de structure théoriques du modèle relaxé par DFT, et je les ai comparés aux facteurs de structure expérimentaux. Le remarquable accord obtenu permet de valider le modèle proposé lors de l'analyse initiale. Ainsi, les résultats de mesures GIXD et de calculs DFT ont confirmé une fois de plus que la phase SP correspond à l'alliage de surface Ag_2Ge, tout comme les résultats des mesures de STM.

Dans le chapitre 6, j'ai étudié la croissance de Si sur Ag(110) à une température de 483K. À l'aide de mesures de STM, j'ai montré que la structure de rangées de pentamères qui se forme en début de croissance est ensuite remplacée par de nouvelles structures. Celles-ci ont l'aspect de monocouches décorées ou non de paires d'adatomes. L'analyse de la surface montre des nanorubans avec des motifs appelés « Ladder×4 », « Ladder×5 » et « Octagon », pouvant s'ordonner en structures (13×4), c(18×4) et c(8×4). L'analyse par GIXD de la croissance montre que la structure (5×2)/c(10×2) associée aux pentamères est remplacée par une reconstruction (13×4). L'analyse de la carte de Patterson montre que la structure correspond à une couche de silicène légèrement déformée. En comparant avec les résultats de simulations DFT effectués à Rome, j'ai déterminé la structure atomique de la reconstruction (13×4) +4adatoms. Les facteurs de structure théoriques calculés selon le modèle (13×4)+4adatoms relaxé par DFT sont en meilleur accord avec les facteurs expérimentaux. Il s'agit d'une couche de silicène sur laquelle 2 paires d'adatomes par maille élémentaire sont présents. Ceux-ci sont situés à l'aplomb des atomes de Si situés en site quadratique de l'Ag(110). On obtient ainsi une configuration « dumbbell » localement.

Mes travaux montrent l'importance du suivi de la croissance et de l'association des techniques de STM, GIXD avec des calculs de DFT pour déterminer la structure des couches épitaxiées lors de dépôts de Si et Ge sur substrat métallique. Alors que le silicène (et « silicène dumbbell ») est observé sur Ag(110) et Ag(111), le germanène n'a pu être obtenu ni sur Al(111), ni sur Ag(111). La différence entre les deux tient sans doute à la taille plus grande des liaisons Ge-Ge par rapport aux liaisons Si-Si, réduisant la portée des interactions pi entre atomes.

Contents

Chapter 1

1 Introduction

In 2004, A. K. Geim and K. S. Novoselov used ordinary cellophane tape to successfully isolate a single layer of carbon atoms for the first time, that was called graphene [1]. They were awarded the Nobel Prize in Physics in 2010 for this research. The structure of graphene is a 2D planar network with a honeycomb lattice where carbon atoms are sp^2 hybridized. Graphene is a zero-gap semiconductor with a high electron mobility at 300K. In the band structure of graphene, near the Fermi level, its valence and conduction bands take a shape of a conical surface (Dirac cone) and meet at the K points in the Brillouin zone. In addition, quantum Hall effect has been observed in graphene [1], [2], characteristic of a two-dimensional electron gas system. Many other properties, giving to graphene a huge potential in domains of semiconductor and high-tech future device [3].

The advent of graphene has promoted the scientific researches on other 2D materials, such as silicene, germanene, boron nitride, transition metal dichalcogenides (TMDCs), 2D oxides etc. For TMDCs, these materials, like WS_2 and MoS_2, presents a “sandwich” structure containing a transition metal atom layer inserted into two chalcogenide layers. This trilayer structure is coupled through van der Waals interaction, whereas atoms are covalently coupled in the trilayers. Similar to graphene, single TMDCs trilayers can be exfoliated from their bulk crystal. These single layers have often different properties from their bulk counterpart. For example, bulk MoS_2 is a semiconductor with an indirect band gap, but a direct band gap is observed for a single MoS_2 trilayer [4]. In addition, the synthesis of other group-IV 2D materials (Xenes), such as silicene [5, 6], germanene[7–9], and stanene[10–12], also becomes a hot topic in the scientific research of 2D materials. Contrary to graphene, a corresponding layered bulk allotrope does not exist in the nature for the elements, thus they cannot be obtained from the exfoliation of a single layer. This means that the synthesis must be performed on a substrate.

In this thesis I present the studies of the growth of silicene and germanene on several substrates. These studies attempt to investigate the growth mechanism and the atomic structure of the layers obtained upon Ge deposition on the Al(111) or Ag(111) surface, Si deposition on the Ag(110) surface.

Firstly, I will present the theoretical studies for free-standing silicene and germanene, including structural parameters, energy band structure, phonon dispersion and other predicted electronic properties. Then, I will introduce previous studies about the growth of Si on different substrates, such as Si/Ag(111), Si/Ag(110), Si/MoS_2, Si/HOPG, etc. Among these substrates, I will give a detailed view of the Si/Ag(111) and Si/Ag(110) systems. Previous works have demonstrated the formation of silicene on the Ag(111) surface with different surface reconstructions [13]. Submonolayer Si deposition on Ag(110) results in the formation of Si nanoribbons with a local pentamer structure. Further growth will be presented in chapter 5. Next, the previous studies of the growth of Ge on the different substrates will be presented, such as Ge/Al(111), Ge(111)/Ag(111), Ge/Pt(111), etc. In contrast with Si/Ag(111), there remains a controversy for the Ge/Al(111) and Ge/Ag(111) concerning the possible formation of layered germanene or of a surface alloy. For this controversy, I will give my answers in chapter 4 and 5.

In chapter 3, I will introduce the experimental techniques employed during my PhD thesis for the growth and investigation of the nanostructures: Scanning tunneling microscopy (STM) and Grazing incidence X-ray diffraction (GIXD). All the experiments are required to be done under UHV conditions. I will present the basics of the techniques and the specific tools and procedures developed in the team to analyze the raw data.

The growth of Ge on the Al(111) surface, kept in the range of RT to 360K, will be presented in chapter 4. The formation and the evolution of the $(3 \times 3)_{Al}R0°$ and $(\sqrt{7} \times \sqrt{7})_{Al}R(\pm 19.1°)$ reconstructions that form upon Ge deposition is studied by both STM and GIXD. Based on real-time STM measurements during Ge evaporation, I will show how the Al(111) surface evolves during growth, demonstrating the formation of an alloyed phase. Then, I will describe a quantitative GIXD study combined with density functional theory (DFT) calculations (performed at IS2M in Mulhouse), aimed to determine the exact atomic structure of Ge/Al(111)-(3×3) structure.

In chapter 5, I will present the growth of Ge on the Ag(111) surface at 380K, using STM, GIXD and DFT calculations. Using real-time STM measurements, the evolution of the surface and the formation of the different phase will be described. Similar to Ge/Al(111) system, the surface evolution, obtained from in-situ STM images, gives an answer to the controversy about the formation of germanene or Ge-Ag surface alloy. Then, combining GIXD and DFT simulations performed at IEMN in Lille, I will determine the precise atomic structure of one of the surface reconstructions, corresponding to a surface Ag_2Ge alloy.

Finally, in chapter 6, I present the additional Si growth on the Si pentamer chains grown on Ag(110) at 483K. Several surface reconstruction are observed by STM. GIXD study of the additional Si deposition on Si DNRs formed on Ag(110) will also be reported. A comparison between the experimental results, obtained by GIXD, and DFT calculations, performed at Roma, will demonstrate that the additional Si growth leads to the formation of silicene with extra pairs of adatoms in a “Dumbbell” configuration.

Chapter 2

2 State of the art – the growth of Ge and Si on metallic surfaces

Contents

2.1 Silicene and germanene

2.1.1 Free-standing silicene

Based on density function theory (DFT), the atomic and electronic structure of two-dimensional(2D) silicon monolayers were investigated theoretically for the first time by Takeda and Shiraishi [14] in 1994. They have proposed that a single layer of Si may have a hexagonal structure similar to the structure of a single layer in graphite. The results of the DFT calculations show that a buckled hexagonal structure is energetically favorable for a Si monolayer instead of a 2D flat stage, which indicated that Si atoms do not form pure sp^2 bonds. The unit cell of this buckled hexagonal structure is composed of two inequivalent sublattices with a difference of height Δ=0.53 Å [1], as illustrated in Fig. 2.1. Takeda and Shiraishi also computed that this hexagonal structure possesses a lattice constant a=3.855 Å [14]. Comparing this buckling to the distance between Si(111) nearest planes (Δ=0.78 Å), this suggests the existence of a mixed sp^2-sp^3 hybridization between Si atoms.

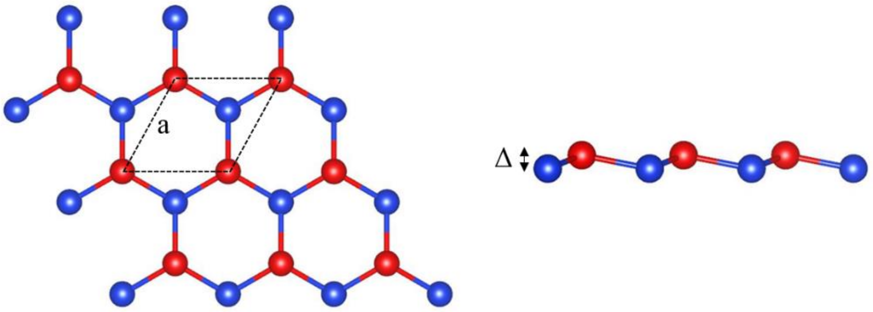

Figure 2.1 Top (left) and lateral (right) view of the structure of Free-standing silicene. The structure consists of two inequivalent sublattices (red and blue) with a buckling Δ and the lattice constant a for the unit cell (dotted rhombus)

In 2007, the name “silicene” appeared for the first time in the study by Guzmán-Verri and Lew Yan Voon [15]. They used the tight-binding model to study the flat structure of silicene, like graphene, the linear bands appear around the Fermi level. In 2009, Cahangirov *et al*. investigated theoretically various possible configuration for Si monolayers, namely the low-buckled (LB) silicene, the high-buckled (HB) silicene (with buckling $\Delta_{HB} \approx 2.0$ Å), and the planar (PL) honeycomb silicene by first-principles calculations [16]. They found a similar result to Takeda's, the LB honeycomb structure is the most stable one with a lattice constant of a= 3.87 Å, a buckling Δ = 0.44 Å, and the nearest neighbor distance (Si-Si) is $d_{Si\text{-}Si} = 2.25$ Å. In their study, they explained the instability of PL silicene and the stability of LB silicene by the theoretical calculations of the phonon dispersions (see Fig. 2.2). For the planar structure, the wavenumber of the ZO mode (out-of-plane optical mode) has negative values around the Γ point of the Brillouin zone (BZ).

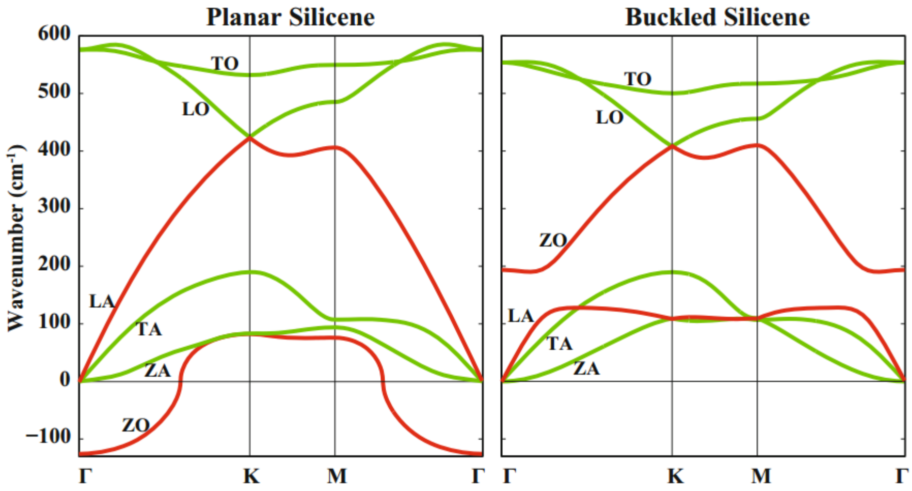

Figure 2.2 The calculated phonon dispersion of planar and buckled silicene. The out-of-plane, transverse and longitudinal acoustic and optical modes are indicated by ZA,TA, LA, ZO, TO and LO, respectively. The LA and ZO modes marked by red line exhibit a difference between planar and buckled structures. Image reproduced from ref. [17]

The ZO mode responds to the inverse motion of Si atoms in two sublattices towards the out-of-plane, and the negative frequency for the ZO mode corresponds to the absence of the restoring force during the motion of Si atoms. For this reason, the planar silicene is not stable. On the contrary, the frequency of all the acoustical branches and the optical branches for the low-buckled structure are positive. Especially, the LA (longitudinal acoustic) mode and ZO mode have a marked difference with those of the planar structure while the other modes barely change.

These stability analyses are based on theoretical calculations and ignore some experimental factors such as thermal fluctuations, the interaction with a substrate, reactivity, etc. This calculated silicene can be regarded as the free-standing (FS) form of silicene. Unlike stable graphene, due to the high reactivity of silicene, it is hard to synthesize free-standing silicene [18].

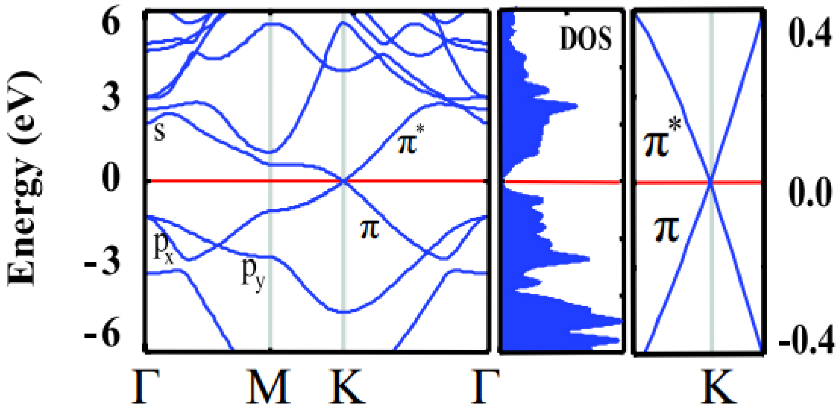

Figure 2.3 Energy band structure and density of states of free-standing silicene. The π and π^* bands crossing at K-K' point presents a linear relationship in the proximity of the Fermi level. Figure adapted from ref. [3]

Regarding the electronic properties of FS silicene, Cahangirov *et al.* have theoretically investigated the energy band structure and the density of states (DOS), as shown in Fig. 2.3. Like graphene, low-buckled FS silicene is semi-metallic. In the BZ, the crossing of π and π^* bands at K-K' point presents a linear relationship near the Fermi level (E_F=0 eV), showing that the electrons of FS silicene are similar to massless Dirac fermions. The Fermi velocity (V_F) is calculated by

$$V_F \cong \frac{\mathrm{E}(\mathbf{q})}{\hbar|\mathbf{q}|} \tag{2-1}$$

Where **q** corresponds to the electronic wavevector and E is the energy. V_F is estimated to be ~10^6 ms^{-1}, comparable to the effective Fermi velocity of graphene $V_F \approx 10^6$ ms^{-1}[1].

However, unlike the atomically flat graphene, the buckled structure may lead to some different properties. Drummond et al. theoretically investigated the variation of the bandgap in a vertical electric field, which showed an almost linear relation with the slope ~0.07 eÅ [19]. Compared to carbon, the spin-orbit (SO) coupling for Si π electron is larger, resulting in a larger SO gap, estimated to 1.5 meV. Silicene is predicted to have the quantum spin Hall effect (QSHE) [20,21].

In the next section, I give a description of Free-standing germanene.

2.1.2 Free-standing germanene

The atomic and electronic structure of 2D Ge monolayer was also investigated theoretically by Takeda and Shiraishi [14]. Similarly to silicene, DFT calculations show that a buckled hexagonal structure for germanene is favorable with respect to a flat structure. FS germanene, similar to FS silicene is composed of two hexagonal sub-lattices with a buckling, as illustrated in Fig. 2.1. Cahangirov *et al.* also studied the low-buckled, the high-buckled, and the planar honeycomb structures of germanene by means of DFT calculations [16]. Their results show that the low-buckled honeycomb structure is the most stable structure for free-standing germanene with a lattice constant of a= 3.97 ± 0.1 Å and a buckling Δ=0.64 Å [16]. The analyses of the stability for the low-buckled and the planar structure have also been investigated by the phonon dispersion shown in Fig. 2.4. In the vibrational modes of the planar structure, one optical branch presents all imaginary frequencies. This evidence indicates that planar germanene is unstable. For LB germanene, contrary to silicene, the ZA modes show imaginary frequencies near the Γ point, which indicates that low-buckled FS germanene is not stable with respect to large wavelength perturbations. However, Şahin *et al.* explained that it is due to the mesh size used in the calculation [22].

For the studies of the electronic structure of FS germanene, Cahangirov *et al.* showed the energy band structure and the DOS in Fig. 2.5. Like silicene and graphene, the band crossing at the K-K’ point shows a linear relationship at the Fermi level, which indicates that SF germanene has a semi-metallic character. The Fermi velocity estimated by the equation (2-1) is to be 0.52×10^6 ms^{-1} [17].

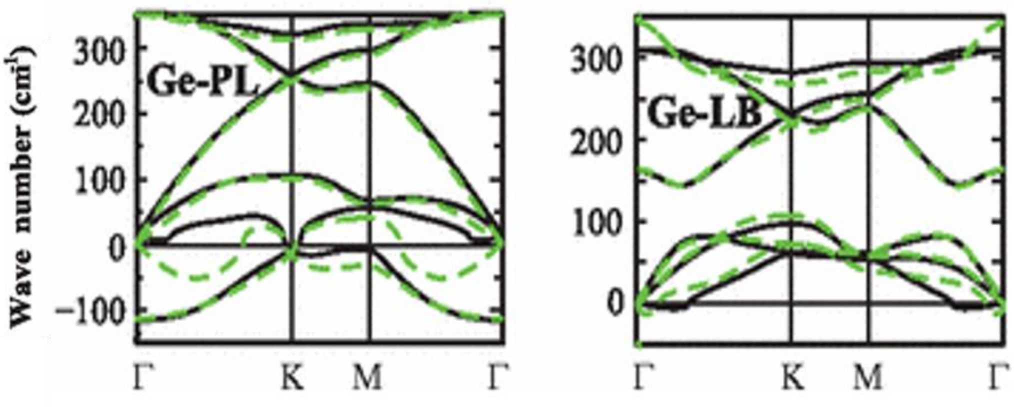

Figure 2.4 The phonon dispersion of planar (Ge-PL) and low-buckled germanene(Ge-LB) calculated by force-constant (black continuous line) and linear response theory (green dashed line), respectively. Image reproduced from ref. [16]

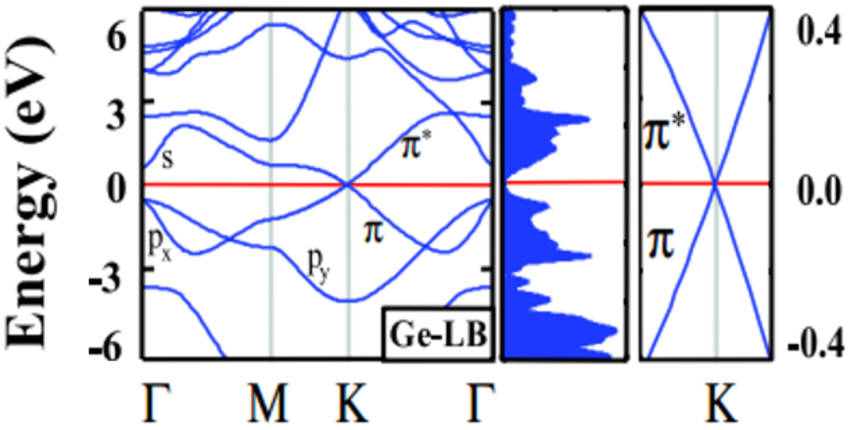

Figure 2.5 Energy band structure and density of states of free-standing germanene. The π and π* bands crossing at K-K' point presents a linear relationship in the proximity of the Fermi level. Figure adapted from ref. [16]

Information on the nature of the hybridization sp^D can be calculated through $D= -1/\cos(\theta)$, while θ is the bond angle [17]. Thus, the value of D for FS silicene and FS germanene is 2.27 (θ=109.5°) and 2.74 (θ=112.4°) respectively, indicating the mixed sp^2-sp^3 hybridization between Ge atoms in FS germanene. FS silicene tends to the sp^2 hybridization, and FS germanene is inclined to the sp^3 hybridization. From the comparison of the buckling of FS silicene and FS germanene, Ge atoms in germanene show a larger SO coupling compared to Si atoms in silicene. Liu *et al.* have computed that the SO gap of SF germanene is 23.9 meV predicting the realization of QSHE at 277K [20]. They predicted that SF germanene has thus a huge potential for high-temperature QSHE.

2.2 Epitaxial growth of silicene

2.2.1 Silicene grown on Ag(111)

Unlike graphene, a natural material composed of layered silicene does not exist. A possible route for synthesizing silicene is to epitaxially grow a Si monolayer on a substrates. Silicene growth has been claimed on many substrates for example, Ag(110) [23–26], Ag(111) [5][27–35], Al(111) [36], Pb(111) [37], Au(111) [38], [39], ZrB2(0001) [40], Ir(111) [41] and HOPG [42], [43]. Among them, the most studied system is by far Si/Ag(111) [5][29][31][33][34][44][45].

2.2.1.1 Single-layer silicene on Ag(111)

In 2010, Lalmi *et al.* have reported the epitaxial growth of silicene on Ag(111) held at ~250°C [27]. From STM and Low-energy electron diffraction (LEED), they hypothesized an hexagonal honeycomb structure for silicene associated with a $(2\sqrt{3} \times 2\sqrt{3})_{Ag}R30°$ reconstruction of the substrate. In STM measurements all atoms are visible and the measured Si-Si distance is 0.19 nm. As this is much smaller than the interatomic distance in bulk silicon (0.235 nm) or for free-standing silicene, these results have remained controversial and have never been reproduced. The reports of Vogt *et al.* [5] and Lin et al. [46] are considered as the first experimental evidence of silicene.

At the same time, Jamgotchian et al. reported that the substrate temperature affects the growth of silicene and the nature of the reconstruction on the Ag(111) surface [31]. Lee *et al.* have summarized the previous works of other researchers about the formation of silicene on Ag(111) under various growth conditions, as illustrated in Fig. 2.5 [13]. Through STM and LEED investigation, silicene may lead to the formation of several surface reconstructions such as $(4\times4)_{Ag}$, $\left(\sqrt{13}\times\sqrt{13}\right)_{Ag}R13.9°$, $(2\sqrt{3}\times2\sqrt{3})_{Ag}R30°$, $(3.5\times3.5)_{Ag}R26°$, that corresponds to $(3\times3)_{Si}$, $(\sqrt{3}\times\sqrt{3})_{Si}R30°$, $(\sqrt{7}\times\sqrt{7})_{Si}R19.1°$ and "dotted phase".

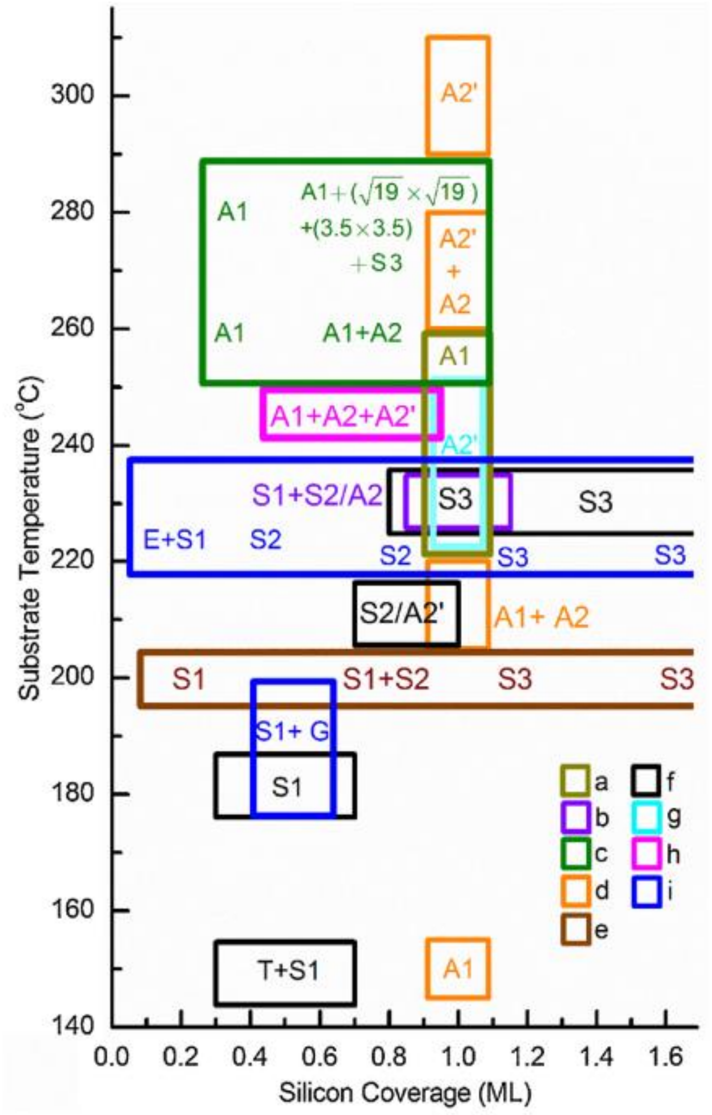

Figure 2.6 Phase diagram of the silicene reconstructions as a function of silicon coverage and the surface temperature. The labels of the different structural phases are described in Table 2.1. At the beginning of the growth, a phase E is observed at the step edges; the label G indicates "dotted phase". The data a-i correspond to refs. [5], [47], [48], [31], [49], [29], [27], [50], [13]. Figures reproduced from ref. [13]

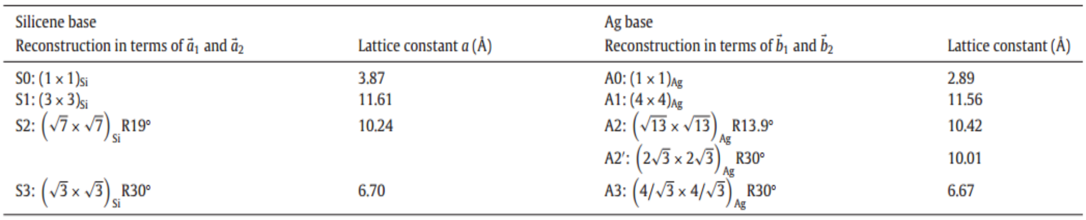

Silicene base Reconstruction in terms of $\vec{a}_1$ and $\vec{a}_2$	Lattice constant a (Å)	Ag base Reconstruction in terms of $\vec{b}_1$ and $\vec{b}_2$	Lattice constant (Å)
S0: $(1\times 1)_{Si}$	3.87	A0: $(1\times 1)_{Ag}$	2.89
S1: $(3\times 3)_{Si}$	11.61	A1: $(4\times 4)_{Ag}$	11.56
S2: $\left(\sqrt{7}\times\sqrt{7}\right)_{Si}$R19°	10.24	A2: $\left(\sqrt{13}\times\sqrt{13}\right)_{Ag}$R13.9°	10.42
		A2′: $\left(2\sqrt{3}\times 2\sqrt{3}\right)_{Ag}$R30°	10.01
S3: $\left(\sqrt{3}\times\sqrt{3}\right)_{Si}$R30°	6.70	A3: $\left(4/\sqrt{3}\times 4/\sqrt{3}\right)_{Ag}$R30°	6.67

Table 2.1 The lattice parameters of various reconstructions with respect to the unit cell of Ag(111) (label A) and with respect to the unit cell of silicene (label S). The table is adapted from ref. [13]

The lattice constants of these reconstructions are shown in Table 2.1. The notation $(n\times n)_{Ag}R\alpha$ means that a surface reconstruction possesses a lattice constant n times larger and a rotation of α degrees with respect to the unit cell of Ag(111), while the $(n\times n)_{Si}R\alpha$ identify a reconstruction with respect to the silicene-(1×1) lattice. As shown in Fig. 2.6, the (4×4) reconstruction can be observed for the growth at the substrate temperature ranging from ~150°C to 290°C while $\left(\sqrt{13}\times\sqrt{13}\right)_{Ag}R13.9°$ and the $2\sqrt{3}\times 2\sqrt{3}_{Ag}R30°$ appeared for the growth above ~210°C. Beyond 300°C, Silicene on Ag(111) exhibits the unique reconstruction of $\left(2\sqrt{3}\times 2\sqrt{3}\right)_{Ag}R30°$. However, beyond 330°C, due to the dewetting of Si adlayer and the formation of 3D clusters on the surface, no silicon reconstruction is observed by LEED [31].

The $(4\times 4)_{Ag}$ reconstruction has been firstly reported by Vogt et al. [5], as shown in Fig. 2.7. Fig. 2.7a shows the surface after the deposition of about one monolayer (ML) of Si forming a $(4\times 4)_{Ag}$ reconstruction with a hexagonal structure. The inset in Fig. 2.7a shows the line profile measured along the white dashed lines, indicating that the average distance between the 2 dark centers is 1.14 nm, corresponding to 4 times the unit cell of Ag(111). In the high-resolution STM topography image (right-lower inset), two triangular arrangements composed of 6 Si atoms in the unit cell of the (4×4) reconstruction are visible.

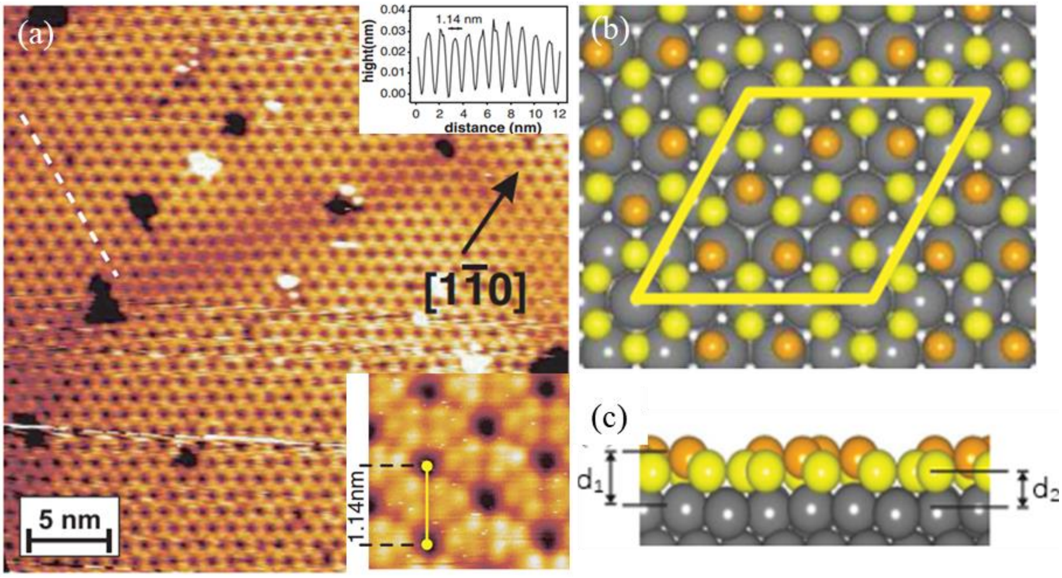

Figure 2.7 (a) STM image of silicene on Ag(111) (U=-1.3V, I=0.35 nA). Right-upper inset: the profiles along the dashed lines shown in (a). The distance between the nearest dark centers is 1.14 nm. Right-lower inset: High- resolution zoom-in STM image (3×3 nm^2; U=-1.3V, I=0.35 nA). (b) Top view of the model for silicene with $(4\times4)_{\mathrm{Ag}}$ reconstruction on Ag(111). (c) Lateral view of (a). Figures reproduced from ref. [5]

The lattice constant of the $(4\times4)_{\mathrm{Ag}}$ reconstruction is about 3 times the one of silicene, which indicates that (3×3) silicene reconstruction corresponds to $(4\times4)_{\mathrm{Ag}}$ reconstruction. On the basis of STM and LEED measurements, Vogt *et al.* [5] and Lin *et al.* [46] have proposed a similar atomic model for the $(4\times4)_{\mathrm{Ag}}$ reconstruction. Based on DFT calculations, Fig. 2.7b and 2.7c show the unit cell of their relaxed model composed of 18 Si atoms, among which 6 are located at a higher distance from the substrate. The corresponding buckling is Δ~0.7 Å, and Ag atoms under the protruding Si atoms are slightly lifted. The Si-Si distance is 2.32 Å, the distance d_1 between the top Si atoms and the first layer of Ag(111) is 2.92 Å while the distance d_2 between the bottom and the surface is 2.17Å. The simulated STM image is in good agreement with the experimental STM images (Fig. 2.7c). Only protruding Si atoms are visible.

In 2016, Curcella et al. have investigated more details about the atomic structure of the (4×4) reconstruction on Ag(111) at 520 K or 570 K, by combining grazing-incidence x-ray diffraction (GIXD) measurement and DFT calculations [51]. The comparison between the experimental and simulated structure factors confirms the model proposed by Vogt *et al.* [5].

For the studies of the $(\sqrt{13}\times\sqrt{13})_{Ag}R13.9°$, the $(2\sqrt{3}\times 2\sqrt{3})_{Ag}R30°$ and the other reconstructions on Ag(111), some theoretical models of these reconstructions have been proposed [28][52][53] and confirmed by GIXD [54].

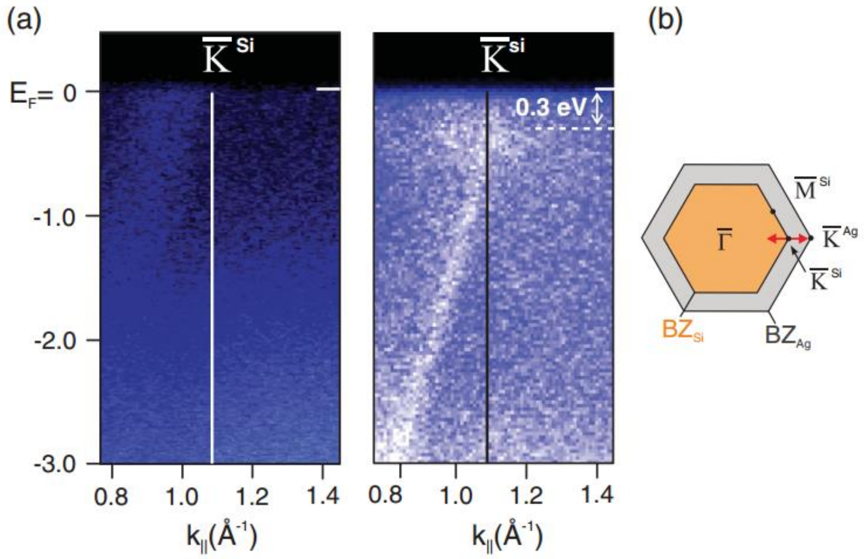

Figure 2.8 (a) ARPES maps for the bare Ag(111) (left) and silicene/Ag(111) (right), along the Γ_{Ag} - $K_{Ag.}$ (b) Brillouin-zone (BZ) scheme for the unit cell of Ag(111) and silicene. The direction of measurements is indicated by the red arrow. Figures reproduced from ref. [5]

Besides the studies of the atomic structure of silicene on Ag(111), the electronic structure of silicene is also an attractive property for this new 2D material. As for the investigation of the electronic band structure, Angular-Resolved Photoelectron Spectroscopy (ARPES) measures the kinetic energy of photoelectrons in relation to the momentum parallel to the sample surface, which reveals the dispersion of the electronic bands. Vogt et *al.* have carried out ARPES measurements with a photon energy of hν=126 eV to map the band structure of $(4\times4)_{Ag}$ silicene along the Ag $\bar{\Gamma}-\bar{K}$ direction [5]. As shown in Fig. 2.8, the band structure near the Fermi level (E_F) exhibits a linear dispersion attributed to a ‘Dirac cone’ and shows a gap opening at K_{Si} point estimated to ~0.6 eV (~0.3 eV is measured between the Si apex and the Fermi level).

However, this conclusion is different from further studies [55], [56].

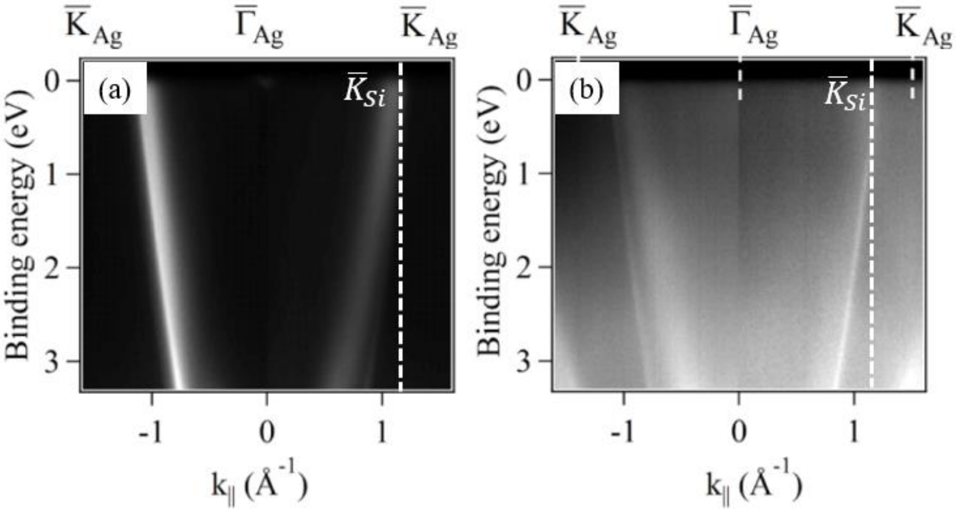

Figure 2.9 ARPES maps for (a) the bare Ag(111) and (b) silicene/Ag(111) (right), along the Γ_{Ag} - K_{Ag}.. Figures reproduced from ref. [55]

Mahatha et *al.* [55] have performed ARPES measurements on $(4\times4)_{Ag}$ silicene, shown in Fig. 2.9. From a comparison between Fig. 2.9a and Fig. 2.9b, they found that the bands of silicene/Ag(111) system display the almost same dispersion compared to the one of bare Ag(111), which reveals that the linear dispersion close to E_F is due to the bulk states of the Ag surface. Furthermore, the dispersion does not show a gap opening at the K_{Si} point. For the other reconstructions, such as $\left(\sqrt{13}\times\sqrt{13}\right)_{Ag}R13.9°$ and $(2\sqrt{3}\times2\sqrt{3})_{Ag}R30°$, those systems display similar band structure without Dirac cones at E_F [55]–[57]. The hybridization between silicene and Ag surface states significantly changes the silicene band structure, indicating that the electronic properties of FS silicene are not preserved in the silicene/Ag system [55], [56].

2.2.1.2 Multilayer silicene on Ag(111)

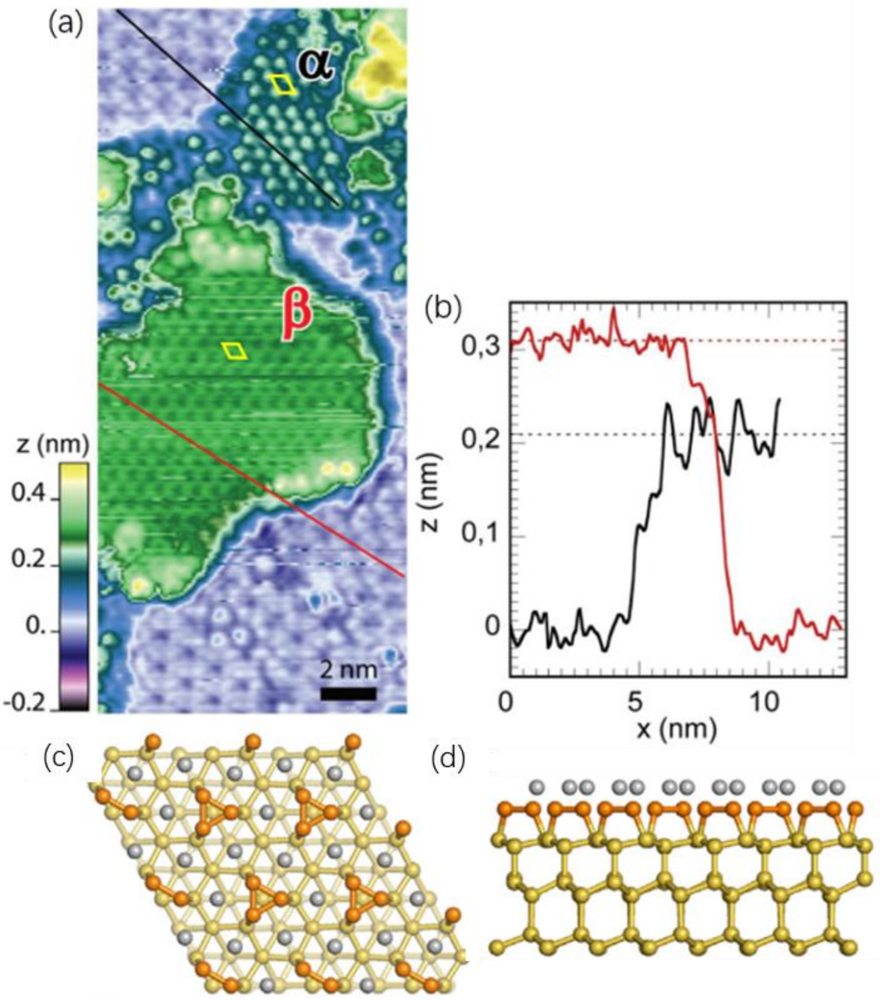

Figure 2.10 (a) STM image (11×25 nm^2; U=1.6V,I=50 pA) after Si deposition at 500K above 1 ML. Two types of the $(\sqrt{3}\times\sqrt{3})R30°$ reconstruction show a different contrast, the unit cell of them is presented by the yellow rhombus. (b) Profiles along the lines shown in (a). (c) Top and (d) side views of the HCT model applied for fitting the experimental structure factors measured by GIXD. The small grey balls represent Ag atoms. The yellow balls represent Si atoms, while the protrusive Si atoms are drawn in orange. Figure reproduced from ref. [34], [35]

Above 1 ML coverage, a new surface reconstruction appears: a $(\sqrt{3}\times\sqrt{3})R30°$ silicene reconstruction corresponding to a$(4/\sqrt{3}\times 4/\sqrt{3})_{Ag}R30°$ reconstruction [29, 45, 47, 48][57–61]. This reconstruction presents two different phases, named α and β [60]. Fig. 2.10a shows the hexagonal structure with the protrusions in the α zone (the bright dots) and the depression in the β zone (the dark spots). The line profiles, in Fig. 2.10a, indicates that the surface corrugation of the α zone (~ 0.06 nm) is larger than the one of the β zone (~0.02 nm) (see Fig. 2.10b), while the step height of the α zone (~0.21 nm) is lower than the one of the β zone (~0.31 nm).

In 2017, Curcella et *al.* have investigated the atomic structure of the $(\sqrt{3}\times\sqrt{3})R30°$ reconstruction [34] and the mechanism for the growth of Si films on Ag(111) at ~500 K [35], by combining GIXD, STM measurement and DFT calculations. From a comparison between the experimental and simulated structure factors, the authors concluded that the $(\sqrt{3}\times\sqrt{3})-\beta$ reconstruction can be described by the Ag-terminated honeycomb chain triangle (HCT) model [34], as illustrated in Fig. 2.10c and 2.10d. However, the phase α was not investigated by GIXD measurements.

Supported by DFT calculations, the α phase is considered as a Ag-free structure [35], i.e. similar to the TDS model proposed in ref. [62]. Thus, Curcella et *al.* have given a description of the mechanism for the growth [35]: Above 1 ML silicene coverage, the Ag-free $(\sqrt{3}\times\sqrt{3})R30°-\alpha$ reconstruction, with additional Si atoms, has formed by expelling the atoms of the outermost Ag layer. Upon the further evaporation of Si, the Ag-free structure is replaced by the Ag-terminated HCT structure ($(\sqrt{3}\times\sqrt{3})-\beta$ reconstruction, and Ag atoms from the outermost layer are also expelled and insert into the other outermost silver layer below silicene monolayer.

2.2.2 Silicon nanoribbons on Ag(110)

Besides the essential studies of the silicene/Ag(111) system, the growth of Si on Ag(110) surface is also an important topic attracting interest in the scientific community. In 2005, Léandri et al. have reported the formation of straight silicon nanoribbons (NRs) on Ag(110) during deposition of Si on Ag(110) at room temperature (RT) [63]. They are parallel to the $\mathrm{Ag}[1\bar{1}0]$ direction and possess a narrow width of 1.6 nm (about $4a_{\mathrm{Ag}[001]}$). Further studies [24–26][64] show the existence of so-called single and double

NRs (SNRs and DNRs) with a width of 0.8 nm and 1.6 nm respectively (see in Fig. 2.11e) [25][26][65]. For growth at higher temperature (460 K), DNRs are observed to be self-assembled and form a 1D grating with a width of 1.6 nm (see Fig. 2.11f) [26], [65]. These self-assembled NRs (SANRs) correspond then to a (5×2) or c(10×2) reconstruction. Above 1 ML Si deposition on Ag(110) at a higher temperature (>460 K), Colonna et al. have reported a c(8×4) reconstruction with 4 adatoms per unit by STM and LEED pattern [65]. In chapter 6, I will present the other reconstructions and the atomic structure above 1 ML Si deposition, 1 ML corresponds to the Ag(110) surface atom density.

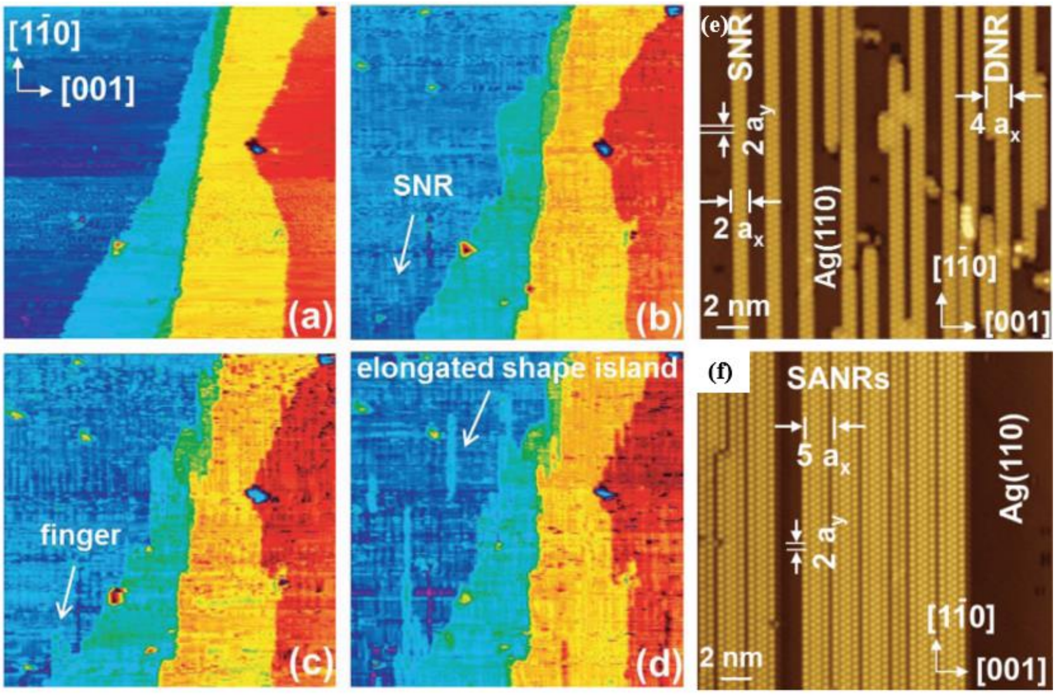

Figure 2.11 (a)-(d) Sequence of STM images (234×234 nm^2; U=1.5 V, I=510 pA) of the same area showing the growth of silicon on Ag(110) surface at room temperature. (a) Bare Ag(110) surface. Different colors indicate the different terraces at different levels (the red terrace is the upper terrace). Corresponding estimated Si coverages are (b) 0.1 ML, (c) 0.2 ML and (d) 0.3 ML. (e) STM images (U=1 V; I=300pA) of Si SNRs and DNRs grown on Ag(111) after 0.3 ML Si deposition at RT. a_x (0.409 nm) and a_y (0.205 nm) are the lattice constants of the Ag(110) unit cell. (f) Formation of SANRs on Ag(110) after 0.5 ML Si deposition at 460 K (U=1 V; I=500pA). Figures reproduce from ref. [26]

In 2013, using STM and GIXD, Bernard *et al.* have presented the growth mechanism of the Si NRs on Ag(111) and provided compelling evidence of an Ag(110) surface reconstruction induced by the growth of NRs [26]. Fig. 2.11a-d shows the evolution of the Ag(110) surface during Si deposition at RT. The bare Ag(110) surface is shown in Fig. 2.11a, the different terraces separated by monoatomic steps are related to the different colors. After 0.1 ML Si deposition, the outlines of the Ag terraces have a visible change, and the Si NRs along $[1\bar{1}0]$ direction can be seen in Fig. 2.11b. After 0.2 ML Si deposition, the change of the terraces is more obvious, the formation of “fingers” occurs at the step edges (see Fig. 2.11c). For higher Si coverage (0.3 ML), these fingers become longer, and elongated shape islands also appear (see Fig. 2.11d). Their orientation is parallel to Ag $[1\bar{1}0]$ direction. From height profiles measured, these fingers and elongated shape islands were shown to correspond to new Ag(110) terraces. This result indicates that, during Si evaporation, the Si NRs form on Ag(110) by expelling Ag atoms. These Ag atoms, depending on the density of the Si NRs, form fingers at the step edges or elongated shape islands. However, they are not observed at a growth temperature of 190°C, due to the high mobility of Ag adatoms at this higher temperature and the low density of SANR domains [26]. Using GIXD, Bernard et al. have investigated the atomic structure of the SANRs and substrate surface. They reported that the substrate surface reconstruction result from the formation of NRs. Thus, they proposed a “missing row” model for the substrate surface underneath the NRs and the SANRs.

Although GIXD is a powerful tool for the investigation of the refinement of the atomic positions, it is not possible to get directly the atomic positions from the measured intensities. From the analysis of the GIXD measurements, Prévot et al. have however determined that the Ag(110) undergoes a missing row reconstruction upon SANR formation [66]. As shown in Fig. 2.12, supported by DFT calculations, Hogan et al. have further proposed a stable missing-row model named “Zigzag (A or B)” [67], while a Pentamers model was proposed by Cerdá *et al.* [68]. Finally, from the comparison between GIXD experimental and simulated structure factors corresponding to the different proposed models, Prévot *et al.* demonstrated that the Pentamer model corresponds to the SANR structure [66].

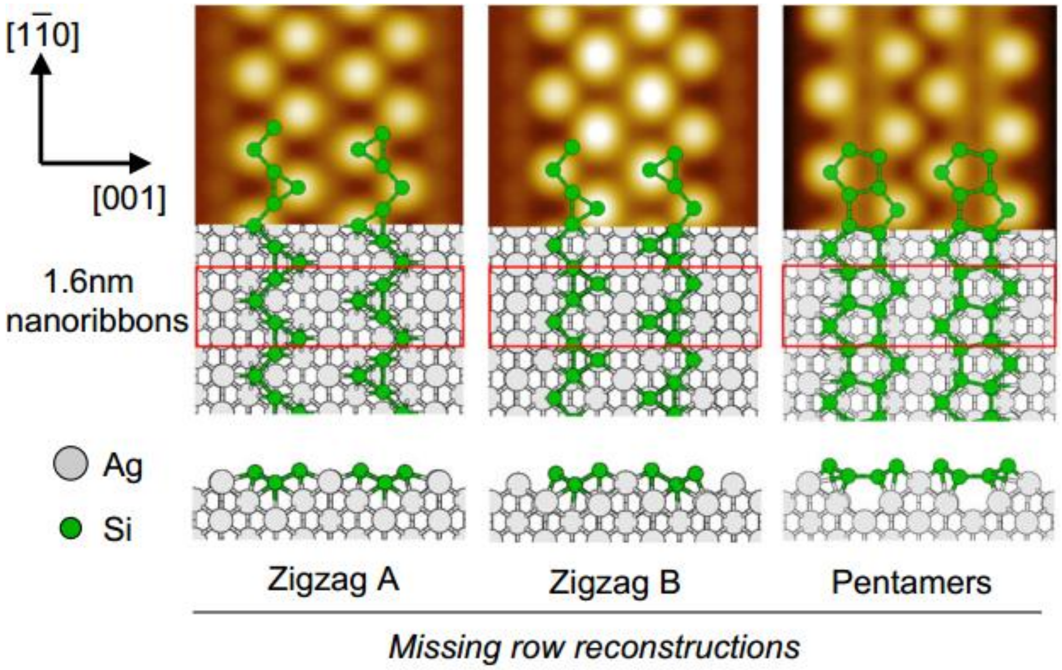

Figure 2.12 Three models of Si NRs on Ag(110) with missing row reconstructions and their simulated STM images. Figure adapted from ref. [66]

2.2.3 Silicon on other substrates

In this section, I will introduce the growth of silicon on other substrates, as summarized in Table. 2.2.

Besides the Si evaporation method, the surface segregation is another method applied to the growth of silicene. In 2012, Fleurence et al. used this method to achieve the synthesis of silicene on $ZrB_2(0001)$ grown epitaxially on Si(111) [40]. After annealing at 750-800°C for ten hours, the oxide-free $ZrB_2(0001)$ surface presents a (2×2) reconstruction related to adatoms [40][69][70]. Using STM measurements, the authors concluded the formation of the $(\sqrt{3}\times\sqrt{3})_{Si}$ silicene structure corresponding to this (2×2) reconstruction, with the unit cell size of 6.32 Å [40].

Substrate	Synthesis method	Growth temperature	Reconstructions	Unit cell size	Buckling	Misfit	Ref.
FS silicene	-	-	(1×1)	3.87Å	0.44Å	-	[16]
Ag(111)	Evaporation	420K- 560K	(4×4)	11.61Å	0.75Å	0.5%	[5],[27-35] [44-62]
		480K- 570K	(√13×√13)R13.9°	10.24Å	0.2Å	1.8%	
		480K- 600K	(2√3×2√3)R30°	10.01Å	0.2Å	2.2%	
		500K	(4/√3×4/√3)R30°	6.3Å	α: 0.6Å β: 0.2Å	2.8%	
Ag(110)	Evaporation	460K	(5×2) or c(10×2)	-	-	-	[23-26][63-65]
		>460K	c(8×4)	-	-	-	
ZrB_2(0001)	Segregation	750°C - 800°C	(2×2)	6,32Å	0.3Å and 0.9Å	5%	[40, 68,70]
Au(111)	Evaporation	530K	Surface alloy	7,3Å×9,2Å	-	-	[38]
	Segregation	560K	(1×1)Si	4,1Å	5pm	6%	[39]
			Surface alloy	7,5Å×9,4Å	-	-	
Pb(111)	Evaporation	350K<T<390K	$(1\times1)_{Si}$-uncover	3,90Å	0,1Å	0,8%	[37]
			Pb-induced $(\sqrt{3}\times\sqrt{3})_{Si}$R30°	6,70Å	-	4,5%	
NaCl/Ag(110)	Evaporation	410K	(3×4)	-	-	-	[74]
Ir(111)	Evaporation	670K	(√19×√19) R23,4° (surface alloy)	11,84Å	-	-	[41, 75]
Pt(111)	Evaporation	750K	(√19×√19) R23,4° (surface alloy)	12,1Å	-	-	[76]

Table 2.2 Formation of the various reconstructions for the growth of Si on the different substrates, including the unit cell size, the buckling, the ratio of misfit, the growth temperature, and experimental synthesis methods. The misfit values are taken from the references.

Concerning the Au(111) surface, Stępniak-Dybala et al. have reported the formation of flat (1×1) silicene and the Si-Au surface alloy using the surface segregation method [38]. After annealing at 560 K, they observed two different areas with hexagonal structure and rectangular one, respectively. Based on STM measurement and DFT calculations, the authors considered the hexagonal structure as (1×1) silicene with the lattice constant of 4.1 Å and the buckling less than 5 pm [38]. The rectangular structure, with the unit cell size of 0.74 nm × 0.94 nm, is considered as a Si-Au surface alloy, which has been reported in the literature [71–73]. In 2017, Sadeddine et al. have also reported the rectangular structure after 1 ML Si deposition on the Au(111) surface at 260°C [39]. In the case of the silicene synthesis via the Si evaporation, the formation of silicene on a Pb(111) thin film grown on Si(111) [37] and on a NaCl film grown on Ag(110) [74] have been also reported. After around 0.5 ML Si deposition on the Pb(111) thin film at 350 - 380 K, the (1×1)-uncovered (on top) and the $\left(\sqrt{3}\times\sqrt{3}\right)_{Si}$-covered (intercalated) silicene structures have been obtained [37].

The former indicates the lattice constant of 3.9 Å and the buckling of 0.1 Å, i.e. more flat than freestanding silicene. From combined STM, LEED, XPS EXAFS and DFT calculations, a model of silicene nanoribbons on a NaCl thin film with a (4×3) reconstruction with respect to the unit cell of Ag(110) has been proposed [74].

Different from the formation of layered silicene, Si growth on several substrates leads to the formation of surface alloys, for example in the case of deposition on Ir(111) [75] and on Pt(111) [76]. Regarding Si growth on Ir(111), Meng et al. have reported the formation of a $\left(\sqrt{3}\times\sqrt{3}\right)_{Si}$ silicene structure corresponding to $\left(\sqrt{7}\times\sqrt{7}\right)_{Ir}$ reconstruction after Si deposition at RT and annealing at 670 K [41]. However, Satta et al. have reported the formation of the Si-Ir surface alloy with the $\left(\sqrt{19}\times\sqrt{19}\right)R23.4°$ reconstruction at the growth temperature of 670 K [75]. Based on the evolution of the Si 2p and Ir $4f^{7/2}$ core level spectra and supported by DFT calculations, they concluded to the formation of the Si-Ir surface alloy and to the thermodynamic instability of layered silicene grown on Ir(111) as compared to the surface alloy [75]. In the case of Pt(111), the growth of Si submonolayer on Pt(111), at a substrate temperature of 750 K, leads to the formation of an ordered surface alloy with the same $\left(\sqrt{19}\times\sqrt{19}\right)R23.4°$ symmetry, which consists of Si_3Pt tetramers [76]

Silicene growth has also been studied on lamellar substrates, such as MoS_2 and HOPG. For Si growth on MoS_2, Chiappe *et al.* have reported the formation of silicene with a lattice constant of 3.2 Å [77]. However, this lattice constant, similar to the one of MoS_2, is much smaller than the one of freestanding silicene. This result was questioned by Bremen et al., they have reported the intercalation of Si between MoS_2 layer [78]. Regarding the growth of silicon on HOPG, several studies have presented the formation of small clusters on HOPG surface, with a Volmer-Weber growth mode [42][79]. Recently, De Crescenzi *et al.* have reported the formation of a $\left(\sqrt{3}\times\sqrt{3}\right)R30°$ reconstruction in-between Si clusters [43]. However, this reconstruction is due to the charge density modulations by defects (clusters and step edges) breaking the lattice periodicity [80].

2.3 Growth of germanene on several substrates

As layered germanene doesn't exist in nature, its synthesis requires a substrate. In the following pages, I will present the growth mode and the structure of germanium on several substrates, such as Au(111) [81–84], Ag(111) [85–87], Pt(111) [88], Al(111) [7][89–93], MoS_2 [94], HOPG [8], Sb(111) [95].

2.3.1 Growth of Ge on Al(111)

The Al(111) surface is a potential substrate for the growth of germanene for three reasons: (i) Al(111) surface possess hexagonal close-packed atomically structure; (ii) the Al(111) lattice parameter (a_{Al} = 4.0 Å) is close to the theoretical one of free-standing germanene ($a_{germanene}$ = 3.97 ± 0.1 Å); (iii) Al and Ge are not miscible in the bulk.

- **Formation of layered germanene**

In 2015, the first study of the growth of germanium on Al(111) has been reported by Derivaz *et al.* [7]. They performed LEED, STM, core-level photoelectron diffraction (XPD) measurements, and DFT calculations. They have observed a $(3\times3)_{Al}$ reconstruction, with respect to the unit cell of Al(111), after the evaporation of 1 ML Ge on Al(111) at about 360 K. A honeycomb network appears on high-resolution STM images in positive (Fig. 2.13a) and negative (Fig. 2.13b) sample bias. In Fig. 2.13a, the line profile along AB in Fig. 2.13c indicates that the surface periodicity a = 8.5 ± 0.1Å corresponds to 3 times the Al(111) surface lattice constant ($a_{Al(111)}$ = 2.86 Å). The line profile along CD, as illustrated in Fig. 2.13d, shows that the distance between two adjacent protrusions d=5.8 ± 0.1 Å is much larger than the distance between Ge atoms in germanene [7].

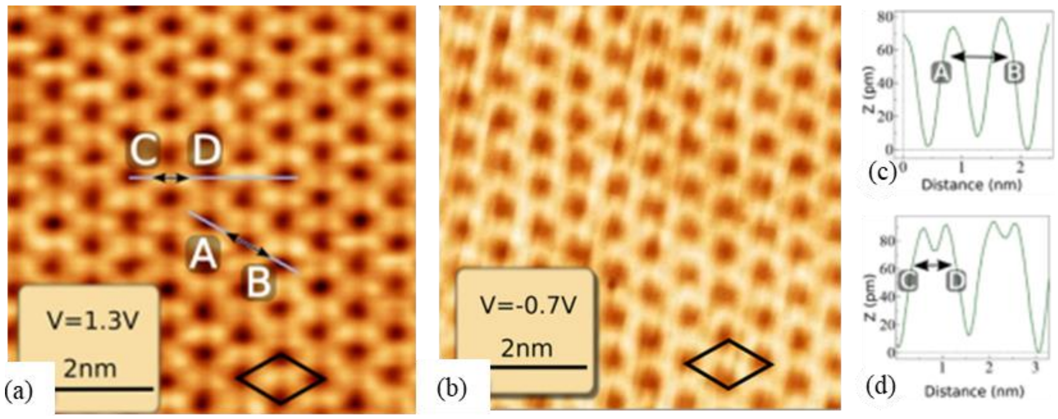

Figure 2.13 High-resolution STM image (a) in positive bias (*U* = 1.3 V, *I* =0.3 nA) and (b) in negative bias (*U* = -0.7 V, *I* = 0.3 nA) of germanene/Al(111). The black rhombus shows the unit cell of germanene. The line profiles along AB and CD in (a) are drawn in (c) and (d), respectively. Image reproduced from ref. [7]

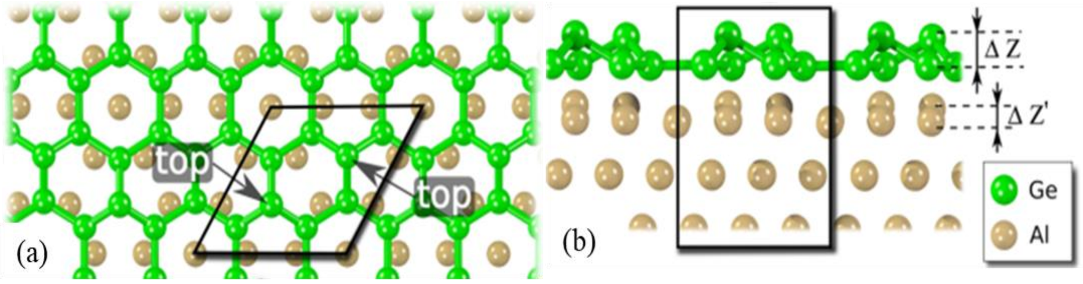

Figure 2.14 Top (a) and lateral (b) view of the atomic model of germanene grown on Al(111). The black rhombus shows the unit cell of germanene with two protruding Ge atoms labeled “top”. The black rectangle is the lateral view of the rhombus zone in (a). Image reproduced from ref. [7]

On the basis of DFT calculations, Derivaz et al. have proposed an atomic model of a germanene monolayer grown on Al(111) with a $(3 \times 3)_{Al}$ surface reconstruction, as shown in Fig. 2.14. In a top view (see Fig. 2.14), this model proposes that a (2×2) germanene reconstruction corresponds to a $(3 \times 3)_{Al}$ reconstruction, with a unit cell composed of eight Ge atoms. Two Ge atoms (labeled top) are located on top of an Al atom, while the other six atoms are located in the Al-Al bridge sites. The side view in Fig. 2.14b shows an upward displacement of Ge and Al atoms, two ‘top’ Ge atoms are shifted by Δz = 1.23 Å compared to the other Ge atoms, and two Al atoms under ‘top’ Ge atoms are lifted by Δz’ = 0.6 1Å with respect to the first plane. In the unit cell, two ‘top’ Ge atoms are shown as two protrusions in Fig. 2.13a. From XPS measurements, Derivaz *et al.* concluded that the interaction between the germanene layer and the Al(111) surface is electrostatic, without covalent bonding [89].

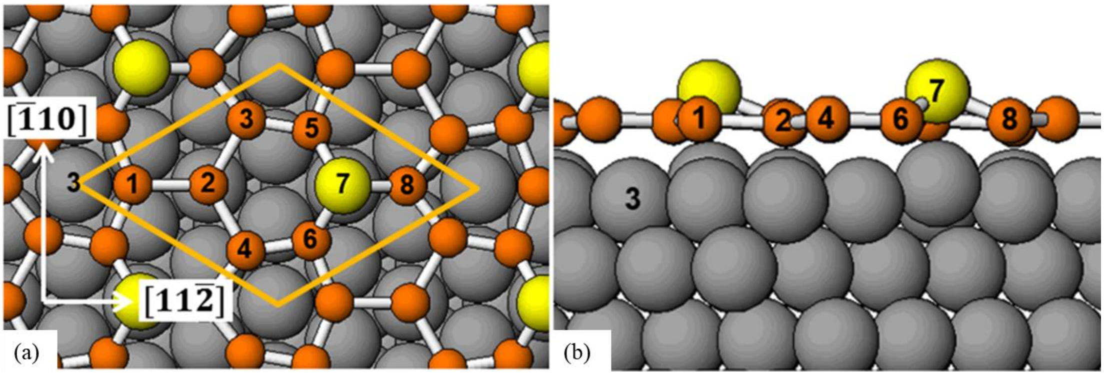

Figure 2.15 Top (a) and side (b) view of asymmetric structural model for germanene on Al(111). In the unit cell (yellow rhombus), the protruding Ge atom (No.7) and other Ge atoms are indicated by yellow and orange balls, respectively. The gray balls denote Al atoms. Images reproduced from ref. [92]

Later on, Fukaya *et al.*, from total-reflection high-energy positron diffraction (TRHEPD), have proposed an asymmetric structure for germanene on Al(111), with one of eight Ge atoms protruding upward in the unit cell [92] (see Fig. 2.15). As compared with the previous model [7], the hexagonal ring in the unit cell is distorted, and only one Ge atom (labeled 7) atop Al atom is uplifted by 0.94 Å with respect to the other Ge atoms. For the Al(111) surface, the Al atom under the uplifted Ge atom is uplifted by 0.42 Å compared to the first Al(111) plane.

Based on STM measurements and DFT calculations, Stephan *et al.* have claimed that the modification of the $(3\times3)_{Al}$ reconstruction with either one or two protruding Ge atoms in the unit cell can be driven by sample-tip interaction during the scan [96]. High-resolution STM image (see Fig. 2.16), obtained within the same experimental condition as in ref. [7], shows a change of contrast between a hexagonal contrast (upper part) and a honeycomb contrast (lower part). The hexagonal contrast exhibits one protrusion in the unit cell, instead of two for the honeycomb contrast. Supported by DFT calculations, Stephan et al. have proposed a structural model named germanene-1H for the hexagonal contrast, with only one uplifted Ge atom located on the hollow site of Al(111) surface in the unit cell [96].

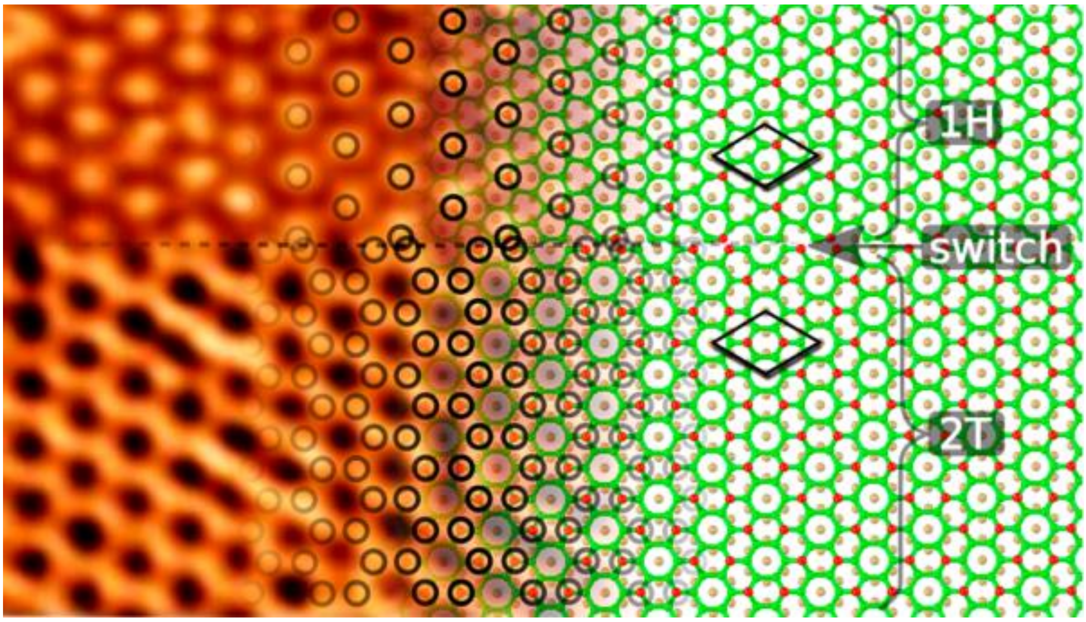

Fig 2.16 Experimental STM image (U= 1V) and the network of two simulated structures, showing the switching between 1H and 2T configuration. The unit cell (black rhombus) of the 1H configuration shows only one protruding Ge atom (red ball), instead of two in the 2T configuration. Green and beige balls correspond to Ge and Al atoms, respectively. The black circles show the correspondence between the uplifted Ge atoms in the calculated network and the protrusions in the STM image. Figure adapted from ref. [96]

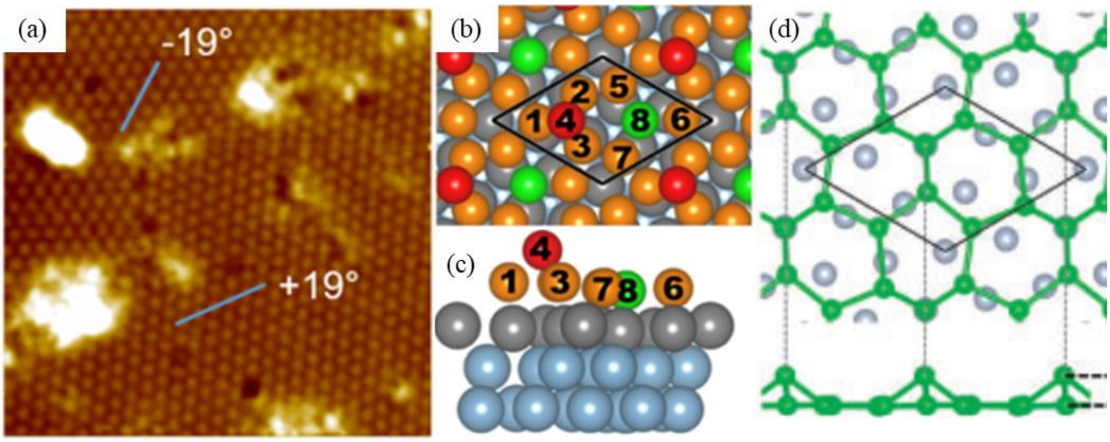

Figure 2.17 (a) STM image (≈ 19×19 nm^2, U = -1.2 V, I = 200 pA) showing the $(\sqrt{7}\times\sqrt{7})_{Al}R(\pm 19.1°)$ reconstruction. (b) Top and (c) lateral view of model for this reconstruction from ref. [91]. (d) Another model for this reconstruction from ref. [90]

Wang et al. [91] and Endo et al. [90] have reported the coexistence of the $(3\times 3)_{Al}$ and $(\sqrt{7}\times\sqrt{7})_{Al}R(\pm 19.1°)$ germanene reconstruction on Al(111) surface.

Wang et al. performed LEED patterns, STM measurements, core-level spectroscopy, and DFT calculations. After the evaporation of 0.6 ML Ge at a substrate temperature of about 470 K, as presented in Fig. 2.17a, the Ge adlayer shows a $(\sqrt{7} \times \sqrt{7})_{Al}R(\pm 19.1°)$ reconstruction. The measured lattice constant of this reconstruction is 7.5 ± 0.05 Å. Based on DFT calculations, Wang et al. have proposed a relaxed atomic model of a (2×2) germanene reconstruction corresponding to $(\sqrt{7} \times \sqrt{7})_{Al}R(\pm 19.1°)$ reconstruction with one of eight Ge atoms uplifted. The corresponding buckling id Δz = 1.96 Å [91]. Fig. 2.17b and 2.17c show the atomic arrangement of this model, where the protruding Ge atom is labeled “4”. On the other hand, Endo et al. have reported the growth of germanene on Al(111) at RT and proposed another model of, corresponding to a $(\sqrt{3} \times \sqrt{3})R30°$ germanene reconstruction for the $(\sqrt{7} \times \sqrt{7})_{Al}$ surface periodicity, as illustrated in Fig. 2.17d, with one of six Ge atoms uplifted in the unit cell and with a buckling Δz=1.44 Å [90]. The authors also concluded that the Ge-$(2 \times 2)/(\sqrt{7} \times \sqrt{7})_{Al}$ system should result in two protruding Ge atoms in the unit cell. The in-plane lattice constant of these two models is different.

For the growth at different substrate temperatures, several studies have reported the coexistence of $(3 \times 3)_{Al}$ and $(\sqrt{7} \times \sqrt{7})_{Al}R(\pm 19.1°)$ phases at substrate temperatures in the 300 - 470 K range and the disappearance of these germanene phases above 480 K ~ 500 K [97–99]. They have also proposed the models of germanene with only one protruding Ge atom located on *fcc* and *hcp* position for the (3×3) and (√7×√7) reconstruction respectively, instead of the top position of underlying Al atoms [97].

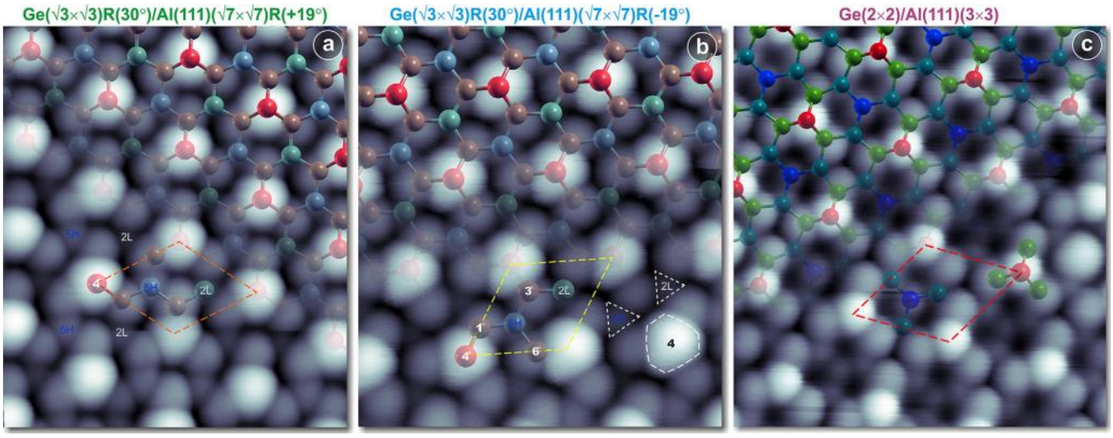

Figure 2.18 Extra-high resolution STM images ((a) 2.8×3.2 nm^2, V = -450 mV, I = 1.8 nA, (b) 2.6×2.9 nm^2, V = -200 mV, I = 0.4 nA, [c] 3.3×3.4 nm^2, V = -2 mV, I = 0.27 nA) for (a, b) $(\sqrt{3}\times\sqrt{3})R30°$ and (c) (2×2) germanene phases on Al(111), respectively. Top view of the models of three germanene phase superimposed on STM images. Red balls represent only one uplifted Ge atom. Images reproduced from ref. [99]

More recently, based on the STM measurements with extra-high atomic-scale resolution and DFT calculations, Muzychenko et al. have also investigated three germanene phases grown on Al(111) [99]. After 0.2 - 0.6 ML Ge deposition on Al(111) at a temperature of ~360K, the extra-high resolution (EHR) STM images in Fig. 2.18 show clearly the atomic arrangement for the $(\sqrt{7}\times\sqrt{7})_{Al}R(\pm 19.1°)$ and $(3\times 3)_{Al}$ surface reconstructions. As presented in these images, the unit cell of these surface reconstructions possesses six and eight atoms with uplifted one, respectively. From the comparison between experimental and simulated STM images, these atoms are shown to be Ge atoms. Combining STM measurements and DFT calculations, the model (see Fig. 2.18) proposed by Muzychenko *et al.* [97][99] matches the experimental results. Thus, the authors concluded the formation of single-layer germanene on the Al(111) surface, instead of the formation of the Al-Ge surface alloy [99].

- **Formation of Al-Ge surface alloy**

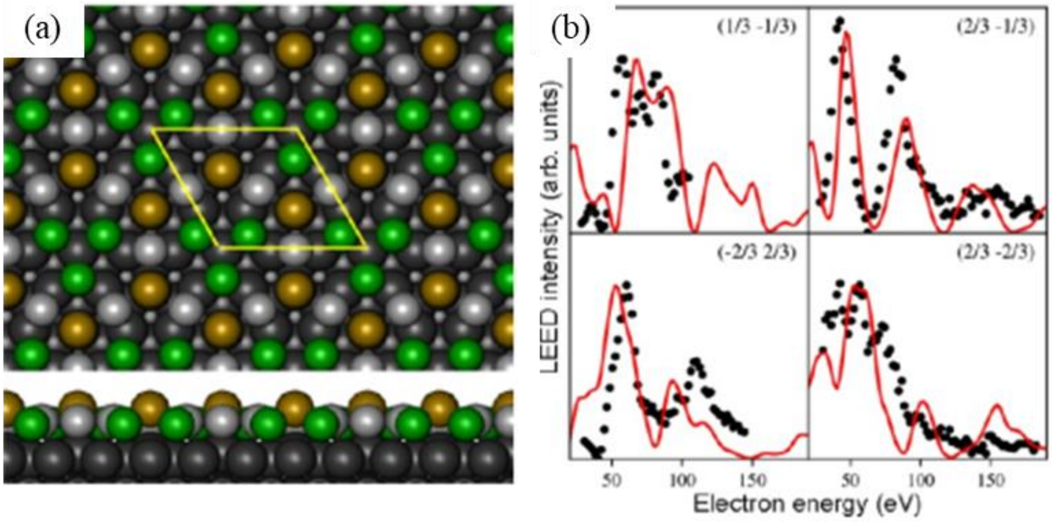

Figure 2.19 (a) Top and lateral view of the relaxed model of Ge -Al alloy. Yellow and green balls indicate Ge atoms in a higher and lower position, respectively. Gray and black balls represent Al atoms in the top layer and in the underlying layer, respectively. (b) Comparison between experimental (black dot) and simulated LEED I-V curve (red line, corresponding 4 spot: (1/3 -1/3), (2/3 -1/3), (-2/3 2/3), and (2/3 -2/3). Figures reproduced from ref. [93]

As discussed above, the growth of Ge on Al(111) surface has been interpreted as the formation of layered germanene. However, the formation of Al-Ge surface alloy has also been proposed in the literature [93][100]. On the basis of the theoretical investigation, Fang et al. have reported that the model of the $(3 \times 3)_{Al}$ reconstruction with only one Ge atom protruding upward in the unit cell is energetically unfavorable as compared to the model with two uplifted Ge atoms in the unit cell [100]. Moreover, they have indicated that the formation of Al_2Ge surface alloy is indeed possible and energetically favorable.

In 2019, combining direct-recoil and time-of-flight spectroscopy (TOF-DRS), electron energy loss spectroscopy (EELS), and DFT calculations, Martinez et al. have proved the existence of Al atoms mixed with Ge atoms at the top layer, revealing the formation of the surface alloy for the growth at a substrate temperature within 100-140℃ [93]. After 1 ML Ge deposition on Al(111), TOF-DRS spectra show that the intensity of Al recoil signal decreases but does not entirely disappear, implying the coexistence of Ge and Al atoms in the top layer. Based on DFT calculations and LEED I-V curve simulations, they have proposed a model for the $(3 \times 3)_{Al}$ reconstruction, as illustrated in Fig. 2.19. The unit cell of this model consists of three Al atoms and five Ge atoms with two uplifted Ge atoms, and the simulated LEED I-V curve for this model is in agreement with the experimental one (see Fig. 2.19b). However, recent STM measurements in ref. [90][91][97–99] don't give a evidence to support this model.

2.3.2 Growth of Ge on Ag(111)

The case of the growth of germanium on Ag(111) is also controversial for the formation of a germanene single layer or the formation of Ag-Ge surface alloy.

- **Formation of Ag-Ge surface alloy**

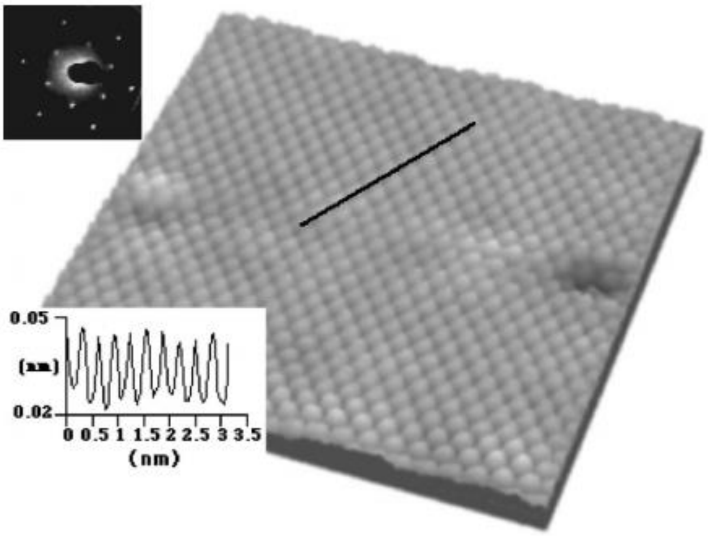

Figure 2.20 Filled-state STM image (6.4×6.4 nm^2; U=-50 mV, I=2.0 nA). Left-upper part: LEED pattern with Ep=52 eV. Lower-left corner: the line profile along black line shown in the image. Image adapted from ref. [85]

In 2000, the first study of the growth of germanene on Ag(111) at room temperature has been reported by Oughaddou et al. [85]. After deposition of 1/3 ML Ge, LEED measurements showed the presence of a $p(\sqrt{3} \times \sqrt{3})R30°$ reconstruction with respect to the Ag(111) surface [hereafter named as $(\sqrt{3} \times \sqrt{3})$], as seen in Fig. 2.20. However, the STM image in Fig. 2.20 presents a surface with a lattice constant of 3.1 ± 0.1 Å, i.e. identical to Ag(111), and with the vertical corrugation of 0.3 Å, not providing any evidence for the existence of the $(\sqrt{3}\times\sqrt{3})$ reconstruction. The XPS study revealed the formation of Ag-Ge surface alloy as evidenced by the disappearance of Ag surface states and the metallic character of the Ge atoms in the $(\sqrt{3}\times\sqrt{3})$ superstructure. Supported by DFT calculations, Oughaddou et al. concluded that the formation of an ordered surface Ag_2Ge alloy is thermodynamically more favorable than the presence of adsorbed Ge adatoms on the surface [85].

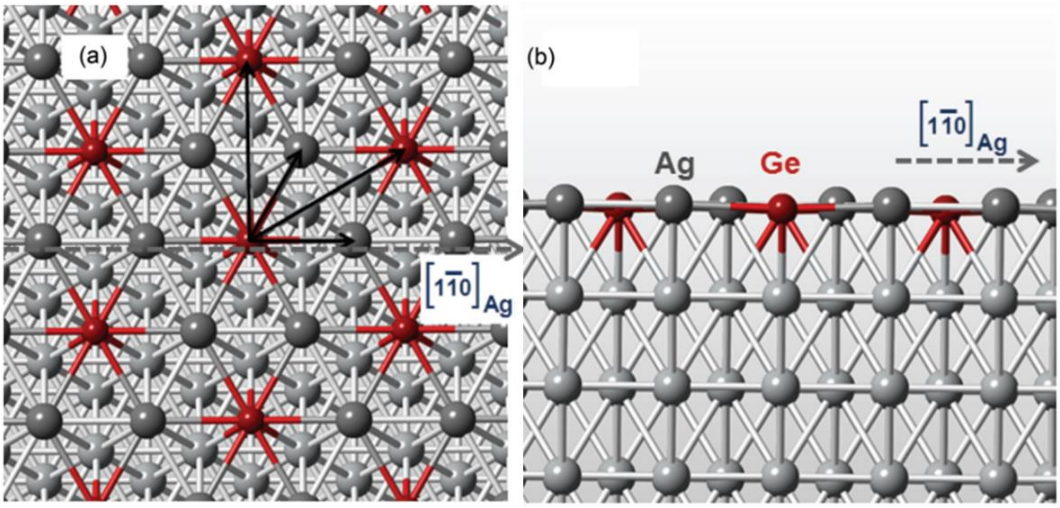

Figure 2.21 (a) Top and (b) lateral view of the relaxed $(\sqrt{3}\times\sqrt{3})$ Ag-Ge model optimized by DFT. Red balls indicate Ge atoms. Dark and light gray balls represent Ag atoms in the top layer and in the underlying layer, respectively. Figures adapted from ref. [101]

A decade later, Golias et al. have performed in situ ARPES to investigate the band structures of the Ag_2Ge surface alloy [101]. Supported by DFT calculations, they have also proposed a model of a substitutional Ag_2Ge surface alloy, where inserted Ge atoms are 0.09 Å lower than Ag top surface atoms, as illustrated in Fig 2.21. However, the simulation of this model cannot reproduce the surface band split at the -M points along the -Γ-K-M line of the $(\sqrt{3}\times\sqrt{3})$ surface Brillouin zone (SBZ).

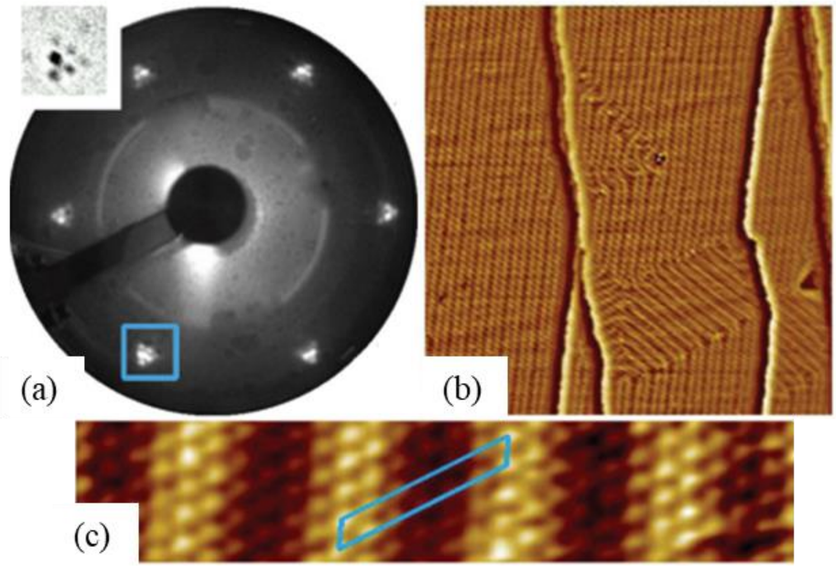

Figure 2.22 (a) LEED pattern with Ep = 25 eV. The inset shows six spots in the √3 position. (b) Filled-stated STM image (130×130 nm^2; U=-50 mV, I=300 pA) exhibiting a striped phase. Three zones of the striped phase are aligned along three different directions, separated by 120°. (c) High-resolution STM image (2.4×12.8 nm2; U=-50 mV, I=300 pA) showing the striped phase with the $(\sqrt{3}\times 6\sqrt{3})$ reconstruction, the unit cell is indicated by blue parallelogram. Figures adapted from ref. [86]

Later on, based on LEED pattern and STM measurements, Wang et al. have reported the atomic structure of Ag-Ge surface alloy [86]. After deposition of 1/3 ML Ge at RT and annealing at 473 K, the resolved LEED pattern in Fig. 2.22a shows six spots forming a triangle near $\sqrt{3}$ positions and no spot at the exact $\sqrt{3}$ position, indicating the imperfect $(\sqrt{3}\times\sqrt{3})$ periodicity and the existence of a long-range modulation. A large-scale STM image in Fig. 2.22b exhibits that a striped structure, with a height difference of about 0.2 Å, is aligned along with three different directions, separated by 120°. Furthermore, a high-resolution STM image shows the local $(\sqrt{3}\times\sqrt{3})$ reconstruction and a long-range modulation, corresponding to a $(\sqrt{3}\times 6\sqrt{3})$ reconstruction presented in Fig .2.22c in good agreement with the LEED pattern shown in Fig 2.22a. The protrusions in the STM image may be associated with Ge atoms in the Ag_2Ge surface alloy. The authors concluded that the complex surface band structure, with several split bands, most likely originates from the structural distortions of the alloy layer [86].

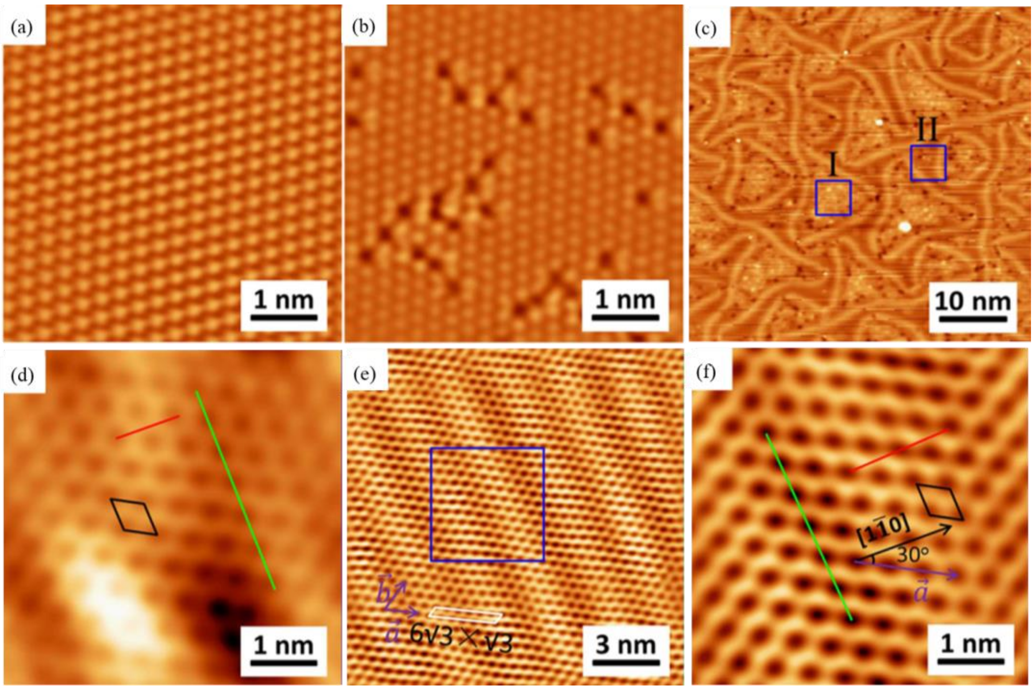

Figure 2.23 High-resolution STM image of (a) the clean Ag(111) surface (5×5 nm^2; U=0.136V, I=0.05 nA) and (b) the surface at very beginning of Ge deposition (5×5 nm^2; U=0.1V, I=0.05 nA). (c) STM image (50×50 nm^2; U=-2V, I=0.05 nA) showing the triangular areas (blue square I) surrounded by distorted stripes (blue zone II). (d) High-resolution STM image of zone II (5×5 nm^2; U=2.5V, I=0.05 nA) in (c). (e) STM image (15×15 nm^2; U=-8mV, I=0.05 nA) of the striped phase. (f) High-resolution STM image(5×5 nm^2; U=2.5V, I=0.05 nA) of the blue zone in (e). Images adapted from ref. [102]

More recently, Liu et al. have investigated the growth of Ge on the Ag(111) surface at RT and 600 K, by STM and ARPES measurements [102]. Compared to the bare Ag(111) surface (see Fig. 2.23a), at the very beginning of Ge deposition at RT, the STM image in Fig. 2.23b shows some randomly distributed hollows on the surface, indicating clear evidence of Ge substitution. At about 1/3 ML Ge coverage, the STM measurement in Fig. 2.23c displays the formation of a triangular pattern with triangular areas (zone I) surrounded by distorted stripes (zone II). In zone II, Fig. 2.23d shows a honeycomb network with $\left(\sqrt{3} \times \sqrt{3}\right)$ reconstruction measured by green line profile, and this reconstruction can be interpreted as a Ag_2Ge surface alloy from its lattice constant (black parallelogram). For deposition of 1/3 ML Ge at 600 K, the formation of the $\left(\sqrt{3}\times 6\sqrt{3}\right)$ striped pattern, as displayed in Fig. 2.23e and 2.23f, was confirmed and also interpreted as a substitutional Ag_2Ge surface alloy [102]. In a very recent study, the LEED diagram corresponding to satellite spots around diffraction conditions of a $\left(\sqrt{3}\times\sqrt{3}\right)$ reconstruction, and previously attributed to the striped phase, has been interpreted as a $\left(19\sqrt{3}\times 19\sqrt{3}\right)R30°$ reconstruction, corresponding to a Ag_2Ge surface alloy contracted by 5% with respect to the Ag(111) surface[136].

- **Formation of layered germanene**

Contrary to these discussions above, some studies have concluded the formation of germanene on Ag(111). Md Sazzadur *et al.* have performed STM and LEED measurements to investigate the growth of Ge on Ag(111) [103]. At different Ge coverage and after annealing at 415 K, they have reported $\left(9\sqrt{3}\times 9\sqrt{3}\right)R30°$, $c\left(\sqrt{3}\times 7\right)$ and (12×12) structures by LEED, that they have associated with the formation of layered germanene with the $\left(9\sqrt{3}\times 9\sqrt{3}\right)_{Ag}R30°$ moiré structure, instead of the Ag_2Ge surface alloy.

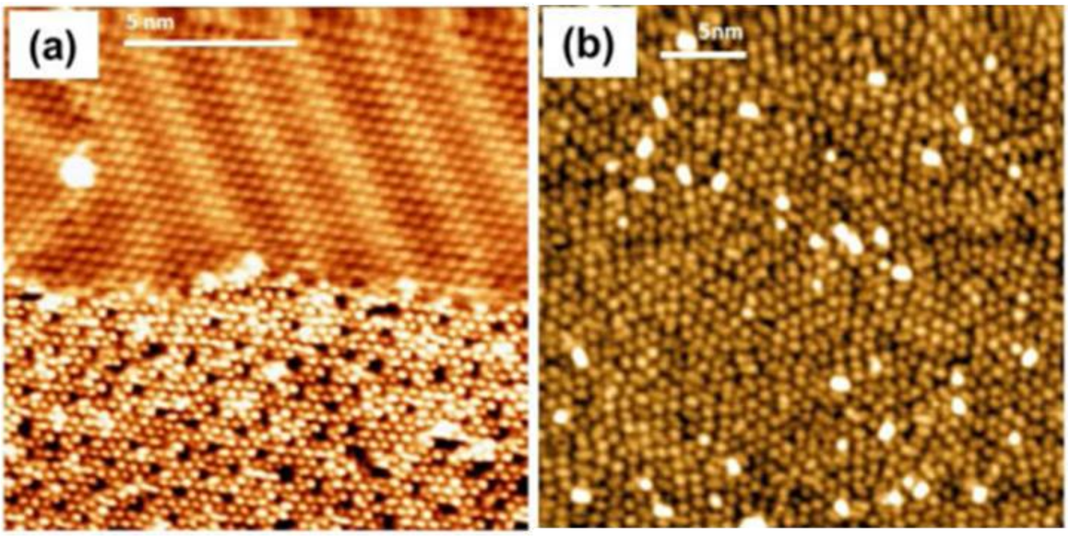

Figure 2.24 (a) STM image (15×15 nm^2; U=-0.65V, I=1.0 nA) showing the coexistence of the SP (upper) and QP (lower). (b) STM image (15×15 nm^2; U=-0.65V, I=1.0 nA) of QP germanene phase with slight disorder. Images adapted from ref. [87]

After the evaporation of about 0.74 ML Ge on Ag(111) at 423 K, Lin et al.

observed the $\left(\sqrt{3}\times 6\sqrt{3}\right)$ striped phase (SP) but, neglecting previous observations, they interpreted it as germanene with a large tensile strain of 12% to 23 % as a function of the direction [87]. For further Ge evaporation, their STM observations, reported in Fig. 2.24a show the coexistence of the striped phase and that they called a quasi free-standing germanene phase (QP), revealing that the SP phase is converted into the QP phase. At a Ge coverage of ~1.08 ML, the SP phase is completely replaced by the QP phase (see Fig. 2.24b). The authors have proposed that the QP phase is also a honeycomb germanene layer, but with a slight compressive strain [87]. Later on, Zhuang *et al.* [104] have reported the formation of the substitutional Ag_2Ge surface alloy at low Ge coverage, and the transition from the striped phase to a disordered honeycomb phase corresponding to the QP phase of Lin *et al.* [87]. With additional Ge deposition, due to the stronger Ge-Ge interaction, Ge atoms in the Ag_2Ge alloy form a disordered honeycomb phase with additional Ge atoms. After the growth of few-layers germanium films on Ag(111), the authors have reported that the outermost surface is a germanene layer with the $(\sqrt{3}\times\sqrt{3})\mathrm{R}30°$ reconstruction with respect to Ge(111) [104].

Besides the molecular beam epitaxy(MBE) method, some studies have reported the formation of germanene via a segregation method [105-107]. Using this method, Yuhara et al. have reported the formation of germanene on a Ag(111) thin-film grown on Ge(111) [105]. After annealing at 480°C, a $\left(7\sqrt{7}\times 7\sqrt{7}\right)_{Ag}R19.1°$ reconstruction forms on the surface with hexagon and dimers protrusions, as presented in Fig. 2.25a and 2.25b. Moreover, the LEED pattern exhibits a $(1.35\times 1.35)_{Ag}R30°$ superstructure. The authors have proposed a model (see Fig. 2.25c) of this reconstruction corresponding to $\left(3\sqrt{21}\times 3\sqrt{21}\right)_{Ge}R10.9°$ germanene superstructure [105], where the unit cell of $(1.347\times 1.347)_{Ag}R30°$ with regard to Ag(111), compared to the primitive germanene unit cell.

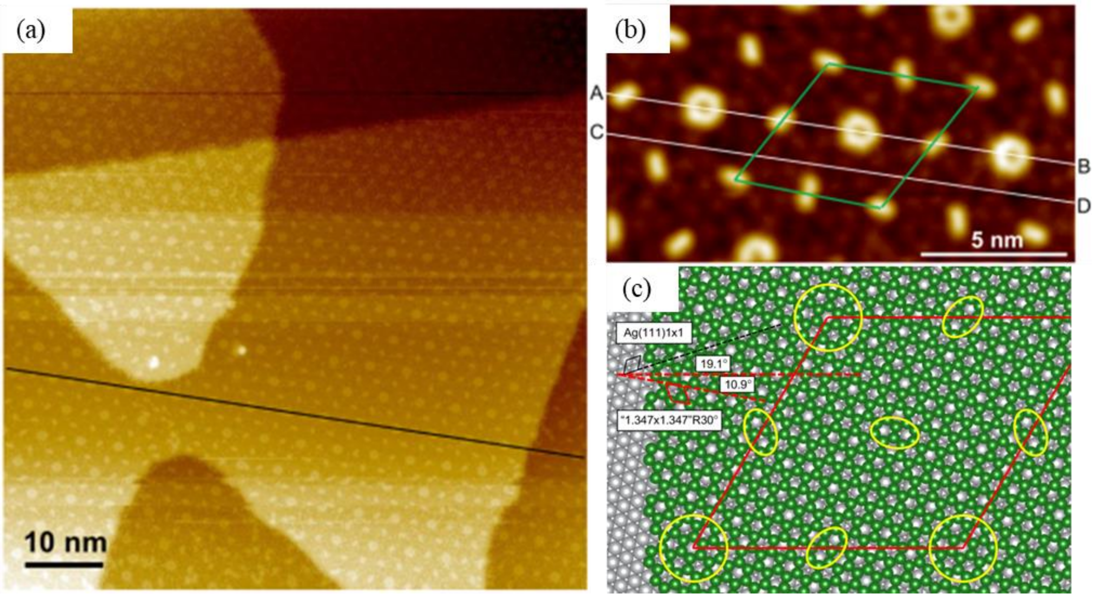

Figure 2.25 (a) Large-scale STM image and (b) High-resolution STM image (U=0.3V, I=200 pA) exhibiting germanene formed on the Ag(111) thin layer grown on Ge(111). Green rhombus represents the unit cell of the $(7\sqrt{7}\times 7\sqrt{7})_{Ag}R19.1°$ reconstruction. (c) a model of $(7\sqrt{7}\times 7\sqrt{7})_{Ag}R19.1°$ corresponding to $(3\sqrt{21}\times 3\sqrt{21})_{Ge}R10.9°$ germanene superstructure, with the local unit cell of $(1.35\times 1.35)_{Ag}R30°$. Yellow circle represent the protrusions in (b). Images reproduced from ref. [105]

As discussed above, these previous studies lack real-time STM measurements for the evolution of the surface, during the growth. These real-time STM measurements are helpful to study the growth mechanisms and to investigate the different reconstructions of the Ge/Ag(111) system. In chapter 5, based on real-time STM and GIXD measurements, I will present the growth of Ge on Ag(111) and the different atomic structures in Ge/Ag(111) system.

2.3.3 Growth of Ge on other surfaces

Most of the studies devoted to germanene growth were done on Ag(111) and Al(111) surface. In the following, I will give a description the growth of Ge on the other substrates, as illustrated in Table. 2.3.

Beside the growth of Ge on the Al(111) [7][89–93][97–99] and Ag(111) surface [85–87][102–108], many studies have reported the formation of layered germanene or the surface alloy on the different substrates, such as Au(111) [81–84][109], Cu(111) [110][111], Sb(111) [95], Pt(111) [76][88][112], MoS_2 [94], and HOPG [8]. Thus, I summarized the results of these studies, and made a table(see Table III) exhibiting the information about the formation of the reconstructions on the different substrates at different temperature.

Substrate	Synthesis method	Growth temperature	Reconstructions	Unit cell size	Buckling	Misfit	Ref.
FS germanene	-	-	-	3.97Å	0.64Å	-	[16]
Al(111)	Evaporation	300K – 470K	(3×3) (√7×√7)	8.58Å 7.58Å	1.23Å 1.44Å	7.6% 9.3%	[7], [89-93]
Ag(111)	Evaporation	300K – 600K	(√3×√3) (local) (√3×6√3)	5.0Å -	- 0.2Å	- L*: 23% T*: 12%	[87]
Ag(111) thin films	Segregation	750K	1.35×1.35 R30° (local) (7√7×7√7) R19.1°	3.9Å 53.5Å	0.1Å -	- 2%	[105]
Au(111)	Evaporation	RT	(√7×√7) R19.1° $\begin{pmatrix} 5 & 0 \\ 8 & -14 \end{pmatrix}$	6,92Å 35,5Å×14,4Å	<0,3Å -	9,2% -	[81] [83]
Cu(111)	Evaporation	RT	$(1\times1)_{Ge}$ (√3×√3)R30°	4,4Å 4,38Å	0Å 0,61Å	11% 10.3%	[110, 111]
Sb(111)	Evaporation	470K	(1×1)Ge Mosaic structure	4,0Å	-	7%	[95]
Pt(111)	Evaporation	RT	(√19×√19) R23.4°	12Å	0,6Å	0,8%	[76]
Ge_2Pt on Ge(110)	Segregation	1100K	$(1\times1)_{Ge}$	4,4Å	0,2Å	11%	[113, 135]
MoS_2	Evaporation	RT	(6×6)	19Å	0,86	4,5%	[94]

Table 2.3 The formation of the various reconstructions after the growth of Ge on the different substrates, including the unit cell size, the buckling, the ratio of misfit, the growth temperature, and experimental synthesis methods.

- **Ge on Au(111)**

The growth of germanene on Au(111) was first reported by Dávila *et al.* [81]. After deposition of about 1 ML Ge at 470 K, combining STM and core-level spectroscopy measurements, they concluded to the formation of layered germanene with a $(\sqrt{7}\times\sqrt{7})_{Au}R19.1°$ reconstruction. The authors have proposed a model of this reconstruction corresponding to a $(\sqrt{3}\times\sqrt{3})$ reconstructed germanene with a buckling less than 0.3 Å. Next year, Dávila and Le Lay have investigated the growth of multi-layer germanene on Au(111) at a substrate temperature of ~200°C [82]. Based on STM and LEED measurements, they have reported the formation of a $\left(3\sqrt{3} \times 3\sqrt{3}\right)_{Ge}$ reconstructed germanene related to $(8 \times 8)_{Au}$ superstructure, after Ge deposition of 3 or 4 ML. From ARPES measurements, they concluded to the presence of a Dirac cone in the band structure, originating from this $\left(3\sqrt{3} \times 3\sqrt{3}\right)$ reconstructed germanene [82].

Contrary to these above conclusions, some authors concluded the formation of a Au-Ge surface alloy instead of germanene. Cantero et al. have performed TOF-DRS measurements to prove the coexistence of Ge and Au atoms on the outermost surface after the formation of multilayer germanene, indicating the formation of the Au-Ge surface alloy [109]. Meanwhile, Muzychenko et al have reported the formation of the Ge-Au surface alloy for Ge coverage below 1 ML at a substrate temperature above 297K . They presented two different growth methods: the deposition of 0.4 ML Ge at RT following by annealing at 500 K and the deposition of 0.7 ML Ge on the surface at 500 K. At about 0.08 ML Ge coverage, the formation of “vacancy-like” defects indicates the substitution between Ge and Au atoms during the evaporation. After the evaporation of 0.4 ML Ge and annealing at 500 K, STM measurement show the formation of an ordered reconstruction with the atomic raw spacing of 5.77 Å. For the second method, the surface appears a diamond-like cubic structure with the unit cell size of (35.5±0.9) Å × (13.8±0.4) Å [83].

Later on, Wang et al. have also reported the formation of the Au-Ge surface alloy [84]. After the evaporation of about 1 ML Ge at RT and annealing at 573 K, the ordered reconstruction with the $\begin{pmatrix} 5 & 0 \\ 8 & -14 \end{pmatrix}$ unit cell formed, where the lattice constant of 35.0Å and 14.4 Å with 93° between two vectors is similar to the reconstruction in ref. [83]. The LEED pattern also gives evidence of the formation this surface reconstruction, instead of the 8×8 periodicity observed in ref. [82]. Moreover, the results of core-level photoelectron spectroscopy(PES) show the existence of the Ge 3d signal after several cycles of sputtering and annealing, revealing the formation of a Ge-Au surface alloy [84]. To summarize, the growth of Ge on Au(111) most probably results in the formation of a Au-Ge surface alloy, instead of germanene monolayer, independently of the Ge coverage.

- **Ge on Pt(111)**

After deposition of 1ML Ge at 300 K and annealing at 1000 K, Ho et al. have reported the formation of a Ge-Pt surface alloy associated with a $\left(\sqrt{19} \times \sqrt{19}\right)R23.4°$ reconstruction [112]. During annealing in a temperature range from 900 K to 1200 K, XPS and LEED measurements demonstrate that the signal of Ge $2p^{3/2}$ decreases without change of the structure, indicating the formation of a Ge-Pt surface alloy. In 2014, Švec et al. also suggested the formation of a Ge_3Pt surface alloy, based on the results of the study of Si/Pt(111) system [76].

In contrast to the formation of a Ge-Pt surface alloy, some authors concluded that germanene formed on Pt(111). Li et al. have reported the formation of germanene on Pt(111) possessing the $\left(\sqrt{19} \times \sqrt{19}\right)R23.4°$ reconstruction with a corrugation of 0.6 Å, after deposition at RT and annealing in a temperature range of 600 -750 K [88]. Supported by DFT calculations, the authors have proposed a model of a reconstructed (3×3) germanene matching with the $\left(\sqrt{19} \times \sqrt{19}\right)_{Pt}R23.4°$ reconstruction. However, with a lack of XPS and STM measurements at atomic resolution, it is difficult to verify the exact atomic structure. The existence of Ge-Pt alloy is a question for the formation of germanene on Pt(111).

- **Ge on other substrates**

After evaporation of 1 ML Ge on MoS_2 at RT, Zhang et al. concluded the formation of germanene with the lattice constant of 3.8 ± 0.2 Å, 20% larger than the one of MoS_2 [94]. Supported by DFT calculations, they have proposed the model of (5×5) germanene reconstruction corresponding to a (6×6) unit cell of MoS_2, with a buckling of 0.86 ± 0.10 Å and an interlayer distance of 5.02 Å. Based on the STS spectrum, V-shape linear dispersion near the Fermi level reveals Dirac feature for germanene grown on MoS_2.

In 2017, Qin et al. investigated the growth of Ge on Cu(111) at RT, using STM, STS and DFT calculations [110]. Below 1 ML Ge coverage, germanium island have a flat honeycomb structure with a lattice constant of 4.40 Å, that was associated with the formation of a relaxed (1×1) germanene structure. However, monolayer germanene does not exhibit any Dirac signature in the STS spectrum. Above 1 ML Ge coverage, bilayer germanene possesses a $\left(\sqrt{3}\times\sqrt{3}\right)\mathrm{R}30^\circ$ reconstruction with regard to Cu(111) and presents a V-shape differential conductivity curve in the STS measurement. Based on DFT calculations, the authors concluded the formation of a Bernal-stacked bilayer structure [110]. However, Li et al. concluded that the V-shape curve originates from the top layer of the AA-stacked bilayer structure, instead of the AB-stacked one [111].

For the growth of 1 ML Ge on Sb(111) at 470 K, Guo et al. have reported the formation of mosaic germanene on Sb(111), with the local (1×1) germanene reconstruction [95]. After the deposition of thin film of Pt on Ge(110) and annealing at 1100 K, the formation of germanene on the Ge_2Pt crystallite have been reported, with the lattice constant of 4.4 ± 0.2 Å and a low buckling of 0.2 Å [135]. In addition, Bremen et al. have reported that germanene grows on the {101} and {011} facets of the Ge_2Pt crystallite [113]. With regard to HOPG, the deposition of Ge on this substrate does not lead to the formation of germanene [80].

To conclude this chapter, I presented the synthesis of layered silicene, germanene, and the surface alloy on the various substrate surfaces. In the chapter that follows, I present the experimental equipment and methods, such as STM, LEED, and GIXD.

Chapter 3

3 Experimental methods

Contents

3.1 Scanning tunneling microscopy (STM)

Scanning tunneling microscopy (STM) is a powerful technique for directly imaging a semiconducting or metallic surface with atomic resolution. In 1981, the STM has been proposed for the first time by Gerd Binnig and Heinrich Rohrer [114], who won the Nobel Prize in physics in 1986. In the following page, I will present the physical principles of STM and methods for image analysis that I have used.

3.1.1 Description of STM

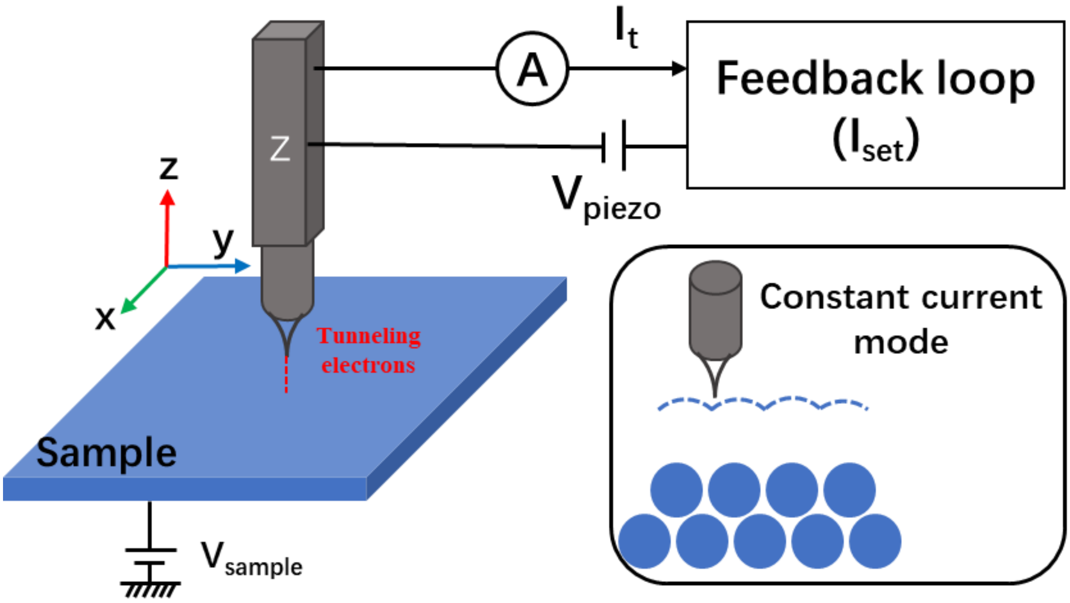

Figure 3.1 Schematic representation of the effect of the feedback loop. For each point the voltage used to the z-piezodrive to adjust the tip at the distance for the constant tunneling current Iset; I_t and I_{set} are respectively the tunneling current and the current requested by the user. Inset: Schematic of the *constant current* acquisition mode.

The principle of STM is to scan the surface with a sharp metallic tip located a few nanometers above the surface, while measuring the tunneling current between the tip and the sample under a given bias voltage. The value of the tunneling current is measured as a function of the distance between the tip and the substrate, as demonstrated later. In the STM setup, the tip is installed on a piezodrive that, upon applying a voltage, can control the movement of the tip on the surface with a sensitivity of less than 1 pm (i.e. 10^{-12} m). Fig. 3.1 presents the functioning of the *feedback loop*. In the *constant current* scanning mode, the feedback loop changes the tip-sample distance by adjusting the voltage (V_{piezo}) applied on the piezodrive, aimed to keep the tunneling current at a set constant value I_{set}. Moreover, the voltage used to change the z-position of the tip is recorded for each scanning point, and it is then converted into the value of an apparent height. As demonstrated later, an apparent height obtained from a STM image could not correspond to a true height in the real space. The *feedback loop* strength depends on its *gain* chosen. A high value of gain corresponds to a rapid response of the piezodrive, which could lead to high-frequency oscillations during scanning. On the contrary, a low gain result in a low response that may lead to the damage of the tip by the high surface obstacle. Regarding STM control system, several parameters can be set by the user, e.g. the image size, the image resolution, the gain of the *feedback loop*, the scanning rate, and the bias voltage between the tip and substrate. Due to the high sensitivity of the STM measurements, the resonance between the tip and the surface, caused by the external vibration, may lead to a periodic noise presented in the STM image.

At INSP, I have used a commercial VT-XA STM from the Scienta Omicron company. As shown in Fig 3.2, the integral equipment of STM is composed of a preparation chamber and a analysis chamber, separated by a mechanical valve. Both chambers work under ultra-high vacuum (UHV) condition, corresponding to a pression p less than 5.10^{-11} mbar. In the preparation chamber, the cleaning of a sample surface can be carried out by sputtering and annealing, using a leak valve for the control of Ar inflow, the sputter gun for the ionization and the bombardment, a heating resistor for the sample heating, and a thermocouple to measure the temperature of the sample. The tip annealing system is applied to clean the surface of the tip, using the direct-current to flash the tip. In addition, low energy electron diffraction (LEED) and Auger electron spectroscopy (AES) experiments can be performed in the preparation chamber (see Fig. 3.2).

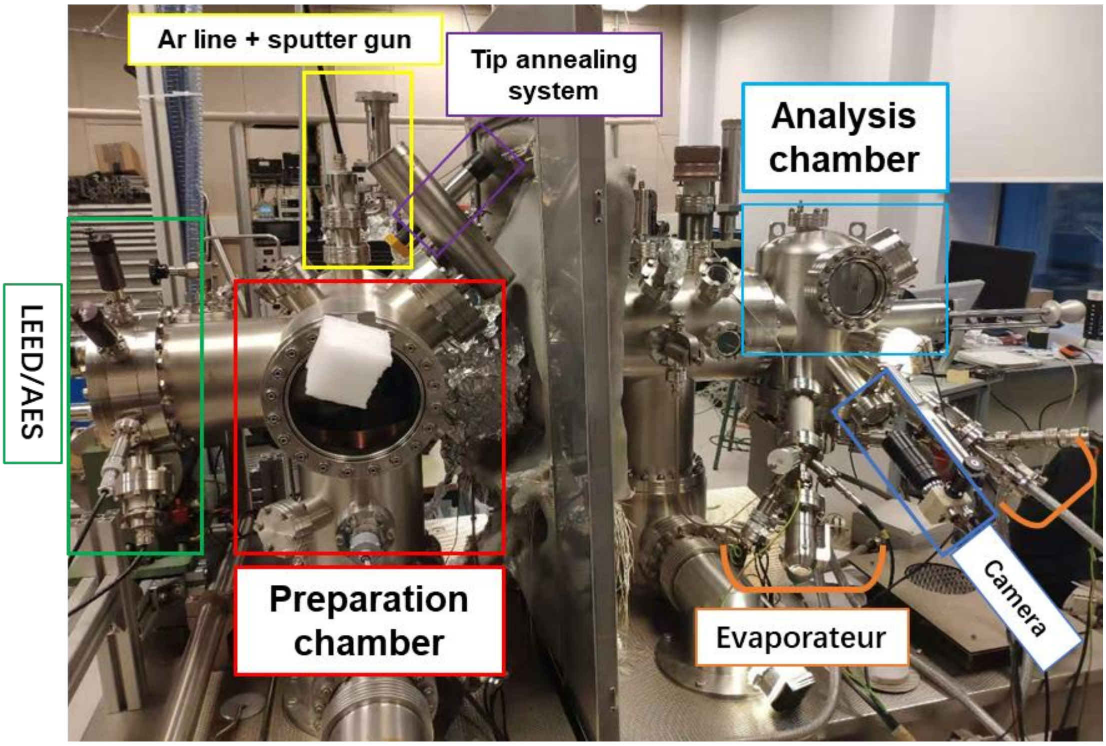

Figure 3.2 Photo of the STM experimental set-up

In the analysis chamber, STM measurements can be performed in a wide temperature range from 40K to 530K, using cryogenic fluids (He, N_2) or a heating resistance. Moreover, this STM system can take the real-time in-situ STM measurements during the evaporation, applying two evaporators installed in two flanges with an evaporation angle of 30°, as illustrated in Fig 3.2. During scanning, external vibrations influence the STM image quality, indicating the importance of the stabilization for the STM. Thus, in the analysis chamber, a mechanical system with four springs and an eddy current damping system is devoted to stabilizing the tip-substrate system in the STM.

In the following section, combining the theoretical basis, I introduce the physical phenomena in STM.

3.1.2 Physical phenomena in STM

In quantum mechanics, quantum tunneling refers to the behavior of microscopic particles such as electrons that can penetrate a potential barrier with a width L, even though the height of the potential barrier U_0 is greater than the energy of the particle E. As described in Fig 3.3, the case of the one-dimensional rectangular potential is considered:

$$U(x) = \begin{cases} 0, x < 0 \; and \; x > L \\ U_{0,} \quad 0 < x < L \end{cases} \tag{3-1}$$

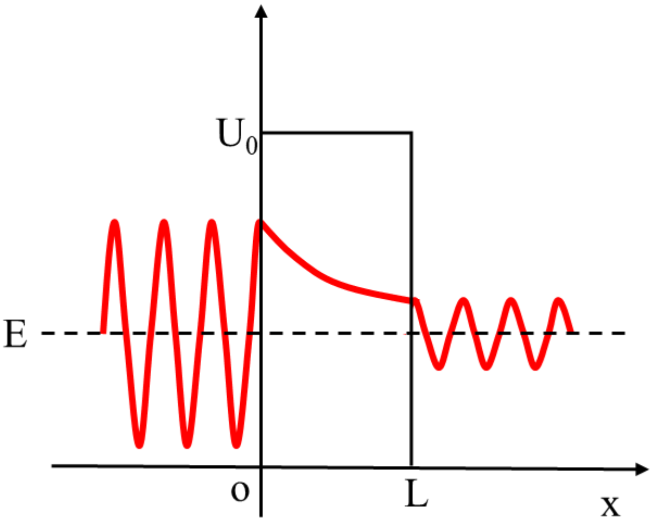

Figure 3.3 Transmission of the wave function across a 1D rectangular potential barrier with height U_0 and width L.

If we assume that a plane wave hits the potential barrier, the solution of the time-independent Schrödinger equation $H\psi_k(x)=E\psi_k(x)$ for three zones is presented:

$$\psi(x) = \begin{cases} A_1 e^{ikx} + A_2 e^{-ikx}, & x < 0 \\ B_1 e^{ik'x} + B_2 e^{-ik'x}, & 0 < x < L \\ Ce^{ikx}, & x > L \end{cases} \tag{3-2}$$

with two wavevectors k and k':

$$k = \frac{(2mE)^{1/2}}{\hbar} \text{ and } k' = \frac{[2m(E-U_0)]^{1/2}}{\hbar} \tag{3-3}$$

Where m is the mass of microscopic particles. Based on the continuity boundary conditions at t x=0 and x=a, i.e. $\psi_-(0)= \psi_+(0)$, $\psi'_-(0)= \psi'_+(0)$, $\psi_-(L)= \psi_+(L)$, and $\psi'_-(L)= \psi'_+(L)$, the relation of the coefficients (A_1, A_2, B_1, B_2, and C) can be determined. The transmission coefficient, used to describe the statistical fraction of electrons transmitted through the barrier, can be acquired by C/A_1:

$$T_k(E,L) = \left|\frac{C}{A_1}\right|^2 = [1 + (k\kappa)^2 \sinh^2(\kappa L)]^{-1} \tag{3-4}$$

$$\text{Where } \kappa = \frac{[2m(U_0 - E)]^{1/2}}{\hbar} \tag{3-5}$$

If the potential barriers exhibits a strong attenuation, for κL >> 1, Eq. (3-4) reduces to

$$T_k = \frac{4}{(k\kappa)^2} e^{-2\kappa L} \tag{3-6}$$

When the tip is very close to the sample surface, the vacuum between each other is considered as a potential barrier of a few eV corresponding to the work function of ~4eV for a metal φ_m [115]. For Eq. (3-5) with $\varphi_m = U_0 - E_F$ (fermi level E_F), the characteristic penetration length (1/κ) is estimated at about 1Å. This indicates that, due to the exponential relation in Eq. (3-6), a variation of the barrier width in a few angstroms strongly influence the transmission coefficient, i.e. the value of the tunneling current.

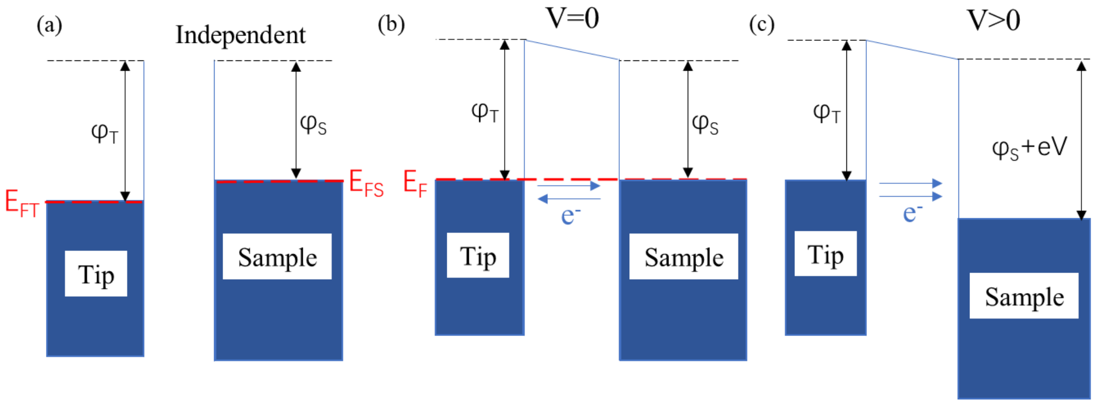

Figure 3.4 Representation of tunneling process in a tip-vacuum-sample junction: (a) The Fermi levels of two independent electrodes. (b) In tunneling condition, the balance of Fermi level between the tip and the sample takes place. (c) Using a positive bias voltage to the sample, the shift of the Fermi level induce the flow of tunneling electrons from the tip to the empty states of the sample.

Fig. 3.4 shows a schematic of the tunneling process and the formation of the tunneling current. If a metallic tip is not connected to a sample via an external circuit, there is no tunneling electrons between them, and they have their own independent Fermi energy (E_{FT} and E_{FS}) and work function (φ_T and φ_S), as illustrated in Fig. 3.4a. If they are connected without a bias voltage applied, the Fermi levels are aligned (see Fig3.4b). By applying a positive bias voltage (V>0) between the tip and the sample, as shown in Fig 3.4c, the Fermi level of the sample shifts to a lower level with respect to that of the tip, leading to a tunneling current. For the inverse case (V<0), the flowing direction of electrons and the tunneling current reverses.

For the theoretical analysis of the tunneling current, Bardeen has proposed a model, which describes that the electron tunneling occurs between a state of the tip ψ_u and a state of the sample ψ_v [116]. In perturbation theory at first order, the tunneling current can be written as:

$$I = 2 \times \frac{2\pi e}{\hbar} \sum_{u,v} f(E_u)[1 - f(E_v + eV)]\, |M_{uv}|^2 \delta(E_u - E_v) \qquad (3\text{-}7)$$

Where f(E) is the Fermi-Dirac distribution f(E)=(1+exp[(E-E_F)/k_bT])-1, V is the bias voltage, M_{uv} is the tunneling matrix element, E_u is the energy of state ψ_u, E_v is the energy of state ψ_v, and the factor 2 is related to electron spin. If the limits of small voltage and low-temperature, Eq. (3-7) reduces to:

$$I = \frac{4\pi e^2 V}{\hbar} \sum_{u,v} |M_{uv}|^2 \delta(E_v - E_F)\delta(E_u - E_F) \qquad (3\text{-}8)$$

With

$$M_{uv} = -\frac{\hbar^2}{2m} \int (\psi_u^* \nabla \psi_v - \psi_v \nabla \psi_u^*)\, d\vec{S} \qquad (3\text{-}9)$$

In this case, $\Sigma_{u,v}$ can be replaced by ∫ρ(E)dE, Eq. (3-8) can be rewritten as:

$$I = \frac{4\pi e^2 V}{\hbar} \rho^T(E_F^T)\rho^S(E_F^S)|M|^2 \qquad (3\text{-}10)$$

Where ρ^T and ρ^S are the local density of states of the tip and of the substrate, respectively. Eq. (3-10) shows that the tunneling current is a function of the local density of states at the Fermi level of the tip and the sample surface.

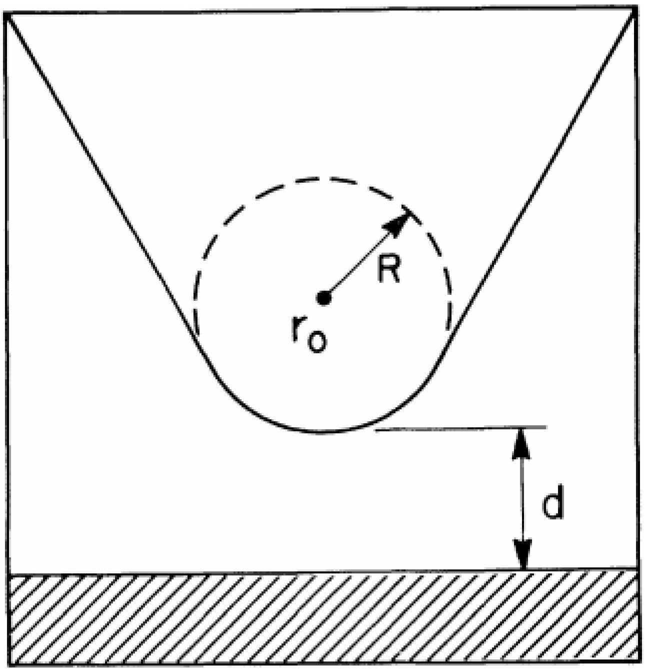

Figure 3.5 Model of the tip proposed by Tersoff and Hamann [117, 118]. The tip is described as a sphere of radius R, located at the position r0. d represents the nearest approach distance between the tip and the sample. Image reproduced from ref. [117, 118]

As described above, Bardeen's model can estimate the tunneling courant with the given electronic structure of the tip and the sample. But it is difficult to measure precisely the structure of the tip, and the electronic structure of the tip apex is not known. Tersoff and Hamann have proposed a model to simplify the tip with radius R, the wavefunction of the tip is described as a single s-orbital wavefunction [117][118]. They have reported that the tunneling current in Eq. (3-7) can be rewritten:

$$I(\boldsymbol{R}, V) = \frac{16\pi^3 C^2 \hbar^3 e^2}{\kappa^2 m^2} V \rho^T \rho^S(\boldsymbol{R}, E_F^S) \qquad (3\text{-}11)$$

Where C is a normalization constant and the density of states of the tip ρ^T is a constant. Thus, in the Tersoff-Hamann(TH) model, the tunneling current is proportional to the local density of states of the sample surface. In the next section, I give a introduction of the analysis of STM image.

3.1.3 Image analysis

In our STM system, the scanning data are processed by the software Matrix. Measured STM images contain the value of the vertical position of the piezodrive as function of the lateral position of the tip. Images correspond thus to the real topography of the surface but, due to the external vibrations, the electronic noise and piezo drift are also recorded in the images. In order to correct these imperfections and analyze the images, I have used the Gwyddion software [119] and several tools developed with Python by Geoffroy Prévot in INSP. The process of image correction is divided into two major parts.

- **Z corrections**

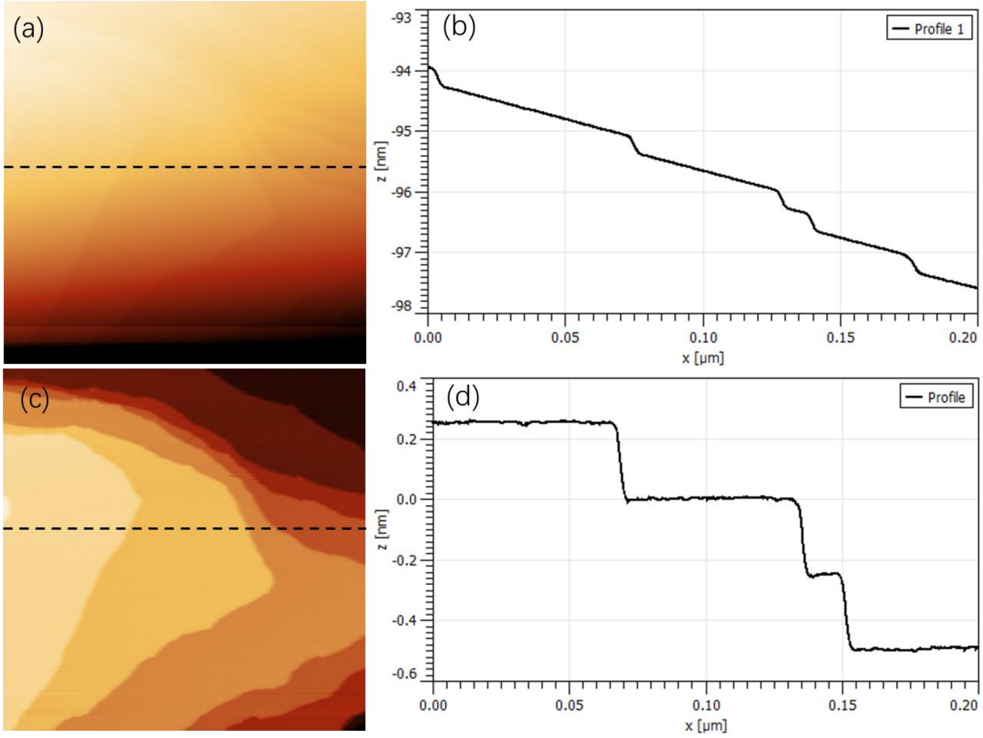

Figure 3.6 STM image (200×200 nm2; V_s=2.2 V, I=20 pA) (a) before the correction and (c) after Z and XY correction. (b, d) The profile along the black dashed line drawn in figure (a) and (b).

(a) Polynomial correction

Fig. 3.6a shows a raw STM image with the disorientation of the surface with respect to the z-direction. This problem make the topography of the surface indistinguishable. The subtraction of the plane associated with the disorientation can solve this problem. However, the profiles along the black dashed line indicates that pixels in the same terrasse have different values of z. In order to make terrace oriented perpendicular to the axis z (see Fig. 3.6b-c), the polynomial correction has been carried out. For a planar correction, z'= z - (ax + by + c) if the relationship between the value of the vertical and lateral position is linear. In addition, higher order polynomial correction may be needed for large scan due to non-linear behavior of the piezodrive.

(b) line/line correction (rms correction)

If the tip change during the scan, the absolute value of z is modified. A correction is applied to minimize the quantity $\sum_i \left(z(x_i, y_j) - z(x_i, y_{j+1})\right)^2$, where j and j+1 are consecutive line positions. This correction corresponds to the root mean square (rms) filter, aimed to remove noise induced by the variation of the tip.

(c) Modulo correction

After polynomial correction, the terrace is planar and perpendicular to axis z. Modulo correction corresponds to $z(x_i, y_i)$ mod h, where h is equal to step height. In computing, the modulo operation returns the remainder or signed remainder of a division, after one number is divided by another. In the present case, mod $z(x_i, y_i)$ h = $z(x_i, y_i)$- h×$[z(x_i, y_i)/h]$, where $[z(x_i, y_i)/h]$ refers to the integer part of this division. Each line is corrected by a constant in order to set his position to 0 modulo stepheight. In addition, in-situ STM images after modulo correction can be used to compute the coverage of the outgrowth, as I will show in chapter 4 and 5.

(d) A combination of rms and modulo correction

If single rms or modulo correction cannot adapt to a STM image, a combined rms and modulo correction is applied to treat this image.

(e) Working on whole image or an image with masked part

- **XY correction**

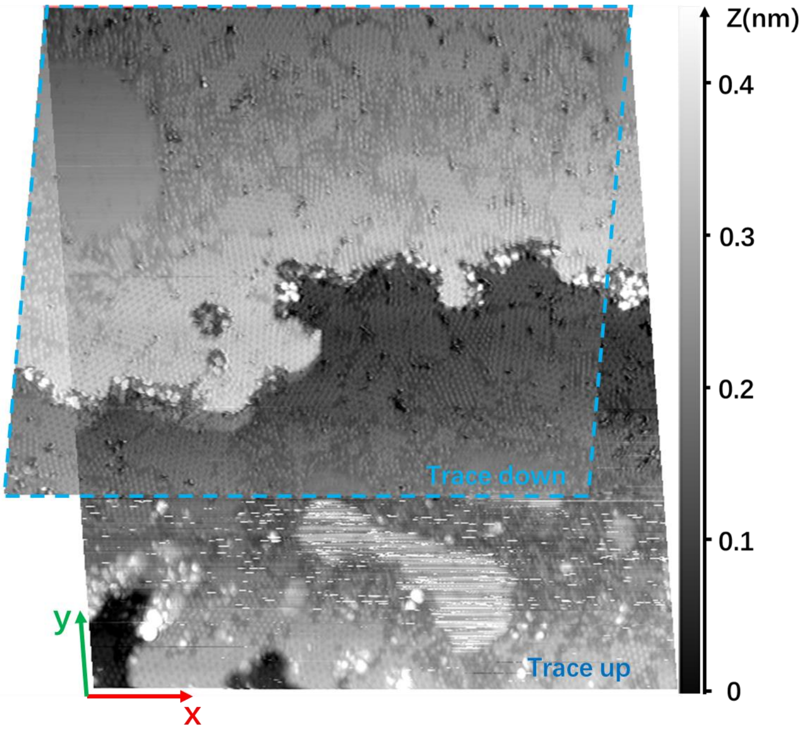

Figure 3.7 Up-Down twigs STM image obtained at 300K after Si deposition on Ag(111) held at 488K. After XY correction with a linear drift, these two image show a same area at the same position. Size of image: 100×100 nm^2. Tunneling condition: V_s=1.7 V, I_t= 100 pA.

The STM image obtained is not a square due to piezo drift. After scanning, the scanning-up and scanning-down image are not completely identical, corresponding to in-plane distortion induce by thermal and piezoelectric drift. XY correction is thus used to compensate for this distortion. Concerning in-situ STM images, each image needs to be treated with XY correction for displaying the evolution of the same area. Thus, XY correction corresponds to two types of drift: linear and non-linear drift.

(a) Linear drift

A linear drift is described as $x' = x + a_x t$ and $y' = y + a_y t$ along the x-axis and y-axis, where ax and ay correspond to a drift rate. Fig. 3.7 presents twin images, i.e. the scanning-up and scanning-down image, with a linear drift. Via a superimposition of these two images, a common area is shown in the same position, e.g. the upper-right part of Fig. 3.7.

(b) Nonlinear drift

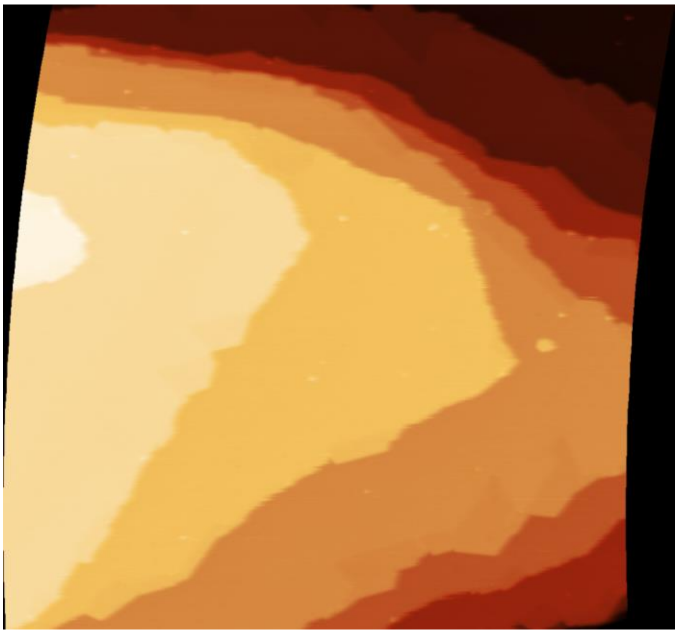

Fig 3.8 Adjacent STM image obtained after Fig. 3.6c after XY correction with a nonlinear drift.

Concerning in-situ STM images, each of them is obtained from the corresponding real-time images after z correction. Different from the up-down images, there is a non-linear drift between consecutive real-time images. A comparison between a reference image and a new image can thus implement XY correction with a nonlinear drift. Fig. 3.8 displays the adjacent STM image obtained after Fig. 3.6c. After XY correction with a nonlinear drift, these images can present the evolution of in-situ area.

3.1.4 Preparation of the STM tips

As described in section 3.1.2, the tunneling current is related to the radius of the tip [118]. This means that the atomically-sharp tip plays a very important role in the lateral resolution that determines the quality of STM images. For the fabrication of STM probes, I used the method of chemical etching. A tungsten filament (diameter 0.25mm, purity 99.95%) is mounted on the tube with about 2.5mm beyond the end of the tube. Then, this W filament is dipped in a 2 mol/L NaOH solution with 2mm below the solution surface. And a metallic ring, half dipped in the solution, is applied to be an electrode. When a bias voltage is used between the tip and the metallic ring, the etching happens at the air-solution interface, and an electrochemical reaction takes place:

$$W(s) + 2OH^-(aq) + 2H_2O(l) \rightarrow WO_4^{2-}(aq) + 3H_2(g)$$

During the etching, the tip located at the interface slowly forms a meniscus, and the rate of the reaction becomes slower resulting from a decrease in the reaction area. At the interface, the section of the filament becomes thinner and thinner. Until this thin section cannot afford the weight of the lower, the drop-off occurs, and a sharp tip forms. At this moment, the power supply must be switched off, and the tip leaves the solution rapidly to stop the reaction. After cleaning with ethanol and water, the tip is transferred into the preparation chamber. The thin oxide layer (WO_3) on the surface of the tip can be removed by using the tip-annealing system. The tip is heated up to about 1000℃ via a direct-current of about 6A during 40s, the reaction between WO_3 and W produces the WO_2 vapor for the elimination of the thin oxide layer [120].

3.1.5 Shadowing effect

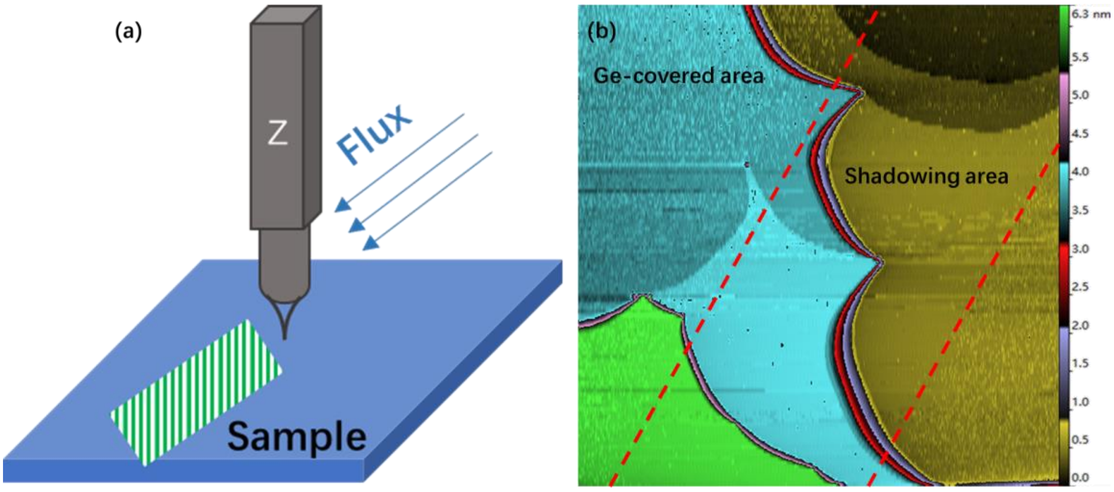

Figure 3.9 (a) Schematics of the shadowing effects induced by the STM tip. (b) STM image obtained during Ge deposition on the Ag(111) surface kept at 300K. The boundary between the shadowing area and the Ge-covered areas is drawn by the red dashed line. Compared to Ge-covered areas, Ge coverage in the shadowing area is much smaller. Size of image: 1600×1600 nm^2. Tunneling condition: V_s=1.7V, I_t= 40 pA.

Depending on the tip shape, small or large shadowing effects can occur during deposition. As the STM tip remains very close to the surface, the tip blocks the incoming Ge flux, and the area behind the tip with respect to the direction of flux is not covered by Ge, as illustrated Fig. 3.9a. During scanning, the tip and its shadow move over the surface together, which leads to local inhomogeneities on the surface. Fig. 3.9b shows a STM image obtained during Ge deposition on Ag(111) held at 300K. As can be seen in this figure, there is a shadowing area running through this image without Ge covered, caused by the shadowing effects. In order to avoid the influence of the shadowing effects on the growth, I have performed experiments for which the tip was removed during evaporation in order to avoid shadowing effects.

3.2 Low energy electron diffraction (LEED)

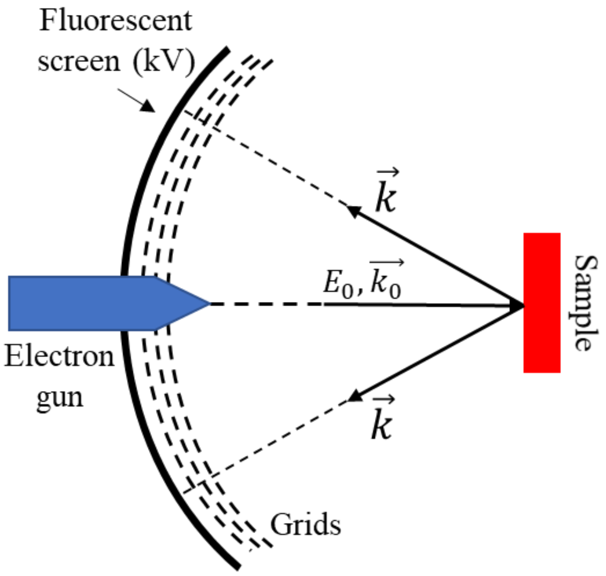

Figure 3.10 Schematic representation of LEED instrument

Low energy electron diffraction (LEED) is a powerful technique that can determine the structure of the sample surface. In the LEED experience, as shown in Fig. 3.10, a monothetic electron beam with energy E_0 in the range of 10eV to 300eV is emitted from an electron gun, and the incident beam is perpendicular to the sample surface. After the interaction with the sample surface, the elastically scattered electrons are selected by grids, avoiding the influence from the inelastically scattered electrons, and form several bright spots on the fluorescent screen. The diffraction pattern displayed corresponds to intersection of the reciprocal space of the surface structure with Ewald's sphere. The condition of the diffraction pattern can be written as:

$$a \sin\theta = n\lambda \tag{3-12}$$

Where a is the interatomic distance, θ is the scattering angle, n is an integer, and λ is the wavelength of the electrons. After the deposition, I use the LEED pattern to determine symmetries of the surface reconstruction with respect to the unit cell of the substrate. But, the determination of the exact structure need another technique. In next section, I give an introduction of a technique – X-ray diffraction.

3.3 X-ray diffraction (XRD)

In this section, I will present the X-ray diffraction theory, grazing incidence X-ray diffraction (GIXD) measurements and the methods for the analysis of the GIXD data.

3.3.1 X-ray diffraction theory

The X-ray diffraction (XRD) is based on Thomson scattering model. In the low-energy limit, the X-ray scattering is considered as the elastic scattering of electromagnetic radiation. In the case of the crystal, the scattered waves produce constructive interference along the favored directions, known as the X-ray diffraction pattern. As scattering cross sections are weak, multiple scattering can be often neglected, which is called kinematic approximation

Based on Thomson scattering model, the incoming wave and the wave scattered by an electron of the atoms can be described as $A_i e^{i\boldsymbol{k_i r}}$ and $A_s e^{i\boldsymbol{k_f r}}$, where A_i and A_s is the amplitude of the incoming and the scattered wave, the k_i and k_f is the incident and the scattered beam wavevector, and the r is the position of the electron. If ρ(r) is the density of electron within an atom, the amplitude scattered by an atom(A_d) with Z scattering electrons can be written as:

$$A_d = A_s \int \rho(\boldsymbol{r})\, e^{i\boldsymbol{qr}} d\boldsymbol{r} \tag{3-13}$$

Where $\mathbf{q}=\mathbf{k_f}-\mathbf{k_i}$ indicates the momentum transfer. The atomic scattering factor is defined as:

$$f_0(\boldsymbol{q}) = \int \rho(\boldsymbol{r})\, e^{i\boldsymbol{qr}} d\boldsymbol{r} \tag{3-14}$$

This indicates that different atoms have different atomic scattering factors due to their different electron density. When $\mathbf{q}=\mathbf{0}$, $f_0(\mathbf{0}) = \int \rho(\boldsymbol{r})\, d\boldsymbol{r} = Z$ i.e., all electron within the atom scatter in phase. When $\mathbf{q}\neq\mathbf{0}$ and finite, the atomic scattering factor decreases.

In the case of atoms in a crystal lattice, the position of each atom is given by three basis vectors:

$$\boldsymbol{R_m} = m_1\boldsymbol{a_1} + m_2\boldsymbol{a_2} + m_3\boldsymbol{a_3} + \boldsymbol{r_m} \qquad (3\text{-}15)$$

Where **a1**, **a2**, and **a3** represent three lattice vectors that define the unit cell, m is an integer, and $\mathbf{r_m}$ represents the positions of the atoms relative to the unit cell. Thus, the amplitude scattered by a crystal can be written as:

$$A_c(\boldsymbol{q}) = A_s \sum_m f_m(\boldsymbol{q}) e^{-i\boldsymbol{qR_m}} = A_s F(\boldsymbol{q}) \sum_{m_1=0}^{N_1-1} \sum_{m_2=0}^{N_2-1} \sum_{m_3=0}^{N_3-1} e^{-i\boldsymbol{q}(m_1\boldsymbol{a_1}+m_2\boldsymbol{a_2}+m_3\boldsymbol{a_3})} \qquad (3\text{-}16)$$

Where N_i are the numbers of unit cells on the crystal edges parallel to three lattice vector **a1 a2 a3**, and the structure factor F(**q**) is described as the resultant of the scattered wave by the different atoms in the different positions $\mathbf{r_m}$ within the unit cell:

$$F(\boldsymbol{q}) = \sum_m f_m(\boldsymbol{q}) e^{-i\boldsymbol{qr_m}} \qquad (3\text{-}17)$$

As discussed above, the equations (3-16) and (3-17) are derived on the assumption that the atoms are fixed in definite positions without any displacement. If the thermal vibrations of the atoms in the crystal are considered, the instantaneous position of the atom is defined as a summation of the average position $\mathbf{R}_m$ and the vibrational displacement $\mathbf{u}_m$, $\boldsymbol{R}'_m = \boldsymbol{R}_m + \boldsymbol{u}_m$. Thus, Eq. (3-17) can be rewritten as Debye-Waller(DW) factor [121]:

$$F(\boldsymbol{q})_{DW} = \sum_m f_m(\boldsymbol{q})\, e^{-iB_m(q/4\pi)^2} e^{-i\boldsymbol{qr_m}} \qquad (3\text{-}18)$$

Where B_m is a factor related to the average square of the vibrational displacement of the atom along the **q** direction. For the study of the surface reconstruction, the DW factor consists of the in-plane part and the out-of-plane part with the factor B_{xy} and B_z, respectively. As a result of the symmetry of the hexagonal structure, B_x=B_y=B_{xy} for the Ag(111) and Al(111) surface. Concerning the unit cell of the Ag(110) surface, B_x, B_y, and Bz are independent.

The diffracted intensity by a crystal is equal to the square of the amplitude (Eq. (3-17)):

$$I(\boldsymbol{q}) = A_s^2|F(\boldsymbol{q})|^2 \frac{\sin^2\left(\frac{1}{2}N_1\boldsymbol{q}\boldsymbol{a_1}\right)}{\sin^2\left(\frac{1}{2}\boldsymbol{q}\boldsymbol{a_1}\right)} \frac{\sin^2\left(\frac{1}{2}N_2\boldsymbol{q}\boldsymbol{a_2}\right)}{\sin^2\left(\frac{1}{2}\boldsymbol{q}\boldsymbol{a_2}\right)} \frac{\sin^2\left(\frac{1}{2}N_3\boldsymbol{q}\boldsymbol{a_3}\right)}{\sin^2\left(\frac{1}{2}\boldsymbol{q}\boldsymbol{a_3}\right)} \tag{3-19}$$

Besides the structure factor, the non-zero diffraction beams satisfy the Laue conditions:

$$\boldsymbol{q}\boldsymbol{a_1} = 2\pi h \quad \boldsymbol{q}\boldsymbol{a_2} = 2\pi k \quad \boldsymbol{q}\boldsymbol{a_3} = 2\pi l \tag{3-20}$$

In the case of a 3D crystal, these three Laue equations are equivalent to the Bragg law. Thus, three integers h, k, and l represent the Miller index (hkl), and **q** is reciprocal vector. Eq. (3-19) reduces to:

$$I_{\boldsymbol{hkl}}(\boldsymbol{q}) = A_s^2|F_{hkl}(\boldsymbol{q})|^{\boldsymbol{2}}N_1^2N_2^2N_3^2 \tag{3-21}$$

The intensity of diffracted spots depends on the structure factor that depends upon the atomic positions. Thus, the diffraction pattern composed of Bragg spots exhibits the 3D symmetries of a crystal.

Regarding two-dimensional crystals like surfaces, the atomic positions are given by two basis vectors:

$$\boldsymbol{R_{mm_1m_2}} = \boldsymbol{m_1a_1} + \boldsymbol{m_2a_2} + \boldsymbol{r_m} \tag{3-22}$$

Where $\mathbf{r_m}$ is the position of an atom relative to the surface unit cell. The basis vector $\mathbf{a_3}$, normal to the surface, is dropped. This indicates that the last Laue equation isn't simultaneously satisfied, and diffraction intensity is non zero for continuous values of q_z. Thus, the diffraction pattern is composed of rods perpendicular to the surface. The intensity is given by:

$$I_{hk}(l) = A_s^2|F_{hk}(l)|^2N_1^2N_2^2 \tag{3-23}$$

For a semi-infinite crystal, the diffraction pattern also consists of diffraction rods called crystal truncation rods (CTRs). The intensity by Eq. (3-19) in first approximation is given by

$$I_{hk}(l) = A_s^2 |F_{hk}(l)|^2 N_1^2 N_2^2 \frac{1}{2\sin^2(\pi l)} \tag{3-24}$$

Taking account of the surface reconstruction, or an adsorbed layer after the growth, the diffraction pattern appears the new diffraction rods with new periodicity. Moreover, the diffraction rods related to the substrate still exists in the diffraction pattern.

The diffracted intensity is a real quantity, not containing any information about the phase of the diffracted wave ($e^{i\mathbf{qr}}$): it is not possible to determine the structure of the crystal directly by performing an inverse Fourier transform of the diffracted intensity. The Patterson function is thus introduced to avoid the phase problem. For in-plane conditions, the 2D Patterson function is an approximation of the electron density-density autocorrelation function within the surface unit cell [122]:

$$P(x,y) = 2\sum_{HK} |F(H,K)|^2 \cos\left(2\pi(Hx + Ky)\right) \tag{3-25}$$

Where F(H, K) indicates the specific structure factors measured for in-plane conditions and x, y are the coordinates in the unit cell. From Eq. (3-14) and Eq. (3-17),

$$P(\boldsymbol{r_m}) = \int_{\boldsymbol{r}} \rho(\boldsymbol{r})\, \rho(\boldsymbol{r} + \boldsymbol{r_m}) d\boldsymbol{r} \tag{3-26}$$

As can be seen, the Patterson function is composed of maxima related to the vectors between atoms in the unit cell. These vectors are weighted, each maximum is obtained by convolution of the individual electron densities of two atoms and its value depends on the number of electrons in the atoms. The contributions of atoms with larger atomic numbers in the unit cell are therefore particularly visible. Thus, the corresponding 2D Patterson map contains structural information. This is a useful tool to investigate a atomic structure that I use to determine the structure in case of the

Ge/Ag(111) and Si/Ag(110) discussed in Chapter 5 and 6 respectively.

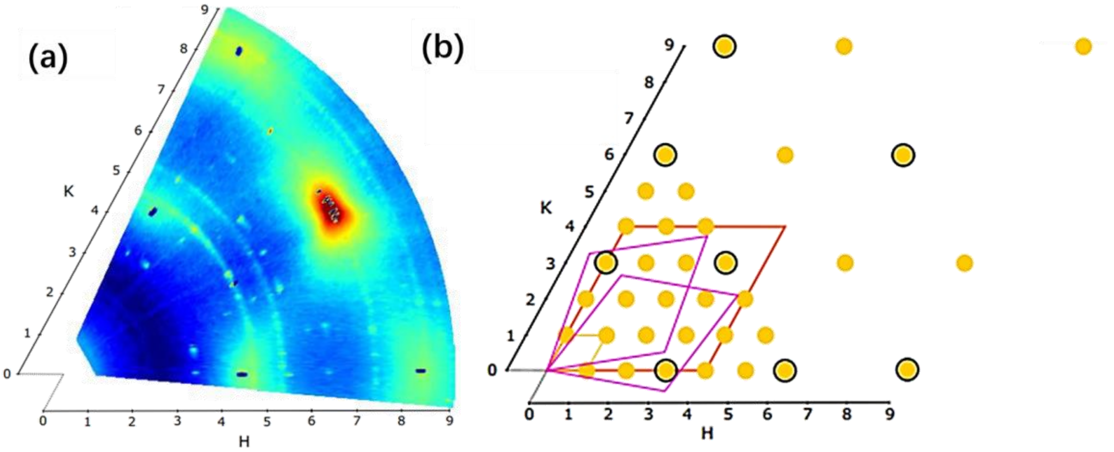

Figure 3.11 (a) In-plane diffraction map of the reciprocal space obtained by GIXD measurements performed at 570 K. (b) The corresponding schematic representation of the diffraction spots and rods for (a). The indexing of the axis refers to the (4 × 4) silicene reconstruction. The unit cells of the structures are indicated by parallelograms: yellow for the (4 × 4), pink for the two domains of the (1.338 × 1.338)R ± 10.02° and finally red for the Ag(111) unit cell. Yellow dots and ones with black circle indicate the (H, K) positions of the in-plane rocking scans. Figures reproduced from ref. [51]

In the case of Si/Ag(111), about 1ML Si deposition on Ag(111) kept at 570K leads to the formation of the (4×4) and (1.338×1.338)R(±10.02°) reconstruction with respect to the Ag(111) lattice [52][123]. Fig. 3.11a shows the GIXD map of the diffracted intensity for in-plane conditions (L=0.05) for 1ML of Si deposited at 570K. In addition, Fig. 3.11b presents the corresponding schematic representation of the diffraction spots and rods measured. The indices (H, K, L) refer to the (4×4) reconstruction basis (a = b = 11.56 Å, c= 7.075 Å and α = β = 90°, γ = 120°). Besides the (4n, 4m, 0.05) (n, m= integer) spots related to CTRs from Ag(111), the (3n, 3m) rods associated with the (4×4) structure have been observed (see Fig. 3.11a), because of (3×3) reconstructed silicene on the (4×4) Ag(111) cell [51]. Moreover, the other rods are diffracted from the (1.338×1.338)R(±10.02°) reconstruction domains.

3.3.2 Grazing incidence X-ray diffraction (GIXD)

3.3.2.1 GIXD geometry

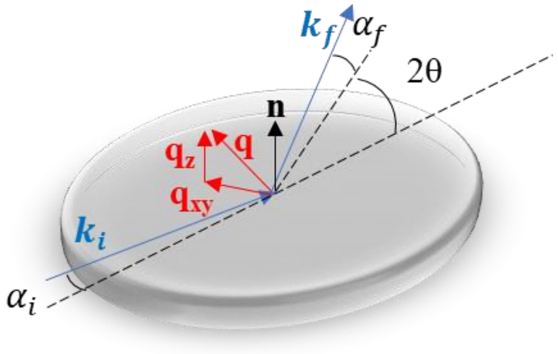

Figure 3.12 Schematic representation of grazing incidence diffraction geometry

Fig. 3.12 exhibits a grazing incidence diffraction geometry showing the X-ray incidence (diffracted) angle α_i (α_f), the wavevectors $\mathbf{k}_i$ ($\mathbf{k}_f$), and the momentum transfer **q** composed of in-plane (q_{xy}) and out-of-plane (q_z) component. The relation between **q** and $\mathbf{k}_i$ ($\mathbf{k}_f$) has been described in the last section. In a GIXD measurement, the grazing incidence angle (αi) is in the range of 0.1 to 1°. For X-ray, the refractive index of solid can be written as $n = 1 - \delta + i\beta$, where the coefficient δ is of the order of 10^{-5}, and the adsorption coefficient β is a few 10^{-6}. Moreover, the critical angle of total reflection $\alpha_c = \sqrt{2\delta}$. If α_i is below α_c, the incident X-ray is total reflected without transmission. The penetration depth is a function of the ratio of the incident angle to the critical angle (α_i/α_c)[9,10]. If $\alpha_i/\alpha_c<1$, the penetration depth is small enhancing surface sensitivity. For high surface sensitivity and high-quality signal, an intense X-ray source also plays an important role, e.g. synchrotron. During my Ph.D., I have finished 3 GIXD measurements in beamline SixS at synchrotron SOLEIL for Ge/Al(111), Ge/Ag(111), and Si/Ag(110). The sample was analyzed with 18.46 keV X-rays at a grazing incidence angle of 0.2°. The results of these experiments will be presented in the following chapters.

3.3.2.2 Data acquisition

As described in section 3.3.1, the intensity of each reciprocal position (hkl) is associated with the structure factor. Fig. 3.13 shows the Z-axis diffractometer geometry and Ewald construction during the measurements. As shown in Fig. 3.13a, the sample can be rotated around Z-axis by the angle ω, the position of the detector is determined by γ and δ, and α is the incidence angle. In addition, the diffracted X-rays were detected by a 2D detector.

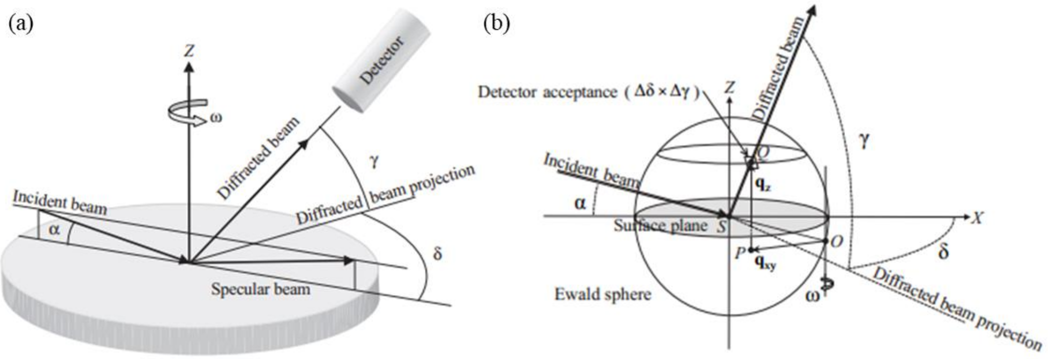

Figure 3.13 (a) Schematic diagram of the Z-axis diffractometer geometry exhibiting the incident angle α, the sample rotation around Z-axis by ω, and the azimuths γ and δ. (b) Perspective view of Ewald sphere. Images reproduced from ref. [124]

Fig. 3.13b shows the relative Ewald sphere construction. In the reciprocal space, the position on the sphere can be described by the in-plane and out-of-plane momentum transfer, i.e. $\mathbf{q}_{xy}$ and $\mathbf{q}_z$. During GIXD measurements, the diffraction intensity measured is a function of the angle ω. If the detector acceptance (Δδ×Δγ) is large enough, the measurement of the diffraction intensity corresponds to a detection of an area on the sphere (see Fig. 3.13b). It indicates that the angular trace of the intensity of the diffraction rod at a value of q_z is obtained with the Ewald sphere. The integral of the profile intensity is related to the structure factor (F_{qxqyqz}), by means of geometrical corrections. Note that the measured value of the structure factor must be constant in a range of Δq_z associated with Δγ. After GIXD measurement, the raw data contains the value of δ, γ, ω and the intensity of diffracted signals for each measured point. For the intensities of the diffraction rod, GIXD measurements at different values of q_z have been performed by displacing the detector. However, these data is separated. The data integration is a necessary step after data acquisition.

3.3.2.3 Data integration

The raw data contains the spatial position of measured points and the corresponding diffraction intensities at the point. However, these spatial positions are in a coordinate system (O-δγω) referring to the real space. The task of the data integration is thus to rebuild the intensity as a function of the position in the reciprocal space, using the raw data.

The measurements by the 2D detector, at the different value of qz, includes the diffraction signal from the ordered structure, and the background from disordered part of the sample, and scattering by the Be windows and other part of the apparatus. The integration of the data of these measurements forms a 3D volume of the reciprocal space, which describe a 3D diffraction pattern. This integration can be implemented in the BINoculars software [125] developed in Python (i.e. a scripting language). The workflow for the integration is separated into three major steps: input, projection, and space. Concerning the first step – input, BINoculars collects the raw data of each measurement acquired by a 2D detector. In the next step, the projection class converts the diffractometer angles (δγω) of each pixel into reciprocal-lattice coordinates (HKL or $Q_xQ_yQ_z$) set by the user. Finally, using the binning operation in the space class, the intensity of each pixel is accumulated at the discrete grid located at the corresponding reciprocal-space position. Due to the large acceptance of the 2D detector, the intensity of some pixels may be measured several times during the different scans at different detector positions. In order to data reduction and low error, BINoculars computes the average intensity per coordinate. After the space class, the integration of the images by the 2D detector finishes and forms a reciprocal-space 3D intensity data.

3.3.2.4 Data analysis

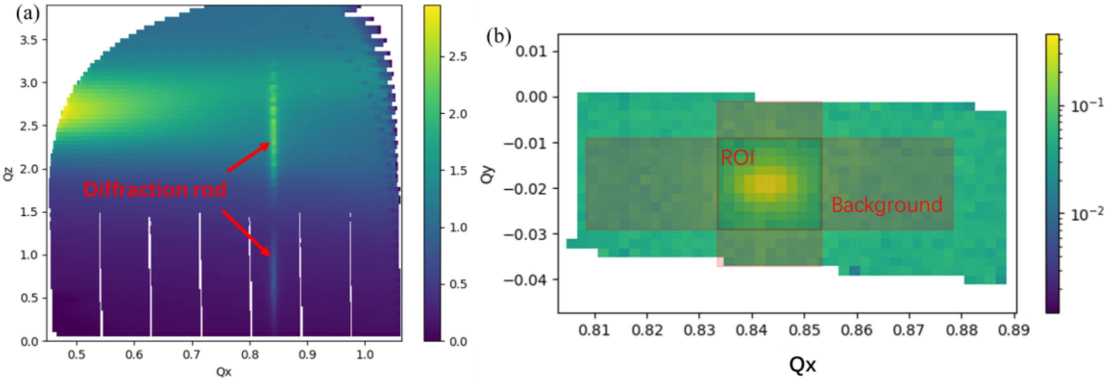

Figure 3.14 (a) Diffraction rod related to the (3×3) reconstruction of Ge on Al(111). (b) The selected ROI and the background in a slice of a diffraction rod for the fitting and integration by BINoculars.

Another important feature of BINoculars is the data analysis, including the data visualization, curve fitting, and data integration. In BINoculars software, the diffraction rod can be projected along one (or two) reciprocal-lattice axis selected by the user, as shown in Fig. 3.14a. The 3D diffraction pattern consists of the reciprocal surfaces (Q_xQ_y plane) at consecutive values of Q_z with a small ΔQ_z. In order to fit the whole diffraction rod measured, the region of the interest (ROI) and the background are selected for each slice, as illustrated in Fig. 3.14b. The selected ROI in each slice can be fitted with a 2D Lorentzian function automatically. The structure factors can thus be calculated by the integrated intensities that are fitted in each slice. However, the fit with only 2D Lorentzian function could cause errors because of a variation of the background. A useful homemade software which has been developed by G. Prévot is the *binoviewer*. Different from BINoculars, there are more chooses for the fitting function, e.g. 2D Lorentzian, 2D Gaussian, pseudo-Voigt function, etc. This can better fit with each slice, and the structure factors calculated have a smaller error.

Chapter 4

4 Growth of germanium on Al(111)

Contents

In chapter 2, I have summarized the previous studies about the growth of Ge on the Al(111) surface. Their conclusions are controversial as for the formation of layered germanene [7][90–92][96–99] or Ge-Al surface alloy [93][100]. In this chapter, I will give evidence of the formation of Ge-Al surface alloy after Ge deposition, by STM, GIXD, and DFT calculations.

The present chapter is organized as follows. In the first part, I describe the formation and the evolution of the $(3 \times 3)_{Al}R0°$ and $(\sqrt{7} \times \sqrt{7})_{Al}R(\pm 19.1°)$ reconstructions. Then, using real-time STM measurements, I present the evolution of the surface during the growth of Ge on the Al(111) surface at different growth temperatures. From a precise analysis of in-situ STM images, I give evidence of the synthesis of a Ge-Al surface alloy after Ge evaporation. In the last part, I present the results of combined GIXD measurements and DFT calculations, aimed to determine the exact atomic structure of the $(3 \times 3)_{Al}R0°$ reconstruction corresponding to a mixed honeycomb layer on top of an alloyed interfacial layer (i.e. a two-layer surface alloy).

4.1 STM experimental detail

4.1.1 Experimental method

The Al(111) substrate plays an essential role in the epitaxial growth of Ge on this surface, implying the importance of the preparation of the surface. As described in chapter 3, the substrate preparation is performed in the preparation chamber under UHV conditions. The Al(111) surface is prepared by repeated cycles of Ar+ ion bombardment and annealing in the preparation chamber. After the completion of the Al(111) sample preparation, the experiments and STM measurements were performed in the analysis chamber. The Ge was evaporated from a heated crucible using a commercial e-beam evaporator Omicron Nanotechnology installed on the analysis chamber. The deposition flux of Ge was ~ 0.1ML/h, where 1ML corresponds to the Al(111) surface atom density.

4.1.2 Data analysis

After STM measurements, a precise analysis of STM images is necessary. The surface evolution is followed by scanning precisely successive images of the same area. For this purpose, as described in section 3.1.3, successive STM images obtained during Ge evaporation are corrected by leveling, deformation, and cropping, using a software developed by the team at INSP. After these processes, in-situ STM images are obtained, which can describe the evolution of the surface. In corrected STM images, each pixel of a given terrace is assigned to the same value related to the level of the terrace. Thus, I introduce a new quantity, namely the integer reduced height $\tilde{h}$ given by

$$\tilde{h} = int\left(round\left(\frac{h}{h_{step}}\right)\right) \tag{4-1}$$

Where h is the position of the terrace and h_{step} is the step height, equal to 0.234 nm for Al(111). Prior to evaporation, the terrace with the lowest apparent height is set to the value $h=h_{step}$ ($\tilde{h}$ = 1). The reduced mean height $\langle\tilde{h}\rangle$ thus is given by

$$\langle\tilde{h}\rangle = \frac{\sum_{\tilde{h}=1}^{N} A(l)\times\tilde{h}}{\sum A(l)} \tag{4-2}$$

Where A(l) is the area of the terrace at the *l*th level shown in STM image, $\tilde{h}$ is the reduced height of each terrace and $\tilde{h} = l$, and N is an integer representing the largest reduced height (i.e. the highest level). If, during evaporation, outgrowths form on the terraces, their coverage is obtained by

$$\theta_{outgrowth}(t) = \langle\tilde{h}(t)\rangle - \langle\tilde{h}(0)\rangle \tag{4-3}$$

Where $\langle\tilde{h}(t)\rangle$ is the reduced mean height for an in-situ STM image obtained after evaporation time of t, and $\langle\tilde{h}(0)\rangle$ corresponds to the image acquired before evaporation.

Concerning the coverage of Ge-covered areas $\theta_{\text{Ge-covered}}$ (i.e. reconstruction domains), the Gwyddion software is used to estimate the coverage for each in-situ STM image, using the different apparent heights for Al and Ge-covered areas.

For a given composition of the germanene phase, the coverage of the outgrowth is proportional to the germanene coverage. For Ge-covered domains, let us assume a composition $Al_{1-\alpha}Ge_{\alpha}$ ($0 < \alpha \leq 1$) of the Al(111) planes modified by Ge adsorption. The relationship between the coverage of the outgrowth and reconstruction domains thus can be given by $\theta_{outgrowth} = \alpha\theta_{Ge\text{-}covered}$. Concerning the growth of Ge on the Al(111) surface, there are three possibilities:

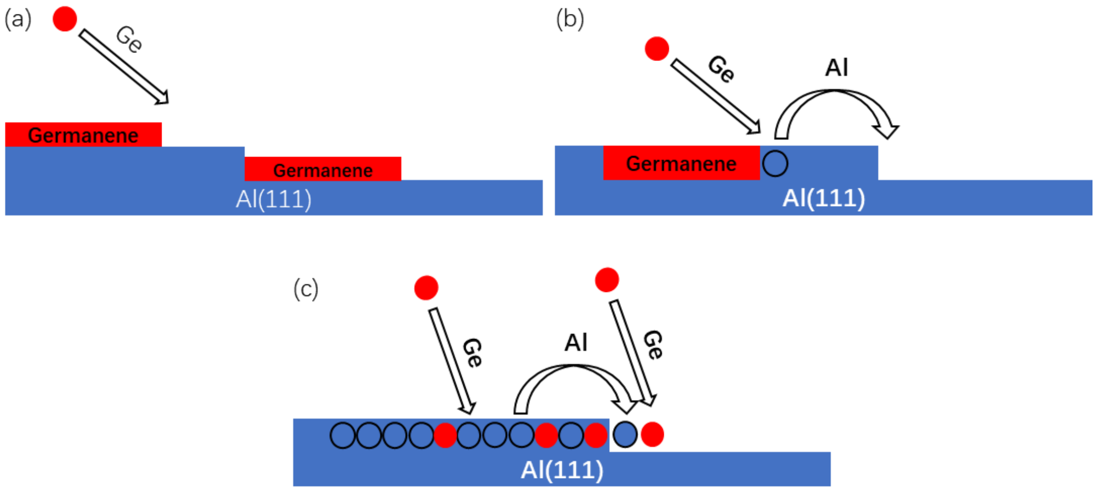

Figure 4.1 Schematic diagram of the growth of Ge on the Al(111) (a) in the case of α=0, (b) α=1 and (c) 0<α<1. The red circle represents Ge atoms in the evaporation flux and the black one denotes expelled Al atoms. The red rectangles indicate germanene grown on the Al(111) surface. The outermost Al layer (black circles) mixed with Ge atoms (red circles) indicate the formation of the Al-Ge surface alloy on the Al(111) surface with the insertion.

- **Formation of germanene or clusters without Ge adsorption**

If Al(111) step edges do not move during the Ge evaporation, the corresponding coverage of the outgrowth vanishes ($\theta_{outgrowth}=0$). It indicates that Ge deposition leads to formation of layered germanene or without modification of the Al(111) surface, as shown in Fig. 4.1a. Thus, the parameter α is equal to zero (α=0).

- **Formation of inserted germanene**

Within this model, during Ge evaporation, Al atoms in the outermost Al(111) layer are replaced by Ge atoms that form layered germanene (see Fig. 4.1b). Then, the expelled Al atoms could condense at the step edges and form outgrowths corresponding to a coverage of $\theta_{\mathrm{outgrowth}}$. The formation of germanene on Al(111) indicates that Ge-covered areas does not contain any Al atoms. In this case, the coverage of the outgrowth is equal to the one of Ge-covered domains, i.e. $\theta_{\mathrm{outgrowth}} = \theta_{\mathrm{Ge\text{-}covered}}$. Thus, $\alpha=1$. This case is similar to the case of Si/Ag(111) [126].

- **Formation of a Ge-Al surface alloy**

If Ge deposition on Al(111) results in the formation of the Ge-Al surface alloy, the value of α is less than 1. As displayed in Fig. 4.1c. part of the Al atoms are replaced by Ge atoms so that the Ge-covered area is larger than the outgrowth area ($\theta_{\mathrm{outgrowth}} < \theta_{\mathrm{Ge\text{-}covered}}$). In the case of the formation of the Ge-Al surface alloy, the value of α corresponds to $0<\alpha<1$.

In the next section, a series of in-situ real-time STM measurements were carried out, which presents the epitaxial growth of Ge on Al(111) kept at a fixed temperature in a range of RT to 360K.

4.2 Study by STM measurements

4.2.1 Formation of two reconstructions on Al(111)

Fig. 4.2a shows a large-scale STM image obtained after submonolayer Ge deposition on the Al(111) surface kept at RT. The different colors correspond to the terraces at different levels, and the green terrace in the left part is higher than the yellow one in the bottom-right part. The surface is characterized by bare Al(111) areas and two different surface reconstruction domains with ordered hexagonal structures.

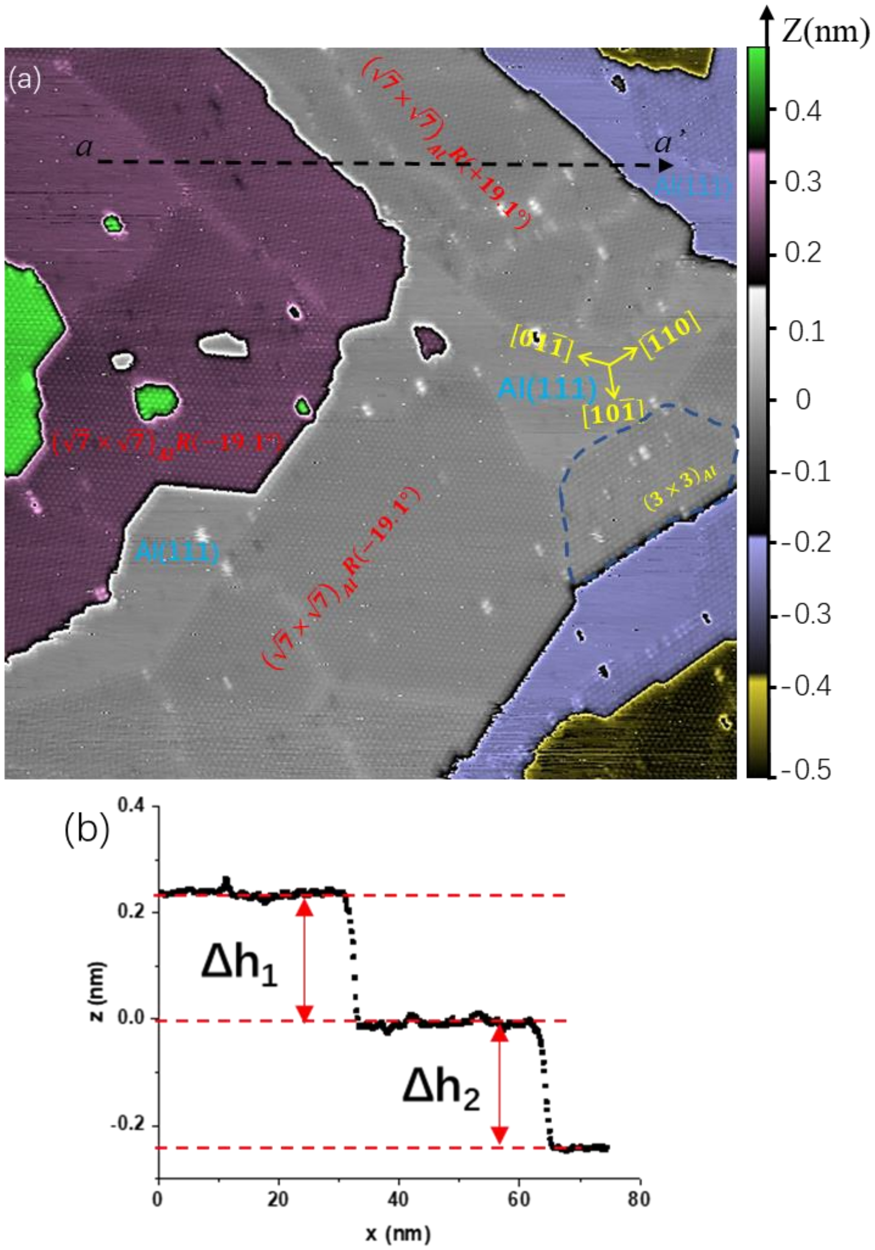

Figure 4.2 (a) Large-scale STM image (100×100 nm^2; U=2.0V, I=30 pA) after ~0.5ML Ge deposition on the Al(111) surface held at RT. The terraces at different levels are presented by the colors at right side of (a). The yellow solid triple arrows represent the main crystallographic directions of the Al(111) surface and (3×3) reconstruction. (b) The linear profiles along the dotted black line (aa').

As can be seen in Fig. 4.2a, Ge-covered domains (i.e. reconstruction domains) can be distinguished from the bare Al(111) areas due to their atomic corrugation. The line profile measured along the dotted black line aa' is drawn in Fig. 4.2b. In this figure, the apparent step height between the reconstruction domains (i.e., violet and gray terrace) is $\Delta h_1 = 0.24 \pm 0.01$ nm that is similar to the Al step height for $\Delta h_{Al(111)} = 0.234$ nm). The apparent terrace height between the terrace covered with the reconstruction domains and the Al(111) area is $\Delta h_2 = 0.23 \pm 0.01$ nm. This observation indicates that the apparent mean height of the Ge-covered areas is 0.1Å lower than Al(111) domains in a same terrace. Concerning the reconstruction domains, three reconstructions appear on the surface with different orientations, as presented in Fig. 4.2a. The previous studies have shown that submonolayer Ge deposition on Al(111) at different growth temperatures (from RT up to 360K) results in the formation of two surface reconstructions, namely $(3 \times 3)_{Al}R0°$ and $(\sqrt{7} \times \sqrt{7})_{Al}R(\pm 19.1°)$ (hereafter (3×3) and (√7×√7)), with respect to the unit cell of the Al(111) surface [7], [90]–[93], [97]–[100].

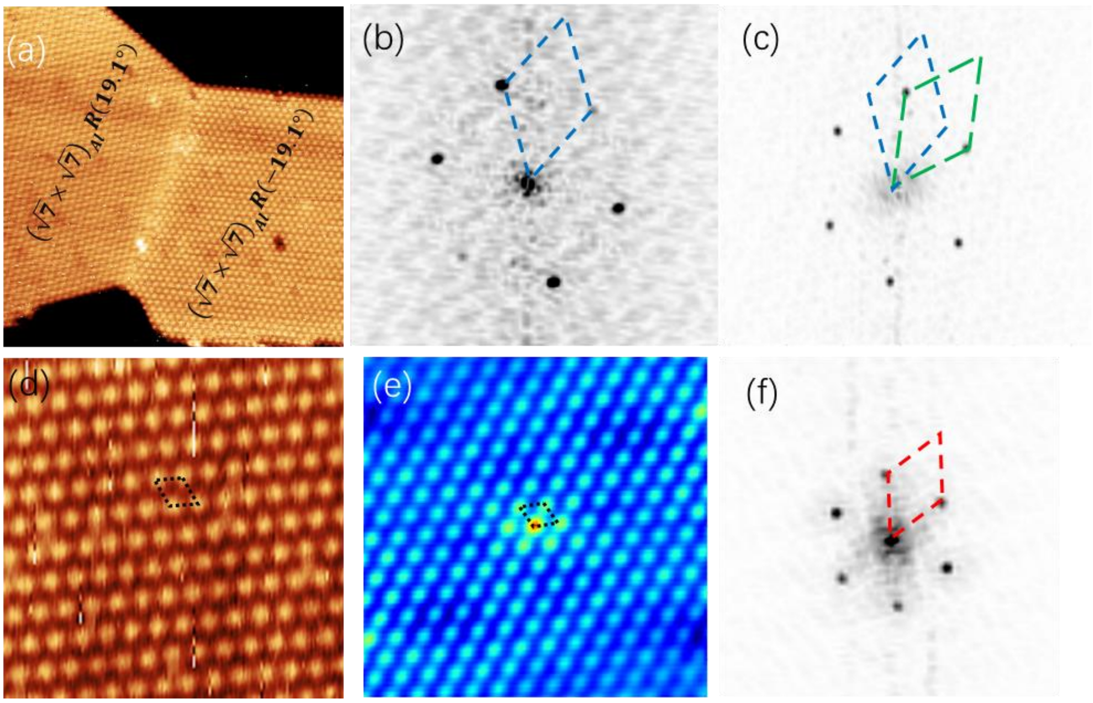

Figure 4.3 (a) Atomic resolution STM image of the (√7×√7) (40×40 nm2; U=2.0V, I=30 pA). The left part corresponds to the (√7×√7)R19.1° reconstruction, while the right part indicates the (√7×√7)R-19.1° one. (b, c) Corresponding Fast Fourier Transform images related to the left and right part of (a). The dashed blue and green rhombus denote the hexagonal unit cell of the (√7×√7)R±19.1° in the reciprocal space. (d) Atomic resolution STM image of the (3×3) reconstruction (10×10 nm2; U=0.9V, I=50 pA). The unit cell of the (3×3) reconstruction is indicated by the dotted black rhombus. (e) Corresponding self-correlation images. The dotted black rhombus represents the unit cell of the (3×3) reconstruction. (f) Corresponding Fast FFT images.

Fig. 4.3a and 4.3d display two atomically resolved STM images presenting the hexagonal atomic arrangement of the (√7×√7) and (3×3) surface reconstructions on the Al(111) surface, respectively. For the (√7×√7) superstructure, there are two reconstructions with different rotated angles, i.e. (√7×√7)R19.1° and (√7×√7)R-19.1°. The matrix of their unit cell can be written as $\begin{pmatrix} 3 & -1 \\ 1 & 2 \end{pmatrix}$, for a rotated angle of 19.1° and $\begin{pmatrix} 2 & 1 \\ -1 & 3 \end{pmatrix}$, for an angle of -19.1°, with respect to the Al(111) unit cell ($a_0 = b_0 = 2.864$Å, $c_0 = 7.015$ and $\alpha = \beta = 90°$, $\gamma = 120°$). The theoretical lattice constant of the (3×3) and (√7×√7) corresponds thus to 8.67Å and 7.64Å, respectively. Using two-dimensional fast Fourier transform (2D FFT), the measured lattice parameter of these three hexagonal structures shown in Fig. 4.3a and 4.3d is indeed 0.85 ± 0.01 nm and 0.76 ± 0.01 nm, corresponding to the (3×3) and (√7×√7) surface reconstruction, respectively. Fig. 4.3b and 4.3c show two FFT images obtained from the left part and right part of Fig. 4.3a associated with the (√7×√7)R19.1° and (√7×√7)R-19.1° reconstructions. The angle between the reconstructions in left and right part is measured to be 38° ± 1°.The rotated angle of the (√7×√7) structures is also measured to be $\alpha = \pm 19° \pm 0.5°$ from the orientation of the (3×3) structure (see Fig. 4.3e), which is in agreement with the theoretical value of ±19.1°. In addition, these STM images display only one protrusion in the unit cell of these reconstructions, which is the same as the STM measurements shown in ref. [90][91][97–99] and different from STM observation reported in ref. [7] for two protrusion in the unit cell.

As can be seen in Fig. 4.2a, the (√7×√7) reconstruction consists of smaller areas separated by discommensuration lines (DLs), while the (3×3) reconstruction domain contains no DLs. This is an important distinction between these two reconstruction domains. Fig. 4.4 shows a detailed view of the (√7×√7) reconstruction domain with an atomic resolution. Three areas and their orientation of atomic rows are labeled as A (yellow), B (blue), and C (green), respectively. At both sides of the DL, a shift of the atomic rows between the neighboring domains is clearly visible (see Fig. 4.4). The value of the shift is $na_{\sqrt{7}}/7$, where $a_{\sqrt{7}}$ is lattice parameter of the (√7×√7) structure with respect with the Al(111) unit cell (i.e. $a_{\sqrt{7}}=a_0\times\sqrt{7}=7.58$Å) and n = 1~ 7. A shift of the atomic rows between A and B domain (Δ_1) is measured to be $3a_{\sqrt{7}}/7$, and between C and A (Δ_2) is measured to be $4a_{\sqrt{7}}/7$. The formation of domains boundaries in the (√7×√7) domain could originate from a shift of the atomic rows at the both sides of the DL [97].

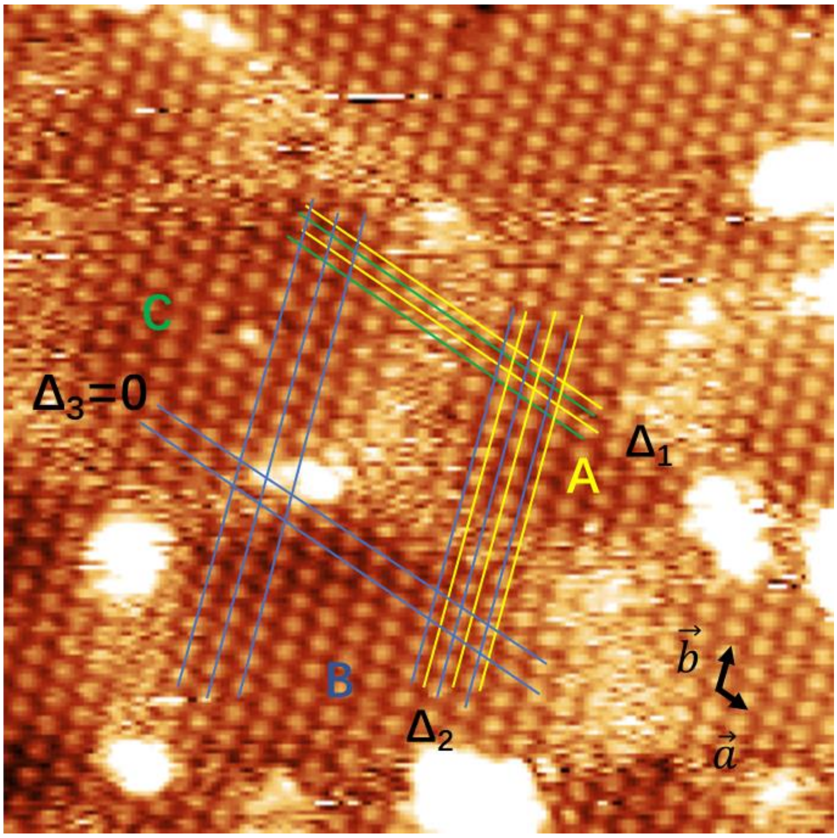

Figure 4.4 Detailed view of the (√7×√7) reconstruction. The yellow, blue, and green solid lines indicate the direction of the atomic rows in three areas labeled as A, B, and C with different colors, respectively. Δ is the shift of the atomic rows. The vector ***a*** and ***b*** represent the lattice vectors of the (√7×√7) unit cell. Size of the images 20 × 20 nm^2. Tunneling conditions: $V_S = 0.9$ V, I = 50 pA.

However, there is a DB without a shift of the atomic rows between B and C area. This may be result from constraints from other domains with a shift of the atomic rows or a imperceptible shift of the order of $1/\sqrt{7}\ a_{\sqrt{7}}$.

4.2.2 Evolution of the surface during Ge deposition

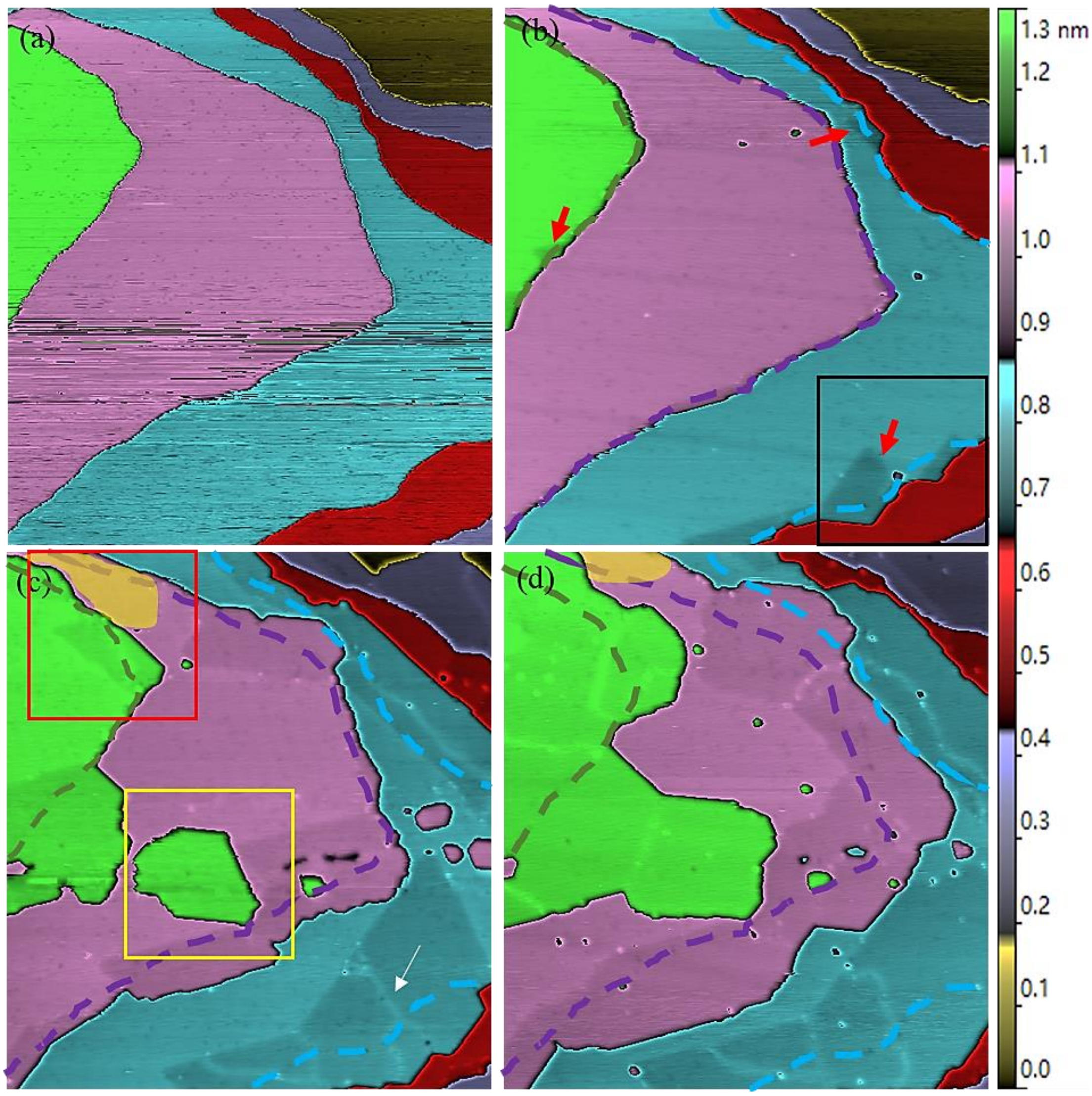

Figure 4.5 Evolution of the Al(111) surface during Ge deposition at RT for (a) 0 min, (b) 30 min (θ_{Ge} = 0.04 ML), (c) 70 min (θ_{Ge} =0.11 ML), (d) and 370 min (θ_{Ge} = 0.5 ML). In (b), the red arrows indicate that the reconstruction areas first appear near a step edge. In (c), the white arrow indicates the discommensuration line in the (√7×√7) reconstruction domains. The dashed dark green, violet, and blue lines represent the initial outline of the boundary of the green, violet, and blue terrace. Size of the images 129 × 143 nm^2. Tunneling conditions V_S = 2.0 V, I = 20 pA.

Fig. 4.5 shows the evolution of the surface during Ge deposition on the Al(111) surface held at RT. Before Ge evaporation, the bare Al(111) surface shows large and flat terraces separated by single atomic steps (see Fig. 4.5a). The different colors correspond to the terraces at different levels, the green terrace is higher than the dark yellow one. The noisy part at the center of Fig. 4.5a may result from the instability of the tip apex. After evaporating 0.04 ML of Ge (1 ML corresponds to the Al(111) surface density), the presence of Ge-covered areas is clearly visible at step edges as shown by the red arrows in Fig. 4.5b. Compared to the Al(111) surface, Ge-covered areas show a lower apparent height. Fig. 4.6a displays a detailed view of Fig. 4.5b corresponding to the position of the continuous black square drawn in Fig. 4.5b, respectively. This figure shows that the Ge-covered area has a hexagonal structure. It corresponds to the (√7×√7) reconstruction domain, as determined by 2D FFT. In Fig. 4.5b, the other Ge-covered areas also correspond to (√7×√7) domains. After further Ge evaporation (about 0.11ML coverage), the step edges move toward the descending direction, forming outgrowths on the inferior terraces, and Ge-covered domains expand, as illustrated in Fig. 4.5c. Note that the presence of discommensuration lines is clearly visible in Ge-covered areas. It indicates that the areas with DLs correspond to the (√7×√7) structure domains. In addition, new islands appear on the surface (see Fig. 4.5c). Fig. 4.6b and 4.6c present a detailed view of the areas indicated by the continuous red and yellow squares drawn in Fig. 4.5c. As determined by FFT, the Ge-covered domain in the left part of Fig. 4.6b is associated with the (3×3) reconstruction, and this is the only (3×3) domain in Fig. 4.5. The detailed view of Fig. 4.6c shows that the largest island (i.e. the largest green island) corresponds to the (√7×√7) structure domain. Small violet islands are also covered with Ge atoms with a (√7×√7) reconstruction. After total Ge deposition (coverage ~0.5 ML), the Ge-covered islands on the inferior terraces becomes larger and connects to the terraces. The (√7×√7) reconstruction domains continue to enlarge, but the size of the (3×3) structure domain decreases (see the size of the yellow areas in Fig. 4.5c-d). The fraction of the Ge-covered domain and the Al(111) is 0.81 and 0.19, respectively. In reconstruction domains, the fraction of the (3×3) reconstruction domains is estimated to be about 0.035 in Fig. 4.2, 0.02 in Fig. 4.5c, and 0.008 in Fig. 4.5d, much smaller than the one of the (√7×√7) domains. It indicates that the (√7×√7) structure could be more stable at RT.

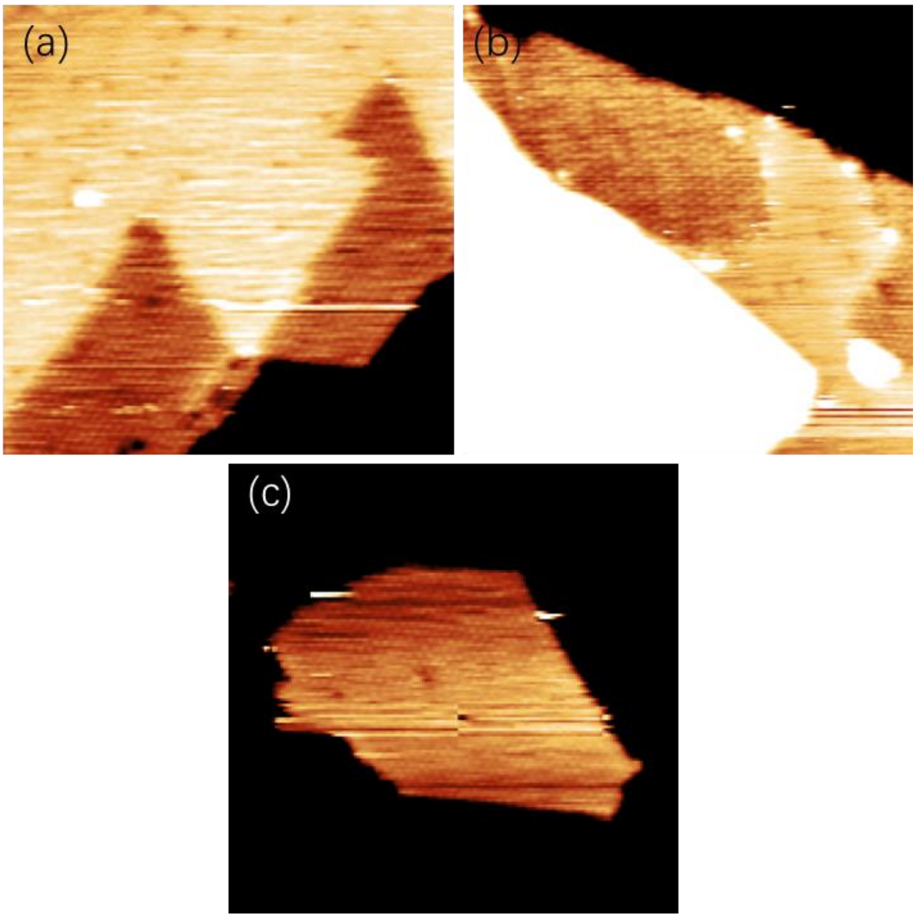

Figure 4.6 Detailed view of Fig. 4.5b and 4.5c (40×40nm2) corresponding to the position of the continuous (a) black, (b) red, and (c) yellow squares drawn in Fig 4.5

In the case of the growth Si on the Ag(111) surface [126], Ag atoms on the surface are replaced by Si atoms, and expelled Ag atoms condense at the step edges or grow new islands. The outgrowths and new islands are initially free of silicon and then covered with Si as Si evaporation continues. In the present case, the growth of reconstructions begins at the step edges (see Fig. 4.5b and Fig. 4.6a), where the nucleation can occur due to a lower nucleation barrier [97]. The reconstruction domains expand inside the upper terrace and in the outgrowths. More precisely, these outgrowths are instantaneously covered with Ge entirely. This evolution is observed in the formation of new islands, as presented in Fig. 4.5c and 4.6c. If the initial domain is the Al(111) area, the growing outgrowths correspond to Al domains, as can be seen in the area nearby the yellow domain shown in Fig. 4.5c and 4.5d.

4.2.3 Transition between the (√7×√7) and (3×3) reconstructions

As described in section 4.2.1, Ge deposition at 300K leads to the formation of the (√7×√7) and (3×3) reconstructions on Al(111). Compared to the fraction of the surface covered with (√7×√7) domains, the fraction of the surface covered with (3×3) reconstruction domains is very small.

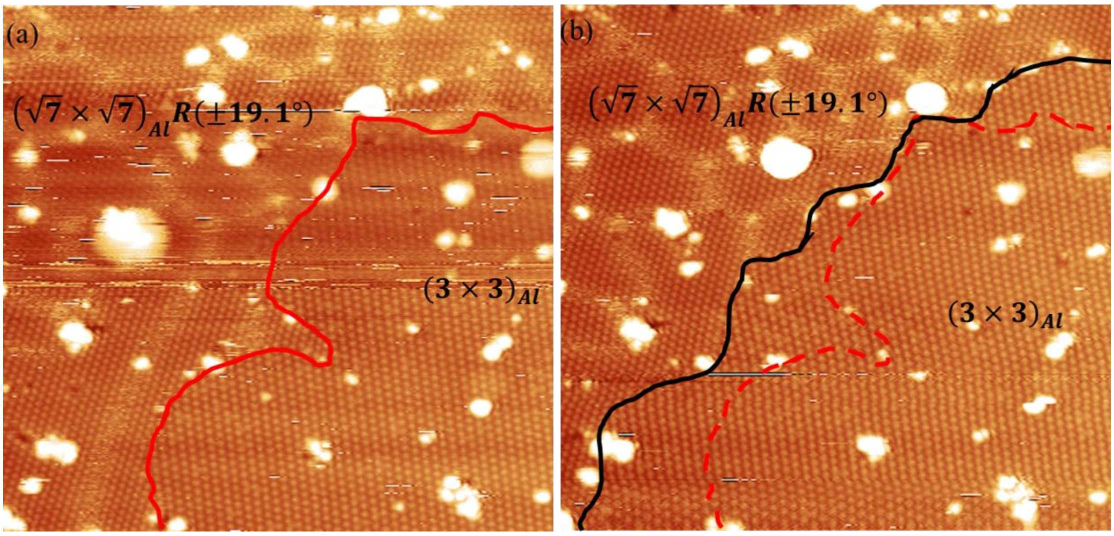

Figure 4.7 Evolution of the (3×3) and (√7×√7) reconstruction domains during Ge deposition on Al(111) held at 357K shown in two adjacent STM images with a time interval of 10 min. In (a), the boundary between the (3×3) and (√7×√7) areas is marked by a red solid line. In (b), the previous and new boundaries are indicted by a red dotted and black solid lines. Size of the images 48 × 47 nm^2. Tunneling conditions: V_S = 0.9 V, I = 50 pA.

Let us take a look on the evolution of reconstructions during Ge evaporation at T_{growth}= 357K. Fig. 4.7 shows two successive in-situ STM images obtained during Ge deposition on the Al(111) surface kept at 357K. The time interval between these two STM measurements is 10 minutes. Using 2D FFT, two reconstructions shown in Fig. 4.7 have been determined, the reconstruction domain in the upper-left part corresponds to the (√7×√7) structure while the bottom-left part is associated with the (3×3) reconstruction. In Fig. 4.7a, a boundary between the (√7×√7) and (3×3) reconstruction domain is drawn by a solid red line. As presented in Fig. 4.7b, the current boundary is labeled by a solid black line after 10 minutes Ge evaporation, whereas the former is marked by a dotted red line. A comparison between these two in-situ images indicates that the domain of the (3×3) reconstruction grows whereas the (√7×√7) domain shrinks. It indicates that, at a growth temperature of 357K, additional Ge deposition on the (√7×√7) structure domains could lead to their transformation into a (3×3) reconstruction.

4.2.4 Artificial tip-induce STM resolution

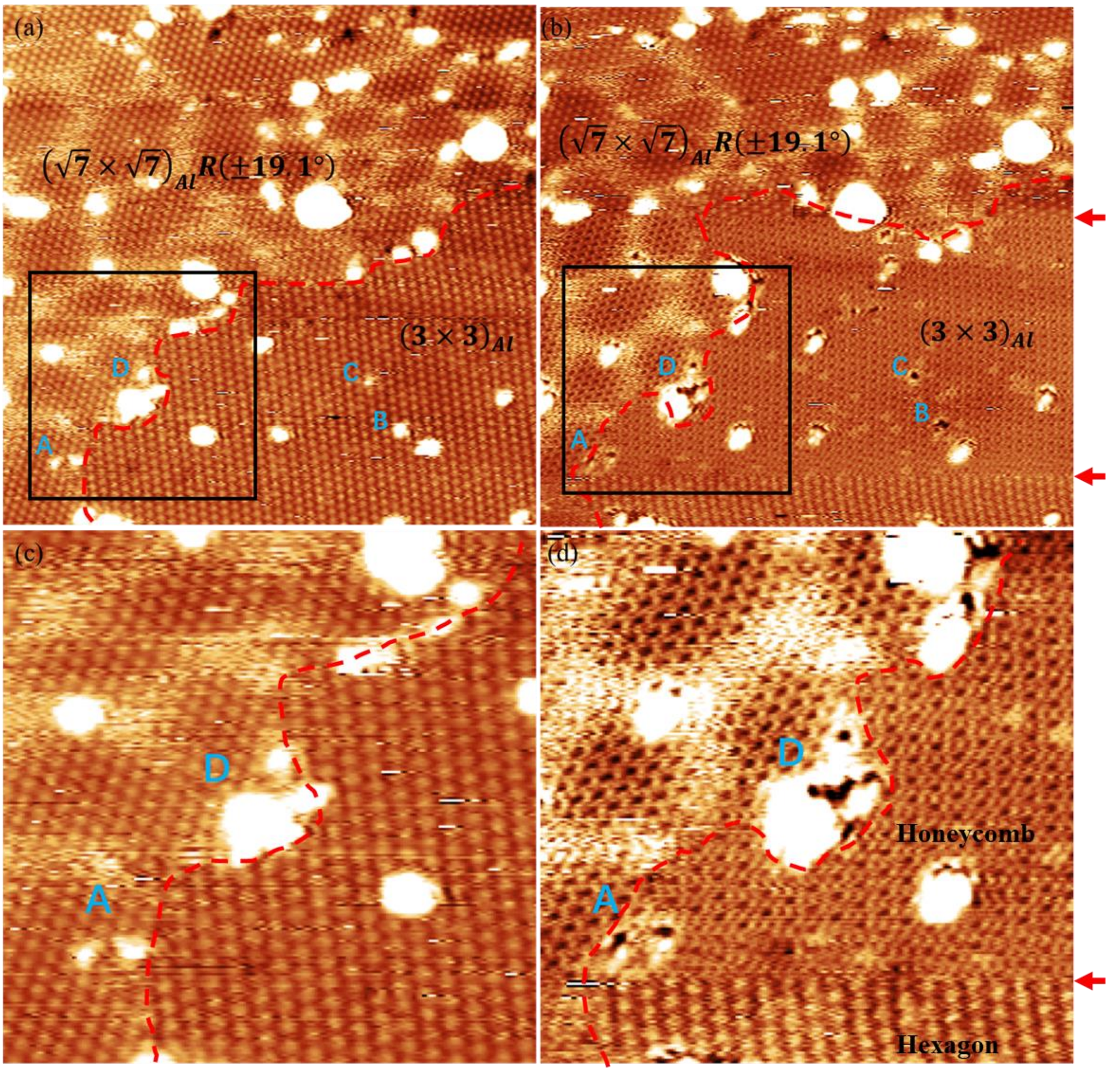

Figure 4.8 Two adjacent STM images ($46 \times 48\ \text{nm}^2$) in the same tunneling conditions (V_S = 0.9 V, I = 50 pA) with a time interval of 10 min after Ge evaporation at 357K. The same defects labeled as A, B, C, and D in the two image display different contrast. In (b), the red arrows indicated the switch of the contrast. (c), (d) A detailed view of (a) and (b) corresponding to the areas indicated by the continuous black squares shown in (a) and (b).

Fig. 4.8.a-b shows two consecutive STM images acquired with a small time interval of 10 minutes. Fig. 4.8c and Fig. 4.8d present a detailed view of Fig. 4.8a and b corresponding to the position of the continuous black squares drawn in Fig. 4.8.a-b. The boundary between the two reconstructions is drawn by a dashed red line. In addition, the periodicity of a reconstruction is measured by FFT. As can be seen in Fig. 4.8a and 4.8c, both (√7×√7) (the upper-left part) and (3×3) (the bottom-right part) reconstruction domains display a hexagonal structure. From the STM image in Fig. 4.8b, one can see that both reconstructions present a honeycomb arrangement in the middle of the image and a hexagonal arrangement in the other areas. In addition, honeycomb structure domains have the same periodicity for the corresponding domains in Fig. 4.8a, as investigated by FFT. The sudden switch of the contrast occurs twice, marked by the red arrows in Fig. 4.8b and 4.8d. As discussed in section 2.3.1, Stephen et al. have reported that the transformation observed for (3×3) domains result from a tip-surface interaction and corresponds to the change from one to two Ge atoms protruding upward in the unit cell [96]. However, this explanation cannot be employed to verify the contrast change of the (√7×√7) reconstruction. In order to explain this observation, I have selected four defects labeled as A, B, C, and D shown in Fig. 4.8.a-b. These defects present different appearances in these two images. Defects A and D shown in Fig. 4.8c are protruding, whereas the ones in Fig. 4.8d are indenting. It reveals that the contrast change results from the artificial modification of the STM tip apex. It has also been explained by the presence of a double-tip termination resulting into the appearance of two atoms per unit cell instead of forming then a honeycomb pattern [97].

4.3 Formation of the Ge-Al surface alloy

In section 4.2, I have described the growth of Ge on the Al(111) surface and the formation of the (√7×√7) and (3×3) reconstructions. In this section, from a precise analysis of real-time STM measurements, I give evidence of the formation of the Ge-Al surface alloy.

From a precise analysis of in-situ real-time STM images obtained during Ge deposition at 300K, the dependence of the coverage of the outgrowth with the one of Ge-covered areas is drawn in Fig 4.9. In this figure, the coverage of the outgrowths and of the reconstruction domains are related through two linear relationships, revealing a different surface evolution during Ge deposition. The first linear relationship, indicated by the solid red line drawn in Fig 4.9, shows that $\theta_{outgrowth} = \alpha\theta_{Ge\text{-}covered}$ where the value of α is equal to $0.60\pm0.05 < 1$. It indicates that Ge deposition on Al(111) kept at 300K results in the formation of a Ge-Al surface alloy, different from the formation of layered germanene reported in ref. [7][90–92][96–99]. In other words, the (√7×√7) and (3×3) reconstructions correspond to Ge-Al surface alloy structures.

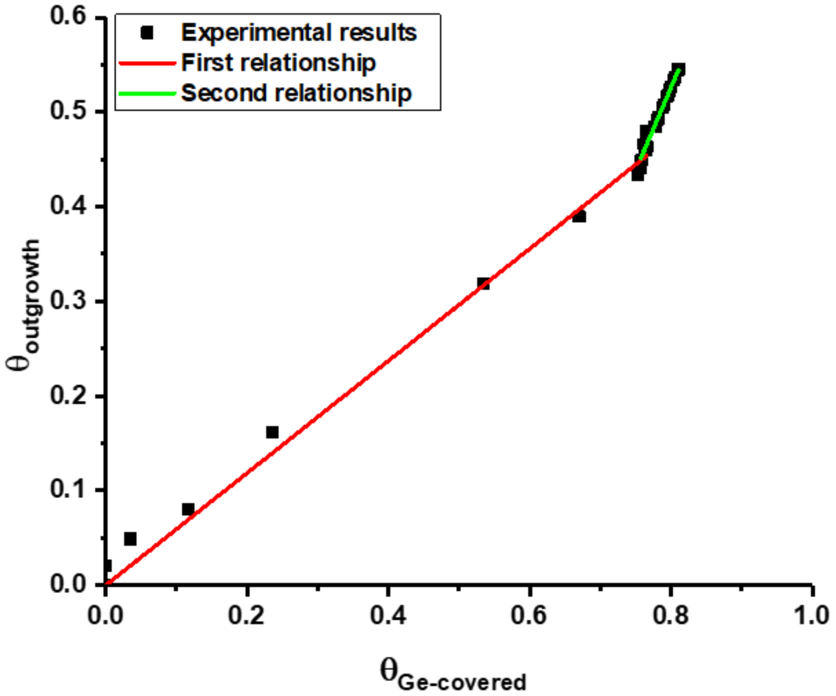

Figure 4.9 Fraction of the outgrowth as a function of the reconstruction areas coverage rate during growth at 300K. The experimental result indicated by black squares show two linear relationship labels as red and green solid line, respectively.

Concerning the second linear relationship indicated by the solid green line in Fig 4.9, Eq. (4-1) is rewritten as $\theta_{outgrowth} = 1.75\theta_{Ge} - 0.88$ with $\alpha > 1$. The case of $\alpha > 1$ indicates that the outgrowth grows faster than the formation of the surface reconstruction domains. It may be interpreted as the formation of Ge clusters or more probably, to the shadowing effects induced by the STM tip, and the different diffusion coefficient for Ge and Al atoms on Ge-covered and bare Al areas. When the Ge-covered areas have percolated, diffusion of Ge atoms up to the area scanned under the tip becomes reduced, and the Ge coverage evolves very slowly with time.

In this section, I have given evidence of the formation of the Ge-Al surface alloy after Ge deposition on Al(111), using real-time in-situ STM measurements. In the following section, I will present the results of combined grazing-incidence X-ray diffraction measurements and DFT calculations, aimed to determine the accurate atomic structure of the (3×3) reconstruction grown on Al(111).

4.4 Study by GIXD

4.4.1 Experimental detail

Grazing incidence X-ray diffraction (GIXD) is a powerful technique for elucidating the structure of ordered surface reconstructions. It has been recently used to obtain the precise atomic positions for silicene epitaxial layers on Ag(111)[12,13]. The GIXD experiments were performed at the SIXS beamline of SOLEIL synchrotron. The preparation of the Al(111) substrate was performed with the same procedure presented in section 4.1.1. The germanium was deposited on the Al(111) substrate maintained at a fixed temperature in a range of 300K to 414K. Regarding the experiments of Ge deposition at 373K, the Ge flux was held constant with ~1.4ML/h, where 1ML corresponds to the Al(111) surface atom density. For the experiments of the deposition at other temperatures, a deposition rate is estimated to be 0.7ML/h. In reciprocal space, the position of the diffracted signal is described by the (h, k, l) indices referring to the Al(111) surface unit cell with $a_0 = b_0 = 2.864$Å, $c_0 = 7.014$ Å and $\alpha_0 = \beta_0 = 90°$, $\gamma_0 = 120°$. The reciprocal lattice constants can be obtained by $|\mathbf{a_0}^*| = |\mathbf{b_0}^*| = 4\pi/(\sqrt{3}|\mathbf{a_0}|)$ and $|\mathbf{c_0}^*| = 2\pi/|\mathbf{c_0}|$, the angle between $\mathbf{a_0}^*$ and $\mathbf{b_0}^*$ is equal to 60°. Regarding the (3×3) reconstruction, the unit cell can be described as a hexagonal Bravais lattice with the lattice constants $a_3 = b_3 = 3a_0 = 8.589$Å, $c = c_0 = 7.014$Å. The (H, K, L) indices refer to the $(3\times3)_{Al}$ reconstruction basis. In the reciprocal space, the basis of this reconstruction can be expressed as:

$$\boldsymbol{a}^*_{(3\times3)} = \frac{1}{3}\boldsymbol{a}^*_0 \quad \boldsymbol{b}^*_{(3\times3)} = \frac{1}{3}\boldsymbol{b}^*_0 \quad \boldsymbol{c}^*_{(3\times3)} = \boldsymbol{c}^*_0 \tag{4-4}$$

As regards the $(\surd7)_{Al}R(\pm19°)$ reconstruction, the unit cell can also be described as a hexagonal lattice with the lattice constants $a_{\surd7}=b_{\surd7}=\surd7a_0=7.575$ Å, $c=c_0=7.014$Å. Due to the rotated angle with respect to the unit cell of Al(111), the basis of the (√7×√7) reconstruction in the reciprocal space indicates two groups related to the matrix of the unit cell described in section 4.2.1:

$$\boldsymbol{a}^*_{(\surd7)} = (2\boldsymbol{a}^*_0 + \boldsymbol{b}^*_0)/7 \quad \boldsymbol{b}^*_{(\surd7)} = (-\boldsymbol{a}^*_0 + 3\boldsymbol{b}^*_0)/7 \quad \boldsymbol{c}^*_{(\surd7)} = \boldsymbol{c}^*_0 \tag{4-5}$$

$$\boldsymbol{a}^*_{(\surd7)} = (\boldsymbol{3a}^*_0 - \boldsymbol{b}^*_0)/7 \quad \boldsymbol{b}^*_{(\surd7)} = (\boldsymbol{a}^*_0 + 2\boldsymbol{b}^*_0)/7 \quad \boldsymbol{c}^*_{(\surd7)} = \boldsymbol{c}^*_0 \tag{4-6}$$

The intensity is measured by rotating the sample around the normal to its surface, keeping the detector at fixed position. This measurement is known as angular rocking scan (ARS) or simply ω-scan. The h-scan (k-scan) refers to the diffracted intensity measurements in a range of Δh (Δk) for the same (k(h), l) value.

4.4.2 Appearance of two reconstructions in reciprocal space

The results of STM measurements, as discussed in section 4.2, show that Ge deposition on Al(111) leads to the formation of the (√7×√7) and (3×3) reconstruction. In this section, I present GIXD measurements for these two reconstructions.

- **(3×3) reconstruction in reciprocal space**

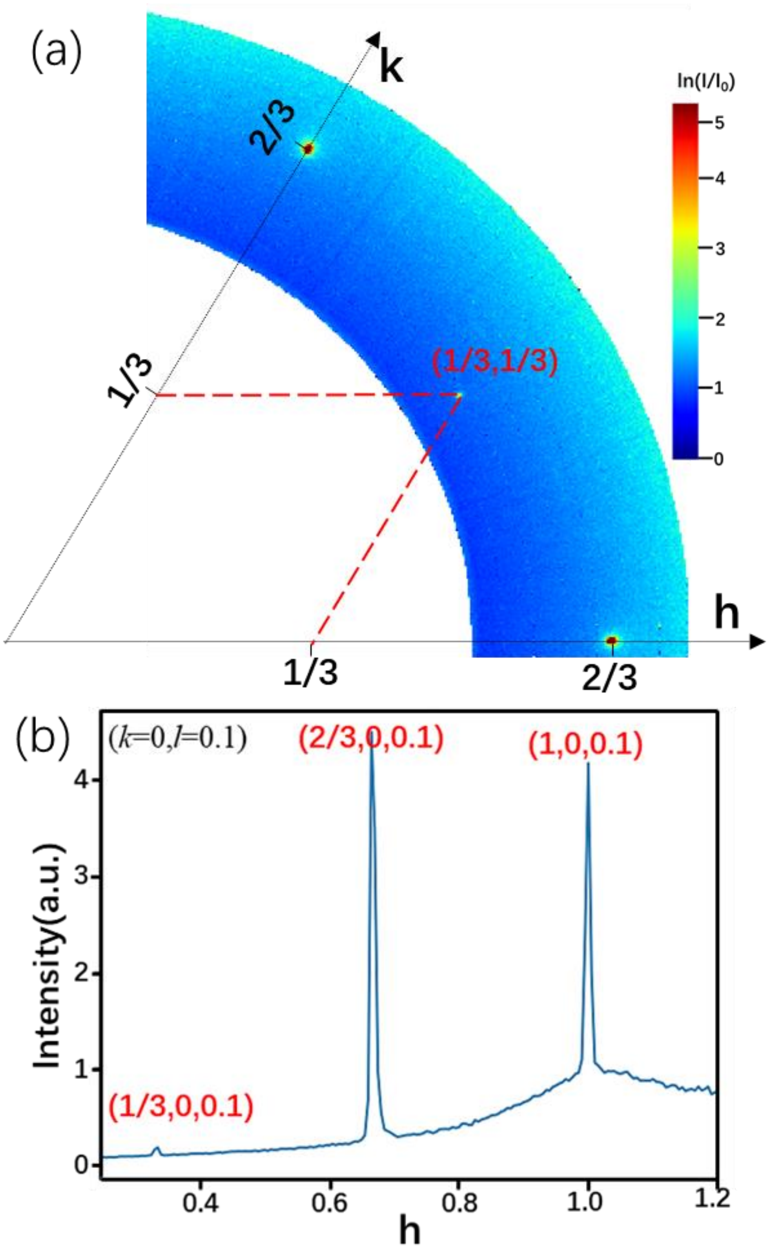

Figure 4.10 (a) In-plane diffraction map (l=0.10) of the reciprocal space obtained by GIXD measurements about 1ML Ge deposition on the Al(111) surface kept at 373K. The red dashed parallelogram corresponds to a (3×3) supercell. (b) The intensity evolution between the reciprocal spots (0.2, 0, 0.1) and (1.2, 0, 0.1) after ~1ML Ge deposition on Al(111) at RT.

In Fig. 4.10a the GIXD map of the diffracted intensity for in-plane conditions (l=0.1) is shown, obtained after about 1ML Ge deposition on the Al(111) surface kept at 373K. The presence of diffraction spots is clearly visible, and they are found at fractional values of (h, k), i.e. (2/3, 0, 0.1), (1/3, 1/3, 0.1), and (0, 2/3, 0.1). Based on the reciprocal lattice vectors of the (3×3) reconstruction described by Eq. (4-4), these diffracted signals are associated with the (3×3) reconstruction. Fig 4.10b shows the intensity evolution of an h-scan, i.e. the diffracted intensity between the reciprocal points (0.2, 0, 0.1) and (1.2, 0, 0.1), for the measurements acquired after Ge deposition. The peaks at h=1/3 and h=2/3 are associated with the (3×3) structure, whereas the peak at h=1.0 corresponds to the crystal truncation rods (CTR) of the substrate (integer values of h and k indices). The diffracted intensity at h=1/3 is much weaker than that at h=2/3.

- **(√7×√7)R(±19°) superstructure**

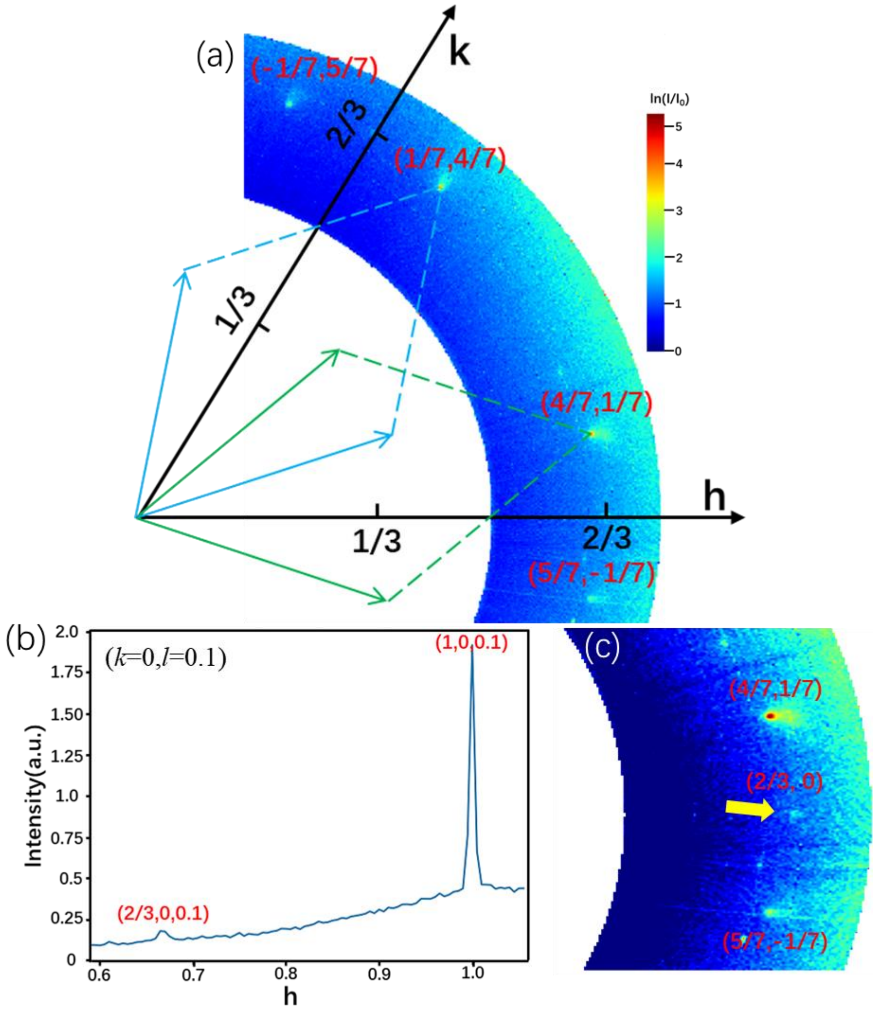

Figure 4.11 (a) In-plane diffraction map (l=0.10) of the reciprocal space obtained by GIXD measurements after about 0.8ML Ge deposition on the Al(111) surface held at 300K. The blue and green rhombus correspond to (√7×√7)R(-19°) and (√7×√7)R(+19°) superstructure, respectively. (b) The intensity evolution between the reciprocal spots (0.6, 0, 0.1) and (1.1, 0, 0.1) after Ge deposition.(c) A detailed view around (2/3, 0, 0.1) condition.

Fig. 4.11a shows the GIXD map of the diffracted intensity for in-plane conditions (L=0.1) for about 0.8ML of Ge evaporated at 300K. Thus, this diffraction map is related to the (√7×√7) reconstruction. As shown in this map, the presence of the diffraction spots associated with the (√7×√7) reconstruction is clearly visible. The positions of these diffracted signals in the reciprocal space correspond to (-1/7, 5/7, 0.1), (1/7, 4/7, 0.1), (4/7, 1/7, 0.1) and (5/7, -1/7, 0.1), as illustrated in Fig. 4.11a. The rotated angle between (-1/7, 5/7, 0.1) and (1/7, 4/7, 0.1) spot is measured to be 38°, which is in good agreement with the theoretical value obtained from the matrix presented in section 4.2.1. Two groups of the reciprocal lattice vectors of the (√7×√7) reconstruction, corresponding to Eq. (4-5) and Eq. (4-6), are drawn as the blue and green rhombus, respectively.

In Fig. 4.11b one can see the diffracted intensity between the reciprocal points (0.6, 0, 0.1) and (1.1, 0, 0.1), acquired after Ge deposition at 300 K; the h-axis refers to the unit cell of Al(111). The peak at h=2/3 related to the (3×3) structure is visible, which indicates the formation of the (3×3) structure after Ge deposition at 300K. Fig 4.11c displays a detailed view of the in-plane diffraction intensity around (2/3, 0, 0.1). Compared to the intensity at (4/7, 1/7, 0.1) and (5/7, -1/7, 0.1), the diffraction signal associated with the (3×3) structure is much weaker. This intensity is also much weaker that the one measured after evaporation at 373K. These two observations indicate that the coverage of the (√7×√7) reconstruction domains is much larger than the one for the (3×3) structure after Ge deposition at RT, which is in good agreement with STM observations described in section 4.2.

4.4.3 Real-time GIXD measurements

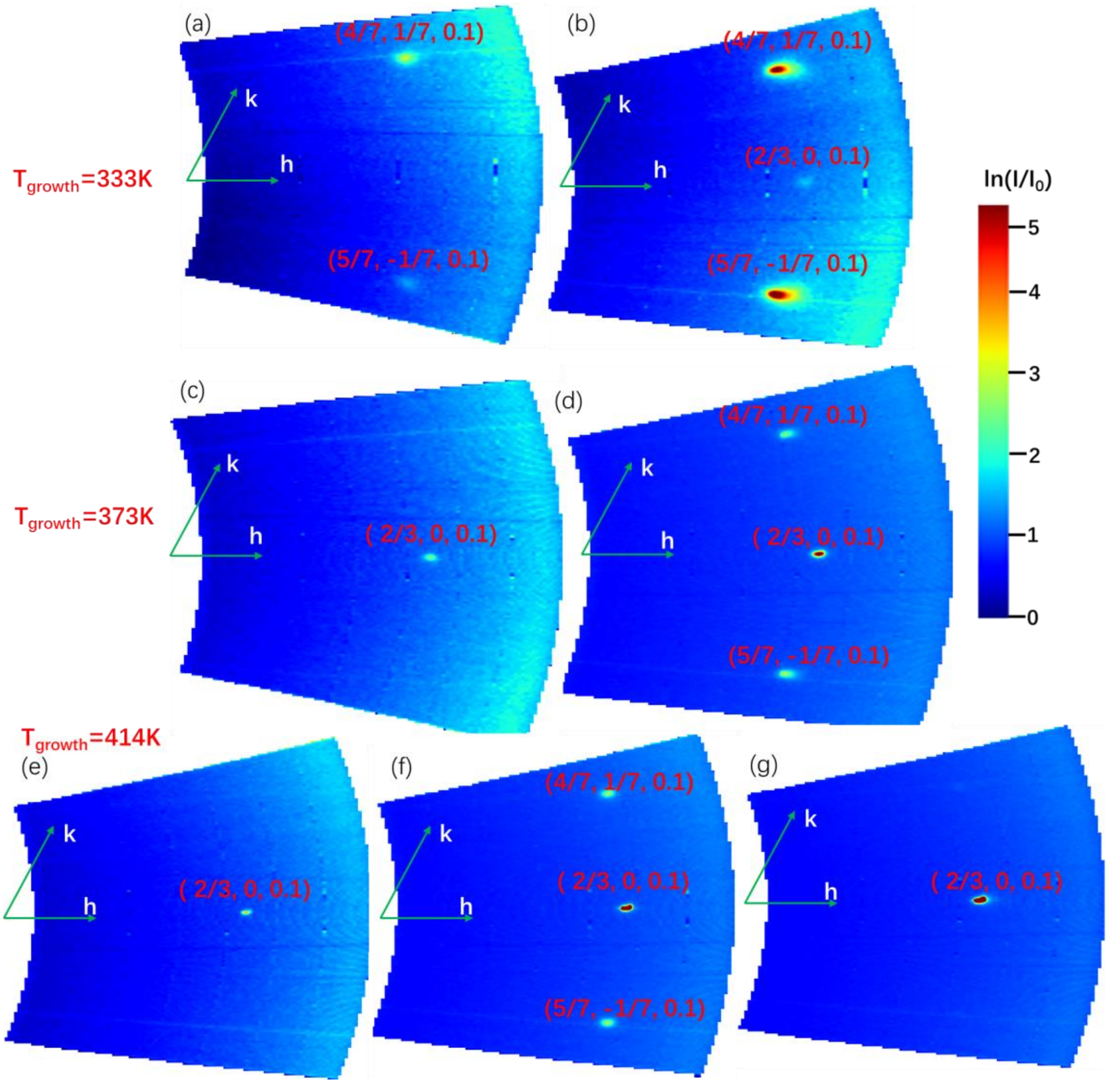

Figure 4.12 Evolution of the in-plane diffraction intensity during Ge deposition at (a-b) 333K, (c-d) 373k and (e-f) 413K. These in-plane maps are obtained after (a) 8 min, (b) 30 min evaporation at 333K, (c) 7 min, (d) 19 min evaporation at 373K, (e) 6 min, (f) 15 min, (g) 74 min evaporation at 413K.

Fig. 4.12 presents the GIXD maps of the diffracted intensity for in-plane conditions (L=0.1), obtained during Ge deposition at different growth temperatures, i.e. 333K, 373k and 413K. These maps have been obtained from in-plane ω-scans performed near the (2/3, 0, 0.1) spot. Thus, around the (2/3, 0, 0.1) spot, diffraction signals may appears at the (4/7, 1/7, 0.1) and (5/7, -1/7, 0.1) positions related to the (√7×√7) reconstruction, as shown in Fig. 4.11a.

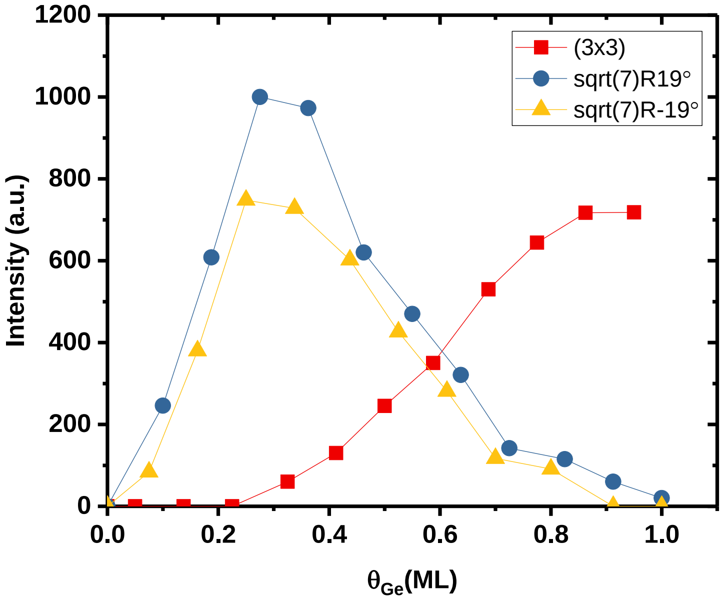

Figure 4.13 Evolution of the diffracted intensity for the (2/3, 0, 0.1) (red squares), (4/7, 1/7, 0.1) (blue circles) and (5/7, -1/7, 0.1) (yellow triangles) position related to the (3×3) and (√7×√7) reconstruction, during Ge deposition on the Al(111) surface kept at 333K.

Fig. 4.12a-b presents the evolution of the diffraction intensity during Ge evaporation at 333K. At beginning of Ge evaporation (8 min of evaporation, i.e. 0.08 ML Ge), the (4/7, 1/7, 0.1) and (5/7, -1/7, 0.1) spot firstly appears on the in-plane diffraction map of the reciprocal space (see Fig 4.12a). It indicates that the formation of the (√7×√7) reconstruction domains preferentially occurs during Ge deposition at 333K. As can be seen in Fig. 4.12a, the intensity at the (5/7, -1/7, 0.1) position is weaker than that at (4/7, 1/7, 0.1). This may results from a larger coverage of the (√7×√7)R(+19°) structure or the scanning order (i.e. the (5/7, -1/7, 0.1) spots detected firstly). After 30 min of evaporation (i.e. ~ 0.35ML Ge coverage), the diffraction signal at (2/3, 0, 0.1) start to appear on the map (see Fig. 4.12b), indicating the formation of the (3×3) reconstruction. Fig. 4.13 shows the evolution as a function of Ge coverage θ_{Ge} of the diffracted intensity near the (2/3, 0, 0.1) position. From Fig. 4.13, one can see that the growth of the (√7×√7) structure saturates for ~0.35 ML Ge coverage. As Ge deposition continues, the diffraction intensity related to the (√7×√7) structure decreases whereas the one associated with the (3×3) reconstruction grows with the coverage. This indicates that additional Ge deposition results in a transition from the (√7×√7) domains to the (3×3) domains. This behavior has already been described by STM observations for Ge deposition at 357K shown in section 4.2.3.

Concerning higher growth temperatures, Fig. 4.12c-d and Fig. 4.12e-g describe the evolution of the diffraction intensity during Ge evaporation at 373K and 414K, respectively. Different from the growth at 333K, the appearance of the first diffracted signal is visible at the (2/3, 0, 0.1) position (see Fig. 4.12c and 4.12e). It reveals that a higher temperature promotes the formation of the (3×3) structure. As Ge evaporation continues, the diffraction spots related to the (√7×√7) structure (i.e. (4/7, 1/7, 0.1) and (5/7, -1/7, 0.1)) begins emerging on the diffraction map as shown in Fig. 4.12d and 4.12f. In the end of the evaporation, the diffraction signals associated with the (√7×√7) structure disappear, as shown in Fig. 4.12g for 414K and Fig. 4.10 for 373K. This indicates that the transition from the (√7×√7) structure to the (3×3) one takes place.

Based on real-time GIXD measurements, I summarized several aspects concerning the growth of Ge on the Al(111) surface kept at the different temperatures:

- Ge deposition, on the Al(111) surface at a low growth temperature, promotes the growth of the (√7×√7) structure. On the contrary, a higher growth temperature makes for the formation of the (3×3) structure. Their dividing line of the growth temperature corresponds to 360K ~ 370K.
- The (√7×√7) and (3×3) structure can coexist during Ge deposition held at a fixed temperature in a range of 300K to 414K, but they have different coverages.
- A transition from the (√7×√7) structure to the (3×3) one can occurs during Ge deposition at a growth temperature above 300K (RT).

4.5 Atomic structure of the Ge-Al surface alloy

In the previous studies, several models of the surface reconstructions have been proposed in the literature. As described in section 2.3.1, Derivaz et al. have proposed the model of a (2×2) germanene reconstruction corresponding to the $(3\times3)_{Al}$ periodicity with two of eight Ge atoms protruding upward in the unit cell [7], as shown in Fig 2.28. However, this model is not in agreement with STM measurements showing only one protrusion in the unit cell. Then, a model of the $(3\times3)_{Al}$ surface reconstruction corresponding to asymmetric (2×2) germanene structure has been proposed, with one Ge atom protruding upward in the unit cell [3,4][6,7]. A similar model proposed for the (√7×√7) superstructure corresponds to (√3×√3)R(30°) germanene with only one Ge protrusion in the unit cell [90], [97], [99]. The results of STM measurements reported in section 4.2 reveal that the growth of Ge on Al(111) results in the formation of a Ge-Al surface alloy. Indeed, these germanene models cannot be used to calculate theoretical structure factors. However, the model of the Ge-Al surface alloy proposed by Martinez et al. [93], with two uplifted Ge atoms in the unit cell, does not match with STM measurements. Thus, these previous models cannot be used to compute theoretical structure factors ($|F_{th}|$) for fitting with experimental ones ($|F_{exp}|$).

In this section, I present the results of combined GIXD measurements and DFT calculations, aimed to determine the atomic structure of the (3×3) reconstruction. Based on experimental structure factors, I give a description of the simulation of theoretical atomic configurations using a homemade software developed by G. Prévot and comparison with the results of DFT simulations performed at IS2M (Mulhouse).

4.5.1 Simulation detail

- **Simulation method**

Curcella et al. determined the atomic structure of the $(4\times4)_{Ag}$ silicene on the Ag(111) surface, using GIXD measurements and DFT calculation [51]. Based on the $(4\times4)_{Ag}$ silicene model proposed by Vogt et al. [5], they have used DFT to obtain a relaxed configuration. The theoretical structure factors calculated from the relaxed configuration were compared with the experimental ones showing a good agreement. The value of χ^2 was introduced to verify the agreement between the theoretical ($|F_{th}|$) and experimental ($|F_{exp}|$) structure factors:

$$\chi^2 = \frac{1}{N_{pts}-N_{par}}\sum^{N_{pts}}\left(\frac{F_{th}-F_{exp}}{\sigma_{exp}}\right)^2 \tag{4-7}$$

Where N_{pts} is the number of the experimental structure factors, N_{par} indicates the number of the free parameters and σ_{exp} is the experimental uncertainty, which takes into account the statistical uncertainty given by the number of counted photons and an overall 10% uncertainty. A lower value of χ^2 means that the theoretical structure factors acquired from the configuration have a better agreement with the experimental ones. It reveals that the configuration with the lowest energy and χ^2 is best fitted.

No available model of Ge-Al surface alloy can be used to be a reference. Thus, I take a new simulation method to obtain a theoretical configuration:

(i) I set several simulation principles, such as a model of the Al(111) substrate, the amount of substituted Al atoms, atomic positions of each layer, etc. The setting of the simulation principles is based on several conditions.

(ii) The structure of the reconstruction has several possibilities. Each possible configuration is used to compute the theoretical structure factors fitting with the experimental ones. The agreement is acquired by χ^2 adding an energetic term in order to avoid unphysical configurations.

(iii) Reasonable configurations with a small value of χ^2 are relaxed by DFT calculations. Then, the value of $|F_{th}|$ calculated from the relaxed configurations are compared with the value of $|F_{exp}|$.

(iv) Using DFT calculations, a thermodynamic study for various models is performed. Based on the agreement determined by χ^2 and the stability of configurations, the best fitted configuration is found.

- **Principle of the simulation**

Let us take a look at the simulation principles for the $(3\times3)_{\mathrm{Al}}$ reconstruction on the Al(111) surface. The structure of Al(111) substrate possesses the space group p3m1 symmetries with a ABC-stacking in the unit cell. In addition, high-resolution STM measurements show that the (3×3) structure possesses the p3m1 symmetries [97], [99]. Thus, Wyckoff positions (a, b, c, d, and e) are introduced to define symmetry sites in each layer. For an Al(111) plane, there are three possible atomic configurations for the 9 atoms inside a (3×3) cell. They are drawn in Fig. 4.14. The first one corresponds to atoms belonging to the Wyckoff positions 1a, 1b, 1c, and 6e (hereafter *abce*). The two other configurations correspond to three groups of atoms in 3d positions (hereafter *ddd*). Table 4.1 presents these Wyckoff positions in a fractional coordinate system for a (3×3) cell.

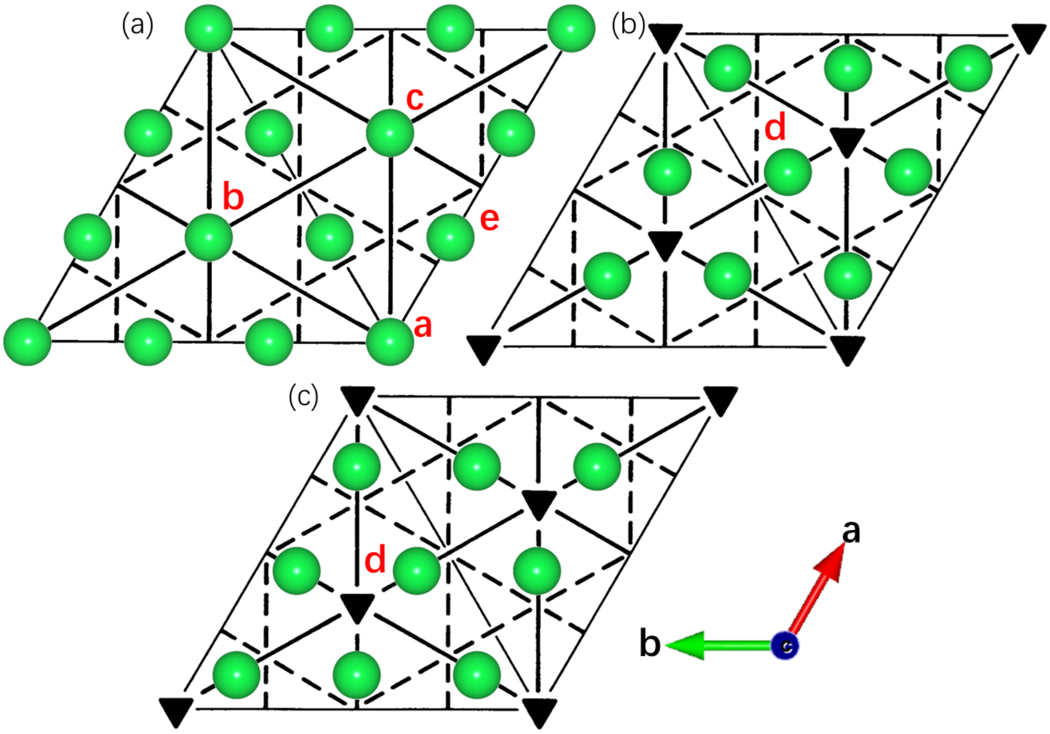

Figure 4.14 Atomic configuration for Al(111) planes with the p3m1 symmetries. Different configurations are indicated by Wyckoff position (a) abce and (b), (c) ddd, respectively. Mirror and glide planes are drawn in black continuous and dotted lines respectively. Triangles indicates 3-fold rotation axes. Lattice vectors are indicated by the red and green arrow.

Wyckoff letter	**Multiplicity**	**Coordinates in a fractional coordinate system**
a	1	(0, 0, z)
b	1	(1/3, 2/3, z)
c	1	(2/3, 1/3, z)
d	3	Fig .4.14 (b): (1) (2/9, 1/9, z);(2) (5/9, 1/9, z);(3) (2/9, 4/9, z) Fig. 4.14 (c): (1) (1/9, 2/9, z);(2) (4/9, 5/9, z);(3) (2/9, 4/9, z)
e	6	(1/3, 0, z)

Table 4.1 Wyckoff positions associated with the p3m1 symmetries in a fractional coordinate system for a Al(3×3) cell.

In order to investigate the atomic structure of the surface, I have assumed that Ge deposition could lead to the formation of a single-layer or to a two-layer Ge-Al alloy structure on the Al(111) surface. Note that the structure of each plane in each configuration must respect the p3m1 symmetries. Regarding the first layer (surface plane), it could contain at least 3 Ge atoms and at most 9 atoms. For the second layer (interfacial plane), I have assumed that it has the structure of a substitutional alloy with a majority of Al atoms. Some Al atoms in the *abce* or *ddd* layer are thus replaced by at most 3 Ge atoms, respecting the p3m1 symmetries. In the case of the *abce* layer, Ge atoms could replace zero, one, two or three Al atoms. For the ddd layer, the amount of substitutional Ge atoms is zero or three. Concerning the third and other layers, it correspond to the Al(111) bulk. Thus, 1888 atomic configurations have been analyzed. Concerning each possible configuration, the atomic positions in the surface layer are completely free, and the bounds are set for the atoms in the second and third layer, while the atoms in the other layers remain fixed.

Considering the reasonable configurations, it is possible in the simulation program to add a term that minimizes the interatomic interacting energy (E), in the form of a Lennard-Jones potential. This term can be given by

$$E = \sum_{\substack{i,j \\ d_{ij}<1.1d_0}} A\left[\left(\frac{d_0}{d_{ij}}\right)^{12} - 2\left(\frac{d_0}{d_{ij}}\right)^{6} + C\right] + E_{offset} \tag{4-8}$$

Where d_{ij} is the distance between atoms i and j. A and d_0 depends on the chemical nature of atoms i and j. C is a constant term equal to $2 \times 1.1^{-6} - 1.1^{-12}$ used to avoid any discontinuity of the interaction at the cutoff value. As the minimum of the Lennard-Jones potential is negative, E_{offset} is a term used to make minimum of the interatomic interacting energy E greater than or equal to 0. In the present case, the value of the equilibrium distance d_0 of Al-Al and Ge-Ge is 2.86Å and 2.45Å, respectively. The value of the Al-Ge equilibrium distance could be considered as an intermediate value between the Al-Al and Ge-Ge distance, being 2.66 Å. For a dimensionless bonding energy (A), A=5 for Al-Al bonds, A=1 for Ge-Ge bonds, and A=2 for Al-Ge bonds. Using this additional term associated with the interatomic interacting energy, the expression of χ'^2 is given by

$$\chi'^2 = \chi^2 + \frac{E}{N_{pts}-N_{par}} \tag{4-9}$$

Where χ^2 is acquired from Eq.(4-7) and the number of the experimental structure factors (N_{pts}) is 1274. In the present case, a set of free parameters consists of a scale factor and Debye-Waller (DW) factors along the directions perpendicular and planar to the surface. Each group of atoms in the first two layers possesses independent Debye-Waller (DW) factors in the simulation, whereas all other atoms in the bulk have the same DW factors. Thus the number of free parameters (N_{par}) depends on the precise atomic configuration in the first two layers.

4.5.2 Simulated atomic structure of the $(3\times3)_{Al}$ reconstruction

Based on the simulation principles discussed in section 4.5.1, possible atomic configurations could be divided into three group: (I) surface layer + AlGe(abce) +Al(ddd) +Al(ddd); (II) surface layer + AlGe(ddd) +Al(abce) +Al(ddd); (III) surface layer + AlGe(ddd) +Al(ddd) +Al(abce), The surface layer could contain n groups of atoms, where n is integer less or equal to 5. The AlGe(abce) represents the second layer corresponding to Ge and Al atoms located at the Wyckoff positions *a*, *b*, *c*, and *e*. The simulations for all the possible configurations provides several relationships between the parameters and χ^2. The best fitted configurations have been obtained from a precise analysis of these relationships.

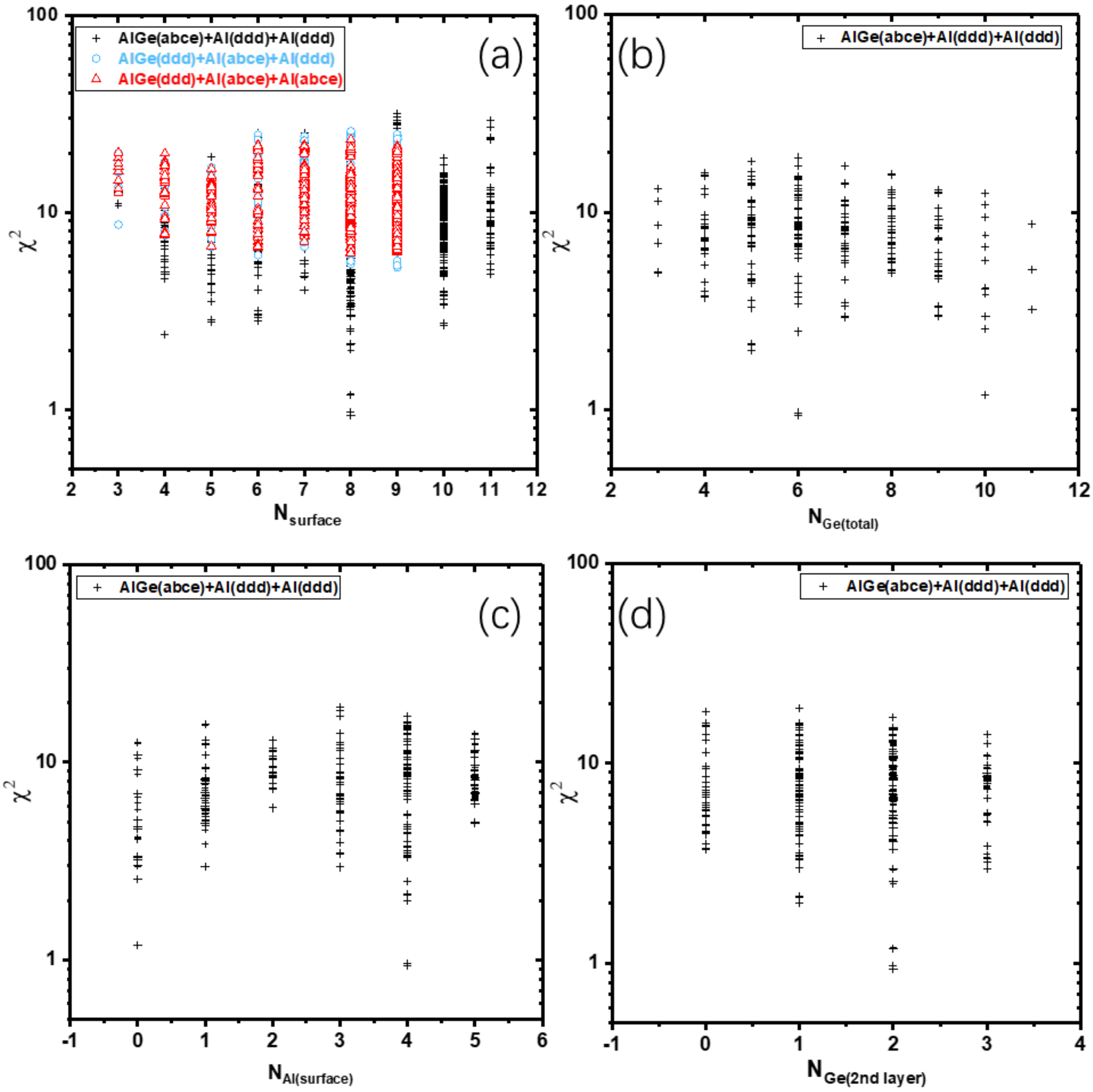

Figure 4.15 The relationship between the number of (a) atoms in the surface layer,(b) the total Ge atoms, (c) Al atoms in the surface layer, or (d) Ge atoms in the second layer and the value of agreement χ^2.

Fig. 4.15 presents four statistic relationships between parameters of possible configurations and the value of χ^2. The distribution of the value of χ^2 related to the number of atoms in the surface plane is drawn in Fig. 4.15a. As can be seen in this figure, the configurations with 8 atoms in the surface layer have a lower value of χ^2 corresponding to a better fit. It means that the first layer of the (3×3) reconstruction has 8 atoms, which is in good agreement with STM observations reported in the previous studies [97,99]. Moreover, the configurations associated with AlGe(abce) +Al(ddd) +Al(ddd) group shows a clear better fit, as compared to the ones related to other two groups. Thus, the configurations related to the simulation group II and III could be excluded. Regarding the number of Ge atoms in the first layer, Fig. 4.15b reveals that the theoretical structure factors, obtained from the structures with 6 or 10 total Ge atoms, have a better fit with the experimental ones. The corresponding quantity of Al atoms in the surface layer is four and zero, as illustrated in Fig. 4.15c. This indicates that two configurations may be possible for the surface plane, corresponding to a Ge-Al surface alloy (Ge_4Al_4) or to germanene (Ge_8). For the structure of the second layer, the statistical relationship shown in Fig. 4.15d suggests that the configurations with 2 Ge atoms in the interfacial plane are better fitted. As discussed above, the result of the simulation reveals two configurations giving a perfect agreement with the experimental result (χ^2 ~ 1), i.e. a Ge_4Al_4 layer on top of a Ge_2Al_7 plane (hereafter Ge_4Al_4/ Ge_2Al_7) and a Ge_8 layer on top of a Ge_2Al_7 plane (hereafter Ge_8/ Ge_2Al_7).

- **Ge_4Al_4/ Ge_2Al_7 model**

Concerning the Ge_4Al_4/ Ge_2Al_7 system, the results of simulations indicate that the best fit corresponds to a configuration with Al_a+Ge_c+Ge_d+Al_d for the first layer and Ge_a+Ge_b+Al_c+Al_e for the second plane, where atom_letter indicates Al(Ge) atoms located at the Wyckoff positions (*abcde*). Other configurations showing a similar agreement are symmetrical through a translation of 1/3 of the unit cell along diagonal. The comparison between the theoretical structure factors, obtained from this configuration, and the experimental ones, acquired by GIXD measurements, is shown in Fig. 4.16. The value of χ^2 is equal to about 0.9, which shows a perfect agreement.

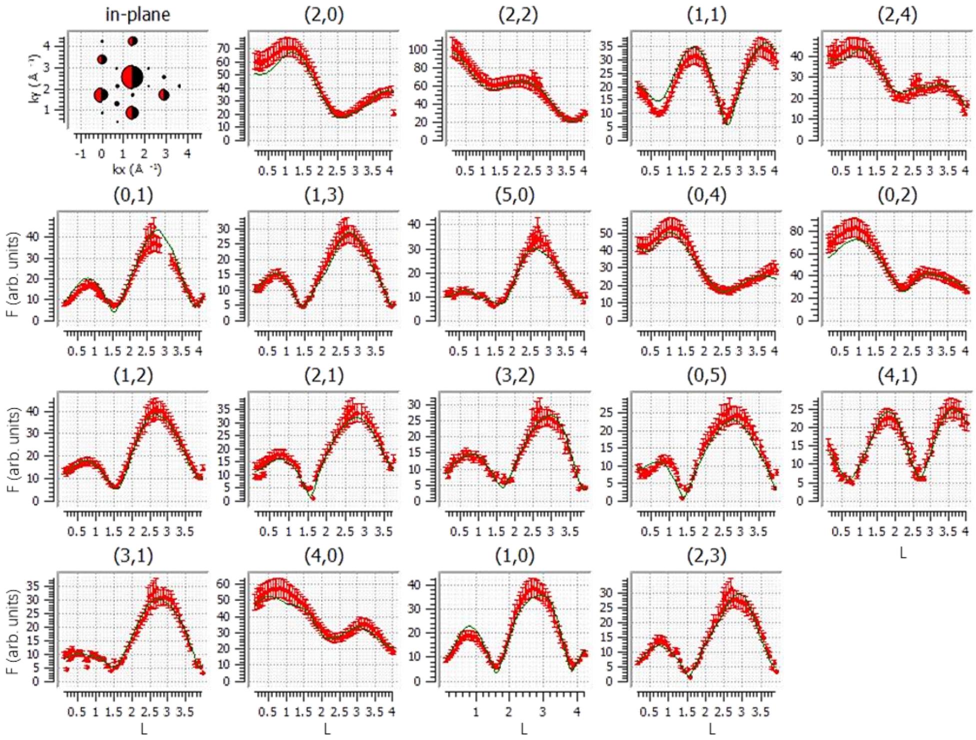

Figure 4.16 Comparison between the theoretical structure factors (green solid line), calculated from the Ge_4Al_4/Ge_2Al_7 configuration, and the experimental one (red dots) measured after the growth of Ge on Al(111) at 373K, along several diffraction rods and for in-plane structure factors (L=0.1). The (H, K, L) indices are related to the (3×3) unit cell.

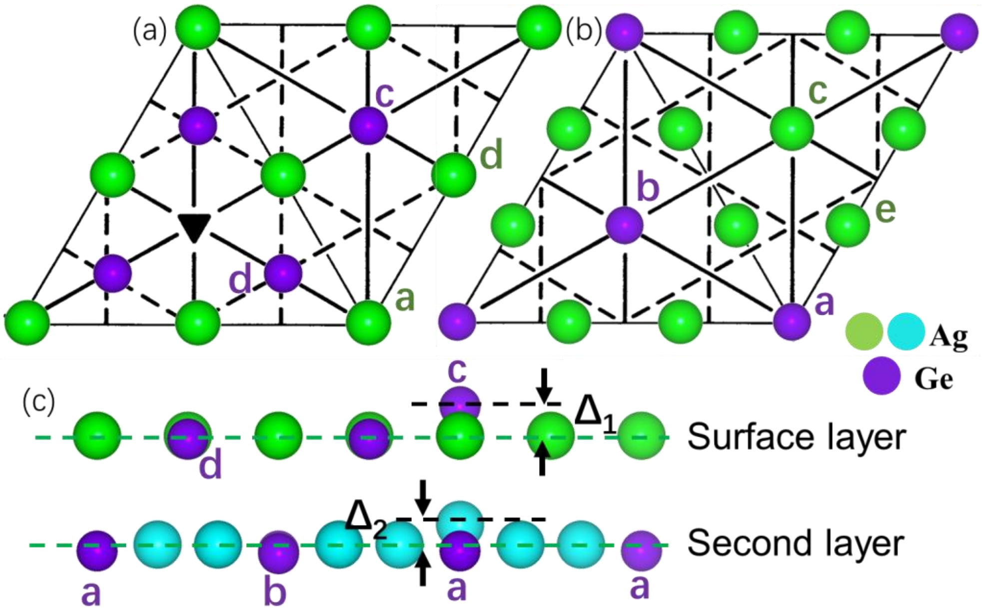

Figure 4.17 Top view of (a) the first layer and (b) second layer configuration. (c) Lateral view of the atomic model of the Ge_4Al_4/Ge_2Al_7 configuration. Violet balls represent Ge atoms. Green and blue balls indicate Al atoms in the first and second layer, respectively.

Fig. 4.17 displays the optimal configuration for Ge_4Al_4/Ge_2Al_7 corresponding to (Al_a + Ge_c + Ge_d + Al_d)/(Ge_a + Ge_b + Al_c + Al_e)/Al(ddd)/Al(ddd) structure. Concerning the surface plane (i.e. Ge_4Al_4), Al atoms belong to the Wyckoff positions 1a and 3d, while Ge atoms are located at the positions 1c and 3d, as shown in Fig. 4.17. Fig. 4.17b displays a top view of the configuration of the second layer (i.e. Ge_2Al_7), where seven Al atoms are located at the Wyckoff positions 1c and 6e whereas two Ge atoms belong to 1a and 1b respectively. As shown in Fig. 4.17a, the 8 atoms in the surface plane are arranged in a honeycomb lattice with a (3×3) periodicity, with one uplifted atom with respect to the others (see Fig. 4.17c). The protruding atom correspond to a Ge atom located at the 1c position in the first layer, with a buckling Δ_1 of 0.69 Å. The other Ge atoms in the surface layer are slightly lower than Al atoms (about 0.08 Å lower). As shown in Fig. 4.17, the highest Ge atom is located above an Al atom that is also uplifted (about 0.47 Å). The spacing between the first two layers is equal to 2.58 Å larger than the Al(111) interlayer spacing 2.34 Å. In the interfacial layer, Ge atoms at the 1a and 1b positions are 0.22 Å and 0.15 Å lower than Al atoms at the 6e positions, respectively.

- **Ge_8/ Ge_2Al_7 model**

Fig. 4.18 displays a comparison between the theoretical structure factors, obtained from the optimal Ge_8/Ge_2Al_7 configuration, and the experimental structure factors. The agreement is also very good, with $\chi^2 \approx 1.2$ only slightly higher than the value χ^2 obtained for the Ge_4Al_4/Ge_2Al_7 model. Fig. 4.19 presents the optimal Ge_8/Ge_2Al_7 configuration associated with the formation of layered germanene on the Ge_2Al_7 surface alloy layer. For the first layer, 8 Ge atoms belonging to the Wyckoff positions (1a, 1c, $3d_1$, $3d_2$) are arranged in a honeycomb lattice with a (3×3) periodicity, with only one protruding atom at the 1c position with respect to other Ge atoms. The buckling Δ_3 is equal to about 0.64 Å, and the protruding Ge atom is located atop an Al atom that shows a buckling of Δ_4= 0.53 Å (see Fig. 4.19b). A top view of the second layer is shown in Fig. 4.19b, and Ge atoms are about 0.24 Å lower than the Al atoms layer. In addition, the interlayer spacing is equal to about 2.47 Å.

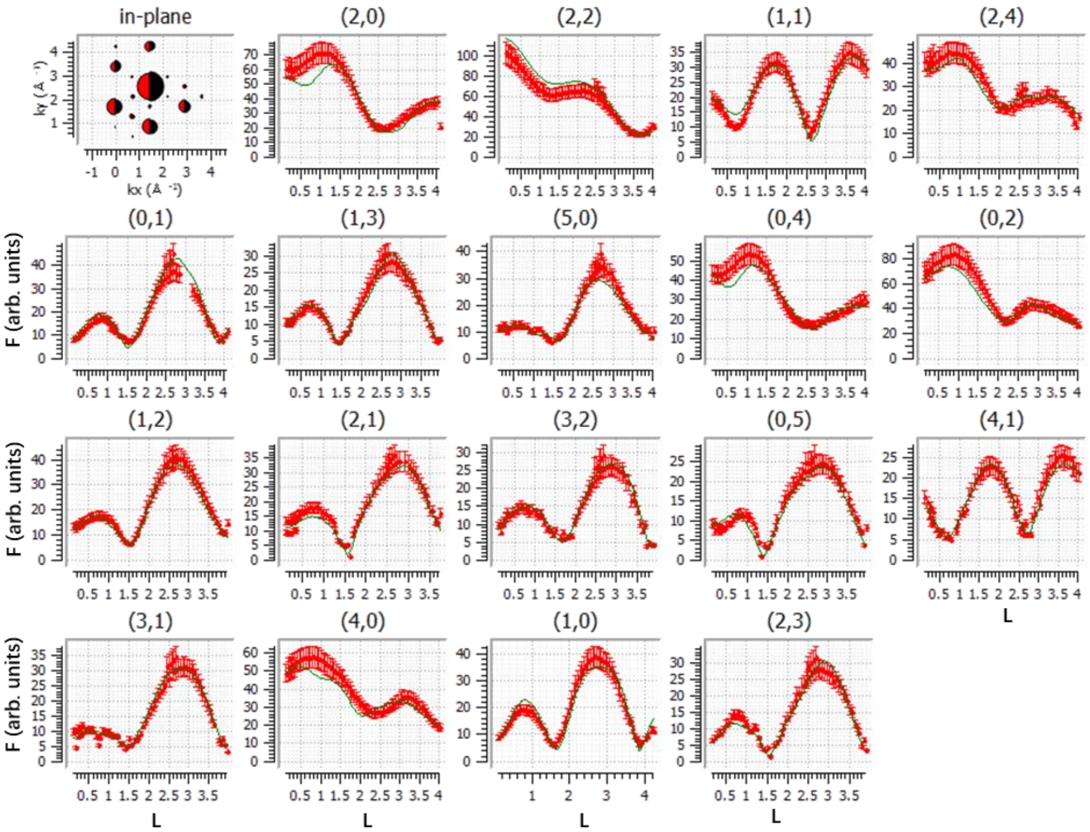

Figure 4.18 Comparison between the theoretical structure factors (green solid line), calculated from the best fitted configuration for Ge_8/Ge_2Al_7, and the experimental one (bleu dots) measured after the growth of Ge on Al(111) at 373K, along several diffraction rods and for in-plane structure factors (L=0.12). The (H, K, L) indices are related to the (3×3) unit cell.

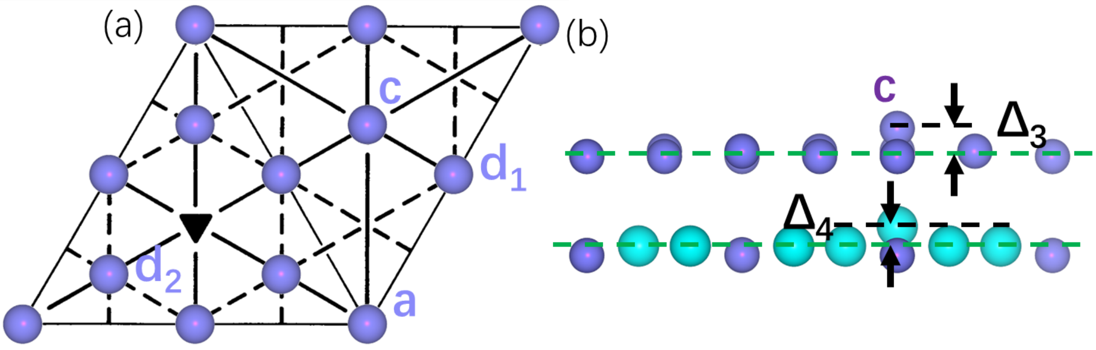

Figure 4.19 (a) Top view of the surface plane configuration and (b) lateral view of the atomic model of the Ge_8/Ge_2Al_7 configuration. Violet balls represent Ge atoms. Blue balls indicate Al atoms.

4.5.3 Experimental structure factors Vs the theoretical ones obtained from the configuration relaxed by DFT

From the comparison between theory and experiments, it is difficult to determine which configuration is the best fit for the (3×3) reconstruction, Ge_8/Ge_2Al_7 or Ge_4Al_4/Ge_2Al_7 model. Therefore, DFT calculations are used to relax configurations and investigate the stability of configurations. DFT simulations have been performed in the group of P. Sonnet at IS2M in Mulhouse. In this section, I present the result of combined DFT calculations and GIXD measurement, aimed to determine the best fitted model for the (3×3) structure.

Surface plane	Interfacial plane	χ^2
Ge_4Al_4	Ge_2Al_7	2.1
Ge_8	Ge_2Al_7	10.1
Germanene	Al_9	26.6

Table 4.2 Comparison of the agreement between experiments and Ge_8/Ge_2Al_7, Ge_4Al_4/Ge_2Al_7, Germanene/Al_9 models relaxed by DFT.

As GIXD measurements give only structural information and no energetic information, some of the models obtained from the previous analysis may have a very high surface energy. The relaxation of configuration by DFT could minimize the surface energy for each model. In addition, the 1H germanene model (germanene/Al_9) presented in ref. 10 is introduced as a reference. After relaxation, the theoretical structure factors (F_{th}) are computed from the configurations relaxed by DFT. From a comparison between the experimental and theoretical structure factors, corresponding χ^2 for relevant configurations are given in Table 4.2. A good agreement ($\chi^2 = 2.1$) is obtained with the Ge_4Al_4/Ge_2Al_7 model, while a poor agreement is obtained with the Ge_8/Ge_2Al_7 ($\chi^2 = 10.1$) and germanene/Al_9 ($\chi^2 = 26.6$) model. Indeed, the atomic positions found after relation by DFT are very close to the optimal configuration presented above for the Ge_4Al_4/Ge_2Al_7 model, whereas they sensibly differ for

Ge_8/Ge_2Al_7. This indicates that the Ge_4Al_4/Ge_2Al_7 model clearly corresponds to the best configuration found.

In conclusion, the results of the combined GIXD measurements and DFT calculations reveals that the (3×3) reconstruction corresponds to a two-layer Ge-Al surface alloy.

4.6 Discussion

In this chapter, I have reported the growth of submonolayer Ge on the Al(111) surface kept at a temperature in a range from 300K up to 420K, using STM and GIXD measurements. According to numerous previous studies, submonolayer Ge deposition on Al(111) should result in the formation of layered germanene [7], [90]–[92], [96]–[99].

Based on the experimental structure factors measured by GIXD, the result of the simulation reveals the two best fitted configurations for the $(3\times3)_{Al}$ reconstruction, i.e. Ge_4Al_4/Ge_2Al_7 and Ge_8/Ge_2Al_7. It indicates that the unit cell of the outermost honeycomb layer has 8 atoms with one atom uplifted. This is a remarkable agreement with the recent high-resolution STM observations of Muzychenko et al. [99]. They have concluded that Ge deposition on Al(111) leads to the formation of layered germanene [97], [99]. However, these two fitted models show that a (3×3) honeycomb layer stays on top of an alloyed plane, as initially proposed by Fang et al. [100]. Although STM is a powerful technique for investigating a solid surface with atomic resolution, it is hard to determine the atomic species and the exact atomic structure of the sublayer from STM images. From an analysis of GIXD measurements and DFT calculation , the protrusion in the top layer is a Ge atom above an Al atom that is also uplifted, whereas Muzychenko [99] concluded that the protruding Ge atom was on a threefold fcc position. More recently, Chen et al. have reported the theoretical study of the stable configuration on the pure Al(111) surface or Al_2Ge surface alloy [127]. In the case of Ge on Al_2Ge, they have found that the most stable configuration is the Al_4Ge_4 BHS-1T on Al_2Ge surface alloy, i.e. buckled hexagonal superlattice with one adsorbed Ge atom of the Al atoms being protruded upward in the unit cell (BHS-1T). Their results give theoretical support for the formation of two-layers alloy.

After relaxation of the configurations by DFT, it is clear that only the Ge_4Al_4/Ge_2Al_7 model correctly reproduced the experimental structure factors acquired by GIXD.

Another confirmation is obtained from the comparison with STM results. Indeed, from a precise analysis of in-situ STM images (see Fig 4.5), the relationship between the coverage of the outgrowth and the surface reconstruction domains (see Fig 4.9) presents that $\theta_{\text{outgrowth}} = \alpha\theta_{\text{Ge-covered}}$ with $\alpha = (0.6\pm0.05)$ which demonstrates the formation of a surface alloy, and indicates the number of Al atoms involved in the alloy.

As concern the Ge_8/Ge_2Al_7 configuration, 11Al atoms (9 in the surface plane and 2 in the interface plane) are replace with Ge atoms, which correspond to $\alpha=11/9=1.22$. This is far from the STM observations. Another possibility is that only 2 Al atoms are replaced in the initial surface plane and that the germanene layer is located above the initial Al plane, leading to $\alpha = 2/9 = 0.22$, which does not correspond to the experiments.

For the Ge_4Al_4/Ge_2Al_7 configuration, the value of α should be equal to 0.78 (i.e. 7/9), due to 7 Al atoms (5 in the surface plane and 2 in the interface plane) in the (3×3) cell replaced by Ge atoms. This is in much better agreement with the STM experiments. The difference between these two values may result from the uncertainty in the estimation of the coverage of the reconstruction domains and outgrowths shown in STM images. Thus, the growth of Ge on Al(111) results in the formation of a two-layers surface alloy, i.e. Ge_4Al_4/Ge_2Al_7.

4.7 Summary of the results of Chapter 4

A combined experimental investigation, on the basis of GIXD and real-time STM measurements, and theoretical study, based on DFT calculations, has given new and original results concerning the structure and growth of Ge on Al(111) at the different substrate temperatures.

(i) Based on STM measurements, the growth of Ge on Al(111) results in the formation of two reconstructions, (3×3) and (√7×√7). Combining STM and GIXD measurements, the coverage of the reconstruction depends on the growth temperature, indicating the higher coverage of the (√7×√7) reconstruction at RT or lower growth temperature and the higher one of the $(3\times3)_{Al}$ superstructure at a higher temperature. The transition between the two reconstructions occurs during Ge deposition.

(ii) As shown in Fig 4.9, the linear relationship between the fraction of the outgrowth and the reconstruction domains coverage demonstrates the formation of a Ge-Al surface alloy.

(iii) Concerning the (3×3) reconstruction, I have simulated a wide range of possible configurations. Based on the experimental structure factors, the results of the simulation suggest two configurations, corresponding to Ge_4Al_4/Ge_2Al_7 and Ge_8/Ge_2Al_7 structure.

(iv) Compared to other configurations relaxed by DFT, the relaxed Ge_4Al_4/Ge_2Al_7 configuration has the lowest value of χ^2. It also displays the best agreement with STM results. Thus, the Ge_4Al_4/Ge_2Al_7 model is the best fitted configuration for the (3×3) reconstruction, which also gives evidence of the formation of the two-layer Ge-Al surface alloy on Al(111).

Chapter 5

5 Growth of germanium on Ag(111)

Contents

Similar to the growth of Ge on the Al(111) surface, the previous studies about the growth of Ge on the Ag(111) surface also lead to different viewpoints, which focus on the formation of Ge-Ag surface alloys [85][86][101][102] or layered germanene [87][103–107] after Ge deposition on Ag(111).

The present chapter is organized as follows. In the first part, I present real-time STM measurements during the growth of Ge on Ag(111) kept at a fixed temperature in a range of 380K to 430K. Then, based on the STM images acquired in situ during the growth, I give evidence of the formation of the Ge-Ag surface alloy on the Ag(111) surface during Ge deposition. In the last part, by combined GIXD measurements and the results of DFT calculations, I show that the atomic structure of the stripe phase corresponds to a Ag_2Ge surface alloy.

5.1 STM experimental detail

The Ag(111) substrate was prepared by repeated cycle of Ar^+ ion sputtering and annealing in the preparation chamber, before transfer in the STM chamber. The Ge deposition flux was about 0.1 monolayer per hour, where 1ML corresponds to the Ag(111) surface atomic density. The flux calibration was performed by assuming that the striped phase corresponds to 1/3 ML. Note that one monolayer of germanene corresponds to θ_{Ge}=1.06 ML.

5.2 Results of STM measurements

In this section, according to real-time STM measurements, I describe the evolution of the surface and the formation of the different phases. Then, I report the relationship between the Ag concentration in the surface layer and the Ge coverage, which gives evidence of the formation of a Ag-Ge surface alloy during growth.

5.2.1 Formation and evolution of the different phases

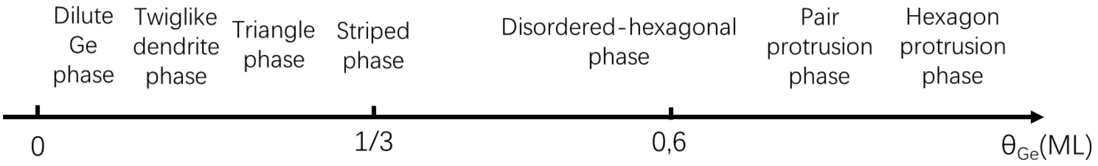

Figure 5.1 Evolution of the formation of the different phase depending on Ge coverage. The completion of the striped phase corresponds to 1/3ML as a reference.

During the submonolayer Ge deposition on Ag(111) held at a fixed temperature in a range of 380K to 430K, seven surface phases have been observed, namely the dilute Ge phase, the twiglike dendrite phase, the triangle phase, the striped phase, the disordered-hexagonal (DH) phase, the pair protrusion phase, and the hexagon protrusion phase. Fig. 5.1 displays the evolution of the formation of the different surface phases, depending on Ge coverage (i.e. evaporating time).

- **Dilute Ge phase**

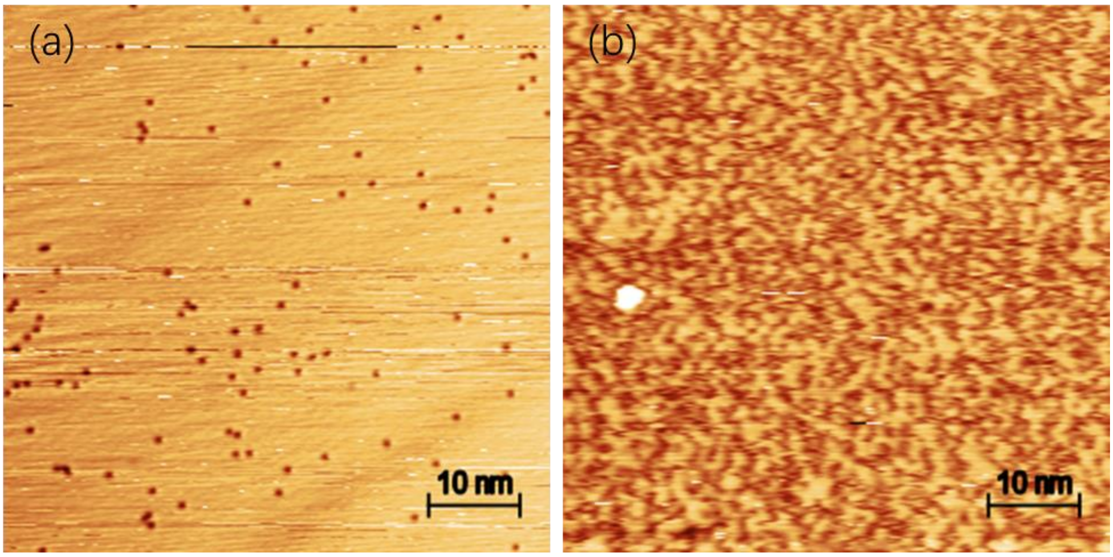

Figure 5.2 Detailed view of the dilute Ge phase (a) for θ_{Ge}=0.0025ML and (b) at saturation, i.e. just before the formation of twigs. These two STM images are acquired during Ge deposition at 380K. Tunneling conditions: (a) V_S = 1.5 V, I = 30 pA; (b) V_S = 1.4 V, I = 30 pA.

At the very beginning of Ge deposition, the STM image shown in Fig. 5.2a displays some dark spots on the surface. The previous study have reported that these isolated dark spots correspond to substitutional Ge atoms that occupy randomly the surface [102]. In the case of Si/Ag(111), similar observations have been reported after a small amount of Si deposition on Ag(111) at RT [128]. Although these Ge atoms present a darker contrast corresponding to a lower level shown in the STM image, it cannot be directly concluded that substitutional Ge atoms are located at a position lower than Ag atoms, as the tunneling current of the STM tip is associated with the electronic density of states. As deposition time increases, this dilute Ge phase becomes denser, and substitutional Ge atoms self-organize by atomic diffusion on the surface and form dark filaments, as shown in Fig. 5.2b. These Ge areas are separated by nearly pure Ag regions, with a characteristic length of 2-3nm.

- **Twiglike dendrite phase**

Fig. 5.3a and 5.3b show two consecutive STM images acquired at 5 min time interval, presenting a detailed view of the growth of the twiglike dendrite phase. When the density of the dilute Ge phase reaches saturation point (see Fig. 5.2b), further Ge evaporation leads to the formation of the twiglike dendrites phase (see Fig. 5.3a). It reveals that a first-order phase transition occurs between the dilute Ge phase and the twiglike dendrite phase. As shown in Fig. 5.3a, twiglike dendrites appear as darker domains on the surface, corresponding to a lower apparent height. In addition, they are roughly oriented along the <112> direction of Ag(111) and surrounded by the dilute Ge phase areas. From a comparison between these two consecutive STM images (see Fig. 5.3 and Fig. 5.4), dendrites grow along the <112> direction of Ag(111) and connect each other. Moreover, they form by the assembly of three-pointed hollow stars with a small Ge dilute phase domain in the center indicated by the red arrow in Fig. 5.3a. Fig. 5.3c presents an atomic resolution STM image showing a detailed view of the surface with the dilute Ge phase and twiglike dendrite phase, after deposition of a low Ge coverage at 419K. As can be seen in this figure, the appearance of three different structures is clearly visible, a honeycomb structure shown in the upper part of the image, a hexagonal structure around the honeycomb structure, and some isolated black spots.

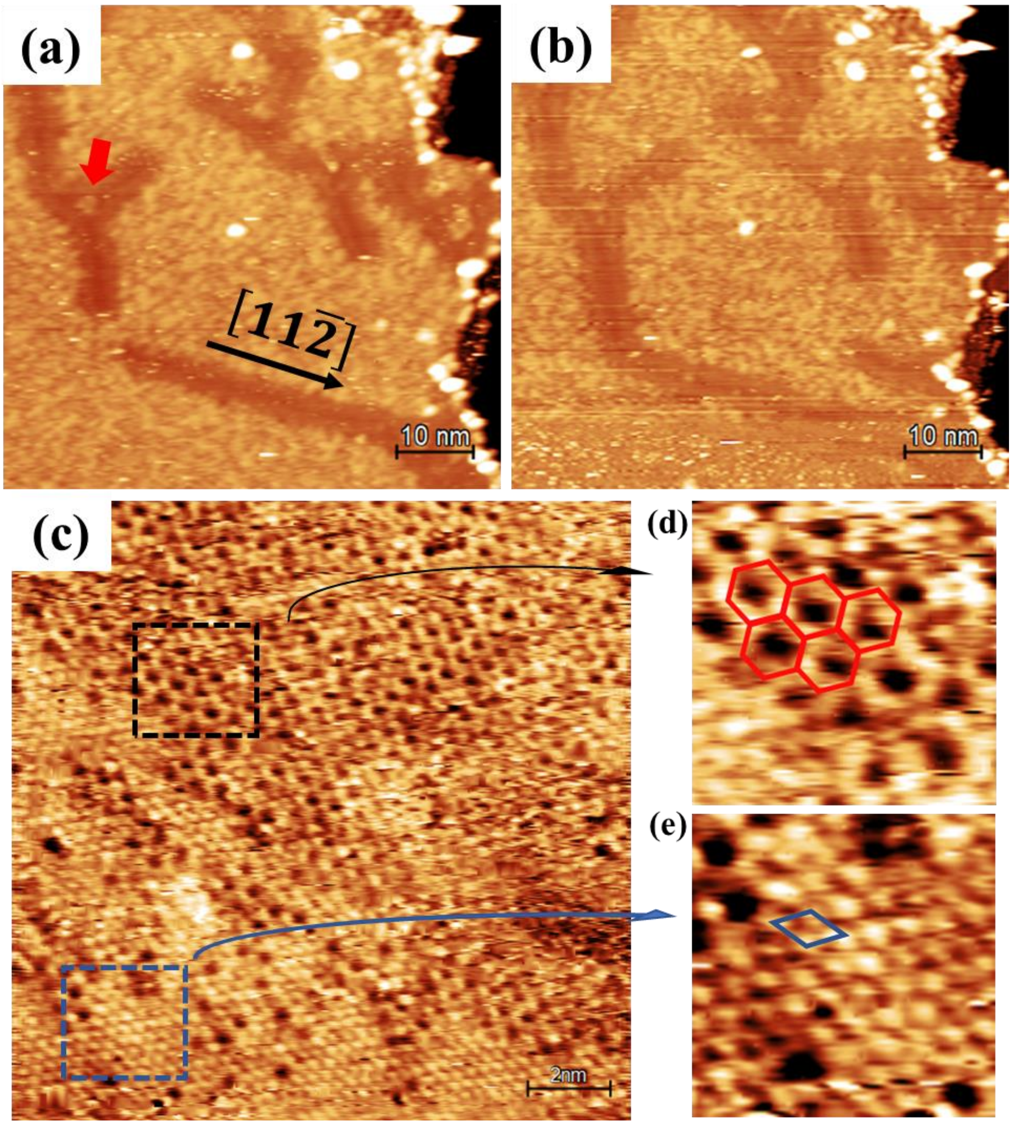

Figure 5.3 Evolution of the Ag(111) surface during Ge deposition at 380K. (a) - (b) Consecutive images (65 × 65 nm^2) acquired at 5 min time interval. The images show the formation of dark twig-like dendrites, oriented along the <112> directions. (c) Detailed view of the boundary between the diluted phase and a twig. A detailed view of the dashed (d) black and (e) red squares in image (c). Deposition temperatures are 380 K (a, b) and 420 K (c). Images (a) and (b) are acquired during deposition, image (c) is acquired at 300 K after deposition. Tunneling conditions: (a)- (b)Vs= 1.4 V, I= 30pA; (c) $V_S = -0.3$ V, I = 0.5 nA.

These spots indicate Ge atoms in substitutional positions, corresponding to the dilute Ge phase. Fig. 5.3d and 5.3e display a detailed view of the honeycomb and hexagonal structure domains indicated by black and blue dotted squares in Fig. 5.3c, respectively.

Using the bidimensional Fast Fourier transform (2D FFT), the lattice constants of honeycomb and hexagonal structure are measured to be 0.52nm ± 0.01nm and 0.29nm ± 0.01nm. These two values are in good agreement with the theoretical value of the lattice constants of the (√3×√3) (0.500nm) and Ag(111) unit cell (0.289 nm), respectively. It indicates that the honeycomb structure corresponds to the (√3×√3) reconstruction and the hexagonal structure is associated with the Ag(111)-(1×1) structure. As shown in Fig. 5.3a-b, the darker dendrites thus correspond to the (√3×√3) reconstruction domains, and the lighter areas in their vicinity to the Ag(111)-(1×1) ones.

Triangle phase

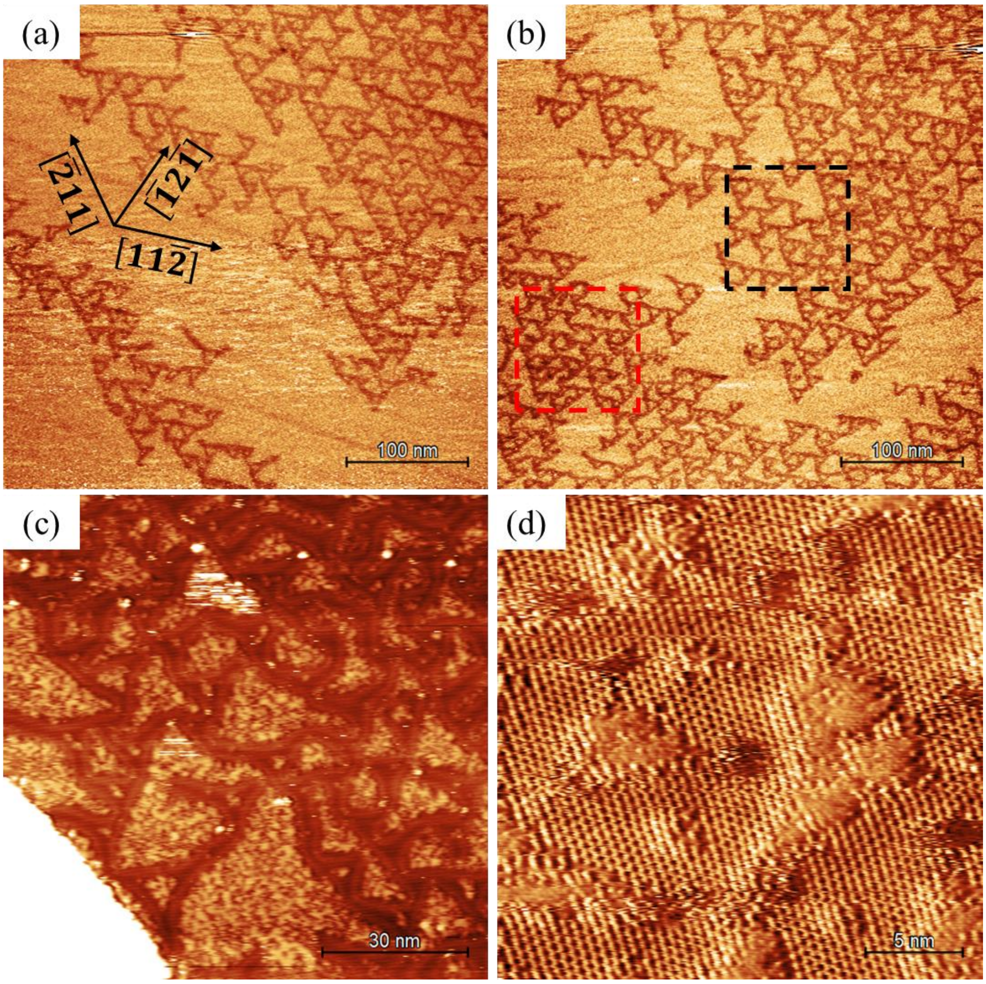

Figure 5.4 (a) - (b) Consecutive images acquired at 9 min time interval during Ge deposition on Ag(111) kept at 420K. The images present the formation of the triangle phase. Size of the images: 400 × 400 nm^2. (c)Triangular network formed on Ag(111) surface after deposition of Ge at 380K. Size of the image: 68 × 68 nm^2. (d) Detailed view of the triangle phase. Tunneling conditions: (a)-(b) V_S = 1.7V, I = 30pA ; (c) Vs= 1.4 V, I= 30 pA; (d) V_S = 0.4 V, I = 0.2 nA. (c) and (d) are acquired at 300K after Ge deposition at 400K.

Fig. 5.4a and Fig. 5.4b show two successive in-situ STM images obtained at 9 min time interval during Ge deposition on Ag(111) kept at 420K. These two images give a detailed description of the growth of the triangle phase. As Ge coverage increases, the local density of the twiglike dendrites increases, and dense twiglike dendrites connect each other forming triangular networks where the dilute Ge phase domains have a triangular sharp. This can be seen in Fig. 5.4a and 5.4b. It indicates a second-order phase transition where the twiglike dendrite phase transform into the triangle phase. As discussed previously, the growth of the dendrites is roughly oriented along the <112> direction of Ag(111). Thus, as shown in Fig. 5.4a, three sides of a triangle could be oriented along the $[11\bar{2}]$, the $[\bar{2}11]$, and the $[\bar{1}2\bar{1}]$ directions, respectively. These triangles could be regarded as equilateral ones, but their size is not uniform. Fig. 5.4c displays the formation of the triangle phase during Ge deposition at 380K. Compared to the triangle phase shown in Fig. 5.4a-b, it suggests that the higher growth temperature results in the formation of the triangle phase with a more ordered network and a more regular shape. Fig. 5.4d presents a detailed view of the triangle phase. From 2D FFT analysis, the lattice constant of the honeycomb structure is measured to be 0.50nm, corresponding to the $(\sqrt{3}\times\sqrt{3})$ reconstruction.

Fig. 5.5a and 5.5d show two detailed views of Fig. 5.4b corresponding to the position of the dashed black and red squares drawn in 5.4b, respectively. In these two figures, triangular patterns seem to form ordered reconstructions, and they are oriented in the same direction since they derive from the twiglike dendrite phase. Fig. 5.5(b, e) and Fig. 5.5(c, f) show self-correlation and FFT images corresponding to the triangle phase in Fig. 5.5a and 5.5d, respectively. The triangle phase in Fig. 5.5a appears as a quasi-hexagonal array of triangles with a lattice constant of ~21nm measured by 2D FFT. Concerning the triangle phase in Fig. 5.5d, it shows a slightly disordered hexagonal array with a lattice constant of ~11.3 nm and a rotated angle of 30° with respect to the unit cell in Fig. 5.5a. In addition, two self-correlation images indicate that these two hexagonal arrays appear together due to triangles nested within each other.

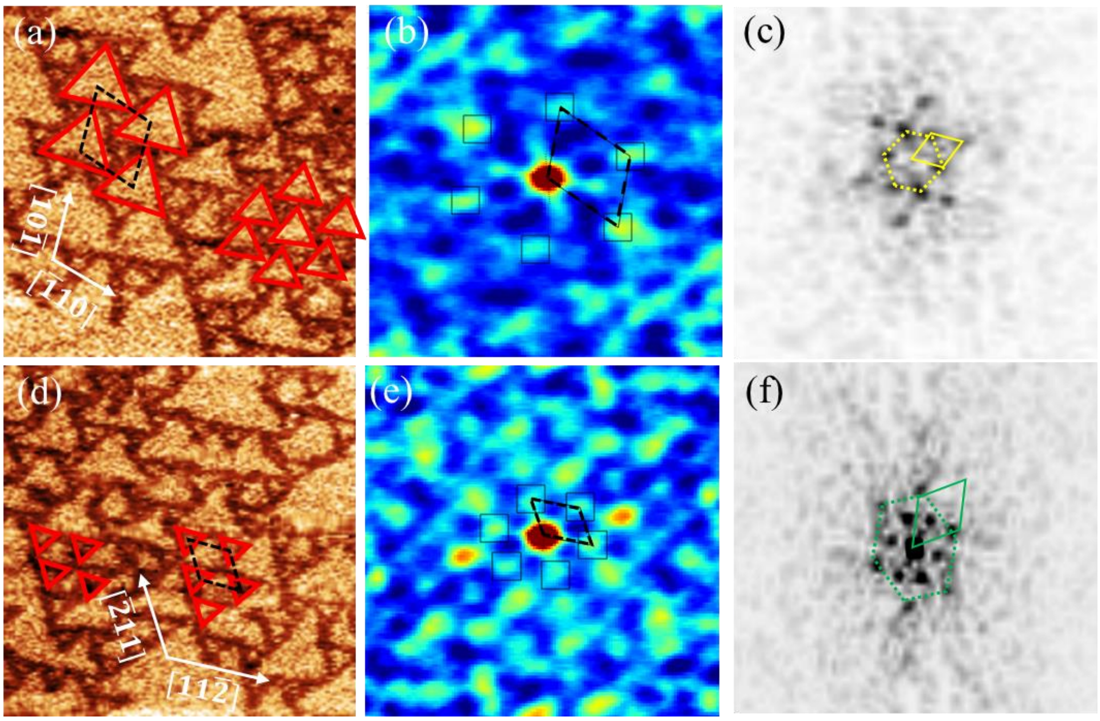

Figure 5.5 (a,d): Detailed views of Fig. 5.4b (100×100nm^2) corresponding to the position of the dashed black and red squares drawn in Fig. 5.4b. Some of the triangles formed by dendrites are indicated in red. The dotted black rhombus indicates the unit cell of the superstructure composed of triangles. The rotated angle between the unit cells in Fig. 5.5a and 5.5d is equal to 30°. (b,e): Corresponding self-correlation images. (c,f): Corresponding FFT images. The hexagonal unit cells are distorted due to the drift. Tunneling conditions: (a, d) Vs =1.7 V, I= 30 pA

As shown in 2D FFT images (Fig. 5.5c and 5.5f), the two groups of quasi-hexagonal spots are clearly visible with an angle of 30° between these two hexagons. Due to the tip drift during a scanning, these two hexagons have a slight distortion. The periodicity of the triangle phase is associated with the size of triangles and the density of triangles in a local area, the lattice constant thus depends on Ge coverage and the zone measured by 2D FFT. As Ge deposition continues, the (√3×√3) regions enlarge and the size of triangles decreases, which leads to a variation of the periodicity of the triangle phase. For different Ge coverages, the periodicity of triangle patterns has been measured in several domains. The value of the periodicity is in the range of about 10 nm to 22 nm.

- **Striped phase**

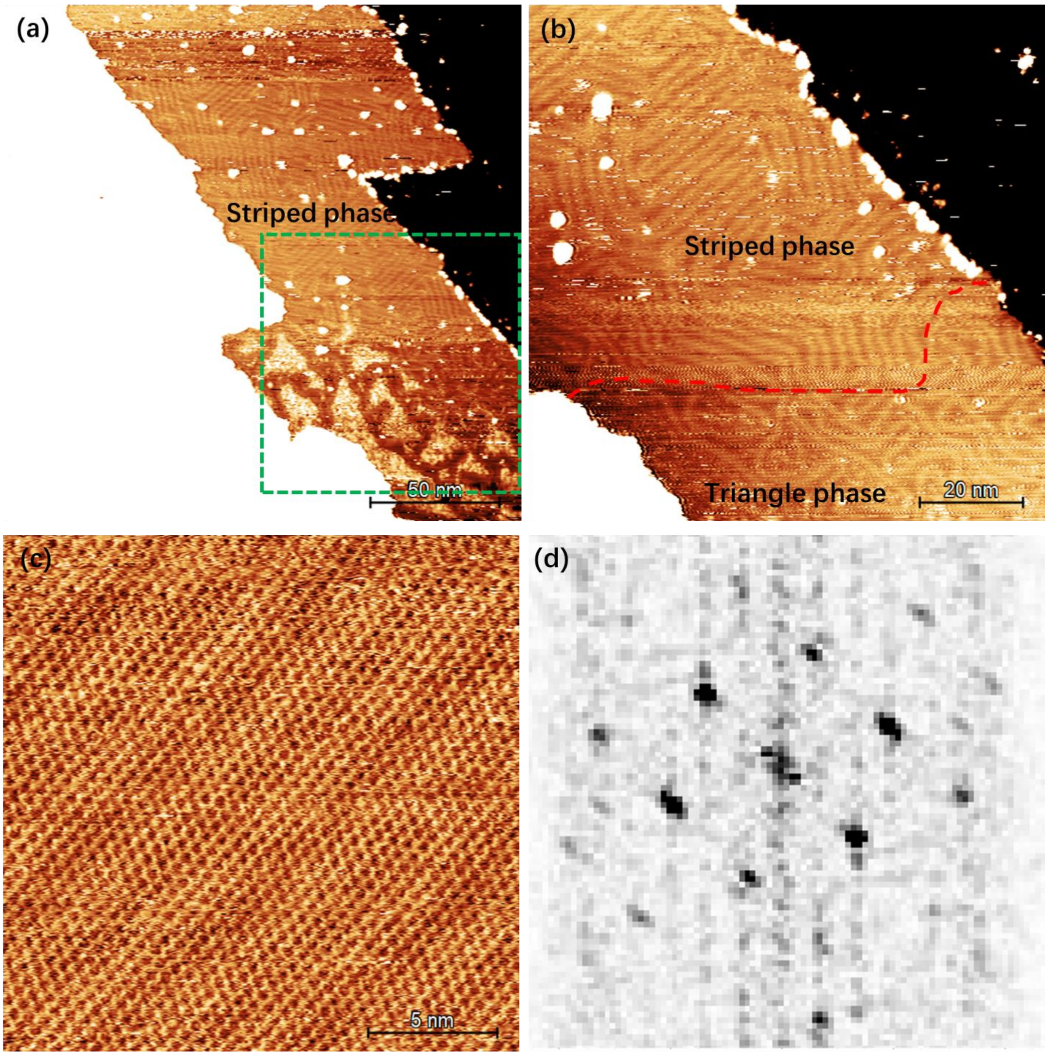

Figure 5.6 (a) STM image (200×200nm^2) of the coexistence of the triangle phase and the striped phase acquired during Ge deposition at 380 K. (b) Detailed view of (a) (100×100nm^2) corresponding to the domain indicated by the dashed green square shown in (a), acquired just after (b) The dotted red line represents the boundary between the striped phase shown in the upper part and the triangle phase in the bottom part. (c) Detailed view of the striped phase(20×20nm^2), acquired at 300 K after deposition. (d) Corresponding FFT image: Tunneling conditions: (a) Vs =1.0 V, I= 100 pA; (b) Vs =1.0 V, I= 50 pA; (c) Vs =0.3 V, I= 0.2 nA.

For $\theta_{Ge} \approx 1/3$ ML, the third transition from the triangle phase to the striped phase occurs suddenly. Fig. 5.6a shows a STM image measured during Ge deposition on Ag(111) kept at 380K (about 0.3ML Ge coverage). As shown in this figure, the striped phase domains appear in the upper-left part of this image, and the triangle phase domains appear in the bottom-right part. It indicates that the coverage is slightly higher at the top of the image than at the bottom due to the shadow effect of the tip during Ge evaporation. Fig. 5.6b shows a detailed view of Fig. 5.6a obtained 9 mins after Fig.5.6, and corresponding to the position of the dashed green square drawn in Fig. 5.6a. For the triangle phase domains, compared to the same area shown in Fig. 5.6a, the diluted phase in the center of the triangle is replaced by the twiglike dendrite phase. This image shows that the striped phase initially follows the orientation of the initial twigs, but very rapidly transforms into larger domains with a single orientation (the stripes are oriented along <112>) with 120° between the orientation for each striped phase domain. It suggests that this reorganization into large areas does not imply a large amount of material transport. Fig. 5.6c and 5.6d present a detailed view of the striped phase with the honeycomb structure and the corresponding FFT image. The results of 2D FFT indicate that the striped phase presents a local (√3×√3) periodicity.

- **Disordered-hexagonal (DH) phase**

As Ge coverage increases and exceeds 1/3ML, the disordered-hexagonal (DH) phase begins to form on the surface after the completion of the striped phase, which indicates that a fourth-order transition occurs, as shown in Fig. 5.7a. The frontier between the striped phase regions and the DH phase ones is clearly visible in Fig. 5.7a. The growth of the DH phase begins at step edges, and similar observations have been reported in ref. [87], but also inside large terraces in ours observations (i.e. black dashed circles in Fig. 5.7a). Fig. 5.7b shows a STM image acquired at RT after Ge deposition, which displays a detailed view of the boundary between these two phases. In a detailed view of the DH phase (see Fig. 5.7c), some hexagon protrusion domains have been observed. The results of 2D FFT indicate that the DH phase in Fig. 5.7c appears as a disordered hexagonal array (Fig. 5.7d-e) with a lattice constant of 0.43±0.02 nm. This value of the lattice constant is higher than the one reported in the previous study (0.391 nm) [87] and the one of free-standing germanene (0.397 nm) [16].

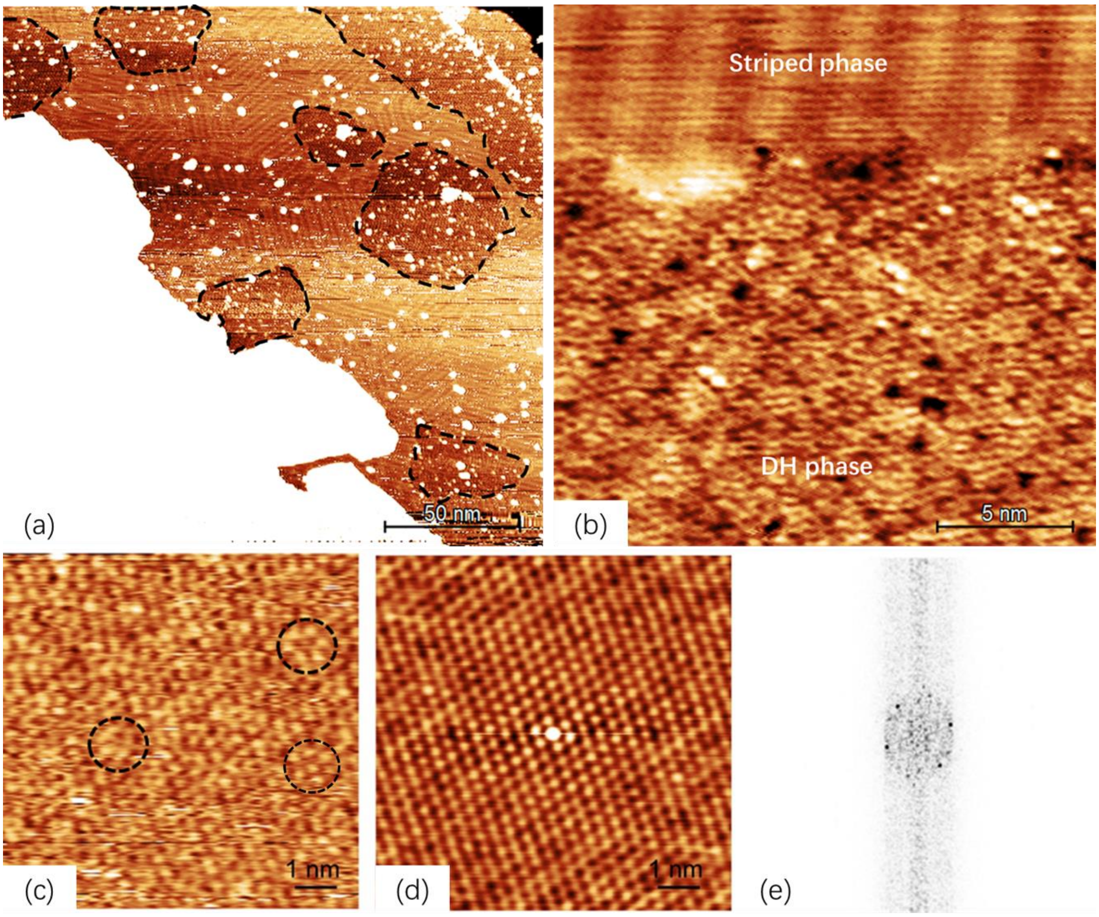

Figure 5.7 (a) STM image (200×200nm^2) of the coexistence of the striped phase and the DH phase acquired after Ge deposition at 380 K. The dotted black lines indicate the boundary between the striped phase and DH phase. (a,d): Detailed view (20×20nm^2) of the boundary between the DH phase and striped phase, acquired at 300 K after Ge deposition. (c) Detailed view of the DH phase. The quasi-hexagonal structures are indicated by the dotted black circles. (d) Corresponding self-correlation images for (c). (e) Corresponding FFT images for (c). Tunneling conditions: (a) Vs =1.4 V, I= 30 pA; (b) Vs =0.1 V, I= 2 nA (c) Vs =0.4 V, I= 0.1 nA.

- **Hexagon and pair protrusion phases**

After the completion of the formation of the DH phase, additional Ge deposition results in the formation of several new structures, as illustrate in Fig. 5.8a. In this figure, two phases appear on the surface with two types of protrusions, namely hexagon protrusion phase and pair protrusion phase. These two surface phases have already been observed in the case of the growth of Ge thin film on the Ag(111) kept at 450K [104]. In addition, these two types of protrusions also have been observed in the case of the

Ag(111) thin film on Ge(111) after annealing at the temperature of 753K [105]. Different from the Molecular beam epitaxy(MBE) method applied in ref. [104], combined hexagon and atomic pair protrusions form a $(7\sqrt{7}\times7\sqrt{7})_{Ag}R19.1°$ supercell with respect to Ag(111) (1×1) after annealing [105]. In the present case, each phase forms in separated domains.

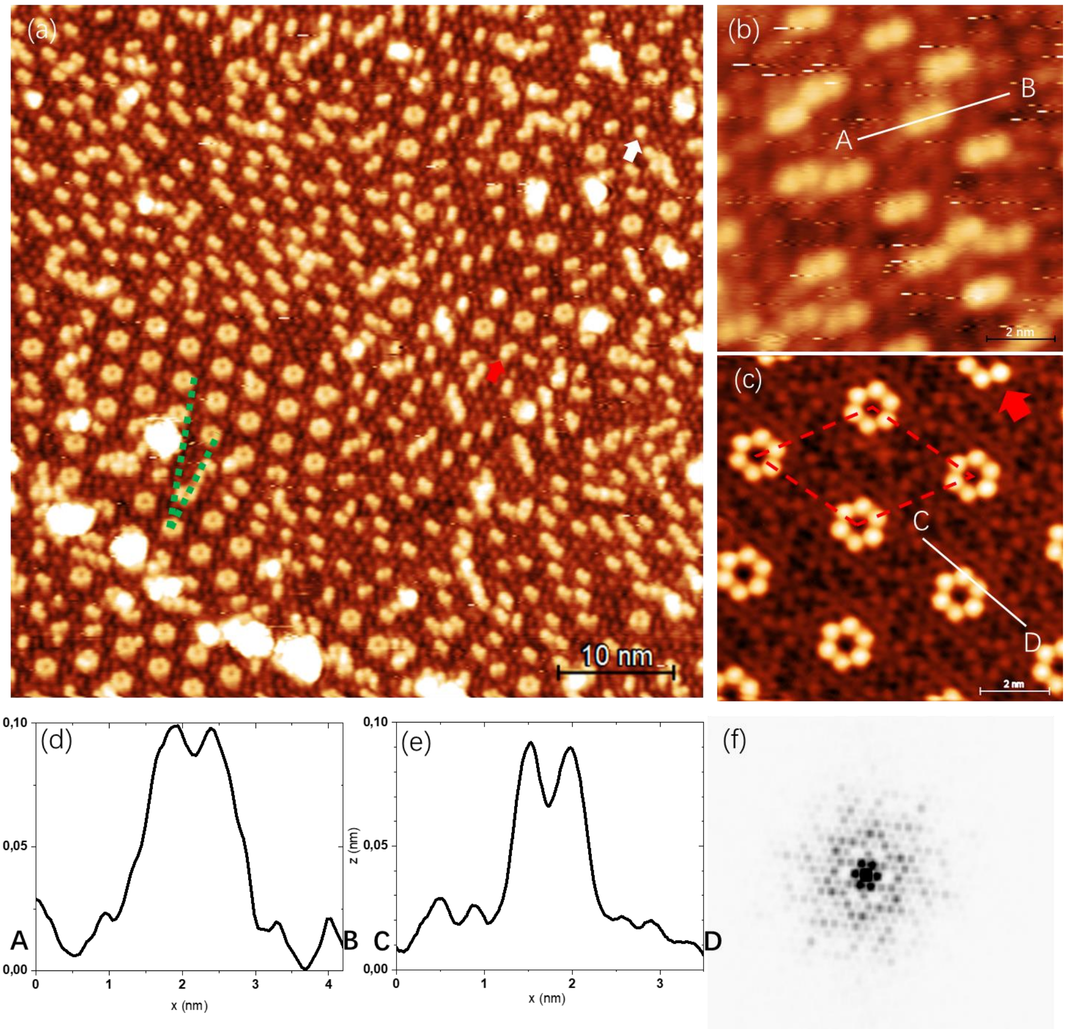

Figure 5.8 (a) STM images (60×60nm^2) acquired after the completion of the formation of the DH phase at 427 K. The hexagon protrusion phase and pair protrusion phases appear on the surface (b) Detailed view of the atomic pair protrusion phase. (Size of the image: 10×10nm2) (c) High-resolution STM image (10×10nm^2) of the hexagon protrusion phase. The red arrow indicates the half-hexagon protrusions shown in the upper-right part. (d)-(e) Line profiles along AB and CD in (b) and (c) respectively. (f) 2D FFT images measured in the hexagon protrusion phase domains. Tunneling conditions (a)-(b) Vs =1.7 V, I= 20 pA; (c) Vs =0.3 V I= 2 nA.

As shown in Fig. 5.8a, the hexagon protrusion phase appears in the bottom-left part of the image and has ordered structures, compared to the pair protrusion phase shown in the other domains. For the hexagon protrusion phase, there is a rotated angle of 11° between two hexagon-protrusion domains. A few hexagon protrusion patterns form in the pair protrusion phase domains. In addition, three-protrusion patterns and single protrusions also appear on the surface, indicated by the red and white arrows shown in Fig. 5.8a. Fig. 5.8b and 5.8c display a detailed view of these two phases, the hexagon and pair protrusions consist of six and two individual spots, respectively. Fig. 5.8d and 5.8e display the line profiles measured along the lines AB and CD drawn in Fig. 5.8b and 5.8c. The distance between two protrusions in the pair phase is estimated to be 0.46 ±0.03nm, as well as the size of the hexagon of protrusions. The bright protrusions are about 0.065±0.005nm higher than other darker spots. The 2D FFT plot of Fig. 5.8c show hexagonal patterns (see Fig. 5.8f) with a lattice parameter of 30.61 ± 0.5Å. As compared with the lattice constant of Ag(111) (i.e. 2.889Å), this lattice constant could correspond to 2.889Å×$\sqrt{109}$=30.16Å. If the hexagon protrusion phase could be associated with the $\left(\sqrt{109}\times\sqrt{109}\right)_{Ag}R\pm 5.5°$ reconstruction with respect to the unit cell of Ag(111), the matrix of its unit cell can be written as $\begin{pmatrix}12 & -5\\ 5 & 7\end{pmatrix}$ with -5.5° and $\begin{pmatrix}12 & -7\\ 7 & 5\end{pmatrix}$ with 5.5°. The angle measured in Fig. 5.8a is in good agreement with the theoretical rotated angle of this reconstruction. Thus, the rotated angle and the lattice constant measured reveal that the hexagon protrusion phase corresponds to the formation of the $\left(\sqrt{109}\times\sqrt{109}\right)_{Ag}R\pm 5.5°$ reconstruction. For the pair protrusion phase, this breaks the pseudo hexagonal symmetry of the DH phase. As shown in Fig. 5.8a and 5.8b, the pair protrusions in each domain have the same orientation, and the angle between the domain with different orientations is 60° (or 120°). Underneath the pair protrusions, the sublayer does not correspond to the hexagonal structure due to pair protrusions with the same orientation in a local domain. As indicated by the red arrow in Fig. 5.8c, the half-hexagon protrusions correspond to three-protrusion patterns shown in Fig. 5.8a. Maybe, pair protrusions could be regarded as a precursor to half-hexagon and hexagon protrusions. As continuous Ge evaporation, pair protrusions and Ge adatoms could combine, leading to the formation of half-hexagon or hexagon protrusions.

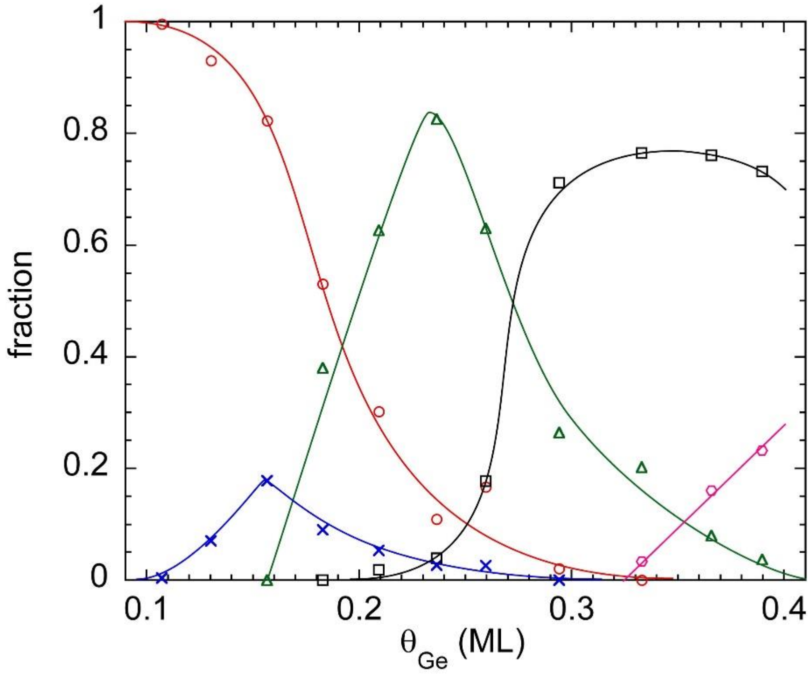

Figure 5.9 Fraction of the different phases as a function of Ge coverage during growth at 380K. Red dots: diluted phase, blue crosses: twigs, green triangles: triangles, black squares: SP, pink hexagons: DH phase. Lines are guides for the eyes. Note that although consisting in the mixing of two phases, the triangle phase is counted as a whole.

Ge deposition on Ag(111) results in the formation of seven surface phases: dilute Ge phase, twiglike dendrite phase, triangle phase, striped phase, disordered-hexagonal phase, hexagon protrusion phase, and pair protrusion phase in a sequence of the deposition time. In Fig. 5.9, the dependence of the surface fraction of each phase with Ge coverage is shown. Concerning the surface fraction of each phase, I have used the Gwyddion software to estimate the fraction of each reconstruction in each in-situ STM image measured during Ge deposition at 380K. As can be seen in Fig. 5.9, the succession of the different phases related to Ge coverage is clearly visible. The transitions between the different structures are smooth, due to the coverage gradient in each of the successive recorded STM images. The growth curve of the DH phase presents a linear relationship, as indicated by the pink line in Fig. 5.9. Thus, the Ge coverage for the completion of DH phase is estimated to be $\theta_{Ge} \approx 0.6$ML.

5.2.2 Evolution of the surface during Ge deposition

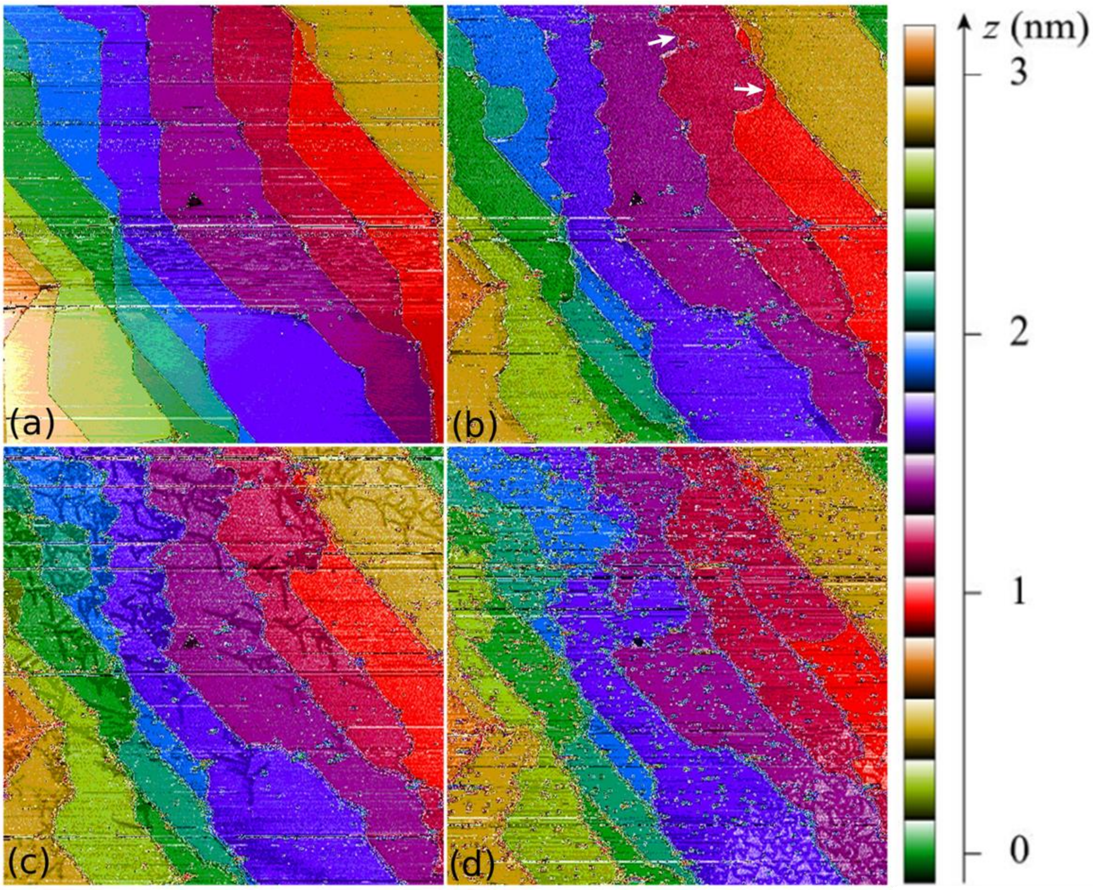

Figure 5.10 Evolution of the Ag(111) surface during Ge deposition at 380 K for (a) 0 min, (b) 100 min (θ_{Ge} = 0.08 ML), (c) 190 min (θ_{Ge} = 0.16 ML), and (d) 360 min (θ_{Ge} = 0.30 ML). In (b), the white arrows indicate the outgrowths that have grown during Ge deposition. Size of the images: 580 × 580 nm^2. Tunneling conditions V_S = 1.4 V, I = 30 pA.

In Fig. 5.10, in-situ STM images measured in real time present the surface evolution during Ge evaporation on Ag(111) kept at 380K. Fig. 5.10a shows a bare Ag(111) surface with flat and large terraces before Ge deposition. The different colors correspond to the terraces at different levels, the green terrace at the upper-right corner is lower than the light brown one in the bottom-left corner. At the center of the image, a dark triangular defect appears on the violet terrace, which can be regarded as a reference point to follow the surface evolution during evaporation. The noisy parts on the images may result from Ge atoms adsorbed onto the tip or to tip vibration during scanning. After ~0.08 ML Ge deposition on Ag(111), the step edges move outwards with respect to the terraces before evaporation (see Fig. 5.10a), forming outgrowths on the inferior terraces, as indicated by the white arrows in Fig. 5.10b. Due to the shadowing effect, outgrowths grow faster in the upper part of the image than in the bottom part(see Fig. 5.10b). After about 0.16 ML of Ge deposited on Ag(111), dark twiglike dendrites appear on the surface with a lower apparent height, as shown in Fig. 5.10c. Upon further Ge evaporation (about 0.3ML Ge coverage), outgrowths continue to extend, and the triangle phase has formed, as shown in the lower-right side of Fig. 5.10d. Besides the triangle phase domains, the rest of the areas at a lower apparent level reveals the formation of the striped phase.

The large-scale STM images in Fig. 5.10 have clearly described the surface evolution, but some details about the growth could be neglected. Concerning the formation of outgrowths, I have compared the present case with the growth of Si on Ag(111) [126] and Ag(110) [26]. As regards the growth mechanism of Si deposition on Ag(111), Ag atoms in the outermost layer are replaced by Si atoms and expelled Ag atoms condense at the step edges or form new terraces on the inferior ones. Concerning Si deposition on Ag(110) at room temperature, the formation of a Ag missing-row reconstruction leads to expelled Ag atoms forming outgrowth at step edges. For Si/Ag(111) and Si/Ag(110), the outgrowths and new terraces initially consist of a pure Ag later. Substitutional Si atoms forming the surface reconstruction are only observed upon further Si evaporation. The similarity between the case of Si/Ag and Ge/Ag(111) shows that outgrowths form at step edges and on the inferior terraces.

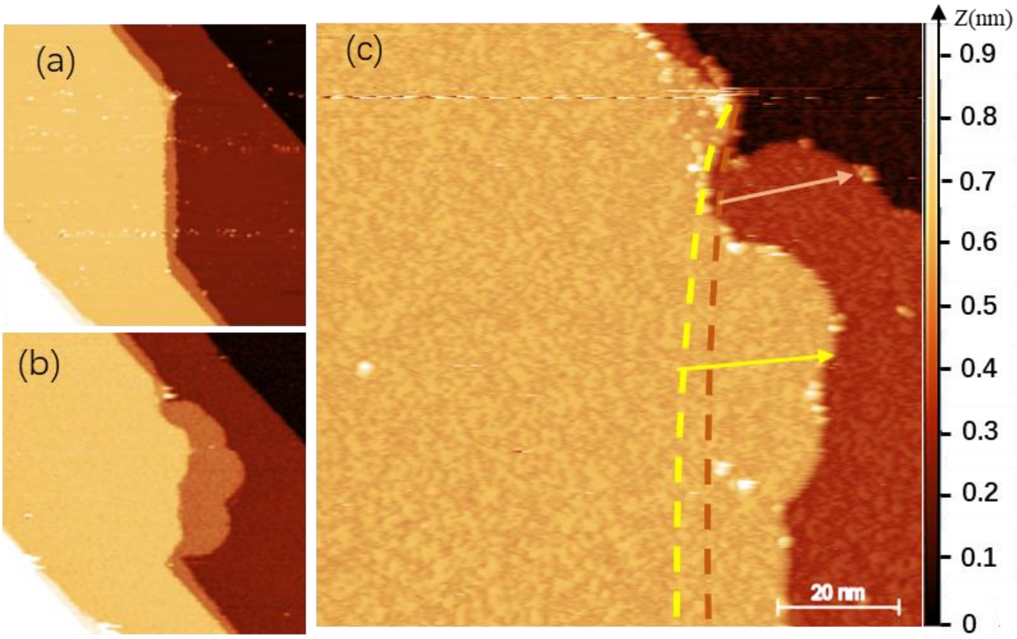

Figure 5.11 In-situ STM images (200×200nm^2) acquired during Ge deposition at 380K for (a) θ_{Ge}= 0 ML and (b) $\theta_{Ge}\approx$ 0.1ML, showing the motion of the outgrowth edge. (c) Detailed view of (b) show that the outgrowth is uniformly covered with the dilute Ge phase. The position of step edges before evaporation is indicated by the dotted lines, and the motion of the step edges are given by the arrows. Size of the image: 100×100nm^2. Tunneling conditions : (a)-(c) V_S = 1.4 V; I = 30pA.

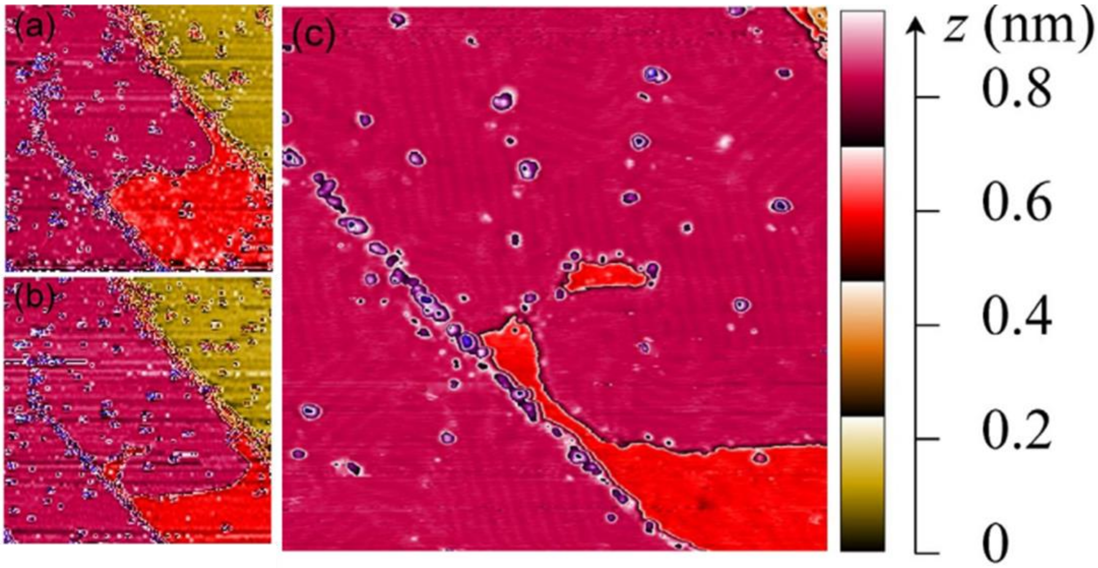

Figure 5.12 Evolution of the Ag(111) surface during Ge deposition at 380K. (a) and (b):consecutive images (170 × 170 nm2) acquired at 40 min time interval showing the motion of the outgrowth edge. The detail (c) show that the outgrowth is uniformly covered with the striped phase, as in the initial terrace. Tunneling conditions : V_S = 1.5 V; I = 30pA.

In the present case the situation is different. Fig. 5.11a a and 5.11b display two in-situ STM images, where the former image is acquired before Ge evaporation and the latter one is measured after about 0.1ML Ge deposition on Ag(111) kept at 380K. Fig. 5.11c displays a detailed view of Fig. 5.11b, the dash lines denote the step edges before the evaporation shown in Fig. 5.11a. Note that the dark areas correspond to the Ge diluted phase. As can be seen in Fig. 5.11, the Ge coverage is the same in the regions of the outgrowths and in the initial terraces, which indicates that the outgrowths are instantaneously (at the timescale of the observation) covered with Ge as soon as they form. This observation has been performed during the growth of the striped phase, as shown in Fig. 5.12.

5.2.3 Ag content in the structure

In this section, I present a relationship between the fraction of Ag atoms in the observed structures and Ge coverage. This relationship gives evidence of the formation of the Ge-Ag surface alloy.

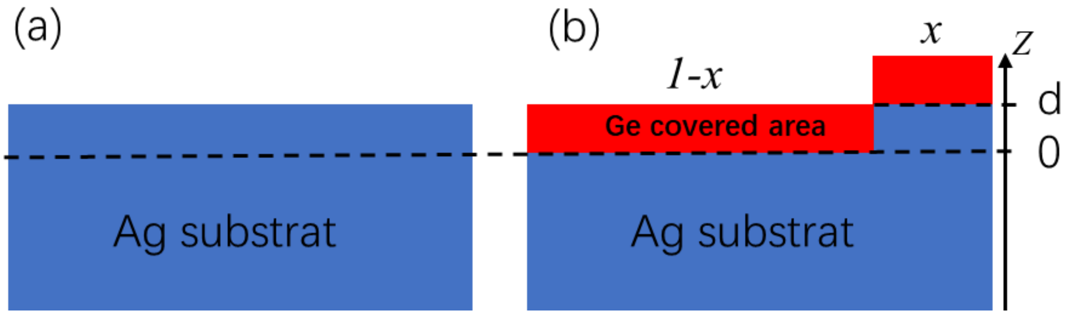

Figure 5.13 Schematic diagram of the calculation method for the fraction of Ag atoms by the outgrowth coverage before the completion of the DH phase. (a) represents the case before Ge deposition. (b) the case related to Ge-covered areas after Ge deposition.

As described in section 5.2.2, the dilute Ge phase uniformly forms on the Ag(111) surface during Ge evaporation. It implies that the fraction of Ag atoms in the observed structures relates to the coverage of the outgrowth. Fig. 5.13 gives a description of the determination of the fraction of Ag atoms in the surface layer from the outgrowth coverage. Before deposition, I consider a planar surface located at z=0 (see Fig. 5.13a). The Ag surface coverage indicates the Ag content in the surface plane and is equal to 1 for the bare surface. After deposition of a given Ge amount, expelled Ag atoms form outgrowths that occupy a fraction x of the surface (see Fig. 5.13b). The surface plane of these outgrowths, with an Ag coverage $\theta_{Ag} < 1$, is now at z=d, where d is the Ag(111) interlayer spacing. Below these outgrowths, the plane at z=0 is a pure Ag plane, whereas in the rest of the surface, the plane at z=0 has a Ag coverage (θ_{Ag}) as it is covered with the same Ag-Ge structure as the outgrowths. The conservation of Ag atoms leads to $1= (1-x)\ \theta_{Ag}+ x(1+\theta_{Ag})$. Thus, $\theta_{Ag}= 1-x$. The Ag concentration in the observed structures is the complement of the coverage of the outgrowth. As discussed in section 4.1.2, the coverage of the outgrowth can be precisely computed from Eq. (4-2) and Eq. (4-3).

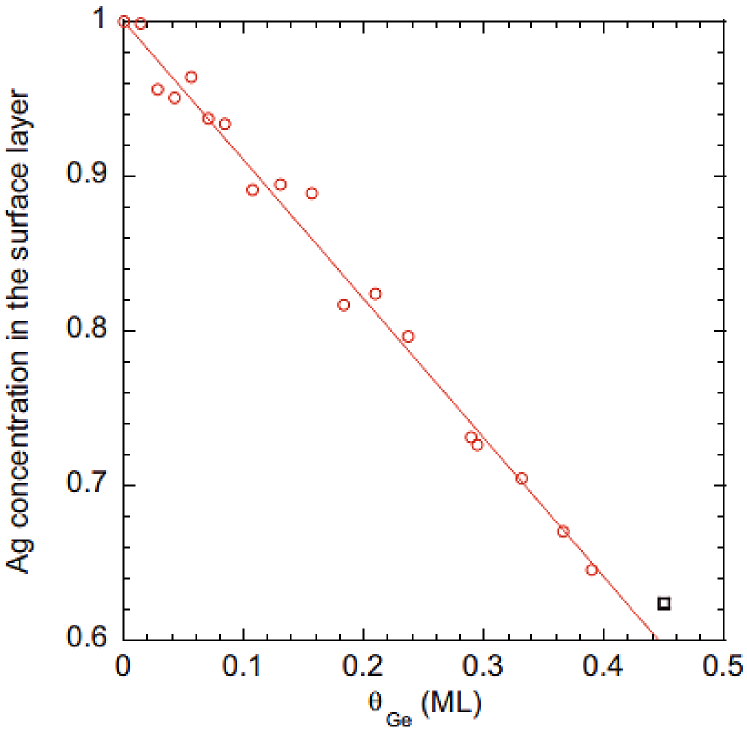

Figure 5.14 Evolution of the Ag concentration in the surface structures, as a function of Ge coverage, during deposition at 380 K. Red circles correspond to the experiment reported in Fig. 5.10. The line is a linear fit with slope −0.9. The black square corresponds to another deposit at the same temperature on an area not affected by the shadowing effect

Based on the analysis of the successive STM images obtained during Ge deposition at 380K, the relationship between Ag concentration and Ge coverage is drawn in Fig. 5.14. As shown in this figure, the dependence of Ag concentration with

Ge coverage presents a linear relationship with the slope -0.9, which indicates that 0.9± 0.1 Ag atom could be replaced by one Ge atom. Due to the formation of some Ag clusters on the surface, the value of the slope could be slightly underestimated. As it is not possible to determine whether they contain Ag or Ge, I have excluded the clusters from the measurements. On the basis of this linear relationship, 0.33 ML Ge deposition on the Ag(111) surface corresponds to an Ag concentration of $c_{Ag}=0.7 \pm 0.03$. Considering the uncertainty related to the measurement, this is in good agreement with a Ag_2Ge surface alloy for the $(\sqrt{3}\times\sqrt{3})$ structure obtained for 1/3 ML. From Fig. 5.14, the Ge coverage for the completion of the DH phase should correspond to approximately twice that for the $(\sqrt{3}\times\sqrt{3})$ structure, i.e., 0.6±0.1 ML. This value is much smaller than the expected coverage of 1.06 ML for monolayer germanene, and demonstrates that the DH structure corresponds to a Ag-Ge surface alloy. The DH structure must contain a significant amount of Ag atoms, i.e., 0.46±0.09 ML related to the completion of this phase for $\theta_{Ge}\approx 0.6\pm0.1$ ML (i.e. 0.46=1-0.9×0.6). In this case, the DH structure is compatible with Ag_3Ge_4. Considering the large error bars related to the measurements (i.e. ~0.1ML), the DH structure also has two possibilities, compatible with AgGe surface alloys for $\theta_{Ge} = 0.5$ ML or $AgGe_2$ surface alloys for $\theta_{Ge} = 0.67$ ML. It reveals that, in both cases, the DH structures are surface alloys with different Ge concentrations. From this analysis of the dependence of the Ag concentration with the Ge coverage, it can be concluded that Ge deposition around 400K on Ag(111) results in the formation of the Ge-Ag surface alloys instead of layered germanene.

5.3 GIXD measurement

In this section, I present the evolution of the surface phase during Ge deposition on Ag(111), from real-time GIXD measurements. In addition, I also present the outcomes of a combined experimental and theoretical study, based on GIXD measurements and DFT calculations, aimed to determine the exact atomic structure of the striped phase.

5.3.1 Experimental detail

Similar to the Ge/Al(111) experiment, the GIXD measurements for Ge/Ag(111) were performed at SIXS beamline of SOLEIL synchrotron. Sample cleaning was achieved by repeated cycles of Ar^+ sputtering and annealing. Ge was deposited on the Ag(111) surface kept at about 420K. The Ge flux is ~ 0.47ML/h as demonstrated later, where 1ML corresponds to the Ag(111) surface atom density. As described in section 5.1, the (√3×√3) structure and the $\left(\sqrt{109}\times\sqrt{109}\right)_{Ag}R\pm 5.5°$ reconstruction have been observed in STM measurements. The (√3×√3) structure basis is $a_{\sqrt{3}}= b_{\sqrt{3}}$=0.50nm, $c_{\sqrt{3}}$=0.7075 nm, and α=β=90° γ=120° and the corresponding matrix of the unit cell can be written as $\begin{pmatrix} 1 & 1 \\ -1 & 2 \end{pmatrix}$. Concerning the $\left(\sqrt{109}\times\sqrt{109}\right)_{Ag}R\pm 5.5°$ reconstruction, the lattice constant corresponds to $a_{\sqrt{109}}= b_{\sqrt{109}}$= 3.016nm, $c_{\sqrt{109}}$=0.7075 nm, and α=β=90° γ=120°. In diffraction maps measured by GIXD, the positions of the diffracted signals are described by the (h, k, l) indices (Miller indexes) referring to the Ag(111) surface basis with $a_0 = b_0$ = 2.889Å, c_0 =7.075 Å, and $\alpha_0 = \beta_0$ =90°, γ_0 = 120°. The (H, K, L) indices correspond to the $c\left(31\times\sqrt{3}\right)$ reconstruction basis (a=8.954nm, b=0.50 nm, c=0.7075 nm, α = β = γ = 90°) that will be shown to correspond to the striped phase.

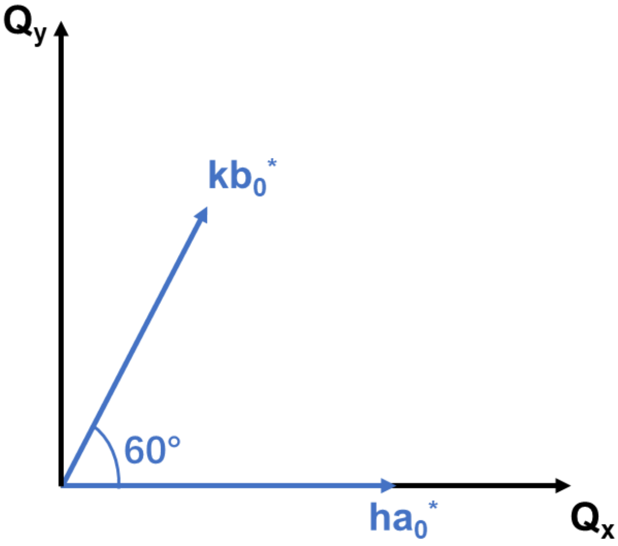

Figure 5.15 The two coordinate systems in the reciprocal space. The black one represents the $Q_xQ_yQ_z$ coordinates. The blue one denotes a coordinate system related to the (hkl) indices.

Besides the Miller indexes, I have also used the $Q_xQ_yQ_z$ coordinates (coordinates of the momentum transfer) to define the positions of a diffracted spot in the reciprocal space. In the present case, the reciprocal lattice of the unit cell of Ag(111) is a hexagonal lattice with lattice constants $|\mathbf{a_0}^*|=|\mathbf{b_0}^*|=4\pi/(\sqrt{3}|\mathbf{a_0}|)$ and $|\mathbf{c_0}^*|=2\pi/|\mathbf{c_0}|$. The corresponding angle between $\mathbf{a_0}^*$ and $\mathbf{b_0}^*$ is equal to 60°. Fig. 5.15 display the two coordinates of the reciprocal space and their relationship. In the reciprocal space, the momentum transfer can be written as $\mathbf{q}= h\mathbf{a_0}^*+k\mathbf{b_0}^*+ l\mathbf{c_0}^*$. Thus, the projection of this vector in the (Q_x, Q_y, Q_z) coordinate is given by

$$Q_x = \frac{4\pi}{\sqrt{3}a_0}\left(h + \frac{k}{2}\right) \tag{5-1}$$

$$Q_y = \frac{4\pi}{\sqrt{3}a_0}\left(\frac{\sqrt{3}k}{2}\right) \tag{5-2}$$

$$Q_z = \frac{2\pi}{c_0} l \tag{5-3}$$

Where $a_0 = a_{Ag}/\sqrt{2}$ and $c_0 = \sqrt{3}\ a_{Ag}$ indicate the lattice constant of the Ag(111) surface. The advantage of the (Q_x, Q_y, Q_z) coordinate is in the calculation of the spacing between diffraction spots (Δq) and the corresponding periodicity. The lattice constant of the $c(31 \times \sqrt{3})$ reconstruction is $a_{c(31\times\sqrt{3})} = 31a_0 = 89.6$Å, $b_{c(31\times\sqrt{3})} = \sqrt{3}a_0 = 5.0$ Å, and $c_{c(31\times\sqrt{3})} = c_0 = 7.075$ Å with $\alpha = \beta = \gamma = 90°$. The lattice parameters of the hexagonal $(\sqrt{109} \times \sqrt{109})_{Ag}R5.5°$ superstructure are $a_{\sqrt{109}} = b_{\sqrt{109}} = \sqrt{109}a_0 = 30.16$ Å and $c_{\sqrt{109}} = c_0 = 7.075$ Å.

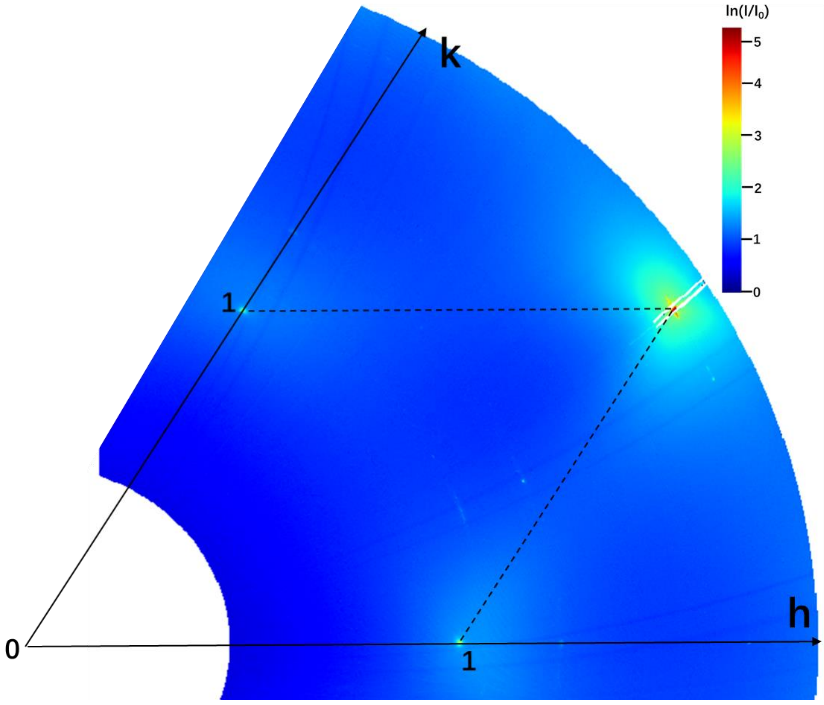

Figure 5.16 In-plane diffraction map (l=0.12) of the reciprocal space obtained by GIXD measurements before Ge evaporation.

5.3.2 Appearance of the surface phases in GIXD measurements

The STM measurements presented in section 5.2 indicate that submonolayer Ge deposition on Ag(111) results in the formation of seven surface phases depending on Ge coverage (see Fig. 5.1). In this section, I report the various GIXD maps of the diffracted intensity for in-plane condition (l=0.12) for the different coverages of Ge evaporated at about 420K. Fig. 5.16 displays the in-plane diffraction map of the reciprocal space obtained by GIXD measurements before Ge deposition. As can be seen in Fig. 5.16, the diffraction spots are associated with the Ag(111) crystal, i.e. (1, 0, 0.12), (0, 1, 0.12), and (1, 1, 0.12). This map could be regarded as a reference for GIXD diffraction maps obtained after Ge evaporation.

- **Striped phase**

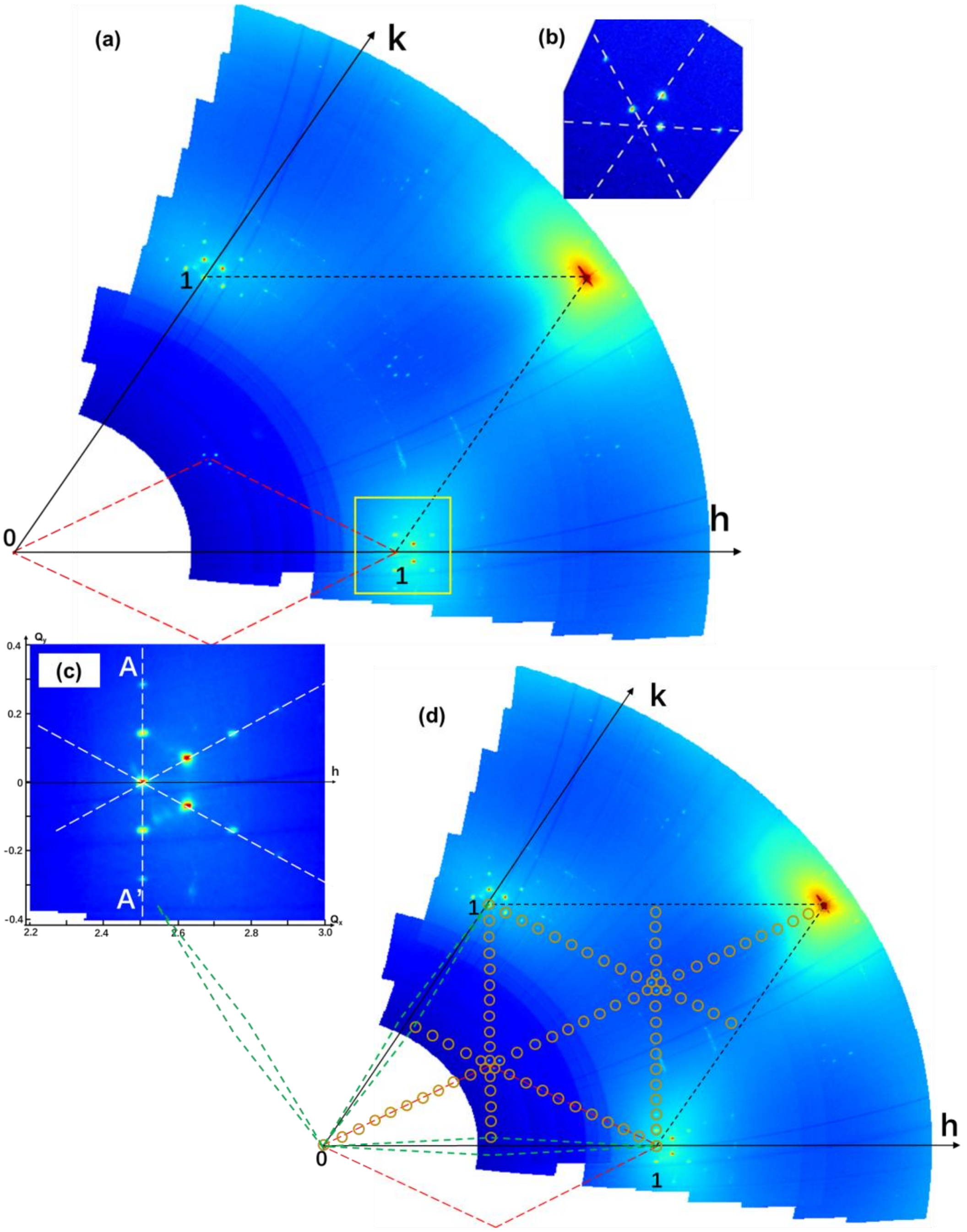

Figure 5.17 Diffracted intensity for in-plane conditions (l=0.12) after evaporation of $\theta_{Ge} \approx 1/3$ ML. (a) large view of the reciprocal space. The black dashed parallelogram corresponds to the Ag(111) surface unit cell. The red dotted parallelogram corresponds to a (√3×√3)R30° supercell. (b) A detailed view around (h=1/3,k=1/3) condition. (c) detailed view around (h=1,k=0) condition, as indicated by the yellow square shown in (a). The white dotted lines correspond to the directions of spot alignments. (d) Schematic representation of the diffraction spots and rods for the c(31×√3) reconstruction. The green dotted parallelogram corresponds to a c(31×√3) supercell. Brown circles indicate the (h, k, 0.12) positions associated with the c(31×√3) reconstruction in the reciprocal space.

In Fig. 5.17a, I report the GIXD map of the diffracted intensity for in-plane conditions, acquired after 44 minutes of Ge evaporation (i.e. about 1/3ML Ge). This diffraction map is associated with the striped phase. As shown in this map, the black dashed parallelogram corresponds to the Ag(111) surface unit cell, while the red one corresponds to the (√3×√3) superstructure. The presence of satellite spots is clearly visible around diffraction spots corresponding to the crystal truncation rods (CTR) of the substrate (integer values of h and k indices). Other sets of satellite spots are also shown around fractional values of (h, k) corresponding to the diffraction conditions of a (√3×√3) reconstruction, i.e. (h, k) = (1/3, 1/3), (2/3, 2/3), etc. A detailed view of the in-plane diffraction intensity around (1/3, 1/3, 0.12) and (1, 0, 0.12) is shown Fig. 5.17b and 5.17c, respectively. These satellite spots are aligned along three directions, indicated by white dotted lines in Fig. 5.17b and 5.17c. These <110> directions are equivalent due to the p3m1 symmetry of the substrate surface. The angle between each alignment is 60°, corresponding to three possible orientations for the striped phase domains. This observation have been performed in STM measurements as shown in Fig. 5.6b.

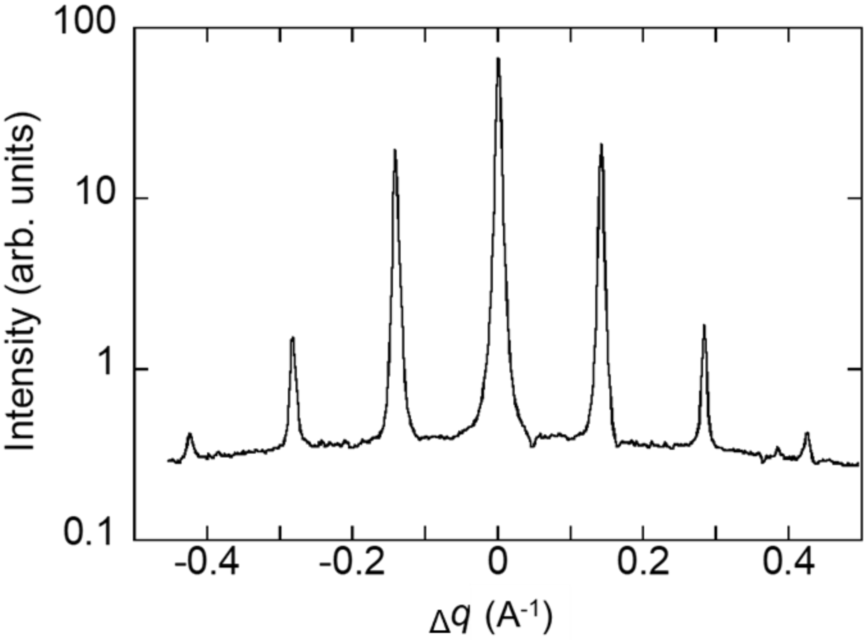

Figure 5.18 Variation of the diffracted intensity for in-plane conditions around the (h=1,k=0) position, along the AA’ direction.

A profile along the A-A’ line shown in Fig. 5.17c is drawn in Fig. 5.18. The central spot (Δq= $0A^{-1}$) corresponds to a CTR of Ag(111) crystal, namely (1, 0, 0.12) shown in Fig. 5.17c, and the other three spots from each side indicate the satellite spots with a lower intensity. The spacing between the spots is measured to be Δq= 0.1412 ± $0.0002Å^{-1}$. The direction along the A-A’ line is perpendicular to the Q_x axis or the [100] direction (i.e. h axis). It indicates that the structure observed has a rectangular unit cell. Thus, this periodicity is equal to be 44.5Å corresponding to $15.4a_0$. As expected from previous works [86], the measured phase appears as a periodic modulation of a (√3×√3) reconstruction, along the {110} directions. As shown in Fig. 5.17d, the reciprocal lattice of the striped phase is drawn by the green dotted parallelograms rotated 60° with respect to each other. Thus, the structure of the striped phase possesses a rectangular centered unit cell. As 15.4 is close to 31/2, the structure measured can be described as a $c(31\times\sqrt{3})$ reconstruction. In the reciprocal space, the positions computed from the $c(31\times\sqrt{3})$ reconstruction basis, indicated by yellow circles shown in Fig5.17d, are in good agreement with the positions of the diffraction spots measured by GIXD(see Fig. 5.17d). The value of $15.4a_0$ is in good agreement with the periodicity of the striped pattern previously observed in STM images [87]. Thus, the diffraction pattern measured by GIXD corresponds to the striped phase with a $c(31\times\sqrt{3})$ reconstruction.

The diffracted intensity and the shape of the spots in Fig. 5.17b and 5.17c are associated with the shape of the X-ray beam diffracted from the sample surface, in the real space, and with the intrinsic width of the diffraction pattern, in the reciprocal space. Regarding the satellite spots around CTRs, the intrinsic width is mainly given by the finite size of the striped pattern domains and by the fluctuation of the striped phase periodicity. In other words, larger and ordered striped phase domains, with the small fluctuation of the periodicity, correspond to a higher intensity and a smaller width of the diffracted spots. Concerning the intrinsic width, the first contribution is the same for all spots whereas the second one increases linearly with the satellite order *n*. The width of the satellite spots is measured to Δq= $1.2\times10^{-3} + 6\times10^{-4}n$ $Å^{-1}$. It reveals that the periodicity is very well defined without large fluctuations, and the size of the domains is of the order of 500 nm.

- **DH phase**

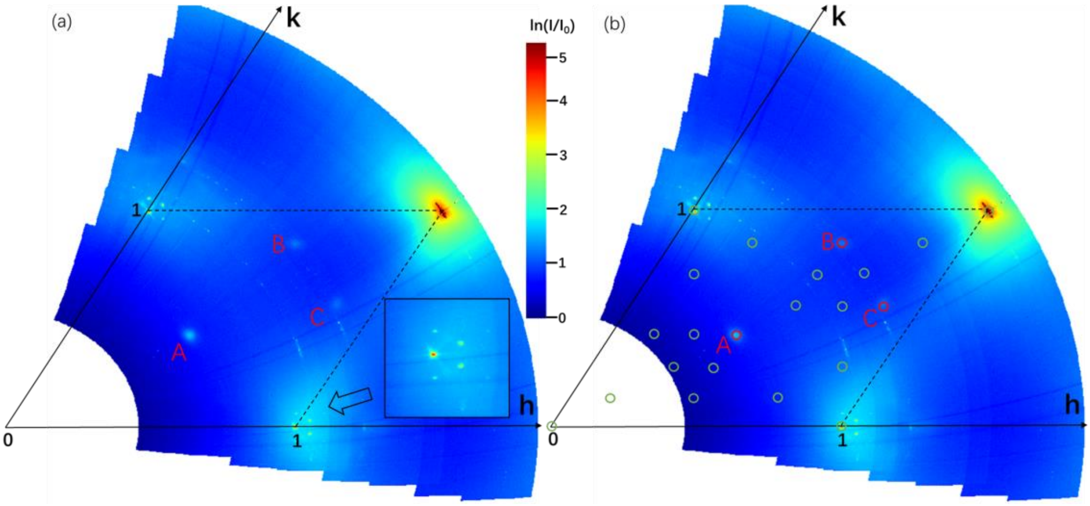

Figure 5.19 (a) Diffracted intensity for in-plane conditions (l=0.12) after evaporation of θ_{Ge} ≈ 0.656 ML. Three spots A, B, and C are associated with the DH phase. Inset: A detailed view near the (1, 0, 0.12) spot. (b) Schematic representation of the diffraction spots and rods for the c(7×√3) reconstruction. Green and red circles indicate the (h, k) positions of the superstructure rods of the c(7×√3), and three red circles also represent the position of A, B, and C.

Fig. 5.19 shows the in-plane diffraction map measured after ~ 81 min of Ge deposition related to a coverage of about 0.65ML. The results of STM measurements reveal that the deposition of 0.65ML Ge on Ag(111) at 420K leads to the formation of the DH phase and the coexistence of the striped phase and DH phase. The diffraction spots around (1, 0, 0.12) and (0, 1, 0.12) are associated with the striped phase (see the inset in Fig. 5.19a). As the transition from the striped phase to the DH phase occurs, the only first order of diffraction is visible for the satellite spots (see Fig. 5.19). Compared to Fig. 5.17, three additional spots (A, B and C) appear at (3/7, 3/7, 0.12), (4/7, 6/7, 0.12) and (6/7, 4/7, 0.12) and are related to the DH phase. From an analysis of the positions of these diffraction signals, the DH phase may correspond to a (7×7) or a c(7×√3) reconstruction. For a (7×7) reconstruction ($a_7 = b_7 = 7a_0$ =20.22 Å and $c_7 = c_0$ =7.075 Å), the reciprocal lattice vectors can be written as: $\mathbf{a}_{7\times7}^* = \mathbf{a}_0^*/7$, $\mathbf{b}_{7\times7}^* = \mathbf{b}_0^*/7$,

$\mathbf{c_{7\times7}^{*}= c_0^{*}}$. These three spots may be associated with a (7×7) reconstruction. Similarly, Fig. 5.19b indicates that these three spots may come from the c(7×√3) reconstruction ($a_{c(7\times\sqrt{3})}= 7a_0$ = 20.22 Å, $b_{c(7\times\sqrt{3})}= \sqrt{3}a_0$ =5.0 Å, and $c_{c(7\times\sqrt{3})} = c_0$=7.075 Å). The c(7×√3) structure is the smallest mesh compatible with the diffraction spots, but the (7×7) structure is compatible with the hexagonal symmetry apparently observed in STM. Compared to the diffracted signals from the striped phase, the spots (A, B, and C) have a larger size(Δq=0.06Å^{-1}) and a lower intensity. It indicates that the DH phase presents a local ordered structure with a small domain size corresponding to the STM observations in Fig. 5.7. As only a small number of spots give rise to measurable intensity, it is not possible to determine, from X-ray diffraction, the atomic structure of the DH phase.

- **(√109×√109) structure**

Fig. 5.20a displays the GIXD map of the diffracted intensity for in-plane conditions (l=0.12), obtained after ~ 118 min of Ge deposition (about 1 ML Ge). Based on STM observations, additional Ge deposition leads to the formation of the hexagon and pair protrusion phases. Thus, the diffraction map may be associated with these two phases. Fig. 5.20b presents a detailed view of Fig. 5.20a corresponding to the position of the dotted black square drawn in Fig. 5.20a, around (h= 1, k= 0, l= 0.12) condition. In Fig. 5.20b, two hexagonal patterns with a rotated angle are clearly visible, and their reciprocal lattice vectors have been drawn (i.e. the red and black arrows). The length of these two sets of vectors is the same and equal to be Δq=0.24 ± 0.002 Å^{-1}, and the rotation angle is 11°. The corresponding periodicity in the real space is calculated as 30.23 ± 0.2 Å, close to √109 × 2.889 Å =30.16 Å. It indicates that these two hexagonal patterns come from the $\left(\sqrt{109}\times\sqrt{109}\right)_{Ag}R\pm 5.5°$ reconstruction, namely the hexagon protrusion phase observed in STM images.

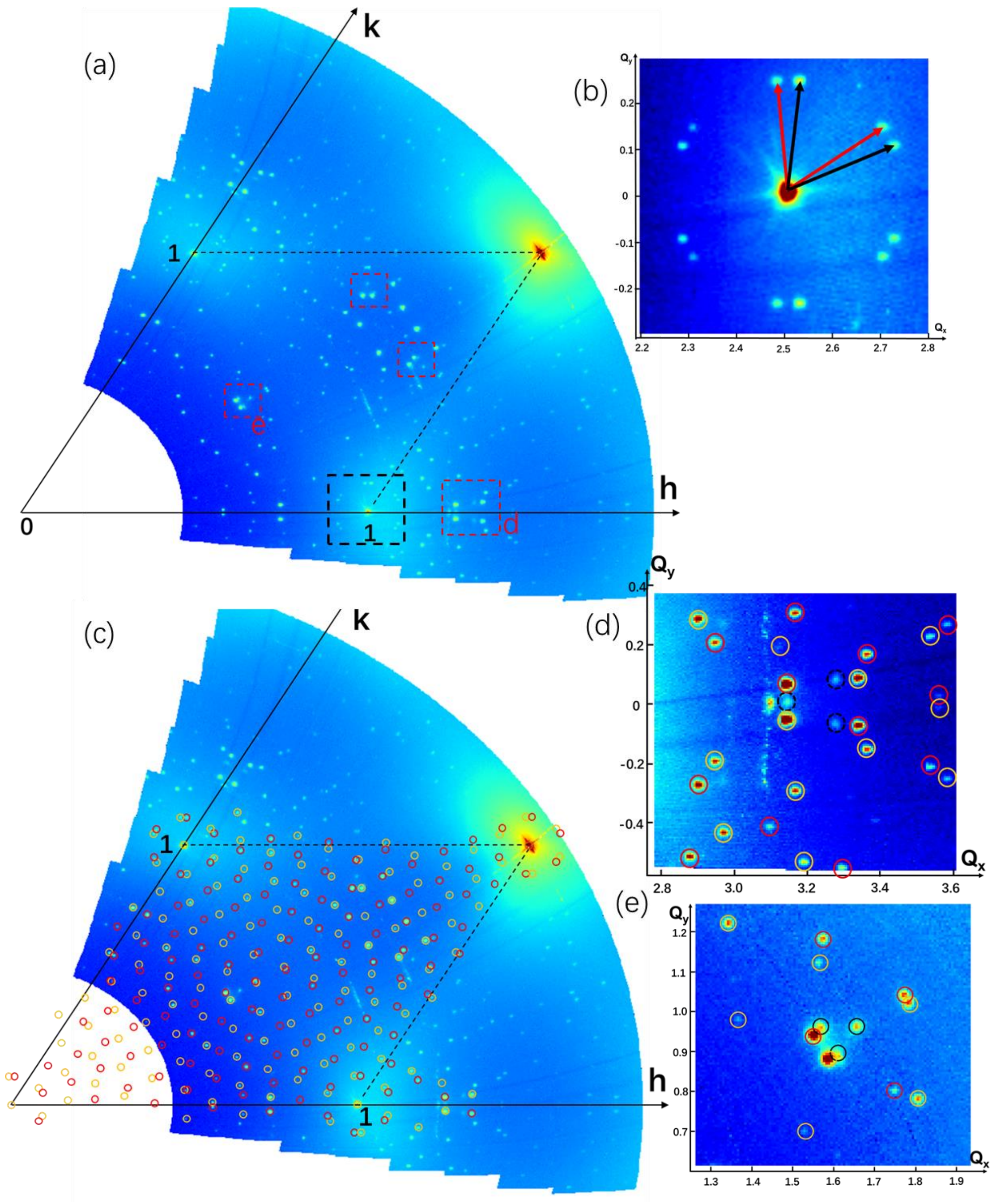

Figure 5.20 Diffracted intensity for in-plane conditions (l=0.12) after evaporation of $\theta_{Ge}\approx 1$ ML. (a) large view of the reciprocal space. The black dashed parallelogram corresponds to the Ag(111) surface unit cell. (b) A detailed view around (h=1,k=0) condition, as indicated by the dotted black square shown in (a). (c) Schematic representation of the diffraction spots and rods for the $\left(\sqrt{109}\times\sqrt{109}\right)_{Ag}R\pm 5.5°$ reconstruction. Red and yellow circles indicate the (h, k, 0.12) positions associated with the $\left(\sqrt{109}\times\sqrt{109}\right)_{Ag}R\pm 5.5°$ reconstruction in the reciprocal space. (d)-(e) detailed view around (h=9/7,k=0) and (h=3/7,k=3/7) condition, as indicated by the dashed red square shown in (a). The black (dashed) circles indicate the diffraction spots uncorrelated with the $\left(\sqrt{109}\times\sqrt{109}\right)_{Ag}R\pm 5.5°$ reconstruction and minor intensity.

Fig. 5.20c displays a comparison between the experimental diffracted signals, measured by GIXD, and the theoretical diffraction spots (i.e. red and yellow circles) computed from the $\left(\sqrt{109}\times\sqrt{109}\right)_{Ag}R\pm5.5°$ reconstruction. It reveals that the positions of the diffracted signals is in good agreement with the theoretical ones. Thus, the diffraction pattern measured by GIXD is associated with the hexagon protrusion phase with a $\left(\sqrt{109}\times\sqrt{109}\right)_{Ag}R\pm5.5°$ reconstruction.

However, a few diffraction spots of small intensity do not correspond to the (√109×√109) structure, as shown in the zones indicated by the dashed red and black squares drawn in Fig. 5.20a. Fig. 5.20d and 5.20e display detailed views of the diffracted intensity around (9/7, 0, 0.12) and (3/7, 3/7, 0.12). As shown in Fig. 5.20d, the spots in the red and yellow circles are related to the (√109×√109) structure whereas the three spots indicated by the black circles are uncorrelated with this structure. Their position is (3.16, 0, 0.11), (3.28, 0.076, 0.11), and (3.28, -0.076, 0.11) in $Q_xQ_yQ_z$ coordinates, corresponding to (1.258, 0, 0.12), (1.289, 0.035, 0.12), and (1.324, 0.035, 0.12) in hkl coordinates. In Fig. 5.20e, the position of the three spots (black circles) is (0.44, 0.41, 0.12), (0.44, 0.44, 0.12), and (0.41, 0.44, 0.12) in hkl coordinates. A precise analysis of the diffraction diagram indicates that these diffracted signals could be associated with an incommensurable structure with the unit cell $\begin{pmatrix} 0.758 & 0.762 \\ -0.758 & 1.511 \end{pmatrix}$. The center of these three spots in Fig. 5.20d and 5.20e is at (0.427, 0.432, 0.12) and (1.291, 0, 0.12), close to (3/7, 3/7, 0.12) and (9/7, 0, 0.12). In addition, the other spots associated with this incommensurable structure are also observed around (4/7, 6/7, 0.12) and (6/7, 4/7, 0.12) conditions (i.e. the dashed red squares), as illustrated in Fig. 5.20a. Moreover, these spots appear very close to the position of the A, B, and C spot shown in Fig. 5.19a. It could correspond to the first structural variation of the DH phase when the Ge coverage increases: the formation of the pair-adatom phase and breakage of the hexagonal symmetry.

5.3.3 Real-time GIXD measurement

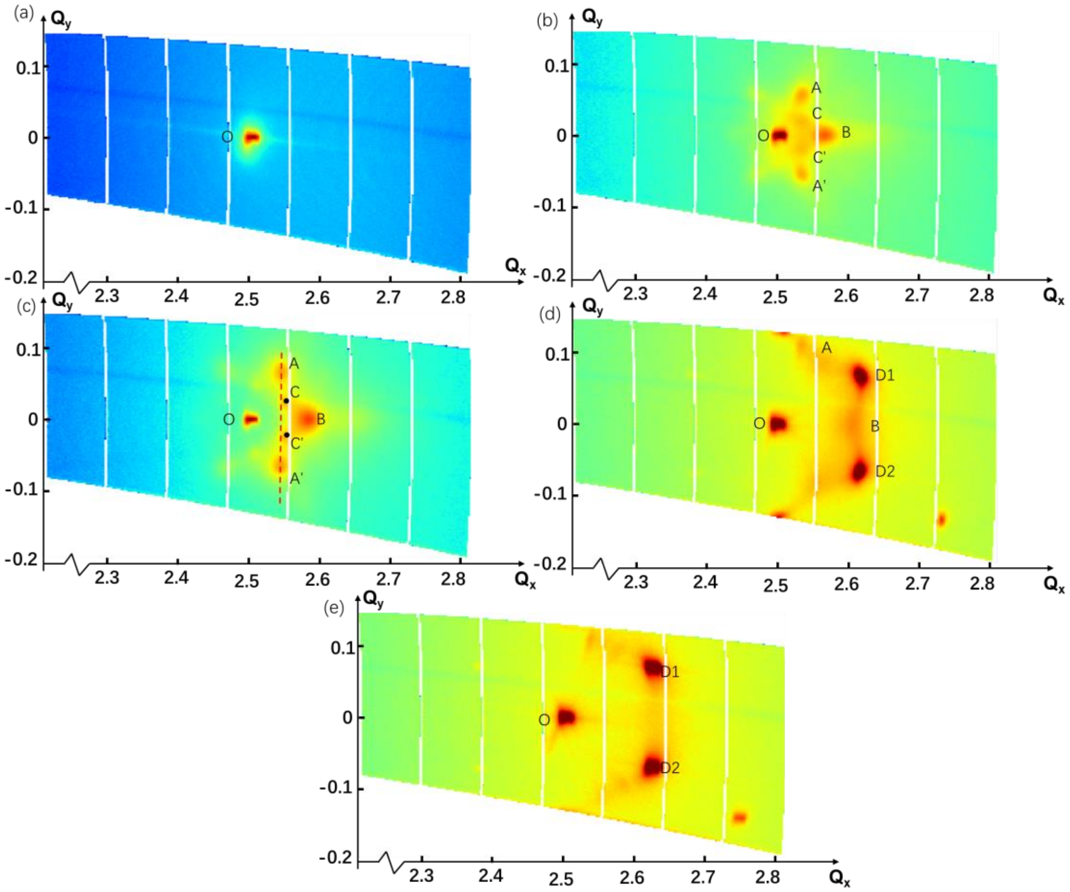

Figure 5.21 Maps of the diffracted intensity measured near in-plane (Q_x=2.506 Å^{-1}, Q_y=0Å^{-1}, Q_z=0.11 Å^{-1}) position during Ge evaporation on Ag(111) at T_{growth}=420K for (a) 0 min, (b) 21 min, (c) 28 min, (d) 35 min, (e) 42 min.

Evaporation time(mins)	Spot position (Q_x, Q_y)	Relative intensity	Δq(Å^{-1})	Periodicity (Å)	Surface phase
0	O (2.506, 0)	NA	0	NA	Ag(111)
21	A (2.536, 0.056)	4.67	0.0635	114.3	Triangle I
	B (2.568, 0)	8.19	0.062	117.0	Triangle I
	C (2.536, 0.018)	2.86	0.035	207.4	Triangle II
28	A (2.548, 0.066)	5.63	0.078	92.74	Triangle I
	B (2.584, 0)	12.5	0.078	92.74	Triangle I
	C (2.552, 0.022)	4.93	0.051	142.3	Triangle II
35	B (2.61, 0)	2.08	0.104	69.76	Triangle I
	D1 (2.622, 0.068)	150	0.134	46.88	Striped pahse
	D2 (2.622, -0.066)	154			
42	D1 (2.63, 0.07)	139	0.142	45.55	Striped phase
	D2 (2.63, -0.07)	107			

Table 5.1 Parameters of each diffraction spot in each map in Fig. 5.21, including the evaporation time, spot positions (Q_x, Q_y), Relative intensity of each spot, reciprocal vector (Δq), periodicity in the direct space, and the corresponding surface phase.

Fig. 5.21 shows various maps of the diffracted intensity around (h=1, k=0, l=0.12) condition, measured during Ge evaporation on the Ag(111) surface held at 420K.They present the evolution of the diffraction spots for Ge coverage less than 1/3ML. In order to facilitate the measurement of the distance between spots, $Q_xQ_yQ_z$ coordinates are used to describe positions of diffraction spots in the reciprocal space(see Fig. 5.21). In Tab 5.1, I report parameters of each spot in each map, i.e. the position of the spots, the diffracted intensity, the spacing between the spots, and the corresponding periodicity in the direct space.

Before the evaporation, single diffraction spot (labeled as O) appears at (Q_x= 2.506, Q_y= 0, Q_z= 0.11) position (see Fig. 5.21a), and corresponds to the diffracted signal at (h=1, k=0, l=0.12) position from the bare Ag(111) crystal. After 21 mins evaporation (about 0.18ML Ge), the diffraction map measured (see Fig. 5.21b) displays five more intense diffraction spots besides O spot. Due to the mirror symmetry, they can be divided into two groups: (i) A and B; (ii) C. Based on their measured positions (see Tab 5.1), the angles between OA(A') and OB and between OC(C') and OB are measured to be 62° ± 2° and 30°± 1°, respectively. It indicates that the spot groups (i) and (ii) can be regarded as two hexagonal pattern with different periodicities and rotated 30° in relation to each other. Their periodicity is measured to be about 11.4 nm and 20.7 nm respectively. This is of course much larger than the periodicity of a ($\sqrt{3}\times\sqrt{3}$) structure (i.e. 0.5nm) and of the c(31×$\sqrt{3}$) structure (4.45nm). The growth curve of each phase shown in Fig. 5.9 indicates the coexistence of the Ge diluted phase, twiglike dendrite phase, and triangle phase for $\theta_{Ge}\approx$ 0.18ML. These signals most probably come from the triangle phase, because the Ge dilute and twiglike dendrite phases do not have a regular shape. These two hexagonal patterns with a rotated angle of 30° between each other could correspond to two quasi-hexagonal arrays composed of the triangles shown in Fig. 5.5a and 5.5d, respectively.

As Ge deposition continues, the diffraction spots shown in Fig. 5.21c have a higher intensity, compared to the spots in Fig. 5.21b. This is due to the growth of the triangle phase for a higher density. In addition, the distance between the O spot and other spots also increases without a variation of their orientation. It means that the periodicity of the two hexagonal structures composed of triangle patterns decreases. As can be seen in Fig. 5.21c and Tab 5.1, the ACC'A' spots are not aligned along the same line (i.e. the dotted red line), which shows that A(A') is not the second-order diffraction spot for the diffracted signal at C(C') spot, which confirms that these spots belong to two different patterns. After 35 mins evaporation (corresponding to about 0.29ML Ge), the intensity of the spots related to the triangle phase decay, and the spots of the group (ii) disappear. New diffraction spots (D1 and D2) appear on the diffraction map in Fig. 5.21d, corresponding to the diffraction spots from the striped phase as presented in Fig. 5.17a. After further Ge evaporation, the spots associated with the triangle phase have nearly completely disappeared, as shown in Fig. 5.21e. It indicates the end of the transition from the triangle phase to the stripe phase.

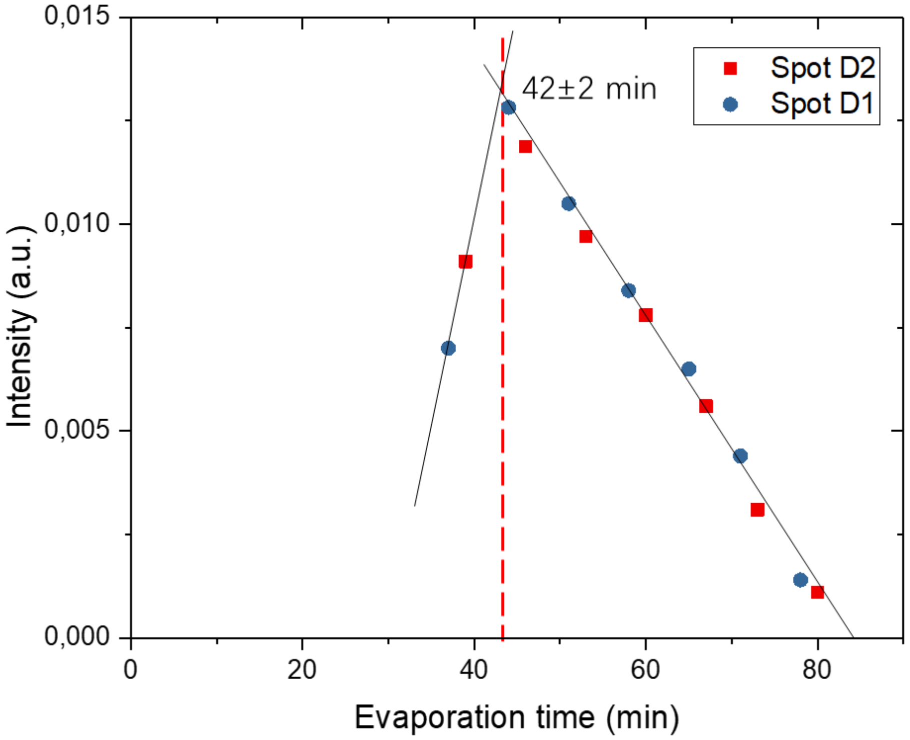

Figure 5.22 Evolution of the integral intensity measured for D1 and D2 spots in Fig. 5.21(d, e), as a function of Ge evaporation time.

Fig. 5.22 presents the evolution of the integral intensity measured at D1 and D2 spots, as a function of Ge evaporation time. The diffraction maps shown in Fig. 5.21 are acquired from in-plane *angular rocking scan* (ARS) measurements (ω-scan). The diffracted signal at D1 spot is detected firstly, and a time interval between D1 and D2 is about 2 min. The first set of the data is measured in Fig. 5.21d. As shown in Fig. 5.22, the completion of the striped phase corresponds to 42 ± 2 min of Ge evaporation, and its disappearance is obtained for about 84 min evaporation. As the completion of the striped phase corresponds to 1/3ML, the Ge flux is ~0.47ML/h. In the next section, I present the results of combined GIXD measurements and DFT calculations, aimed to determine the atomic structure of the striped phase.

5.3.4 Atomic structure of the striped phase

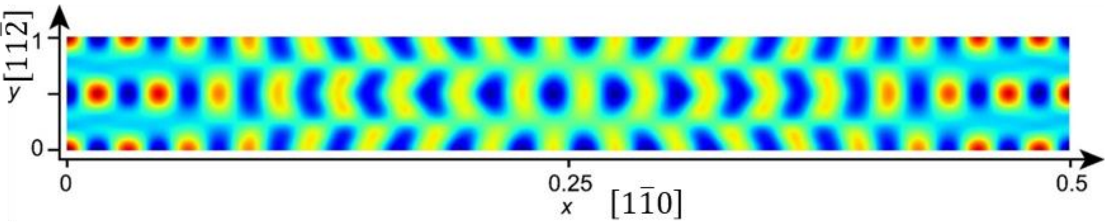

Figure 5.23 Experimental Patterson map of the $c(31\times\sqrt{3})$ structure. Only half of the unit cell has been drawn along x. (size of the Patterson map is 4.478 × 0.500 nm^2).

Fig. 5.23 shows the 2D Patterson map of the $c(31\times\sqrt{3})$ reconstruction computed from the measured in-plane structure factors, by using Eq. (3-25). In this Patterson map, the presence of a nearly perfect hexagonal lattice is clearly visible in the vicinity of the origin ($x\approx 0$) and the center of the unit cell ($x\approx 0.5$). Moreover, this nearly hexagonal lattice corresponds to a slightly contracted (1 × 1) unit cell related to the Ag(111) unit cell. Between $x\approx0.1$ and $x\approx 0.4$ in this Patterson map, the modulation of the electron density-density autocorrelation associated with the $(\sqrt{3}\times\sqrt{3})$ local ordering is not visible. This results from the weaker diffracted intensity of the satellite spots near fractional values of (h, k) with respect to that of the satellite spots near integer values of (h, k) (see Fig. 5.17). This observation is in good agreement with a chemical ordering between Ag and Ge atoms. The results of STM measurements discussed in section 5.2 reveals that the striped phase corresponds to the Ag_2Ge alloy. Indeed, if every third atom is a Ge atom, the intensity associated with $(\sqrt{3}\times\sqrt{3})$ satellites indicates that Hx+Ky=n/3 for Ag atoms (where n is integer except for multiples of three), should roughly scale as$((Z_{Ge}+ 2Z_{Ag}\cos(2\pi/3))^2\approx225$, where $Z_{Ge}=32$ and $Z_{Ag}= 47$ correspond to atomic number. However, the intensity associated with (1×1) satellites should roughly scale as $(Z_{Ge}+ 2Z_{Ag})^2\approx 15900$ due to the integral values of Hx+Ky. A comparison between two values of the intensity reveals that the contribution of the chemical ordering to the autocorrelation function is thus only of the order of 1%. Note that in a model of germanene, with only Ge atoms in a honeycomb lattice, the ratio of the intensity related to $(\sqrt{3}\times\sqrt{3})$ and (1×1) satellites would be much higher, i.e. $(\cos(2\pi/3))^2=0.25$, which is not in agreement with the experimental observations of Fig. 5.17.

As presented in the Patterson map, a set of 33 maxima of correlation is clearly visible along the long side of the $c(31\times\sqrt{3})$ unit cell, corresponding to the $[1\bar{1}0]$ direction. In the vicinity of x≈0.25 or 0.75, the shape of correlations maxima appears as elongated along the y-axis (i.e. $[11\bar{2}]$ direction). This indicates that atoms are periodically spaced along the $[1\bar{1}0]$ direction (see X-axis) but at slightly different positions along the $[11\bar{2}]$ direction (see Y-axis). From these observations, I propose that the striped phase with the $c(31\times\sqrt{3})$ reconstruction has an atomic density 33/31 times higher than the one of the Ag(111) surface and that the atomic positions undulate between the fcc and the hcp sites. Regarding the unit cell of the Ag(111) surface, the fcc and hcp sites are located at $(1/3, 2/3)a_0$ and $(2/3, 1/3)a_0$ ($a_{Ag}=0.2889$ nm), respectively. Their sites in the unit cell of the $c(31\times\sqrt{3})$ reconstruction correspond to y=1/3b and 1/6b individually. This superstructure would thus present a remarkable similarity with the $(22\times\sqrt{3})$ Au(111) reconstruction that has an atomic density 23/22 times higher than the one of an Au(111) bulk plane[11]. In order to verify the hypothesis of the model of the striped phase, the atomic positions of this surface model have been relaxed by DFT calculations, performed by Davide Sciacca at IEMN (Lille). Then, a comparison between the theoretical structure factors, computed from the relaxed configuration by DFT, and the experimental ones measured by GIXD checks the validity of the relaxed model.

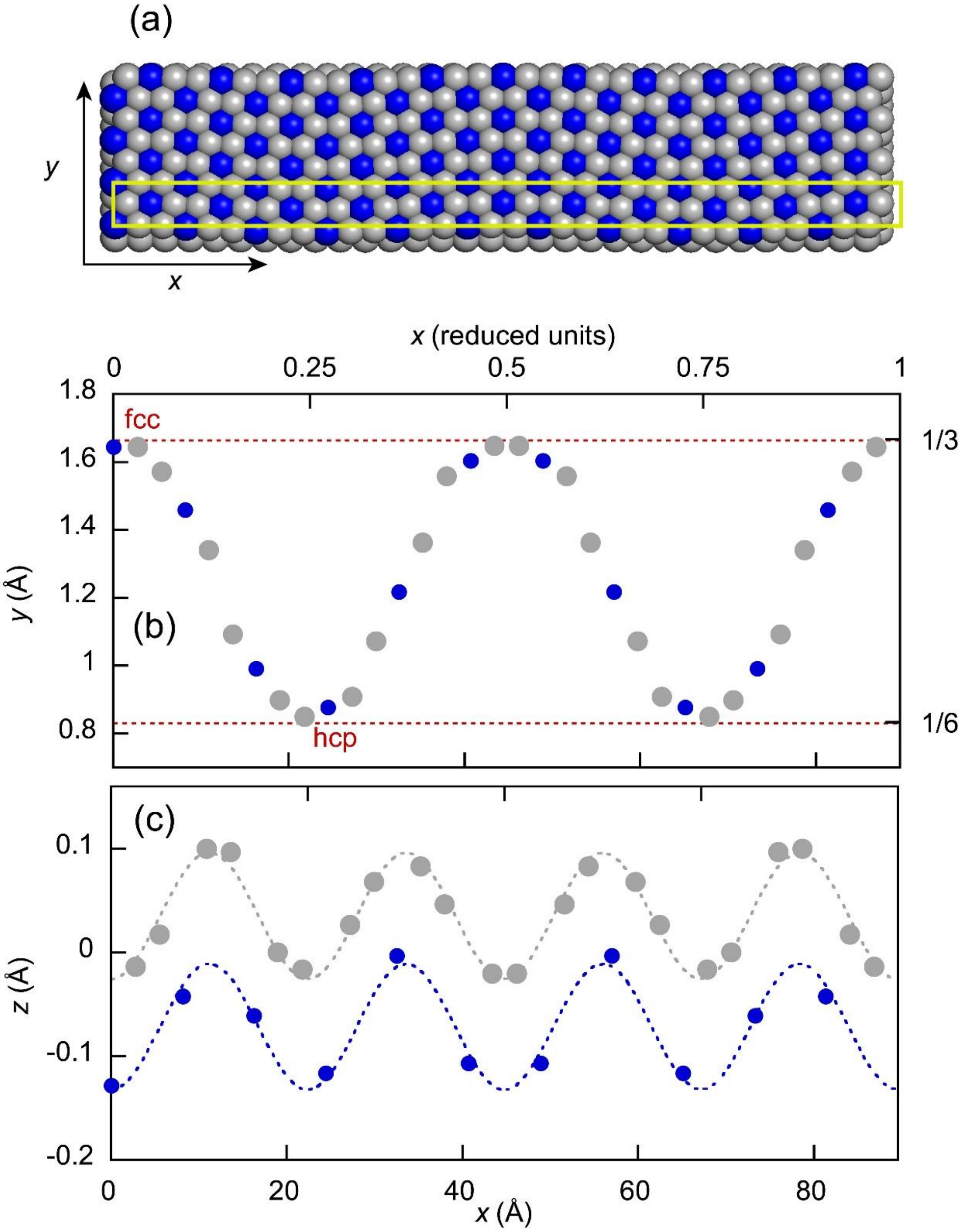

Figure 5.24 Top view (a) and profiles (b, c) along x for surface atoms (blue: Ge, grey: Ag). The lateral scales x and y are given both in reduced units and in Å. The $c(31 \times \sqrt{3})$ unit cell is drawn in yellow.

Fig. 5.24 displays the configuration relaxed by DFT, which corresponds to an Ag_2Ge surface alloy with the local $(\sqrt{3}\times\sqrt{3})$ reconstruction. The y(x) profile in Fig. 5.24b presents an oscillation of the atomic positions between fcc (at y=1/3b) and hcp sites (at y=1/6b). As shown in Fig. 5.24c, the z(x) profiles also display a periodic undulation of the atomic position for Ge and Ag atoms in the reconstruction, respectively. In addition, they show a double frequency as compared with y(x). From a comparison between the average height of these two undulations, Ge atoms are located around 0.1Å below the Ag atoms. Starting from 0, the odd and even minima for z correspond to atoms in fcc and hcp sites respectively, whereas maxima correspond to atoms in bridge position. This results in the periodic striped pattern observed on STM images [86]. As described in Fig. 5.24c, the simulations thus correspond to an apparent periodicity of 2.24 nm and to a buckling of 0.12Å, whereas the buckling was measured by STM to 0.2 Å [86]. The Ge-Ag interatomic distances are slightly smaller for Ge atoms in bridge position (2.662 Å) than for Ge atoms in the fcc position (2.722 Å). This undulation of the atomic positions between the fcc sites and the hcp sites is strongly analogue to the $(22\times\sqrt{3})$ Au(111) reconstruction, for which the surface atomic density is 23/22 times higher than the one of a Au(111) bulk plane, and which also displays a similar striped structure [129].

The theoretical structure factors were computed from the atomic configuration relaxed by DFT. In the present case, only 14 free parameters were used to fit the data: two scale factors (one for the in-plane set and one for the rods) and three sets of the in-plane and out-of-plane Debye-Weller (DW) factors for all Ge atoms, the surface Ag atoms, all Ag atoms of the second plane and the other Ag atoms, respectively. The agreement between experimental (F_{exp}) and simulated (F_{th}) structure factors is estimated by the value of χ^2, the expression of which has already been given in Eq. (4-7). The number of experimental structure factors is N_{pts}=2493, the number of free parameters is N_{par} =14, and the experimental uncertainty (σ_{exp}) takes into account the statistical uncertainty given by the number of counted photons and an overall 10% uncertainty.

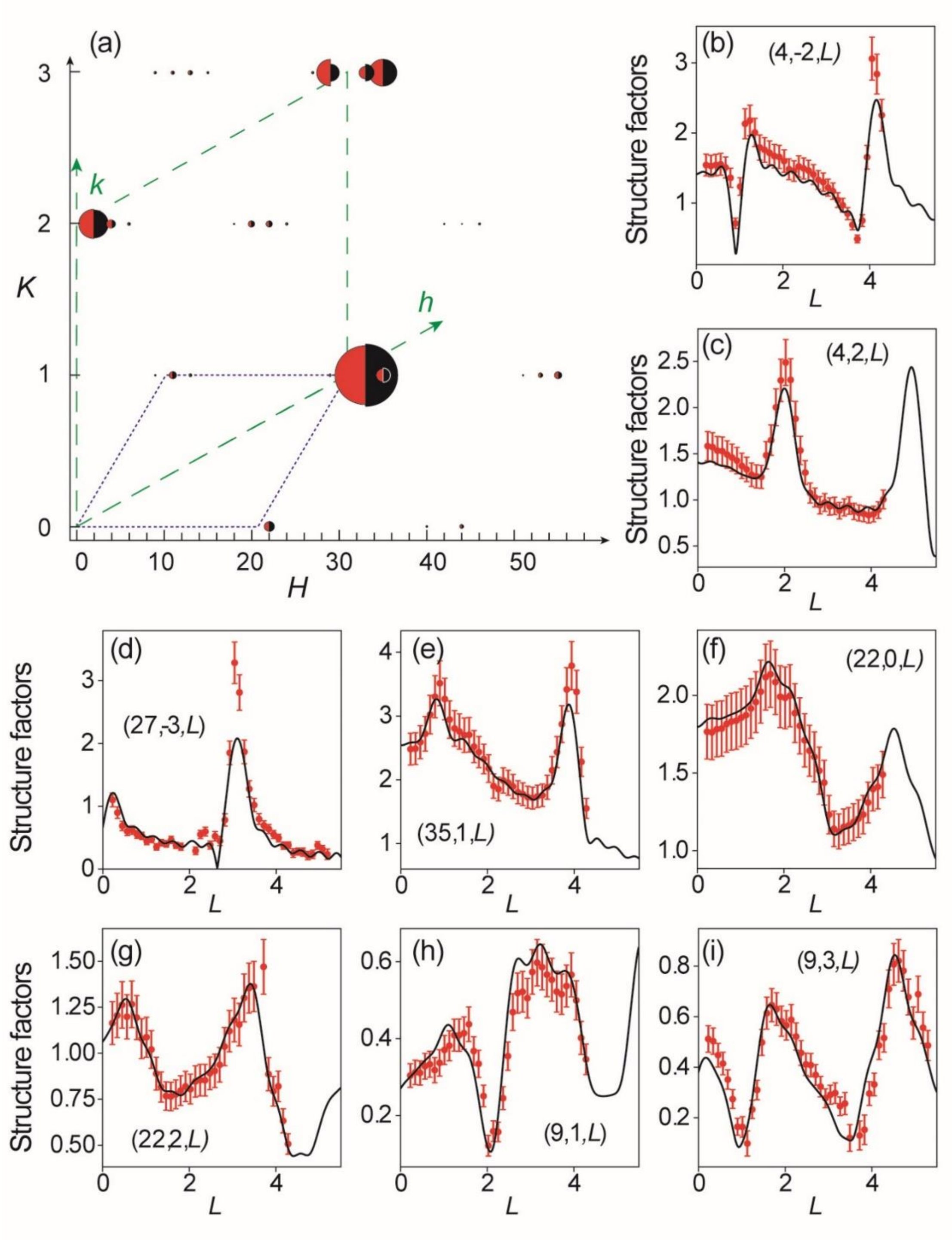

Figure 5.25 (a) In-plane structure factors. Comparison between experimental (red half-disks) and simulated (black half-disks) structure factors. The green dashed parallelogram corresponds to the Ag(111) surface unit cell. The substrate structure factors for integer values of h and k have not been drawn for clarity. The purple dotted parallelogram corresponds to a $(\sqrt{3} \times \sqrt{3})R30°$ supercell. (b-i) Comparison between experimental (red dots) and simulated (black line) structure factors along (H, K, L) satellite rods, near integer values of (h, k) (b-e) or near fractional values of (h, k) (f-i).

In Fig. 5.25, I report a comparison between the experimental structure factors ($|F_{exp}|$) and simulated ones ($|F_{th}|$)for in-plane conditions and along selected rods. Due to the mirror symmetry of the unit cell, the experimental structure factors indicate that F(H, K, 0)= F(-H, -K, 0) and F(H, K, 0)= F(-H, K, 0). Thus, only rods (H, K) in the quadrant corresponding to H>0, K>0 have been presented in a comparison of in-plane structure factors, as illustrated in Fig. 5.25a. The small value of $\chi^2 = 1.90$ reveals a remarkable agreement between experiments and simulations. As can be seen in Fig. 5.25, the simulated structure factors fit very well with the experimental ones of both satellite rods near integer values of (h, k) (see Fig. 5.25b-e) and fractional values of (h, k) (see Fig. 5.25f-i). Concerning the satellite rods F_{exp} in Fig. 5.25b-e, the presence of intense variations at specific integer values of L is clearly visible, for example, near L=1 and near L=4 in Fig. 5.25b and 5.25e, near L= 2 in Fig. 5.25c, or near L= 0 and near L= 3 in Fig. 5.25d. These positions are close to (0, -1, 1 or 4), (1, 0, 1 or 4), (0, 1, 2) and (1, -2, 0 or 3) related to (h, k, l) indices, which corresponds to the Bragg diffraction conditions of the Ag(111) crystal. These intense variations could result from the periodic elastic relaxations that penetrate in the bulk [130], [131]. GIXD is sensitive to these elastic relaxation modes that give specific contributions to the superstructure rods [131]. Such relaxations are induced by the 6.45% misfit between the striped phase and the substrate. Thus, a great fit between experiments and simulations exhibits that DFT simulations describe precisely the interaction of the surface layer and the substrate and that the $c(31 \times \sqrt{3})$ reconstruction corresponds to the structure of the striped phase with local $(\sqrt{3} \times \sqrt{3})$ periodicity and a long-range modulation.

Let us take a look at a remarkable similarity between the $(22 \times \sqrt{3})$ Au(111) reconstruction and the structure of the striped phase. Due to stronger interaction between low-coordinated Au surface atoms, the equilibrium interatomic distance should decrease. For a non-reconstructed surface, this leads to a large tensile surface stress. In order to reduce the surface energy, the Au(111) surface relaxes by increasing the surface atomic density 23/22 times higher than the one of the Au(111) bulk plane

[129]. This reduction of the interatomic distances results in an energy gain higher than the energy cost for the occupation of atoms at bridge positions instead of three-fold coordinated hcp or fcc positions. Different from Au(111), the Ag(111) surface does not spontaneously reconstruct. In the present case, when an Ag atom of the surface is replaced by a Ge atom, as a smaller atomic radius of Ge (0.125nm), this increases the absolute value of the tensile surface stress. Above a critical coverage, the Ge/Ag(111) system relaxes in a configuration where the interatomic distances are decreased, at the cost of the creation of Shockley partial dislocations, i.e., discommensuration lines separating regions where atoms occupy fcc positions, from regions where atoms occupy hcp positions. Such analogous behavior has been also observed in the case of Cu, Ag, Au films on Ru(0001) [132], [133].

5.4 Summary of the results of Chapter 5

In this chapter, using real-time STM measurements, I have followed the growth of Ge on the Ag(111) surface in the 380K-430K temperature range. By combined GIXD measurements and results of DFT calculations, I have investigated the exact atomic structure of the striped phase, namely, the $c(31 \times \sqrt{3})$ reconstruction.

Concerning the results of STM measurement:

- During Ge evaporation, submonolayer Ge deposition on Ag(111) results in the formation of different surface phases: dilute Ge phase, twiglike dendrite phase, triangle phase, striped phase, disordered hexagonal phase, pair protrusion phase, and hexagon protrusion phase depending on Ge coverage.
- The dependence of Ag concentration with Ge coverage drawn in Fig. 5.14 reveals that all of these surface phases correspond to Ge-Ag surface alloys. For 1/3 ML Ge coverage, the striped phase corresponds to the Ag_2Ge surface alloy. The DH phase is also interpreted as an alloy with a larger proportion of Ge atoms.
- After the completion of the formation of the DH phase, additional Ge deposition

results in the formation of the pair and hexagon protrusion phases. Regarding the pair protrusion phase, pair protrusions have the same orientation in a local domain, but they do not show a hexagonal symmetry. For the hexagon protrusion phase, the hexagon protrusion patterns present a (√109×√109) periodicity with respect to Ag(111)-(1×1).

Regarding the results of combined GIXD measurements and DFT calculations:

- Real-time GIXD measurements in Fig. 5.21 reveal that the triangle phase has two nearly hexagonal patterns with a rotated angle of 30°, which could correspond to two hexagonal arrays of triangles shown in Fig. 5.5a and 5.5d. As Ge coverage increases, the lattice constant of hexagonal superstructures and the diffracted signals from the triangle phase decrease.
- Concerning the structure of the DH phase, the in-plane diffraction map in Fig. 5.19 indicates two possibilities: (7×7) or c(7×√3) reconstructions. However, it is impossible to determine the structure of the DH phase.
- The in-plane diffraction map in Fig. 5.20 reveals that the hexagon protrusion phase corresponds to the $\left(\sqrt{109}\times\sqrt{109}\right)_{Ag}R\pm 5.5°$ reconstruction. Besides the diffracted signals from this reconstruction, there are several diffraction spots associated with an incommensurable structure.
- A precise analysis of the diffraction map in Fig. 5.17 reveals that the structure of the striped phase corresponds to the $\mathrm{c}(31\times\sqrt{3})$ reconstruction. From a careful analysis of the experimental Patterson map, I have proposed that the striped phase with the c(31×√3) reconstruction has an atomic density 33/31 times higher than the one of the Ag(111) surface and that the atomic positions undulate between the fcc and the hcp sites.
- The structure factors calculated from the configuration relaxed by DFT are in good agreement with the experimental GIXD structure factors. The striped phase layer shows a buckling of 0.12Å. The Ge-Ag interatomic distances are slightly smaller for Ge atoms in bridge position (2.662 Å) than for Ge atoms in fcc position (2.722

Å).

Chapter 6

6 Growth of silicene on Ag(110)

Contents

In this chapter, I present the growth of additional Si on the (5×2)/c(10×2) superstructure grown on the Ag(110) surface at a growth temperature of 483K. This chapter is mainly divided into two parts. In the first part, I describe the surface evolution and the formation of new superstructures by using STM measurements. In the second part, employing GIXD measurements and DFT calculations, I give the atomic structure of the reconstructions and evidence for the existence of a dumbbell silicene honeycomb structure. This subject was carried out in a collaboration between INSP in Paris, CINaM in Marseille, and ISM in Rome. I have been mainly involved in the GIXD experiment acquisition and data analysis and real-time STM experiments.

6.1 STM studies

6.1.1 Experimental details

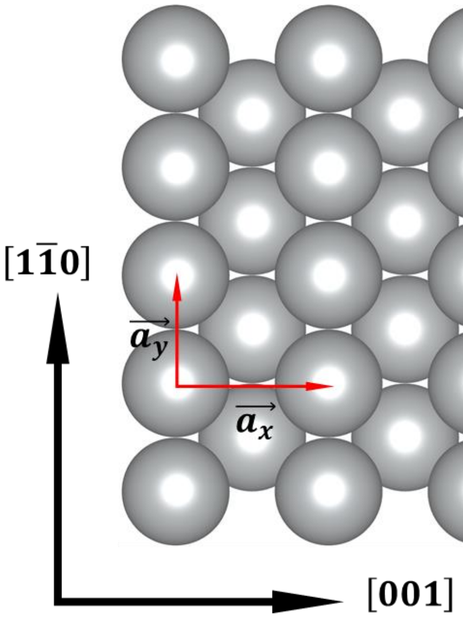

Figure 6.1 Top view of the Ag(110) surface. The basis of the unit cell ($\boldsymbol{a}_x$, $\boldsymbol{a}_y$) is indicated by the red arrows along the [001] and $[1\bar{1}0]$ direction, respectively.

Concerning STM experiments, some of the STM images presented here were acquired at INSP during the growth Si on Ag(110) held at about 483K. The others have been obtained by collaborators at CINaM in Marseille and ISM in Rome. Sample cleaning was achieved by repeated cycles of Ar+ ion bombardment and annealing at 780K in the preparation chamber. Si was evaporated from an evaporator on the Ag(110) substrate. The Si flux is ~ 0.6 ML/h, where 1 ML corresponds to the Ag(110) surface atom density. The atomic structure of the Ag(110) surface is drawn in Fig. 6.1. The lattice parameters of the Ag(110) surface are $a_x = a_{Ag} = 4.085$ Å in the [001] direction and $a_y = a_{Ag}/\sqrt{2} = 2.889$ Å in the $[1\bar{1}0]$ direction, where a_{Ag} is the lattice constant of silver cell equal to 4.085 Å at 300K. For the (5×2) reconstruction, the lattice constants are $a_{(5\times2)} = 20.43$ Å and $b_{(5\times2)} = 5.78$ Å. The STM images acquired were treated with Gwyddion software and a homemade software developed by G.Prévot.

6.1.2 Formation of nanostripes

After completion of the formation of pentamer chains, additional Si deposition at the same growth temperature results in the formation of new superstructures. Fig. 6.2a displays a STM image acquired at 300K after additional Si deposition on the (5×2)/c(10×2) Si overlayer grown on Ag(110) kept at 483K. The left part of this STM image shows new superstructure domains at a higher level compared to the (5×2)/c(10×2) reconstruction domains shown in the right part of the image. They appear as nanostripes running along the $[1\bar{1}0]$ direction, i.e. parallel to the initial pentamer chains. The pentamer chain structure may thus be regarded as a guide for the growth of these nanostripes. As expected, from the profile along the line AB in Fig. 6.2a (see Fig. 6.2b), the width of pentamer chains along the [001] direction, Δx_2 is measured to be 2.10 ± 0.1 nm corresponding to $5a_{Ag}$. On the contrary, the nanostripes have different widths and nanostripe domains are separated by $\Delta x_1 \approx 2.4$ nm from each other (see Fig. 6.2a and 6.2b). The apparent height difference between the nanostripe and the (5×2)/c(10×2) structure domains is $\Delta z_2 = 0.16 \pm 0.01$ nm.

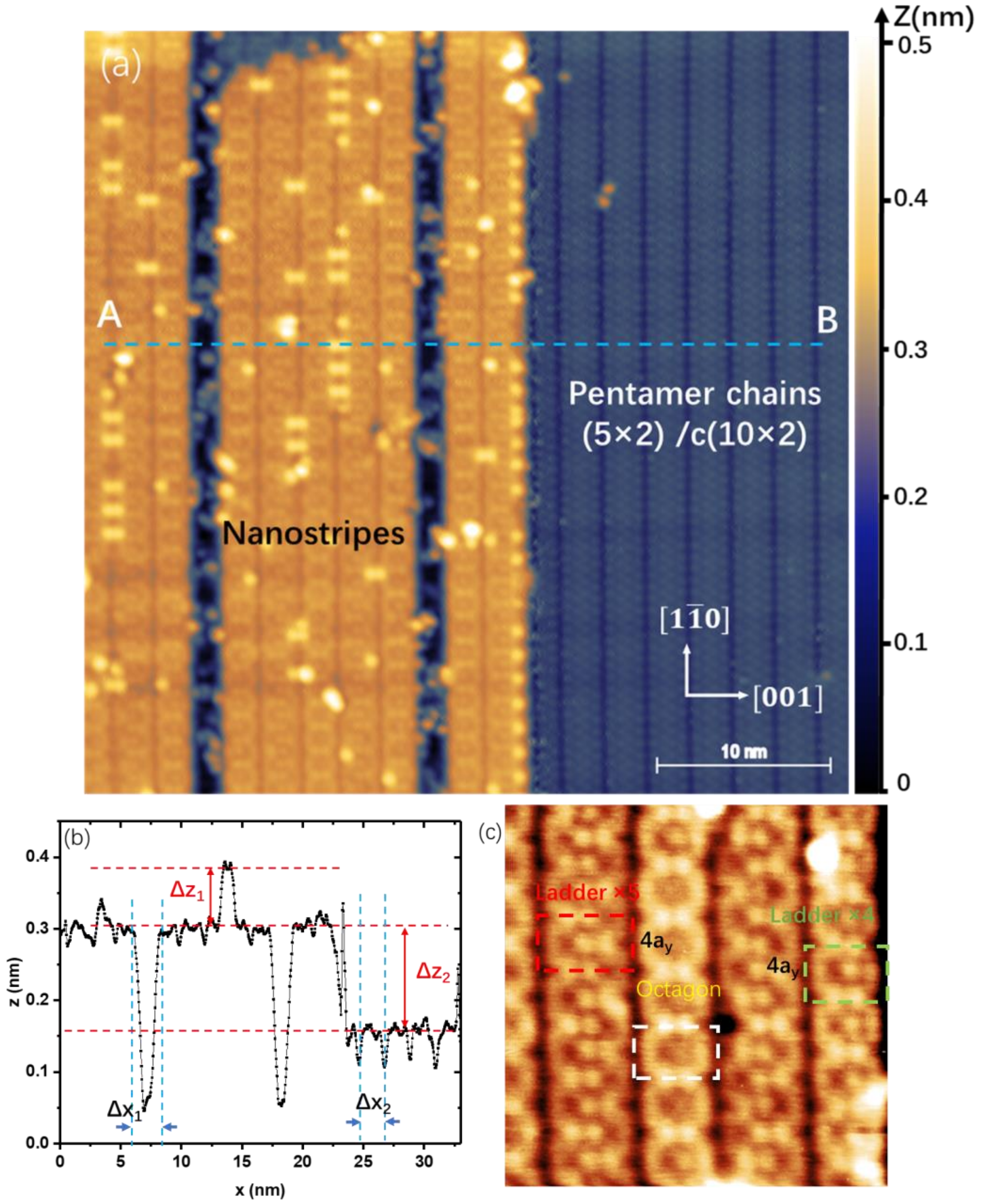

Figure 6.2 (a) STM image (I = 20 pA, U = 1.7 V) showing two Ag(110) terraces with (5×2)/c(10×2) and nanostripe domains. The lower (upper) terrace is reported in blue (yellow). (b) Profiles along the line A-B shown in (a). STM images (10×10 nm^2) of adatom-free motifs: (c) Ladder ×5 (red dashed square), Ladder ×4 (green dashed square) motifs, and Octagon motif (white dashed square) (I = 20 pA, U = 0.6V). All these STM images were obtained at 300K after Si deposition at 483K

As can be seen in Fig. 6.2a, nanostripe domains are decorated with some bright protrusions. These nanostripes do not all have the same pattern, but they all appear as beaded chains with locally ordered domains. Compared to other atoms in nanostripes, an apparent height of bright protrusions (Δz_1) is estimated to be about 0.7Å (see Fig.

6.2b). These protrusions thus could be regarded as adatoms on top of the nanostripes. Fig. 6.2c displays a detailed view of the nanostripes in a domain free of adatoms, showing two different widths associated with three different motifs. A "Ladder" motif is related to a stripe width of $4a_x$ or $5a_x$ (denoted hereafter Ladder ×4 and Ladder ×5), and an "Octagon" motif is related to a width of $4a_x$ (denoted hereafter Octagon). However, all these nanostripes have a ×4 periodicity ($4a_y$) along the $[1\bar{1}0]$ direction. As displayed in Fig 6.2b, the nanostripes with the Ladder ×4 and Ladder ×5 motifs have an analogous structure, which presents alternating groups of two bright protrusions along the $[1\bar{1}0]$ direction. Compared to the Ladder ×4 motif, the Ladder ×5 motif has an extra column of three protrusions on the right side, resulting in an extra p2 symmetry axis. Regarding the Octagon motif, bright protrusions form an octagon in the unit cell.

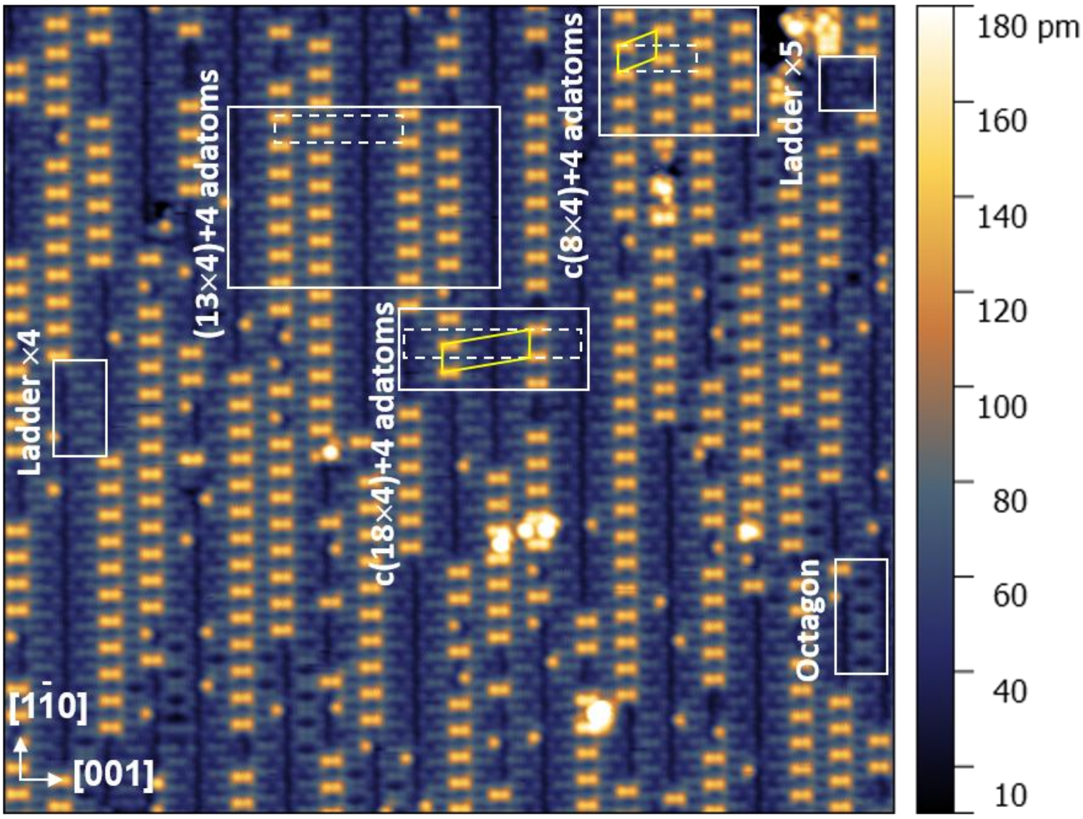

Figure 6.3 STM image (370×330) Å^2 of the Ag(110) substrate after Si deposition at 483 K, above completion of the pentamer chain overlayer. Ladder ×4, Ladder ×5 and Octagon motifs are observed in domains free of adatoms, while c(18×4)+4adatoms, (13×4)+4adatoms and c(8×4)+4adatoms structures are observed on the rest of the surface (the white dashed rectangles highlight the unit cells). The primitive unit cell of the c(8×4)+4adatoms and c(18×4)+4adatoms structures are indicated by yellow parallelograms. I = 20 pA, V_{sample} = 100mV.

Fig. 6.3 shows a STM image of the nanostripe domains covered with adatoms, acquired at 77K by the group of Laurence Masson at CINaM in Marseille. From this figure, one can see that adatoms do not randomly deposit on the surface and almost appears as pairs of adatoms while a small fraction of adatoms are isolated. Three local reconstructions related to pairs of adatoms are clearly visible. These three reconstructions are a c(8×4) reconstruction with 4 adatoms per unit cell (hereafter c(8×4)+4adatoms) already reported by Colonna et al. [65], a (13×4) reconstruction with 4 adatoms per unit cell (hereafter (13×4)+ 4adatoms), and a c(18×4) reconstruction with 4 adatoms per unit cell (hereafter c(18×4)+ 4adatoms). All the expressions of these reconstructions are given with respect to the basis of the Ag(110) unit cell. STM image shown in Fig. 6.3 suggests that these local reconstructions could consist of Ladder×4, Ladder×5, or Octagon motifs decorated with adatom pairs. The size of ordered domains along [001] is small, of the order of 10 nm. In order to determine the atomic structure of these phases observed in STM images, we have performed GIXD experiments, that will be discussed later.

6.1.3 Evolution of the surface

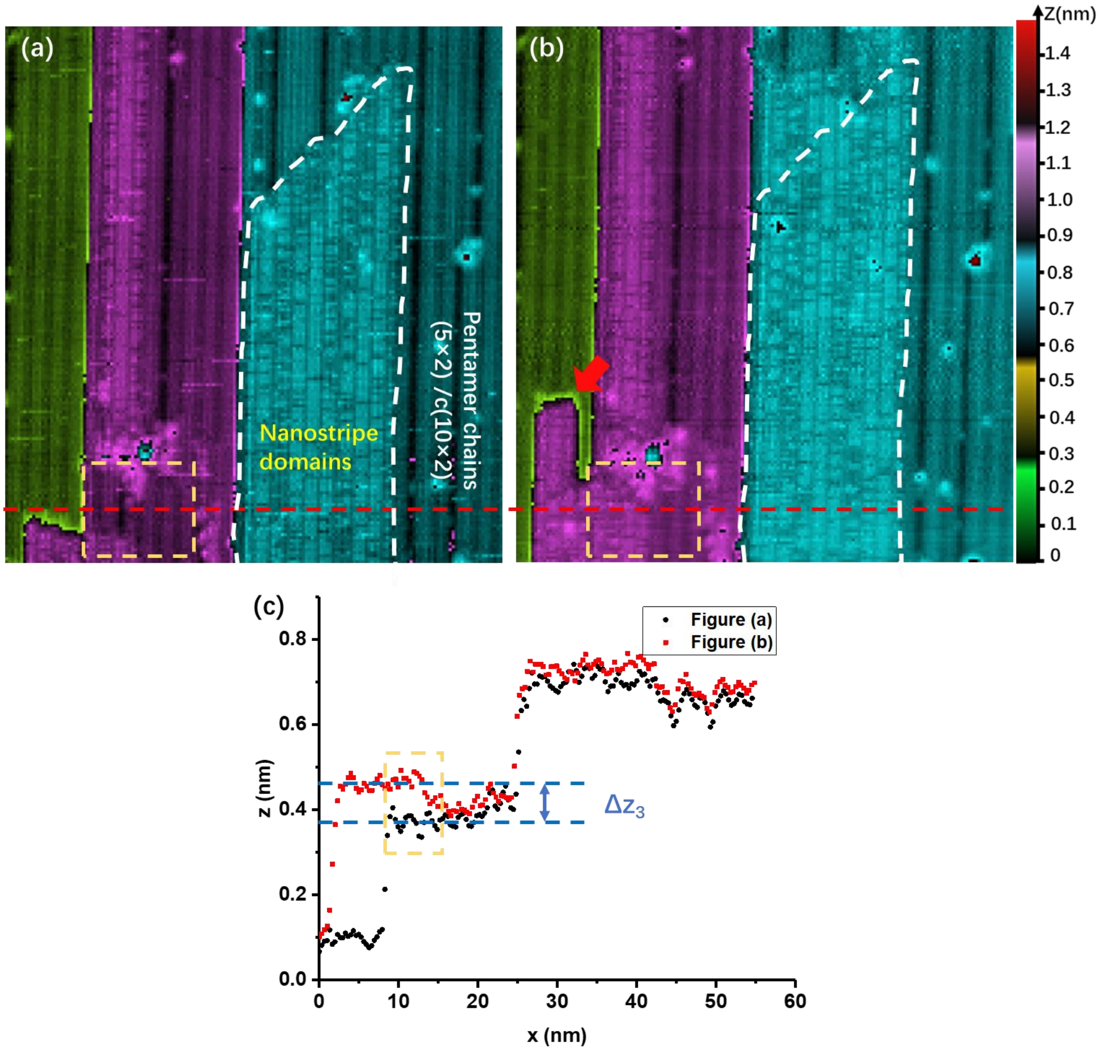

Figure 6.4 Evolution of the surface during Si deposition on (5×2)/c(10×2) Si adlayer grown on Ag(110) held at 483K shown in two in-situ consecutive STM images with a time interval of 10 min. In (a), the boundary between nanostripe and (5×2)/c(10×2) domains on the blue terrace is drawn by the white dashed line. In (b), the red arrow indicates finger structures. Size of the images: 65 × 70 nm^2. Tunneling conditions: V_S = 1.7 V, I = 20 pA. (c) Profile along the red dashed line. The yellow dashed square corresponds to the ones in (a) and (b).

Fig. 6.4a and Fig. 6.4b show two successive in-situ STM images obtained during additional Si deposition on the (5×2)/c(10×2) reconstruction formed on Ag(111) held at ~483K. The colors correspond to terraces at different level, the green terrace in the left part is lower than the blue ones in the right part of the images. The pentamer chain domains are displayed as more ordered pattern, and the areas with small bright squares correspond to the nanostripe phase domains covered with adatoms. From a comparison between these two figures, the (5×2)/c(10×2) structure is progressively replaced by the nanostripe phase. A precise analysis of the image show that nanostripe domains grow either by replacing pentamer domains in a terrace (blue domain) or by forming outgrowths (violet domain). The profile of the red line drawn in Fig. 6.4 demonstrates the formation of the nanostripe phase domains with a higher apparent height than the Pentamer domains ($\Delta z_3 \approx 0.7$ Å). Thus, a possible growth mechanism could be described as follows:

After completion of the formation of the (5×2)/c(10×2) reconstruction, additional Si deposition on pentamer chains results in the formation of nanostripes. As described in section 2.2.2, the (5×2)/c(10×2) structure forms on the missing-row reconstructed Ag(110) surface kept at 460K [26][66]. The addition of Si atoms to the pentamer chains could lead to an instability of the missing-row Ag(110) reconstruction underneath. Thus, the missing-row reconstructed Ag(110) layer could be removed, and expelled Ag atoms could participate in the growth of fingerlike Ag islands on the terrace. The nanostripe phase thus can form on these islands or on the unreconstructed Ag(110) at a lower level.

In the next section, I present the results of combined GIXD-DFT studies for determining the atomic structure of the reconstructions observed in STM images.

6.2 GIXD studies

In this section, I tackle the question of the atomic structure of the adatom-decorated reconstructions by means of GIXD measurements and give evidence of the existence of silicene and dumbbell silicene on Ag(110).

6.2.1 Experimental details

GIXD experiments have been performed on the SIXS beamline at SOLEIL synchrotron facility. Si was deposited on the Ag(110) surface maintained at 483K. with a Si flux of ~2ML/h. Concerning diffraction results, the unit cell of the different reconstructions observed are taken as reference for indexing the reciprocal space. In the present case, two sets of indices have been used: (i) The (h, k, l) indices refer to the Ag(110) surface basis (a_0= 4.085 Å, b_0 = 2.889 Å, c_0= 2.889 Å, α = β= γ =90°); (ii) The (H, K, L) indices refer to the unit cell of a (13×4) reconstruction with respect to Ag(110) ($a_{(13\times4)}$ = 13a_0 = 53.105 Å, $b_{(13\times4)}$ = 4b_0 = 11.556 Å, $c_{(13\times4)}$= 2.889 Å, α = β = γ =90°). Based on the Ag(110) surface basis, the reciprocal lattice vectors can be written as:

For the Ag(110) unit cell,

$$\boldsymbol{a}_{\mathbf{0}}^{*} = \frac{2\pi}{\boldsymbol{a}_{\mathbf{0}}} \quad \boldsymbol{b}_{\mathbf{0}}^{*} = \frac{2\pi}{\boldsymbol{b}_{\mathbf{0}}} \quad \boldsymbol{c}_{\mathbf{0}}^{*} = \frac{2\pi}{\boldsymbol{c}_{\mathbf{0}}} \tag{6-1}$$

For the unit cell of the (13×4) reconstruction (α=β=γ=90°),

$$\boldsymbol{a}_{(\mathbf{13}\times\mathbf{4})}^{*} = \frac{2\pi}{13\boldsymbol{a}_{\mathbf{0}}} \quad \boldsymbol{b}_{(\mathbf{13}\times\mathbf{4})}^{*} = \frac{2\pi}{4\boldsymbol{b}_{\mathbf{0}}} \quad \boldsymbol{c}_{(\mathbf{13}\times\mathbf{4})}^{*} = \frac{2\pi}{\boldsymbol{c}_{\mathbf{0}}} \tag{6-2}$$

For the unit cell of the c(8×4) reconstruction (α=β=γ=90°),

$$\boldsymbol{a}_{\boldsymbol{c}(\mathbf{18}\times\mathbf{4})}^{*} = \frac{2\pi}{8\boldsymbol{a}_{\mathbf{0}}} \quad \boldsymbol{b}_{\mathrm{c}(\mathbf{8}\times\mathbf{4})}^{*} = \frac{2\pi}{4\boldsymbol{b}_{\mathbf{0}}} \quad \boldsymbol{c}_{\boldsymbol{c}(\mathbf{8}\times\mathbf{4})}^{*} = \frac{2\pi}{\boldsymbol{c}_{\mathbf{0}}} \tag{6-3}$$

For the unit cell of the c(18×4) reconstruction (α=β=γ=90°),

$$\boldsymbol{a}_{\boldsymbol{c}(\mathbf{18}\times\mathbf{4})}^{*} = \frac{2\pi}{18\boldsymbol{a}_{\mathbf{0}}} \quad \boldsymbol{b}_{\mathrm{c}(\mathbf{18}\times\mathbf{4})}^{*} = \frac{2\pi}{4\boldsymbol{b}_{\mathbf{0}}} \quad \boldsymbol{c}_{\boldsymbol{c}(\mathbf{18}\times\mathbf{4})}^{*} = \frac{2\pi}{\boldsymbol{c}_{\mathbf{0}}} \tag{6-4}$$

Where a_0, b_0 and c_0 are the lattice vectors related to the unit call of Ag(110), as shown in Fig. 6.1.

6.2.2 Real-time GIXD measurements and experimental structure factors

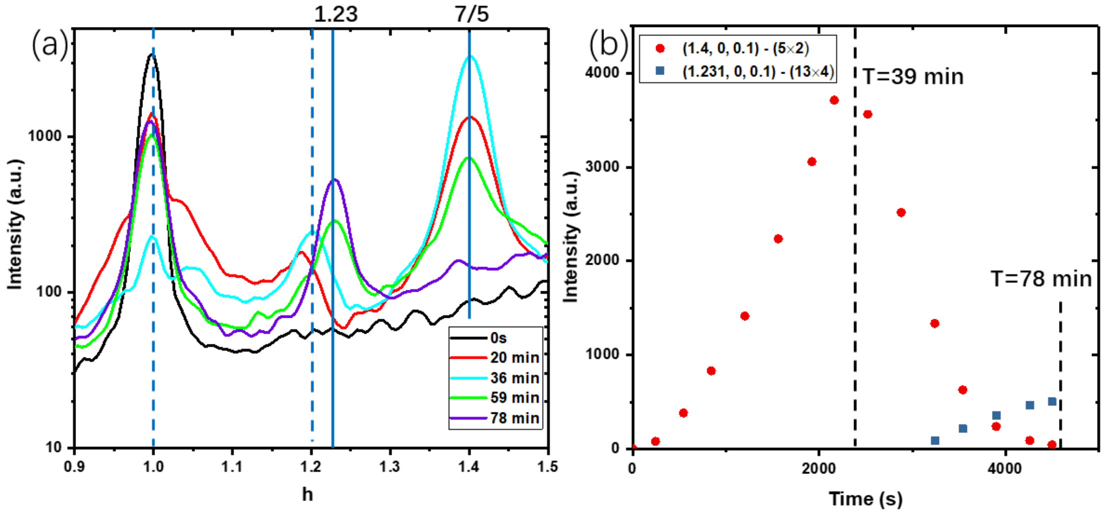

Figure 6.5 (a) Evolution of the diffracted intensity along h direction at (k=0, l=0.1), during Si deposition at ~483K. From black to violet: scan at t= 0 min, 36min, 59 min, 75min. (b) The evolution of the in-plane diffracted intensity of the (1.4, 0, 0.1) and (1.23, 0, 0.1) spot, associated with the (5×2)/c(10×2) structure and the (13×4)+4adatoms reconstruction, respectively.

The growth of Si on Ag(110) has been followed by real-time GIXD measurements. In Fig. 6.5a I report various profiles of the diffraction intensity obtained from scans along the reciprocal space axis h at (k=0, l=0.1) during Si deposition at ~483K. Before Si evaporation, the only visible peak in the [0.9, 1.5] range is at h=1.0, i.e. (1.0, 0, 0.1) spot, corresponding to the crystal truncation rod (CTR). As soon as Si evaporation begins, besides the peak related to the Ag(110) substrate, diffraction peaks at h = n/5 are observed which are associated with the formation of (5×2)/c(10×2) domains of Si DNRs on the Ag(110) surface with the missing-row reconstruction [66], [134]. When the intensity of these peak start to decrease, a new diffraction peak appears at h = 1.232 ± 0.005 ~16/13. It indicates that this peak should be associated with the formation of (13×4) + 4adatoms domains. After 78 min evaporation, its value reaches a maximum whereas the intensity of the peak at 7/5 reaches zero. In addition, the evolution of the peak at h=1.0 is another striking feature that has been reported in ref. [66]. As shown in Fig. 6.5a, the intensity of the peak at h=1.0 decreases until completion of the (5×2)/c(10×2) overlayer. This decay is associated with the formation of a missing row reconstruction of the Ag layer underneath the (5×2)/c(10×2) reconstruction [66]. Upon further Si deposition, a reincrease of the peak at h = 1 and the vanishing of the peaks related to (5×2)/c(10×2) domains reveal that the substrate missing-row reconstruction is lifted. This conclusion is in good agreement with the growth mechanism suggested by real-time STM measurements shown in Fig. 6.4a and 6.4b. Fig. 6.5b presents the evolution of the intensity of the diffraction peak at h = 1.4 and h = 1.232 ± 0.005. The Si deposition was stopped when the intensity of the (1.232, 0, 0.1) spot reaches a maximum (~78 min), i.e. for around twice the evaporation time corresponding to the maximum of the intensity of the (1.4, 0, 0.1) spot (~39 min). The vanishing of the peak at h = 1.4 indicates that the Si pentamer chains have been entirely replaced by the nanostripe phase.

After Si evaporation, the full width at half maximum (FWHM) of the peak at (16/13, 0, 0.1) is measured to be $\Delta h= 0.023$. Note that this small value excludes the facts that the diffracted signal may arise from the superimposition of diffraction from $c(18\times4)_{Ag}$ and $c(8\times4)_{Ag}$ domains, since they would correspond to peaks at h=11/9 (1.222) and h= 5/4 (1.25), which are separated by $\Delta h=0.028$. However, their presence cannot be totally ruled out because they may have a small size with a low density. The FWHM of the peaks is associated with the reconstruction domains size and the lattice parameter dispersion of $\Delta a/a$. Based on the different peaks, the size of the domains and the dispersion of the lattice parameter are estimated to be 40 nm and 0.01, respectively.

The structure factors for both in-plane (l=0.1) and out-of-plane ($l\neq 0.1$) conditions have been acquired after the Si deposition using the same procedure as the one reported in the previous chapters. For in-plane conditions, except for the substrate spots, significant intensity diffracted from the new structure is detected at the (H, K) = (16n+8p, p) (i.e. n, p integer) positions, as shown in Fig. 6.6.

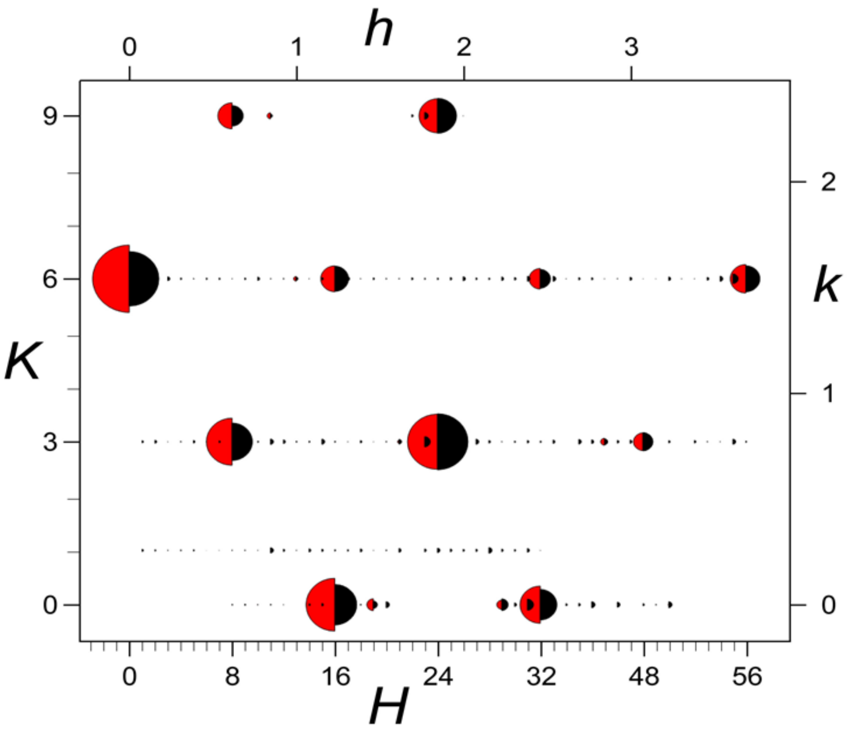

Figure 6.6 In-plane structure factors for the (13×4) structure. Comparison between experimental (red half-disks) and simulated (black half-disks) structure factors (the substrate structure factors for integer values of h and k have not been drawn for clarity). The (H, K, L) indices refer to the unit cell of a (13×4) reconstruction: H=13h, K=4k, and L=l.

Using Eq. (3-25), the Patterson map computed from the corresponding measured in-plane structure factors is presented in Fig.6.7a. It corresponds to the electron density-density autocorrelation function within the surface unit cell [122]. In this map, the presence of two types of spots with different intensities is clearly visible, and the intensity is normalized to its value at the origin. Bright spots, with a relative intensity of 1.0 form a nearly hexagonal lattice with lattice parameters measured to be a = 3.837 Å, b = 3.852Å, γ = 120.1°. These values approximate to the theoretical silicene lattice constant $a_{silicene}$ = 3.85Å [16], but also to the lattice constant of the Si(111) surface: a_{Si} = 3.84Å. Less intense spots correspond to correlations at a smaller distance. They present a honeycomb arrangement and their intensity correspond to the correlation between half of the atoms of the unit cell. Thus, this Patterson map should be in good agreement with a model of Si honeycomb lattice, i.e., where (16×3) hexagonal Si unit cells correspond to (13×4) Ag(111) unit cells. The comparison between experimental

(Fig. 6.7a) and simulated (Fig. 6.7b) Patterson map shows that this is indeed the case.

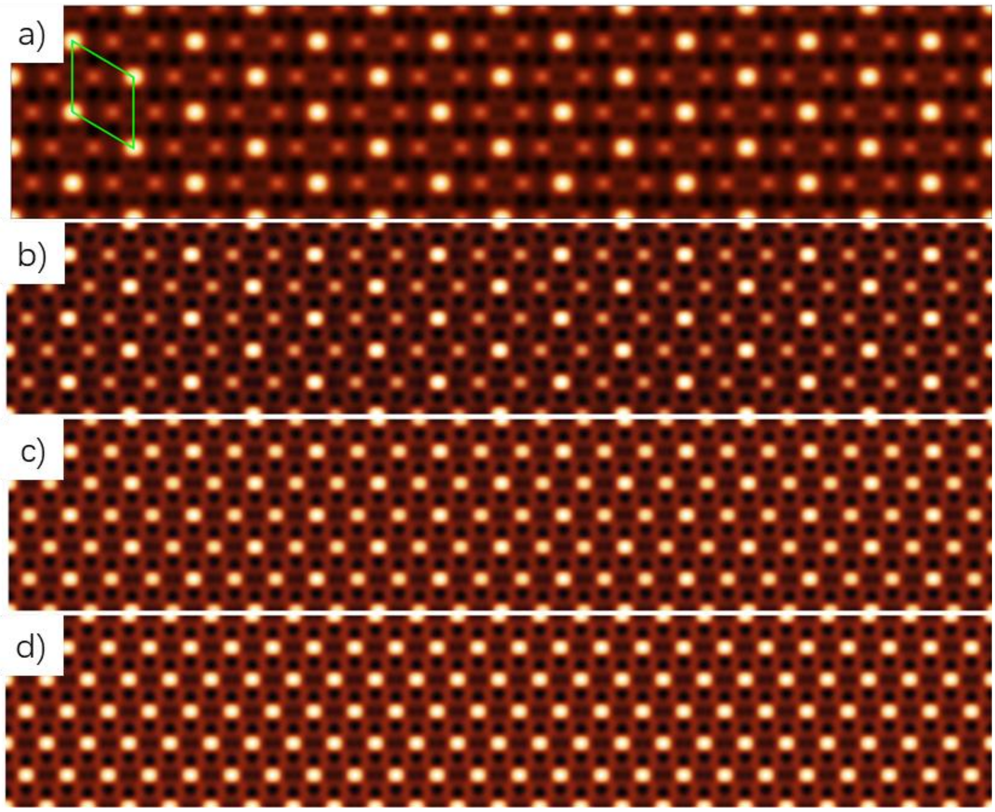

Figure 6.7 (a) Experimental Patterson map of the (13×4) Si/Ag(110) structure. A quasi hexagonal unit cell (a=3.837Å, b=3.852Å, γ=120.1°) is drawn in green. Simulated Patterson map for (b) honeycomb Si layer, (c) AB stacking of honeycomb layers, (d) ABC stacking of honeycomb layers. All layers in (a), (b), (c) and (d) are slightly distorted to fit the (13×4) unit cell.

For the sake of completeness, I have also simulated Patterson maps for bi and tri-layers. Fig. 6.7c and 6.7d display the 2D Patterson maps of honeycomb layers with AB stacking and ABC stacking, respectively. Compared to the experimental map presented in Fig. 6.7a, these two maps show a poor agreement. It indicates that the case of the formation of a diamond-like thin Si film can be ruled out.

6.2.3 Comparison between experimental and simulated structure factors

In section 6.2.2, the diffraction signal related to (13×4) domains has been measured by GIXD. Using DFT, and based on the conclusions of STM and GIXD observations, several honeycomb Si models associated with a (13×4) reconstruction have been proposed, as displayed in Fig. 6.8a-d. The DFT studies have been done by Conor Hogan at ISM in Rome.

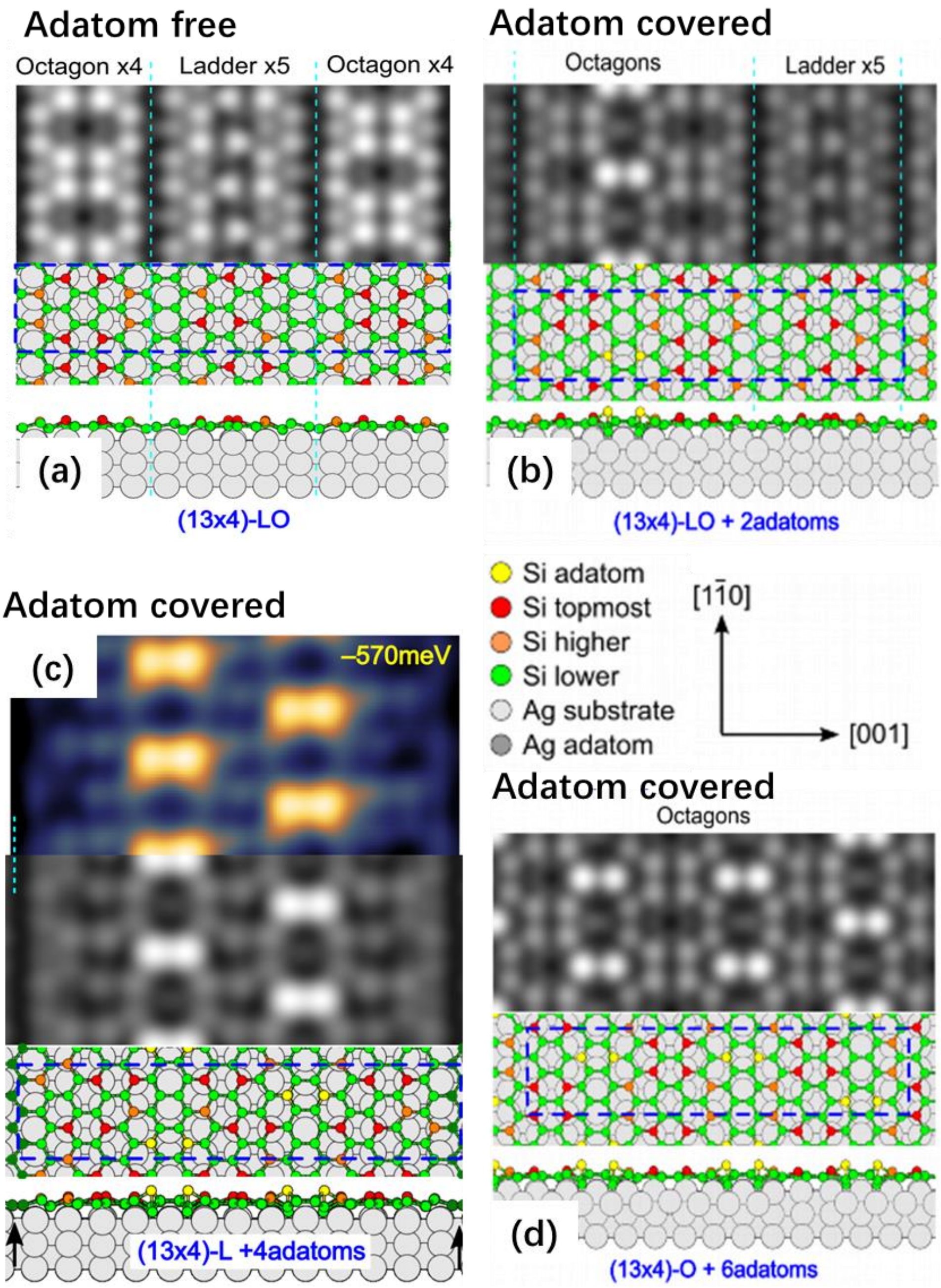

Figure 6.8 Ball-and-stick models and STM simulations of (a) adatom-free and (b) – (d) adatom-decorated silicene configurations associated with the (13×4) structure on Ag(110). Top and side views are shown. Dashed blue rectangles indicate conventional unit cells; primitive (simulation) cells are indicated by magenta shapes. Ladder (L) and Octagon (O) motifs are indicated along with their span in Ag surface unit cells along [001] and demarcated by vertical lines that typically correspond to the position of dark lines in STM. A comparison between the simulated and experimental STM image acquired at CINaM shows a good agreement for the (13×4) reconstruction with 4 adatoms per cell.

For the simulated adatom-free model, the (13×4)-LO configuration is shown in Fig. 6.8 a. This adatom-free model consists of Octagon ×4 and Ladder ×5 motives in the sequence of Octagon-Ladder-Octagon, corresponding to a layered silicene structure. They are in very good agreement with the STM images of Fig. 6.2c.

Concerning the adatom-decorated models, it is assumed that adatoms corresponds to Si adatoms and not to Ag adatoms. Indeed, one expects a high mobility for Ag adatoms at the deposition temperature, since the formation of new Ag terraces is observed. Fig. 6.8b-d display the (13×4)-LO+2atadoms, (13×4)-L+4adatoms, and (13×4)-O+6adatoms configuration, respectively. These adatom-decorated configurations show that adatom pairs on the silicene sheet forms dumbbell structures above the four-fold hollow sites of Ag(110). In Fig. 6.8c, the simulated STM image, obtained from the (13×4)-L + 4adatoms configuration, is in remarkable agreement with the experimental one. This reveals that the pair of bright spots corresponds to adatom pairs on the silicene adlayer forming dumbbells above the Ag(110) hollow sites.

In order to investigate the precise atomic structure, the diffracted intensity along 25 superstructure rods (SRs) has been measured corresponding to 16 inequivalent rods. The corresponding structure factors for various rods of the (13×4) structure is shown in Fig. 6.10. Besides the SRs related to (H, K)=(16n+8p, p), the diffracted intensity of the satellite rods at ΔH= ±3 is also measurable. This indicates that in the (13×4) unit cell a periodic vertical modulation leads to a period of 13/3 ×4.085 Å = 17.70Å, along the [001] direction. It can correspond to STM observations of 3 nanostripes per (13×4) unit cell. In addition, the SRs display weak vertical modulations (see Fig. 6.10), which excludes the possibility of the formation of the several layers on Ag(110). However, the modulations measured indicate that all atoms are not at the same vertical position. In the case of free-standing silicene, the modulation of the different rods should be similar, due to the regular layer buckling. In the present case, large differences between the rod profiles indicate that the silicene sheet related to the (13×4) superstructure cannot correspond to free-standing silicene.

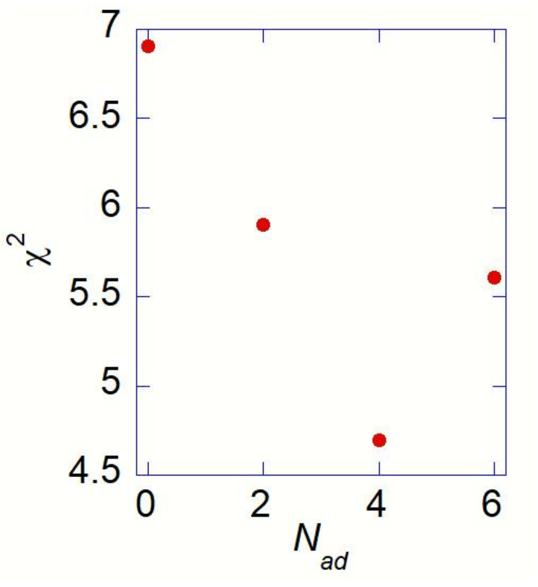

Figure 6.9 Evolution of the value of χ^2 for the (13×4) phase as a function of the number of Si adatoms in the unit cell (N_{ad}).

In order to verify the various proposed models, the theoretical structure factors, computed from the proposed configurations relaxed by DFT, are compared to the experimental structure factors. Concerning the simulation of the theoretical structure factors, only 7 free parameters have been applied: one scale factor and two sets of Debye-Waller (DW) factors for Si and Ag atoms along the H, K, L directions. The agreement between measured and simulated structure factors is estimated by the value of χ^2 acquired from Eq.(4-7). Fig. 6.9 shows the relationship between the value of χ^2 and the number of Si adatoms (N_{ad}) in the unit cell. It reveals that the (13×4)-L+4adatoms model corresponds to the best fit with the smallest value of χ^2=4.7.

In Fig. 6.10, a comparison between F_{exp} and F_{th} shows that the (13×4)-L+4adatoms model (indicated by the solid black line) has a better fit compared to the poorer obtained with the (13×4)-LO structure (dotted blue line). Concerning the comparison for the in-plane condition, as shown in Fig. 6.6, the theoretical in-plane structure factors (black half-disk) computed from the (13×4)-L+4adatoms model are in good agreement with the experimental ones (red half-disk).

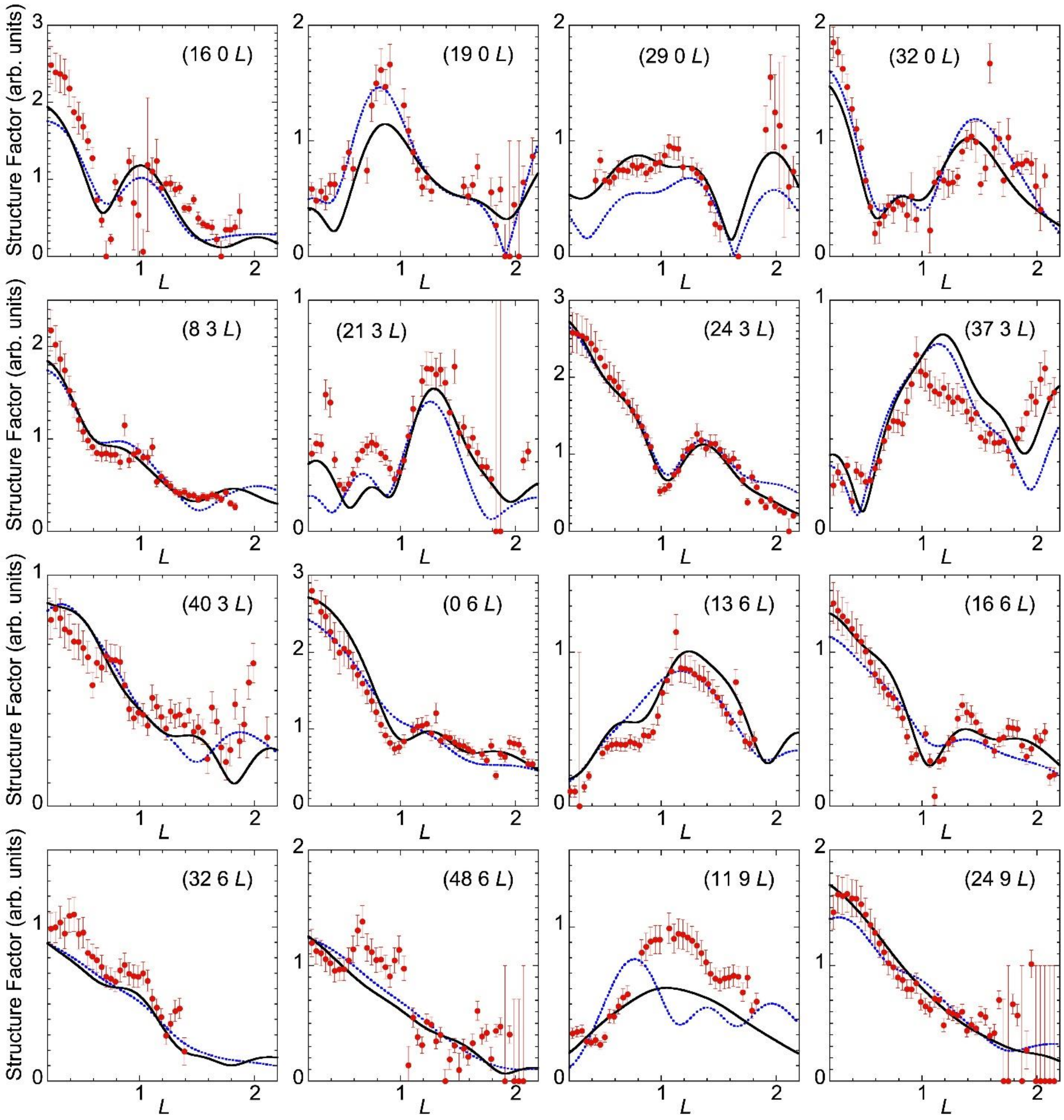

Figure 6.10 Structure factors for various rods of the (13×4) structure. Comparison between experimental (red dots) and computed values, using the (13×4)-LO (dotted blue line) or (13×4)-L+4adatoms (continuous black line) models simulated by DFT.

6.3 Discussion

By combined STM observation, GIXD measurements, and DFT calculations, the (13×4)+4adatoms atomic structure has been determined, corresponding to a dumbbell silicene phase on the Ag(110) surface. This reveals that additional Si evaporation on the surface covered by the pentamer chains leads to the formation of a honeycomb silicene layer, which is itself partially covered with adatoms in dumbbell structures. STM measurements present adatom-free and adatom-decorated nanostripe phases. The former consists of nanostripes with different motifs, namely Ladder ×4, ×5, and Octagon. The latter corresponds to the coexistence of local reconstructions with Si adatoms, i.e. (13×4)+4adatoms, c(18×4)+4adatoms, and c(8×4)+4adatoms. Differing from the STM observations, only diffraction spots related to the (13×4) reconstruction are measured by GIXD. Concerning this fact, there are two possible reasons: different experimental conditions and different quantity measured. For the first possible reason, the growth of Si on Ag(111) is performed in STM setup in Marseille and in GIXD setup in Paris, but the growth conditions cannot be absolutely identical. In GIXD experiments, the substrate temperature may be slightly higher than that in STM measurements. Based on the FWHM of the diffraction intensity peak from the (13×4) cell, the size of the reconstruction domains is estimated to be around 40 nm, significantly higher than the average domain width measured by STM. The other reason may be due to the fact that STM is mainly sensitive to the atomic position of the top-most atoms, whereas GIXD is mainly sensitive to the honeycomb Si lattice.

Based on GIXD observations, using DFT calculations, several models associated with the (13×4) configuration have been proposed, including adatoms-free and adatom-decorated configurations. The proposed models with adatoms show that Si adatoms adsorbed on silicene adlayer are located on top of the Si atoms located at four-fold hollow sites of the Ag(110) surface, forming dumbbell configurations. From a comparison between the experimental structure factors, obtained by GIXD, and the theoretical structure factors, computed from the proposed models, the atomic structure of the (13×4)+4adatoms reconstruction corresponds to (13×4)-L+4adatoms configuration.

All of these demonstrate that additional Si deposition leads to the formation of adatom-free and dumbbell silicene sheets on the Ag(110) surface.

6.4 Summary of the results of Chapter 6

In this chapter, combined STM measurements, GIXD measurements, and DFT calculations, I have investigated the growth of additional Si on the Si pentamer NRs grown on the Ag(110) surface. In addition, I have also determined the atomic structure of the (13×4)+4adatoms superstructure.

- After the complete of the (5×2)/c(10×2) Si overlayer obtained upon Si deposition on Ag(110) kept at 483K, additional Si evaporation results in the formation of the nanostripe phases. The nanostripe phase domains are partially decorated with pairs of adatoms, forming adatom-free and adatom-covered phases.
- The formation of the nanostripes is associated with the release of Ag adatoms, which indicate that the missing row reconstruction observed below the pentamer chains is released.
- As shown in Fig. 6.2c and 6.2d, the adatom-free nanostripe phase has three different motifs: the Ladder ×4, Octagon, and Ladder×5 motifs with a width of $4a_{Ag}$ and $5a_{Ag}$ along the [001] direction, respectively. In domains covered with adatoms, the appearance of several local reconstructions associated with the pairs of adatoms is clearly visible: the c(8×4)+4adatoms, (13×4)+4adatoms and c(18×4)+4adatoms reconstructions.
- DFT simulations give the full set of stable adatom-free and adatom-decorated models. Moreover, simulated STM images are in good agreement with experimental STM measurements. The adatom-free models reveal the formation of silicene sheet on Ag(110), and the adatom-decorated ones indicate the formation of a dumbbell silicene structure, with adatoms located in four-fold hollow site of the Ag(110) lattice.
- From a comparison between the experimental structure factors, obtained from GIXD measurements, and the theoretical ones obtained by DFT calculations, the atomic structure of the (13×4)+4adatoms reconstruction is determined,

corresponding to the (13×4)-L+4adatoms model. This exhibit that additional Si deposition on pentamer chains grown on the Ag(110) surface results in the formation of a dumbbell silicene honeycomb structure.

Conclusions and perspectives

Silicene and germanene growth has been reported on various metallic substrates [5-7][13][23-39][44-47][52,53][58-68][81-93][96-112][126-129][131]. For the most cases, the model of a honeycomb layer is proposed from the comparison between STM experiments and DFT simulations [5,7][37][67,68][92-93][96,97][101][104,105]. However, these studies present some limitations: STM only probes the density of states near the surface. The apparent height in STM images does not correspond to the height in real space. In STM images, only a limited number of protrusions per unit cell are visible, that may be attributed to the topmost atoms. However, their chemical nature is unknown. The positions of the other atoms in the unit cell are also unknown. For DFT computations, very often, only one model is simulated. So it is difficult to determine if it corresponds to the real minimum of energy. Only for Si/Ag(111) [27-35], a large variety of experiments, i.e. STM, GIXD, ARPES and LEED, made it possible to conclude to the formation of a honeycomb Si lattice. However, there is a strong interaction between the silicene layer and the substrate. On the contrary, combined STM/DFT/XPS/GIXD studies of Si/Ag(110) [66, 68] have demonstrated the formation of Si pentamers, associated with a substrate reconstruction. These studies have demonstrated the interest of studying in real time growth by STM and combining GIXD and DFT, which are the most quantitative experimental and theoretical techniques for determining the structure of ordered surface lattices.

During my PhD, I have thus used real-time and in situ STM and GIXD to study the growth and structure of germanene on metal surfaces, namely Ge/Al(111) and Ge/Ag(111). In addition, I have also studied the addition growth of Si on the Si/Ag(110) pentamers. In this thesis, I have performed state-of-the-art experiments and used analysis tool specially developed in the group to follow the surface evolution of Ge/Ag(111), Ge/Al(111), Si/Ag(110). Using STM-VT, I have followed the real-time STM measurements during evaporation at different growth temperatures. After measurements, I have used and Gwyddion software to analyze STM images. After correction of STM image by a homemade software developed by G.Prévot, I have produced in-situ STM images . In order to determine the atomic structure of silicene and germanene growth on Ag and Al surfaces, I have used GIXD measurements. These experiments were performed at the SIXS beamline of SOLEIL synchrotron. The diffracted X-rays were detected by a 2D detector. Concerning the raw data, I have applied BINoculars software to rebuild the intensity as a function of the position in the reciprocal space and a homemade software to analyze data. For DFT simulation, I have used DFT results obtained from our collaborators in Lille or Mulhouse to compute theoretical structure factors and compare them to experimental ones obtained by GIXD.

Using STM and GIXD, I have identified the several ordered structures that form upon Ge evaporation on Al(111) and Ag(111) and upon Si evaporation on /Ag(110). Whereas some of them were already known ((3×3) and (√7×√7) for Ge/Al(111)) or (c(8×4) for Si/Ag(110), the others were either unknown (incommensurable unit cell $\begin{pmatrix} 0.758 & 0.762 \\ -0.758 & 1.511 \end{pmatrix}$ for Ge/Ag(111), c(18×4) and (13×4) of Si/Ag(110)) or not indexed (c(31×√3) and (√109×√109) of Ge/Ag(111)). For germanene growth on Al(111) and Ag(111), real-time STM experiments show that the substrate is involved in the growth, for standard growth conditions, i.e.300 – 360 K for Ge/Al(111) and 380 - 430 K for Ge/Ag(111). This is surprising since Ge and Ag or Al are not miscible in the bulk. Terraces outgrowths form during evaporation. Such outgrowths are instantaneously (at the time scale of the STM acquisition) covered with Ge. This is also the case when Si is evaporated on Si/Ag(110) pentamer network. A quantitative analysis of the evolution of the coverage of the outgrowth with respect of the coverage of the "germanene" domains show that part of the substrate atoms are removed. Thus, Ge-Al or Ge-Ag alloys may form. Concerning Si/Ag(110), as the initial starting point is a missing-row reconstruction, one may suspect that the remaining rows are removed during further growth and that a non-reconstructed substrate is recovered at saturation coverage. For

GIXD experiments, I have measured the diffracted intensities for several ordered phases (see Table 7.1). For Ge/Al(111)-(3×3), Ge/Ag(111)-c(31×√3), Si/Ag(110)-(13×4), I have compared the results with several models computed by DFT. Concerning Ge/Al(111)-(3x3), the best fit corresponds to the Ge_4Al_4/Ge_2Al_7 configuration (see Fig. 4.17) corresponding to a two-layer surface alloy. For Ge/Ag(111)-c(31×√3), the striped phase with a c(31×√3) periodicity has an atomic density 33/31 times higher than the one of the Ag(111) surface and that the atomic positions undulate between the fcc and the hcp sites with a buckling of 0.12Å (see Fig. 5.24). Regarding Si/Ag(110)-(13×4), the theoretical structure factors, computed from a (13×4)-L + 4adatoms configuration (see Fig. 6.8c), is in good agreements with the experimental ones. This model demonstrates that additional Si deposition on pentamer chains grown on the Ag(110) surface results in the formation of a dumbbell silicene honeycomb structure.

Growth	Phases measured by GIXD
Ge/Al(111)	(3×3) and (√7×√7)
Ge/Ag(111)	The triangle phase, c(31×√3) (the striped phase), the DH phase, (√109×√109) and a unknow phase with unit cell $\begin{pmatrix} 0.758 & 0.762 \\ -0.758 & 1.511 \end{pmatrix}$
Si/Ag(110)	(13×4)

Table 7.1 The ordered phases measured by GIXD during different growth.

These studies show that Ge and Si have a very different behavior when deposited on Ag(111). Ge-Ag and Ge-Al alloys form whereas silicene growth is observed. On the contrary, silicene is observed on Ag(110) upon growth on Si pentamers, showing that the missing-row reconstruction initially observed is lifted upon further growth. It is interesting to compare Ge and Si: as Ge-Ge interatomic distances are larger than Si-Si ones, π-π interactions are reduced and one expects a lower tendency for Ge to form germanene than Si to form silicene. However, a 2D allotrope for Ge could exist on Ag(111). The (√109×√109) superstructure may indeed correspond to a pure Ge structure on Ag(111).

Finally, the main perspectives of this work are determination of the atomic structure of the Ge/Ag(111)-(√109×√109) and of the Ge/Al(111)-(√7×√7). Further studies on these structure will help us to understand the growth mechanism for the Ge/Ag(111) and Ge/Al(111). As Ge-Al alloys form on Al(111) after Ge deposition, the study of Si growth on Al(111) at different growth temperatures should be done. It will allows us to investigate a difference between Si and Ge growth on Al(111) and Ag(111).

Appendix A

Publications

Publications based on the results of this thesis:

[1] **Zhang, K.**, R. Bernard, Y. Borensztein, H. Cruguel, and G. Prévot. ‘Growth of Germanium-Silver Surface Alloys Followed by in Situ Scanning Tunneling Microscopy: Absence of Germanene Formation’. Physical Review B 102, no. 12 (14 September 2020): 125418.

[2] Papier à Phys. Rev. B:
Resolving the structure of the striped Ge layer on Ag(111): Ag2Ge surface alloy with alternate fcc and hcp domains
K. Zhang, D. Sciacca, R. Bernard, Y. Borensztein, A. Coati, P. Diener, B. Grandidier, I. Lefebvre, M. Derivaz, C. Pirri, G. Prévot

[3] Papier soumis à J. Phys. Chem. C:
Structure of germanene/Al(111): a two-layers surface alloy
K. Zhang, D. Sciacca, M.-C. Hanf, R. Bernard, Y. Borensztein, A. Resta, Y. Garreau, A. Vlad, A. Coati, I. Lefebvre, M. Derivaz, C. Pirri, P. Sonnet, &R. Stephan, G. Prévot

[4] Leoni, Thomas, Conor Hogan, **Kai Zhang**, Michel Daher Mansour, Romain Bernard, Romain Parret, Andrea Resta, et al. ‘Demonstration of the Existence of Dumbbell Silicene: A Stable Two-Dimensional Allotrope of Silicon’. The Journal of Physical Chemistry C 125, no. 32 (19 August 2021): 17906–17.

Appendix B

Comparison between experimental and simulated structure factors for Ge/Ag(111)

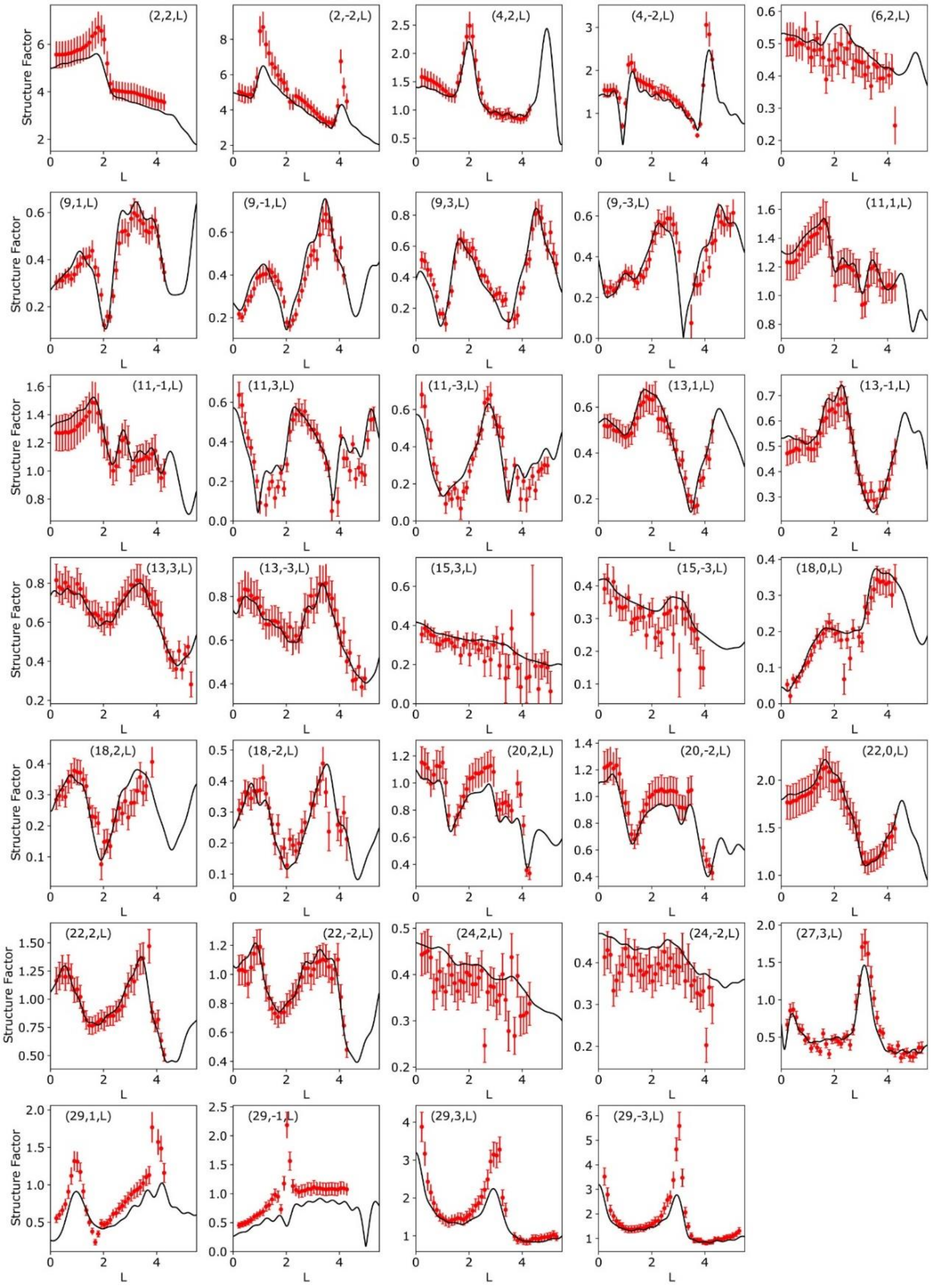

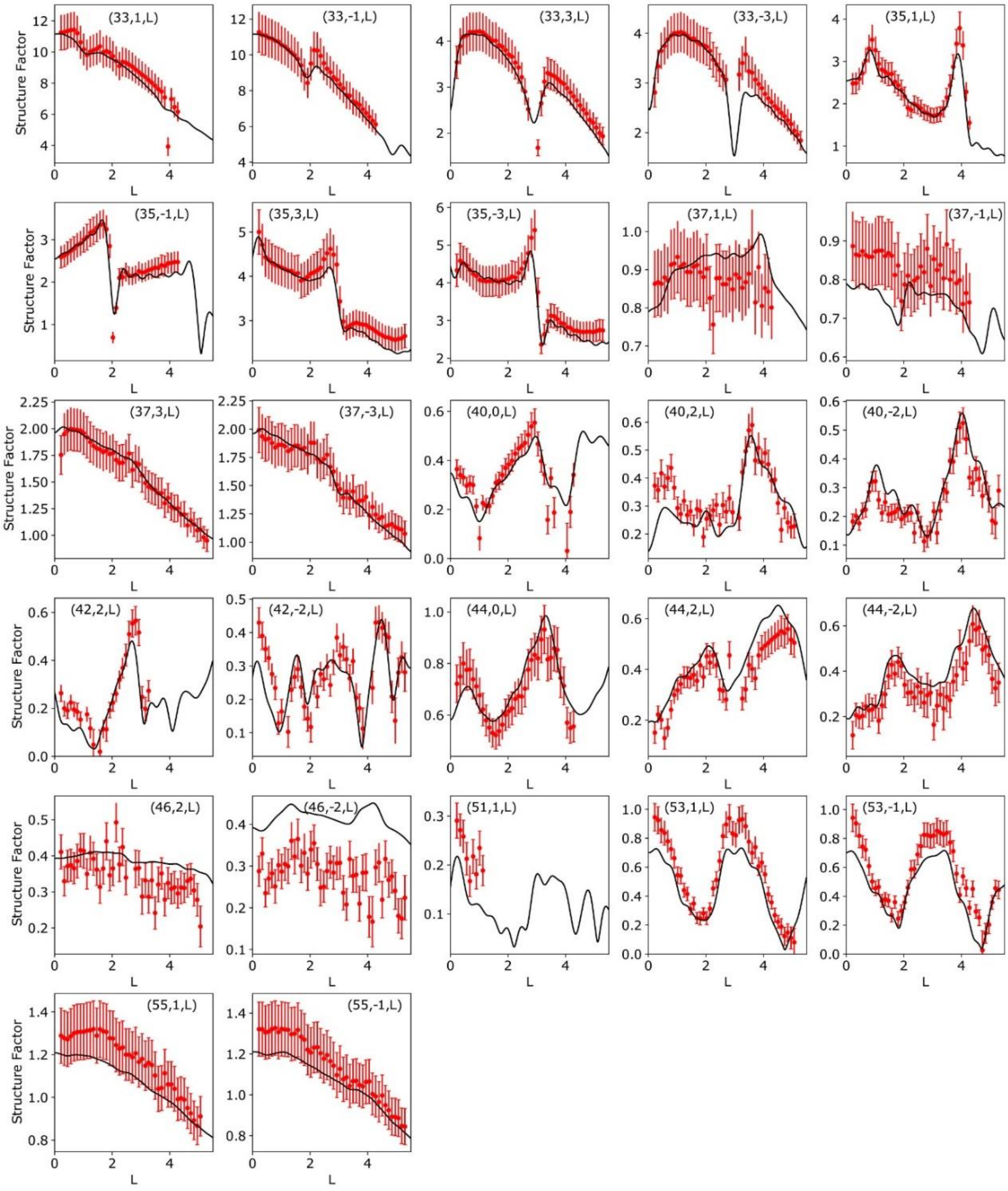

Figure A.1 Comparison between experimental (red dots) and simulated (black line) structure factors along all measured rods.

Bibliography

[1] K. S. Novoselov *et al.*, 'Two-dimensional gas of massless Dirac fermions in graphene', *Nature*, vol. 438, no. 7065, pp. 197–200, Nov. 2005

[2] Y. Zhang, Y.-W. Tan, H. L. Stormer, and P. Kim, 'Experimental observation of the quantum Hall effect and Berry's phase in graphene', *Nature*, vol. 438, no. 7065, pp. 201–204, Nov. 2005

[3] S. K. Tiwari, S. Sahoo, N. Wang, and A. Huczko, 'Graphene research and their outputs: Status and prospect', *J. Sci. Adv. Mater. Devices*, vol. 5, no. 1, pp. 10–29, Mar. 2020

[4] K. F. Mak, C. Lee, J. Hone, J. Shan, and T. F. Heinz, 'Atomically Thin MoS 2 : A New Direct-Gap Semiconductor', *Phys. Rev. Lett.*, vol. 105, no. 13, p. 136805, Sep. 2010

[5] P. Vogt *et al.*, 'Silicene: Compelling Experimental Evidence for Graphenelike Two-Dimensional Silicon', *Phys. Rev. Lett.*, vol. 108, no. 15, p. 155501, Apr. 2012

[6] P. De Padova *et al.*, 'Multilayer silicene: clear evidence', *2D Mater.*, vol. 3, no. 3, p. 031011, Sep. 2016

[7] M. Derivaz *et al.*, 'Continuous Germanene Layer on Al(111)', *Nano Lett.*, vol. 15, no. 4, pp. 2510–2516, Apr. 2015

[8] L. Persichetti *et al.*, 'van der Waals Heteroepitaxy of Germanene Islands on Graphite', *J. Phys. Chem. Lett.*, vol. 7, no. 16, pp. 3246–3251, Aug. 2016

[9] F. d'Acapito *et al.*, 'Evidence for Germanene growth on epitaxial hexagonal (h)-AlN on Ag(1 1 1)', *J. Phys. Condens. Matter*, vol. 28, no. 4, p. 045002, Jan. 2016

[10] V. O. Özçelik, D. Kecik, E. Durgun, and S. Ciraci, 'Adsorption of Group IV Elements on Graphene, Silicene, Germanene, and Stanene: Dumbbell Formation', *J. Phys. Chem. C*, vol. 119, no. 1, pp. 845–853, Jan. 2015

[11] F. Zhu *et al.*, 'Epitaxial growth of two-dimensional stanene', *Nat. Mater.*, vol. 14, no. 10, pp. 1020–1025, Oct. 2015

[12] S. Balendhran, S. Walia, H. Nili, S. Sriram, and M. Bhaskaran, 'Elemental Analogues of Graphene: Silicene, Germanene, Stanene, and Phosphorene', *Small*, vol. 11, no. 6, pp. 640–652, 2015

[13] G.-W. Lee, H.-D. Chen, and D.-S. Lin, 'Growth mode and structures of silicene on the Ag(111) surface', *Appl. Surf. Sci.*, vol. 354, pp. 187–195, Nov. 2015

[14] K. Takeda and K. Shiraishi, 'Theoretical possibility of stage corrugation in Si and Ge analogs of graphite', *Phys. Rev. B*, vol. 50, no. 20, pp. 14916–14922, Nov. 1994

[15] G. G. Guzmán-Verri and L. C. Lew Yan Voon, 'Electronic structure of silicon-based nanostructures', *Phys. Rev. B*, vol. 76, no. 7, p. 075131, Aug. 2007

[16] S. Cahangirov, M. Topsakal, E. Aktürk, H. Şahin, and S. Ciraci, 'Two- and One-Dimensional Honeycomb Structures of Silicon and Germanium', *Phys. Rev. Lett.*, vol. 102, no. 23, p. 236804, Jun. 2009

[17] S. Cahangirov, H. Sahin, G. Le Lay, and A. Rubio, *Introduction to the Physics of Silicene and other 2D Materials*, vol. 930. Cham: Springer International Publishing, 2017

[18] G. Brumfiel, 'Sticky problem snares wonder material', *Nature*, vol. 495, no. 7440, pp. 152–

153, Mar. 2013

[19] N. D. Drummond, V. Zólyomi, and V. I. Fal'ko, 'Electrically tunable band gap in silicene', *Phys. Rev. B*, vol. 85, no. 7, p. 075423, Feb. 2012

[20] C.-C. Liu, W. Feng, and Y. Yao, 'Quantum Spin Hall Effect in Silicene and Two-Dimensional Germanium', *Phys. Rev. Lett.*, vol. 107, no. 7, p. 076802, Aug. 2011

[21] M. Ezawa, 'Spin valleytronics in silicene: Quantum spin Hall--quantum anomalous Hall insulators and single-valley semimetals', *Phys. Rev. B*, vol. 87, no. 15, p. 155415, Apr. 2013

[22] H. Şahin *et al.*, 'Monolayer honeycomb structures of group-IV elements and III-V binary compounds: First-principles calculations', *Phys. Rev. B*, vol. 80, no. 15, p. 155453, Oct. 2009

[23] H. Sahaf, L. Masson, C. Léandri, B. Aufray, G. Le Lay, and F. Ronci, 'Formation of a one-dimensional grating at the molecular scale by self-assembly of straight silicon nanowires', *Appl. Phys. Lett.*, vol. 90, no. 26, p. 263110, Jun. 2007

[24] B. Aufray *et al.*, 'Graphene-like silicon nanoribbons on Ag(110): A possible formation of silicene', *Appl. Phys. Lett.*, vol. 96, no. 18, p. 183102, May 2010

[25] F. Ronci *et al.*, 'Low temperature STM/STS study of silicon nanowires grown on the Ag(110) surface', *Phys. Status Solidi C*, vol. 7, no. 11–12, pp. 2716–2719, Nov. 2010

[26] R. Bernard *et al.*, 'Growth of Si ultrathin films on silver surfaces: Evidence of an Ag(110) reconstruction induced by Si', *Phys. Rev. B*, vol. 88, no. 12, p. 121411, Sep. 2013

[27] B. Lalmi *et al.*, 'Epitaxial growth of a silicene sheet', *Appl. Phys. Lett.*, vol. 97, no. 22, p. 223109, Nov. 2010

[28] H. Enriquez *et al.*, 'Atomic structure of the $(2\sqrt{3}\times2\sqrt{3})$ R 30° of silicene on Ag(111) surface', *J. Phys. Conf. Ser.*, vol. 491, p. 012004, Mar. 2014

[29] B. Feng *et al.*, 'Evidence of Silicene in Honeycomb Structures of Silicon on Ag(111)', *Nano Lett.*, vol. 12, no. 7, pp. 3507–3511, Jul. 2012

[30] Z. Majzik *et al.*, 'Combined AFM and STM measurements of a silicene sheet grown on the Ag(111) surface', *J. Phys. Condens. Matter*, vol. 25, no. 22, p. 225301, Jun. 2013

[31] H. Jamgotchian *et al.*, 'Growth of silicene layers on Ag(111): unexpected effect of the substrate temperature', *J. Phys. Condens. Matter*, vol. 24, no. 17, p. 172001, May 2012

[32] H. Jamgotchian *et al.*, 'Silicene on Ag(111) : domains and local defects of the observed superstructures', *J. Phys. Conf. Ser.*, vol. 491, p. 012001, Mar. 2014

[33] R. Bernard, Y. Borensztein, H. Cruguel, M. Lazzeri, and G. Prévot, 'Growth mechanism of silicene on Ag (111) determined by scanning tunneling microscopy measurements and *ab initio* calculations', *Phys. Rev. B*, vol. 92, no. 4, p. 045415, Jul. 2015

[34] A. Curcella *et al.*, 'Multilayer silicene: clear evidence of Ag-terminated bulk silicon', *2D Mater.*, vol. 4, no. 2, p. 025067, Apr. 2017

[35] A. Curcella, R. Bernard, Y. Borensztein, M. Lazzeri, and G. Prévot, 'The mechanism for the stabilization and surfactant properties of epitaxial silicene', *Nanoscale*, vol. 10, no. 5, pp. 2291–2300, 2018

[36] T. Morishita, M. J. S. Spencer, S. Kawamoto, and I. K. Snook, 'A New Surface and Structure for Silicene: Polygonal Silicene Formation on the Al(111) Surface', *J. Phys. Chem. C*, vol. 117, no. 42, pp. 22142–22148, Oct. 2013

[37] A. Stępniak-Dybala and M. Krawiec, 'Formation of Silicene on Ultrathin Pb(111) Films', *J.*

Phys. Chem. C, vol. 123, no. 27, pp. 17019–17025, Jul. 2019

[38] A. Stpniak-Dybala, P. Dyniec, M. Kopciuszyski, R. Zdyb, M. Jałochowski, and M. Krawiec, ‘Planar Silicene: A New Silicon Allotrope Epitaxially Grown by Segregation’, *Adv. Funct. Mater.*, vol. 29, no. 50, p. 1906053, Dec. 2019

[39] S. Sadeddine *et al.*, ‘Compelling experimental evidence of a Dirac cone in the electronic structure of a 2D Silicon layer’, *Sci. Rep.*, vol. 7, no. 1, p. 44400, Jun. 2017

[40] A. Fleurence, R. Friedlein, T. Ozaki, H. Kawai, Y. Wang, and Y. Yamada-Takamura, ‘Experimental Evidence for Epitaxial Silicene on Diboride Thin Films’, *Phys. Rev. Lett.*, vol. 108, no. 24, p. 245501, Jun. 2012

[41] L. Meng *et al.*, ‘Buckled Silicene Formation on Ir(111)’, *Nano Lett.*, vol. 13, no. 2, pp. 685–690, Feb. 2013

[42] A. V. Nezhdanov, D. O. Filatov, D. A. Antonov, S. Yu. Zubkov, A. I. Mashin, and A. V. Ershov, ‘The morphology, electron structure, and optical properties of self-assembled silicon nanostructures on the surface of highly oriented pyrolytic graphite’, *Semiconductors*, vol. 45, no. 1, pp. 56–60, Jan. 2011

[43] M. De Crescenzi *et al.*, ‘Formation of Silicene Nanosheets on Graphite’, *ACS Nano*, vol. 10, no. 12, pp. 11163–11171, Dec. 2016

[44] K. Kawahara *et al.*, ‘Determination of atomic positions in silicene on Ag(111) by low-energy electron diffraction’, *Surf. Sci.*, vol. 623, pp. 25–28, May 2014

[45] P. Moras, T. O. Mentes, P. M. Sheverdyaeva, A. Locatelli, and C. Carbone, ‘Coexistence of multiple silicene phases in silicon grown on Ag(1 1 1)’, *J. Phys. Condens. Matter*, vol. 26, no. 18, p. 185001, May 2014,

[46] C.-L. Lin *et al.*, ‘Structure of Silicene Grown on Ag(111)’, *Appl. Phys. Express*, vol. 5, no. 4, p. 045802, Mar. 2012

[47] A. Resta *et al.*, ‘Atomic Structures of Silicene Layers Grown on Ag(111): Scanning Tunneling Microscopy and Noncontact Atomic Force Microscopy Observations’, *Sci. Rep.*, vol. 3, no. 1, p. 2399, Dec. 2013

[48] R. Arafune *et al.*, ‘Structural transition of silicene on Ag(111)’, *Surf. Sci.*, vol. 608, pp. 297–300, Feb. 2013

[49] P. De Padova *et al.*, ‘Evidence of Dirac fermions in multilayer silicene’, *Appl. Phys. Lett.*, vol. 102, no. 16, p. 163106, Apr. 2013

[50] D. Chiappe, C. Grazianetti, G. Tallarida, M. Fanciulli, and A. Molle, ‘Local Electronic Properties of Corrugated Silicene Phases’, *Adv. Mater.*, vol. 24, no. 37, pp. 5088–5093, Sep. 2012

[51] A. Curcella, R. Bernard, Y. Borensztein, A. Resta, M. Lazzeri, and G. Prévot, ‘Determining the atomic structure of the (4 × 4) silicene layer on Ag(111) by combined grazing-incidence x-ray diffraction measurements and first-principles calculations’, *Phys. Rev. B*, vol. 94, no. 16, p. 165438, Oct. 2016

[52] H. Jamgotchian *et al.*, ‘A comprehensive study of the (2√3 × 2√3)R30° structure of silicene on Ag(1 1 1)’, *J. Phys. Condens. Matter*, vol. 27, no. 39, p. 395002, Oct. 2015

[53] H. Jamgotchian, B. Ealet, H. Maradj, J.-Y. Hoarau, J.-P. Bibérian, and B. Aufray, ‘A comprehensive analysis of the (√13 × √13) *R* 13.9° type II structure of silicene on Ag(1 1

1)’, *J. Phys. Condens. Matter*, vol. 28, no. 19, p. 195002, May 2016

[54] A. Curcella, R. Bernard, Y. Borensztein, A. Resta, M. Lazzeri, and G. Prévot, ‘Structure and stability of silicene on Ag(111) reconstructions from grazing incidence x-ray diffraction and density functional theory’, *Phys. Rev. B*, vol. 99, no. 20, p. 205411, May 2019

[55] S. K. Mahatha *et al.*, ‘Silicene on Ag(111): A honeycomb lattice without Dirac bands’, *Phys. Rev. B*, vol. 89, no. 20, p. 201416, May 2014

[56] P. M. Sheverdyaeva *et al.*, ‘Electronic States of Silicene Allotropes on Ag(111)’, *ACS Nano*, vol. 11, no. 1, pp. 975–982, Jan. 2017

[57] P. Vogt *et al.*, ‘Synthesis and electrical conductivity of multilayer silicene’, *Appl. Phys. Lett.*, vol. 104, no. 2, p. 021602, Jan. 2014

[58] A. J. Mannix, B. Kiraly, B. L. Fisher, M. C. Hersam, and N. P. Guisinger, ‘Silicon Growth at the Two-Dimensional Limit on Ag(111)’, *ACS Nano*, vol. 8, no. 7, pp. 7538–7547, Jul. 2014

[59] T. Shirai, T. Shirasawa, T. Hirahara, N. Fukui, T. Takahashi, and S. Hasegawa, ‘Structure determination of multilayer silicene grown on Ag(111) films by electron diffraction: Evidence for Ag segregation at the surface’, *Phys. Rev. B*, vol. 89, no. 24, p. 241403, Jun. 2014

[60] J. Sone, T. Yamagami, Y. Aoki, K. Nakatsuji, and H. Hirayama, ‘Epitaxial growth of silicene on ultra-thin Ag(111) films’, *New J. Phys.*, vol. 16, no. 9, p. 095004, Sep. 2014

[61] E. Salomon, R. El Ajjouri, G. L. Lay, and T. Angot, ‘Growth and structural properties of silicene at multilayer coverage’, *J. Phys. Condens. Matter*, vol. 26, no. 18, p. 185003, May 2014

[62] S. Cahangirov *et al.*, ‘Atomic structure of the 3 × 3 phase of silicene on Ag(111)’, *Phys. Rev. B*, vol. 90, no. 3, p. 035448, Jul. 2014

[63] C. Leandri *et al.*, ‘Self-aligned silicon quantum wires on Ag(110)’, *Surf. Sci.*, vol. 574, no. 1, pp. L9–L15, Jan. 2005

[64] M. R. Tchalala *et al.*, ‘Atomic structure of silicene nanoribbons on Ag(110)’, *J. Phys. Conf. Ser.*, vol. 491, p. 012002, Mar. 2014

[65] S. Colonna, G. Serrano, P. Gori, A. Cricenti, and F. Ronci, ‘Systematic STM and LEED investigation of the Si/Ag(110) surface’, *J. Phys. Condens. Matter*, vol. 25, no. 31, p. 315301, Aug. 2013

[66] G. Prévot, C. Hogan, T. Leoni, R. Bernard, E. Moyen, and L. Masson, ‘Si Nanoribbons on Ag(110) Studied by Grazing-Incidence X-Ray Diffraction, Scanning Tunneling Microscopy, and Density-Functional Theory: Evidence of a Pentamer Chain Structure’, *Phys. Rev. Lett.*, vol. 117, no. 27, p. 276102, Dec. 2016

[67] C. Hogan, S. Colonna, R. Flammini, A. Cricenti, and F. Ronci, ‘Structure and stability of Si/Ag(110) nanoribbons’, *Phys. Rev. B*, vol. 92, no. 11, p. 115439, Sep. 2015

[68] J. I. Cerdá, J. Sławińska, G. Le Lay, A. C. Marele, J. M. Gómez-Rodríguez, and M. E. Dávila, ‘Unveiling the pentagonal nature of perfectly aligned single-and double-strand Si nano-ribbons on Ag(110)’, *Nat. Commun.*, vol. 7, no. 1, p. 13076, Dec. 2016

[69] Y. Yamada-Takamura *et al.*, ‘Surface and Interface Studies of GaN Epitaxy on Si(111) via ZrB 2 Buffer Layers’, *Phys. Rev. Lett.*, vol. 95, no. 26, p. 266105, Dec. 2005

[70] Y. Yamada-Takamura, F. Bussolotti, A. Fleurence, S. Bera, and R. Friedlein, ‘Surface electronic structure of ZrB2 buffer layers for GaN growth on Si wafers’, *Appl. Phys. Lett.*, vol. 97, no. 7, p. 073109, Aug. 2010

[71] O. G. Shpyrko *et al.*, ‘Surface Crystallization in a Liquid AuSi Alloy’, *Science*, vol. 313, no. 5783, pp. 77–80, Jul. 2006

[72] O. G. Shpyrko *et al.*, ‘Crystalline surface phases of the liquid Au-Si eutectic alloy’, *Phys. Rev. B*, vol. 76, no. 24, p. 245436, Dec. 2007

[73] M. Kopciuszyński, P. Dyniec, M. Krawiec, M. Jałochowski, and R. Zdyb, ‘Quantum size effect in ultrathin Au films on the Si(111) surface’, *Appl. Surf. Sci.*, vol. 331, pp. 512–518, Mar. 2015

[74] K. Quertite *et al.*, ‘Silicene Nanoribbons on an Insulating Thin Film’, *Adv. Funct. Mater.*, p. 2007013, Nov. 2020

[75] M. Satta *et al.*, ‘The adsorption of silicon on an iridium surface ruling out silicene growth’, *Nanoscale*, vol. 10, no. 15, pp. 7085–7094, 2018

[76] M. Švec *et al.*, ‘Silicene versus two-dimensional ordered silicide: Atomic and electronic structure of Si- (19 × 19) R 23 . 4 ◦ /Pt(111)’, *Phys. Rev. B*, vol. 89, no. 20, p. 201412, May 2014

[77] D. Chiappe *et al.*, ‘Two-Dimensional Si Nanosheets with Local Hexagonal Structure on a MoS $_2$ Surface’, *Adv. Mater.*, vol. 26, no. 13, pp. 2096–2101, Apr. 2014

[78] R. van Bremen, Q. Yao, S. Banerjee, D. Cakir, N. Oncel, and H. J. W. Zandvliet, ‘Intercalation of Si between MoS $_2$ layers’, *Beilstein J. Nanotechnol.*, vol. 8, pp. 1952–1960, Sep. 2017

[79] B. Marsen, M. Lonfat, P. Scheier, and K. Sattler, ‘Energy gap of silicon clusters studied by scanning tunneling spectroscopy’, *Phys. Rev. B*, vol. 62, no. 11, pp. 6892–6895, Sep. 2000

[80] W. Peng *et al.*, ‘Resolving the Controversial Existence of Silicene and Germanene Nanosheets Grown on Graphite’, *ACS Nano*, vol. 12, no. 5, pp. 4754–4760, May 2018

[81] M. E. Dávila, L. Xian, S. Cahangirov, A. Rubio, and G. Le Lay, ‘Germanene: a novel two-dimensional germanium allotrope akin to graphene and silicene’, *New J. Phys.*, vol. 16, no. 9, p. 095002, Sep. 2014

[82] M. E. Dávila and G. Le Lay, ‘Few layer epitaxial germanene: a novel two-dimensional Dirac material’, *Sci. Rep.*, vol. 6, no. 1, p. 20714, Aug. 2016

[83] D. A. Muzychenko, A. I. Oreshkin, S. I. Oreshkin, S. S. Ustavschikov, A. V. Putilov, and A. Yu. Aladyshkin, ‘The surface structures growth’s features caused by Ge adsorption on the Au(111) surface’, *JETP Lett.*, vol. 106, no. 4, pp. 217–222, Aug. 2017

[84] W. Wang and R. I. G. Uhrberg, ‘Investigation of the atomic and electronic structures of highly ordered two-dimensional germanium on Au(111)’, *Phys. Rev. Mater.*, vol. 1, no. 7, p. 074002, Dec. 2017

[85] H. Oughaddou *et al.*, ‘Ge/Ag(111) semiconductor-on-metal growth: Formation of an Ag 2 Ge surface alloy’, *Phys. Rev. B*, vol. 62, no. 24, pp. 16653–16656, Dec. 2000

[86] W. Wang, H. M. Sohail, J. R. Osiecki, and R. I. G. Uhrberg, ‘Broken symmetry induced band splitting in the Ag 2 Ge surface alloy on Ag(111)’, *Phys. Rev. B*, vol. 89, no. 12, p. 125410, Mar. 2014

[87] C.-H. Lin *et al.*, 'Single-layer dual germanene phases on Ag(111)', *Phys. Rev. Mater.*, vol. 2, no. 2, p. 024003, Feb. 2018

[88] L. Li *et al.*, 'Buckled Germanene Formation on Pt(111)', *Adv. Mater.*, vol. 26, no. 28, pp. 4820–4824, Jul. 2014

[89] R. Stephan *et al.*, 'Germanene on Al(111): Interface Electronic States and Charge Transfer', *J. Phys. Chem. C*, vol. 120, no. 3, pp. 1580–1585, Jan. 2016

[90] S. Endo *et al.*, "(√3)×(√3) germanene on Al(111) grown at nearly room temperature"', *Appl. Phys. Express*, vol. 11, no. 1, p. 019201, Jan. 2018

[91] W. Wang and R. I. G. Uhrberg, 'Coexistence of strongly buckled germanene phases on Al(111)', *Beilstein J. Nanotechnol.*, vol. 8, pp. 1946–1951, Sep. 2017

[92] Y. Fukaya, I. Matsuda, B. Feng, I. Mochizuki, T. Hyodo, and S. Shamoto, 'Asymmetric structure of germanene on an Al(111) surface studied by total-reflection high-energy positron diffraction', *2D Mater.*, vol. 3, no. 3, p. 035019, Sep. 2016

[93] E. A. Martínez, J. D. Fuhr, O. Grizzi, E. A. Sánchez, and E. D. Cantero, 'Growth of Germanene on Al(111) Hindered by Surface Alloy Formation', *J. Phys. Chem. C*, p. acs.jpcc.9b02614, May 2019

[94] P. Bampoulis *et al.*, 'Structural and Electronic Properties of Germanene on MoS 2', *Phys. Rev. Lett.*, vol. 116, no. 25, p. 256804, Jun. 2016

[95] J. Gou *et al.*, 'Strained monolayer germanene with 1 × 1 lattice on Sb(111)', *2D Mater.*, vol. 3, no. 4, p. 045005, Sep. 2016

[96] R. Stephan *et al.*, 'Tip-Induced Switch of Germanene Atomic Structure', *J. Phys. Chem. Lett.*, vol. 8, no. 18, pp. 4587–4593, Sep. 2017

[97] D. A. Muzychenko, S. I. Oreshkin, V. I. Panov, C. Van Haesendonck, and A. I. Oreshkin, 'Single and multi domain buckled germanene phases on Al(111) surface', *Nano Res.*, vol. 12, no. 12, pp. 2988–2996, Dec. 2019

[98] E. Martinez, E. D. Cantero, J. D. Fuhr, M. L. Martiarena, O. Grizzi, and E. A. Sánchez, 'Ge films on Au(111) and Al(111): thermal stability', *Mater. Today Proc.*, vol. 14, pp. 148–151, 2019

[99] D. A. Muzychenko, A. I. Oreshkin, A. D. Legen'ka, and C. Van Haesendonck, 'Atomic insights into single-layer and bilayer germanene on Al(111) surface', *Mater. Today Phys.*, vol. 14, p. 100241, Aug. 2020

[100] J. Fang, P. Zhao, and G. Chen, 'Germanene Growth on Al(111): A Case Study of Interface Effect', *J. Phys. Chem. C*, vol. 122, no. 32, pp. 18669–18681, Aug. 2018

[101] E. Golias, E. Xenogiannopoulou, D. Tsoutsou, P. Tsipas, S. A. Giamini, and A. Dimoulas, 'Surface electronic bands of submonolayer Ge on Ag(111)', *Phys. Rev. B*, vol. 88, no. 7, p. 075403, Aug. 2013

[102] Y. Liu *et al.*, 'Role of Atomic Interaction in Electronic Hybridization in Two-Dimensional Ag $_2$ Ge Nanosheets', *J. Phys. Chem. C*, vol. 121, no. 31, pp. 16754–16760, Aug. 2017

[103] M. S. Rahman, T. Nakagawa, and S. Mizuno, 'Germanene: Experimental Study for Graphene Like Two Dimensional Germanium', *Evergreen*, vol. 1, no. 2, pp. 25–29, Sep. 2014

[104] J. Zhuang *et al.*, 'Dirac Signature in Germanene on Semiconducting Substrate', *Adv. Sci.*,

vol. 5, no. 7, p. 1800207, Jul. 2018

[105] J. Yuhara *et al.*, ‘Germanene Epitaxial Growth by Segregation through Ag(111) Thin Films on Ge(111)’, *ACS Nano*, vol. 12, no. 11, pp. 11632–11637, Nov. 2018

[106] K. Ito *et al.*, ‘Growth of two-dimensional Ge crystal by annealing of heteroepitaxial Ag/Ge(111) under N $_2$ ambient’, *Jpn. J. Appl. Phys.*, vol. 57, no. 6S1, p. 06HD08, Jun. 2018

[107] M. Kurosawa, A. Ohta, M. Araidai, and S. Zaima, ‘Surface-segregated Si and Ge ultrathin films formed by Ag-induced layer exchange process’, *Jpn. J. Appl. Phys.*, vol. 55, no. 8S1, p. 08NB07, Aug. 2016

[108] K. Zhang, R. Bernard, Y. Borensztein, H. Cruguel, and G. Prévot, ‘Growth of germanium-silver surface alloys followed by *in situ* scanning tunneling microscopy: Absence of germanene formation’, *Phys. Rev. B*, vol. 102, no. 12, p. 125418, Sep. 2020

[109] E. D. Cantero *et al.*, ‘Growth of germanium on Au(111): formation of germanene or intermixing of Au and Ge atoms?’, *Phys. Chem. Chem. Phys.*, vol. 19, no. 28, pp. 18580–18586, 2017

[110] Z. Qin *et al.*, ‘Direct Evidence of Dirac Signature in Bilayer Germanene Islands on Cu(111)’, *Adv. Mater.*, vol. 29, no. 13, p. 1606046, 2017

[111] F. Li, W. Wei, X. Lv, B. Huang, and Y. Dai, ‘Evolution of the linear band dispersion of monolayer and bilayer germanene on Cu(111)’, *Phys. Chem. Chem. Phys.*, vol. 19, no. 34, pp. 22844–22851, 2017

[112] C.-S. Ho, S. Banerjee, M. Batzill, D. E. Beck, and B. E. Koel, ‘Formation and structure of a (√19×√19)R23.4°-Ge/Pt(111) surface alloy’, *Surf. Sci.*, vol. 603, no. 9, pp. 1161–1167, May 2009

[113] R. van Bremen *et al.*, ‘Ge $_2$ Pt hut clusters: A substrate for germanene’, *J. Appl. Phys.*, vol. 124, no. 12, p. 125301, Sep. 2018

[114] G. Binnig, H. Rohrer, C. Gerber, and E. Weibel, ‘Surface Studies by Scanning Tunneling Microscopy’, *Phys. Rev. Lett.*, vol. 49, no. 1, p. 5

[115] B. E. Nieuwenhuys, O. G. Van Aardenne, and W. M. H. Sachtler, ‘Adsorption of xenon on group VIII and ib metals studied by photoelectric work function measurements’, *Chem. Phys.*, vol. 5, no. 3, pp. 418–428, Sep. 1974

[116] J. Bardeen, ‘Tunnelling from a Many-Particle Point of View’, *Phys. Rev. Lett.*, vol. 6, no. 2, pp. 57–59, Jan. 1961

[117] J. Tersoff and D. R. Hamann, ‘Theory and Application for the Scanning Tunneling Microscope’, *Phys. Rev. Lett.*, vol. 50, no. 25, pp. 1998–2001, Jun. 1983

[118] J. Tersoff and D. R. Hamann, ‘Theory of the scanning tunneling microscope’, *Phys. Rev. B*, vol. 31, no. 2, pp. 805–813, Jan. 1985

[119] D. Nečas and P. Klapetek, ‘Gwyddion: an open-source software for SPM data analysis’, *Open Phys.*, vol. 10, no. 1, Jan. 2012

[120] A.-S. Lucier, H. Mortensen, Y. Sun, and P. Grütter, ‘Determination of the atomic structure of scanning probe microscopy tungsten tips by field ion microscopy’, *Phys. Rev. B*, vol. 72, no. 23, p. 235420, Dec. 2005

[121] B. E. Warren, *X-ray Diffraction*. Courier Corporation, 1990

[122] R. Feidenhans’l, ‘Surface structure determination by X-ray diffraction’, *Surf. Sci. Rep.*, vol.

10, no. 3, pp. 105–188, May 1989

[123] M. S. Rahman, T. Nakagawa, and S. Mizuno, 'Growth of Si on Ag(111) and determination of large commensurate unit cell of high-temperature phase', *Jpn. J. Appl. Phys.*, vol. 54, no. 1, p. 015502, Dec. 2014

[124] O. Robach, Y. Garreau, K. Aïd, and M. B. Véron-Jolliot, 'Corrections for surface X-ray diffraction measurements using the *Z* -axis geometry: finite size effects in direct and reciprocal space', *J. Appl. Crystallogr.*, vol. 33, no. 4, pp. 1006–1018, Aug. 2000

[125] S. Roobol, W. Onderwaater, J. Drnec, R. Felici, and J. Frenken, '*BINoculars* : data reduction and analysis software for two-dimensional detectors in surface X-ray diffraction', *J. Appl. Crystallogr.*, vol. 48, no. 4, pp. 1324–1329, Aug. 2015

[126] G. Prévot, R. Bernard, H. Cruguel, and Y. Borensztein, 'Monitoring Si growth on Ag(111) with scanning tunneling microscopy reveals that silicene structure involves silver atoms', *Appl. Phys. Lett.*, vol. 105, no. 21, p. 213106, Nov. 2014

[127] Q.-X. Chen, H. Yang, and G. Chen, 'Theoretical studies on alloying of germanene supported on Al (111) substrate', vol. 29, no. 10, p. 15, 2020

[128] M. Satta, S. Colonna, R. Flammini, A. Cricenti, and F. Ronci, 'Silicon Reactivity at the Ag(111) Surface', *Phys. Rev. Lett.*, vol. 115, no. 2, p. 026102, Jul. 2015

[129] S. Narasimhan and D. Vanderbilt, 'Elastic stress domains and the herringbone reconstruction on Au(111)', *Phys. Rev. Lett.*, vol. 69, no. 10, pp. 1564–1567, Sep. 1992

[130] B. Croset and G. Prévot, 'Elastic relaxations and interactions for vicinal and self-organized surfaces: Role of crystalline anisotropy', *Phys. Rev. B*, vol. 73, no. 4, p. 045434, Jan. 2006

[131] G. Prévot, A. Coati, B. Croset, and Y. Garreau, 'Direct observation of elastic displacement modes by grazing-incidence X-ray diffraction', *J. Appl. Crystallogr.*, vol. 40, no. 5, pp. 874–882, 2007

[132] G. O. Pötschke and R. J. Behm, 'Interface structure and misfit dislocations in thin Cu films on Ru(0001)', *Phys. Rev. B*, vol. 44, no. 3, pp. 1442–1445, Jul. 1991

[133] W. L. Ling *et al.*, 'Herringbone and triangular patterns of dislocations in Ag, Au, and AgAu alloy films on Ru(0001)', *Surf. Sci.*, vol. 600, no. 9, pp. 1735–1757, May 2006

[134] B. Peng *et al.*, 'First-Principles Prediction of Ultralow Lattice Thermal Conductivity of Dumbbell Silicene: A Comparison with Low-Buckled Silicene', *ACS Appl. Mater. Interfaces*, vol. 8, no. 32, pp. 20977–20985, Aug. 2016

[135] P. Bampoulis, L. Zhang, A. Safaei, R. van Gastel, B. Poelsema, and H. J. W. Zandvliet, 'Germanene termination of Ge 2 Pt crystals on Ge(110)', J. Phys.: Condens. Matter, vol. 26, no. 44, p. 442001, Nov. 2014

[136] Chiniwar S, Huang A, Chen T-Y, Lin C-H, Hsing C-R, Chen W-C, Cheng C-M, Jeng H-T, Wei C M, Pai W W and Tang S-J 2019 Substrate-mediated umklapp scattering at the incommensurate interface of a monatomic alloy layer Phys. Rev. B 99 155408